

Freie Universität



Berlin

# *Operando* Raman investigation of electrochemical CO<sub>2</sub> reduction reaction catalyzed by copper-based materials

## **A Dissertation**

Submitted in Partial Fulfilment of the Requirements for  
the Degree of Doctor rerum naturalium (Dr. rer. nat.)

to the Department of Physics  
of Freie Universität Berlin

by

Shan Jiang

Berlin, 2021

1. Advisor: Prof. Dr. Holger Dau

2. Advisor: Prof. Dr. Peter Strasser

Date of defense: 5 November 2021

## Abstract

Anthropogenic activity causes excessive CO<sub>2</sub> emission in the atmosphere. In the CO<sub>2</sub> reduction reaction (CO<sub>2</sub>RR), CO<sub>2</sub> is converted electrochemically into valuable products including methane, ethylene, and other hydrocarbons. Large-scale employment of efficient CO<sub>2</sub>RR could diminish the use of fossil-fuel resources and thereby counteract rising levels of atmospheric CO<sub>2</sub>. Although plenty of catalysts have been investigated, copper (Cu) is the only metal that can produce reasonable amount of hydrocarbon products with two or more carbon atoms (C<sub>2+</sub> products). However, low selectivity and high overpotentials remain as two obstacles for practical application. The reactivity determinants and reaction mechanisms in CO<sub>2</sub>RR and their relation to formation of specific products are insufficiently understood only. Therefore, *operando* techniques that provide insight in reaction mechanism for the catalyst material during electrocatalytic operation are of great importance.

In this thesis, *operando* Raman spectroscopy was adopted to investigate Cu-based foam-like materials for CO<sub>2</sub>RR catalysis. These Cu foams, which have been characterized regarding CO<sub>2</sub>RR activity previously, are shown to exhibit surface-enhanced Raman scattering (SERS) activity, thereby facilitating the detection of surface-bound molecular species. A normalization procedure was developed for meaningful analysis of the electric potential dependence of the detected species. A comprehensive overview of various potential dependencies of Raman spectra are reported.

Special focus was put on the role of oxides and the bicarbonate electrolyte. Evidence for copper carbonate hydroxide (CuCarHyd), which resembles the mineral malachite, was obtained. Its carbonate ions can be directly converted to CO at low overpotentials. These and further experiments, including <sup>13</sup>C isotope experiments and local pH detection, suggest a basic mode of CO<sub>2</sub>/carbonate reduction at Cu electrodes that contrasts previous mechanistic models: the starting point in carbon reduction is not CO<sub>2</sub> but carbonate ions bound to the metallic Cu electrode in form of CuCarHyd structures. Cu oxides residues could enhance CO<sub>2</sub>RR indirectly by supporting formation of CuCarHyd motifs. The presence of CuCarHyd patches at catalytic potentials may result from alkalization in conjunction with local electrical potential gradients, enabling the formation of metastable CuCarHyd motifs over a large range of potentials. It is conceivable that the interaction of oxide and bicarbonate also may be the key for the enhanced C<sub>2+</sub> production activity.

*Operando* Raman spectroscopy was also used to investigate a bimetallic catalyst CuAg foam that shows a primary selectivity for CO. The Raman spectra on CuAg foam shows an earlier departure of CO from the surface. Further <sup>13</sup>C isotope experiments probed a surface intermediate that can be assigned to the symmetrical stretching vibration of bidentate.

Mass transport limitations of carbonate species may influence the CO<sub>2</sub>RR mechanism. Raman spectroscopy (without SERS) was used to detect the local pH at the Cu foam surface. Severe local alkalization was observed. The same process was analyzed in D<sub>2</sub>O electrolyte and using a flow-cell setup, persistent local alkalization was also observed. Further results of potential influences of local pH change on the CO<sub>2</sub>RR are presented.

## Zusammenfassung

Anthropogene Aktivitäten verursachen einen übermäßigen CO<sub>2</sub>-Ausstoß in die Atmosphäre. Bei der CO<sub>2</sub>-Reduktionsreaktion (CO<sub>2</sub>RR) wird CO<sub>2</sub> elektrochemisch in wertvolle Produkte wie Methan, Ethylen und andere Kohlenwasserstoffe umgewandelt. Der großtechnische Einsatz einer effizienten CO<sub>2</sub>RR könnte den Verbrauch fossiler Brennstoffe verringern und damit dem Anstieg des CO<sub>2</sub>-Gehalts in der Atmosphäre entgegenwirken. Obwohl viele Katalysatoren untersucht wurden, ist Kupfer (Cu) das einzige Metall, das eine angemessene Menge an Produkten mit zwei oder mehr Kohlenstoffatomen (C<sub>2+</sub>-Produkte) erzeugen kann. Allerdings bleiben niedrige Selektivität und hohe Überspannungen zwei Hindernisse für die praktische Anwendung. Die Reaktivitätsdeterminanten und -mechanismen in der CO<sub>2</sub>RR und ihre Beziehung zur Bildung spezifischer Produkte sind nur unzureichend verstanden. Daher sind *operando*-Techniken, die einen Einblick in den Reaktionsmechanismus während des elektrokatalytischen Betriebs ermöglichen, von großer Bedeutung.

In dieser Arbeit wurde *operando* Raman-Spektroskopie eingesetzt, um Cu-Schäume für die CO<sub>2</sub>RR-Katalyse zu untersuchen. Diese Cu-Schäume zeigen oberflächenverstärkte Raman-Streuung (SERS), was den Nachweis von oberflächengebundenen molekularen Spezies ermöglicht. Für eine aussagekräftige Analyse der elektrischen Potentialabhängigkeit der detektierten Spezies wurde ein Normalisierungsverfahren entwickelt. Es wird ein umfassender Überblick über verschiedene Potentialabhängigkeiten von Raman-Spektren berichtet.

Besonderes Augenmerk wurde dabei auf die Rolle der Oxide und des Bicarbonat-Elektrolyten gelegt. Es wurde der Nachweis von Kupfercarbonathydroxid (CuCarHyd) erbracht, das dem Mineral Malachit ähnelt. Seine Carbonat-Ionen können bei niedrigen Überspannungen direkt zu CO umgesetzt werden. Diese und weitere Experimente, einschließlich <sup>13</sup>C-Isotopenexperimenten und lokaler pH-Detektion, legen einen grundlegenden Modus der CO<sub>2</sub>/Carbonat-Reduktion an Cu-Elektroden nahe, der im Gegensatz zu bisherigen mechanistischen Modellen steht: Ausgangspunkt der Kohlenstoffreduktion ist nicht CO<sub>2</sub>, sondern an die metallische Cu-Elektrode gebundene Carbonat-Ionen in Form von CuCarHyd-Strukturen. Cu-Oxidreste könnten die CO<sub>2</sub>RR indirekt verbessern, indem sie die Bildung von CuCarHyd-Motiven unterstützen. Das Vorhandensein von CuCarHyd-Flecken bei katalytischen Potentialen könnte aus der Alkalisierung in Verbindung mit lokalen elektrischen Potentialgradienten resultieren, was die Bildung von metastabilen CuCarHyd-Motiven über einen großen Bereich von Potentialen ermöglicht. Es ist denkbar, dass die Wechselwirkung von Oxid und Bicarbonat auch der Schlüssel für die verstärkte C<sub>2+</sub>-Produktionsaktivität sein könnte.

Mit Hilfe der *Operando*-Raman-Spektroskopie wurde auch ein bimetallischer CuAg-Schaum untersucht, der eine hohe Selektivität für CO zeigt. Die Raman-Spektren zeigen einen früheren Abgang von CO von der Oberfläche. <sup>13</sup>C-Isotopenexperimente fanden ein Oberflächenintermediat, das der symmetrischen Streckschwingung des Bidentats zugeordnet werden kann.

Massentransportbeschränkungen der Carbonat-Spezies könnten den CO<sub>2</sub>RR-Mechanismus beeinflussen. Raman-Spektroskopie (ohne SERS) wurde verwendet, um den lokalen pH-Wert an der Cu-Schaumoberfläche zu bestimmen. Es wurde eine starke lokale Alkalisierung beobachtet. Der Prozess wurde zudem in D<sub>2</sub>O und unter Verwendung eines Durchflusszellen-aufbaus analysiert: es wurde ebenfalls eine anhaltende lokale Alkalisierung beobachtet. Weitere Ergebnisse zu Einflüssen der lokalen pH-Veränderung auf die CO<sub>2</sub>RR werden vorgestellt.

# Table of contents

Glossary.....	VI
1 Introduction.....	1
1.1 Electrochemical CO <sub>2</sub> reduction – a route towards a carbon neutral future.....	1
1.2 Electrochemical reduction of CO <sub>2</sub> : reaction mechanism.....	2
1.2.1 Electrochemical CO <sub>2</sub> reduction reaction (CO <sub>2</sub> RR).....	2
1.2.2 CO <sub>2</sub> activation.....	3
1.2.3 CO to C <sub>1</sub> and C <sub>2+</sub> products.....	4
1.2.4 Electrode morphology effects.....	8
1.2.5 Oxide-derived Cu catalyst.....	8
1.3 Raman spectroscopy and SERS.....	9
1.3.1 Basic theory of Raman spectroscopy.....	9
1.3.2 Raman selection rules.....	12
1.3.3 Isotope labelling.....	13
1.3.4 Raman spectrometer.....	14
1.3.5 SERS.....	14
1.3.5.1 SERS mechanisms: electromagnetic and chemical enhancement mechanism	15
1.3.5.2 Electrochemical SERS.....	15
1.4 Scope and organisation of this thesis.....	16
2 New aspects of <i>operando</i> Raman spectroscopy applied to electrochemical CO <sub>2</sub> reduction on Cu foams.....	17
2.1 Introduction.....	17
2.2 Results and discussion.....	18
2.2.1 The dendritic structure.....	18
2.2.2 <i>Operando</i> SERS spectra and SERS background.....	21
2.2.3 Origin of SERS background and validation of the data analysis method.....	26
2.2.3.1 SERS effect related to Cu oxide.....	26
2.2.3.2 Thiophenol calibration experiment.....	29
2.2.4 Adsorbed species and corresponding assignments.....	30
2.2.4.1 Carbonate adsorption.....	31
2.2.4.2 Adsorbed CO intermediates.....	33

2.2.4.3	Adsorbed intermediates with C-H bonds.....	35
2.3	Conclusions .....	38
2.4	Materials and methods.....	40
2.4.1	Preparation of Cu foams.....	40
2.4.2	Data collection.....	40
2.4.3	Data treatment .....	41
3	The role of bicarbonate/Cu-oxide interaction in Cu catalysed CO <sub>2</sub> electro-reduction ....	42
3.1	Introduction .....	42
3.2	Results .....	43
3.2.1	The origin of peaks at 350, 705, 1530 cm <sup>-1</sup> .....	43
3.2.2	Peak (D) cannot be attributed to adsorbed (bi)carbonate .....	50
3.2.3	Thermodynamics of the system and formation of metastable material .....	51
3.2.4	<i>In-situ</i> formation of CuCarHyd .....	54
3.2.5	CuCarHyd as CO precursor.....	56
3.2.6	CO Intensity relates to (hydro)oxide content. ....	62
3.2.7	CO presence at low overpotential relates to (hydro) oxide .....	63
3.2.8	Discussion .....	64
3.3	Conclusions .....	66
3.4	Materials and methods.....	67
4	<i>Operando</i> Raman research on bimetallic CuAg catalysts for CO <sub>2</sub> reduction to CO .....	69
4.1	Introduction .....	69
4.2	Results and discussion.....	71
4.2.1	CO selectivity on CuAg foams.....	71
4.2.2	CO production pathway on CuAg foams .....	74
4.3	Conclusions .....	78
4.4	Materials and methods.....	78
5	Mass transport and local pH gradient on Cu foam electrode during CO <sub>2</sub> reduction reaction.....	79
5.1	Introduction .....	79
5.2	Results and discussion.....	81
5.2.1	Local pH gradient determination with <i>in-situ</i> Raman spectroscopy.....	81
5.2.2	Local pH during redox potentials .....	86

5.2.3	Local pH in flow cell.....	90
5.2.4	Local pH in D <sub>2</sub> O electrolyte .....	91
5.2.5	Further results related to local alkalization.....	95
5.2.5.1	Local pH alkalization for CO to C <sub>2</sub> product conversion - Time-dependence of Raman spectra .....	95
5.2.5.2	Bubble formation.....	97
5.2.5.3	(Hydro)oxide bands at high overpotentials.....	98
5.3	Conclusions .....	100
5.4	Materials and methods.....	101
6	Summary of key results .....	102
7	References .....	105
8	Appendix .....	117
	Acknowledgement.....	152
	List of publications.....	154
	Selbständigkeitserklärung.....	155

# Glossary

ATR-SEIRAS	Attenuated total reflectance surface-enhanced IR absorption spectroscopy
CA	Chronoamperometry
CCD	Charge-coupled device
CE	Chemical enhancement
CO <sub>2</sub> RR	CO <sub>2</sub> reduction reaction
CORR	CO reduction reaction
CuCarHyd	Copper carbonate hydroxide
CV	Cyclic voltammetry
DFT	Density functional theory
ECSA	Electrochemical active surface area
EM	Electromagnetic effect
ET	Electron transfer
FE	Faradic efficiency
GC	Gas chromatography
HER	Hydrogen evolution reaction
IR	Infrared
K <sub>pi</sub>	KH <sub>2</sub> PO <sub>4</sub> /K <sub>2</sub> HPO <sub>4</sub> buffer
LSV	Linear sweeping voltammetry
OCP	Open circuit potential
OD-Cu	Oxide-derived Cu
PCET	Proton-coupled electron transfer
pzc	potential of zero charge
RDS	Rate-determining step
SERS	Surface enhanced Raman scattering
SPR	Surface plasma resonance
TEM	Transmission electron microscopy
V <sub>RHE</sub>	Potential versus reversible hydrogen electrode
XAS	X-ray absorption spectroscopy
XPS	X-ray photoelectron spectroscopy
η	overpotential



# 1. Introduction

## 1.1 Electrochemical CO<sub>2</sub> reduction – a route towards a carbon neutral future

The concentration of carbon dioxide in the atmosphere has risen from 310 ppm to 410 ppm during the past six decades (Friedlingstein et al., 2020). The rise of the atmospheric CO<sub>2</sub> level perfectly matches with the fossil fuel emissions curve. It is thus clear that it is mainly caused by human activities. Global climate change is a direct consequence of CO<sub>2</sub> emission. During 1980-2018, the global mean surface temperature increased by 0.5 °C and is now 1 °C above the pre-industrial period, which is faster than the equal increase occurred during 1950-2000 (V. Masson-Delmotte et al., 2018). A conservative speculation states that at about 2050, this difference will increase to 1.5 °C or even 2 °C (Hoegh-Guldberg et al., 2019; V. Masson-Delmotte et al., 2018). It should be emphasized that 1.5 °C of global surface temperature change is the tipping point, above which severe environmental consequences have to be expected (Hoegh-Guldberg et al., 2019). For instance, the ice sheet (permafrost) in the north pole will melt and the sea level increase, resulting in inundation of small islands; unusually extreme hot weathers will cause droughts in south Africa or floods in the east Asian area; as well as the destruction of ecosystems including the depletion of reefs, etc (Hoegh-Guldberg et al., 2019).

The imperative of stabilizing global climate change to a maximum of 1.5 °C is urgent and calls for creative solutions (Hoegh-Guldberg et al., 2019). Ever since energy production was and is predominantly based on burning of fossil fuels and unequally consumed between the nations. Today there are still quite many nations that are little developed, and more and more people are experiencing poverty. Therefore, the ultimate goal is to develop environmentally friendly and face the challenges of climate change at the same time (Chu, Cui, & Liu, 2016; Eisenberg, Gray, & Crabtree, 2019; Lewis & Nocera, 2006). This calls for a change in our energy structure. Technologies for clean energy including solar, wind, tide and geothermal heat energy need to be developed (Armaroli & Balzani, 2016; Chu et al., 2016; Eisenberg et al., 2019; Lewis & Nocera, 2006). With consistent effort, electricity can be produced through clean energy and the prices will decrease. This renewable electricity can be combined with electrocatalytic reactions to store energy in chemical bonds (Formal, Bouree, Prevot, & Sivula, 2015; Martín & Pérez-Ramírez, 2019; Yan, Hitt, Turner, & Mallouk, 2020). For instance, electrocatalytic water splitting to into H<sub>2</sub> and O<sub>2</sub> is a promising pathway, although storage of H<sub>2</sub> and the sluggish anodic electrode reaction hindered the practical application so far (Lewis & Nocera, 2006; Nocera, 2012). Technologies aiming at removing CO<sub>2</sub> from the atmosphere are critical in helping control the global temperature (Olah, Prakash, & Goeppert, 2011). Direct conversion of the captured CO<sub>2</sub> back into fuels or valuable chemicals will help to reduce the energy crisis and ideally bring CO<sub>2</sub> emission to net zero at the same time. In addition to reducing water, electrocatalytic conversion of CO<sub>2</sub> back to fuels is of great importance in that sense (Centi, Quadrelli, & Perathoner, 2013; Peter, 2018).

If renewable electricity is available, what can we make with CO<sub>2</sub>? C<sub>1</sub> products like CO are now

considered the most promising option (Bushuyev et al., 2018; P. De Luna et al., 2019). Since CO can be effectively produced although mixed with little amounts of H<sub>2</sub>, they can be directly used as syngas for the Fischer-Tropsch process without the need of separation. Ethylene is an important compound which is indispensable for producing many plastics. The current market price for producing ethylene varies in different countries but all are relatively expensive. Therefore, although the efficiency for the ethylene production by electrochemical CO<sub>2</sub>RR is low, there is a chance for it to become more cost-effective (P. De Luna et al., 2019). Nevertheless, continuous efforts should be devoted to developing efficient, durable, and affordable catalysts, meanwhile understanding the reaction mechanism of this complex reaction can help accelerate this process (C. Chen, Khosrowabadi Kotyk, & Sheehan, 2018; Seh et al., 2017).

## 1.2 Electrochemical reduction of CO<sub>2</sub>: reaction mechanism

### 1.2.1 Electrochemical CO<sub>2</sub> reduction reaction (CO<sub>2</sub>RR)

Electrocatalytic reduction of CO<sub>2</sub> has been widely investigated since the 1980s (Hori, 2008; Hori, Kikuchi, & Suzuki, 1985; Nitopi et al., 2019; Sebastián-Pascual, Mezzavilla, Stephens, & Escudero-Escribano, 2019). To date, many metals have been tested for electrochemical CO<sub>2</sub>RR (Hori, 2008; Qiao, Liu, Hong, & Zhang, 2014). Based on the products, they can be classified into four groups: some metals produce mainly CO, including Au and Ag (Y. Chen, Li, & Kanan, 2012; H. Mistry et al., 2017); some can produce formic acid, including Sn and In (Z. Chen et al., 2020; Detweiler, White, Bernasek, & Bocarsly, 2014); others mainly produce H<sub>2</sub>, for instance Pt (Hori et al., 1985), and the sole metal Cu can produce C<sub>2+</sub> products (Bagger, Ju, Varela, Strasser, & Rossmeisl, 2017; Hori, Murata, & Takahashi, 1989; Hori, Murata, Takahashi, & Suzuki, 1988; Y. Wang et al., 2019; Zhou et al., 2018; Zhuang, Liang, et al., 2018; Zhuang, Pang, et al., 2018). Over 16 different products have been reported for Cu electrodes so far, which are shown in **Figure 1.1** with the number of electrons transferred and the standard electrode potentials (Kendra P. Kuhl, Cave, Abram, & Jaramillo, 2012). CO and formate are produced by CO<sub>2</sub> receiving 2 electrons. The other products need at least 6 electrons to be produced, therefore although the standard electrode potentials for these reactions are close to 0 V<sub>RHE</sub> or even more positive, they are slow kinetically (Kendra P. Kuhl et al., 2012). Therefore, the actual potentials for producing these products are much more negative than the standard electrode potentials, the difference is the so called overpotential ( $\eta$ ). The overpotentials for CO<sub>2</sub>RR products are usually higher than for the hydrogen evolution reaction (HER). The other unique problem for CO<sub>2</sub>RR is the low selectivity for specific products (Kendra P. Kuhl et al., 2012; Hemma Mistry, Varela, Kuhl, Strasser, & Cuenya, 2016; W. Zhang et al., 2018). Regarding the high costs for separation of different products, it is also critical to develop a catalyst that has a high selectivity for specific products. Selectivity is evaluated by Faradaic efficiency (FE) that is calculated by dividing the partial current of a certain product by the total current. The partial current is calculated based on the amounts of electrons transferred for producing this product that is detected by gas or liquid chromatography. FE for CO production on either noble metal catalyst or molecular catalysts have reached above 95% with low overpotential (Tan et al., 2021). However, C<sub>2+</sub> products still suffer from low selectivity. The highest FE achieved for C<sub>2</sub>H<sub>4</sub> production is 87% on a polymer modified Cu catalyst, exceeding the old

record of 70% (X. Chen et al., 2020; Dinh et al., 2018). It is urgent to understand the reaction mechanism of CO<sub>2</sub>RR in detail.

Hori et al. investigated CORR on Cu and found the same distribution of products as for CO<sub>2</sub>RR, therefore they proposed that CO is the intermediate on Cu that can be further reduced to C<sub>2+</sub> products (Hori et al., 1989; Hori, Takahashi, Yoshinami, & Murata, 1997). Therefore, here the CO<sub>2</sub>RR mechanism is divided into two procedures, i.e., the production of CO and the reduction of CO to C<sub>1</sub> and C<sub>2+</sub> products. In the following sections, the proposed mechanism based on theoretical studies and the current progress with a special focus on *in-situ* techniques in detecting the reaction mechanisms are provided.

Product	# e <sup>-</sup>	E	Product	# e <sup>-</sup>	E
<b>Formate</b> 	2	-0.02	<b>Acetaldehyde</b> 	10	0.05
<b>Carbon monoxide</b> 	2	-0.10	<b>Ethanol</b> 	12	0.09
<b>Methanol</b> 	6	0.03	<b>Ethylene</b> 	12	0.08
<b>Glyoxal</b> 	6	-0.16	<b>Hydroxyacetone</b> 	14	0.46
<b>Methane</b> 	8	0.17	<b>Acetone</b> 	16	-0.14
<b>Acetate</b> 	8	-0.26	<b>Allyl alcohol</b> 	16	0.11
<b>Glycolaldehyde</b> 	8	-0.03	<b>Propionaldehyde</b> 	16	0.14
<b>Ethylene glycol</b> 	10	0.20	<b>1-Propanol</b> 	18	0.21

Figure 1.1. Equilibrium potentials and the electrons transferred for CO<sub>2</sub>RR products on Cu. Reproduced from Ref (Kendra P. Kuhl et al., 2012) with permission from The Royal Society of Chemistry.

## 1.2.2 CO<sub>2</sub> activation

CO<sub>2</sub> activation is reported to be the rate determining step (RDS) (Hori, 2008). It is kinetically and energetically demanding to bend the linear CO<sub>2</sub> molecule and make it accept one electron to form a \*COO<sup>-</sup> intermediate. Adsorption on the catalyst surface and stabilization of this intermediate facilitates this reaction (Hori, 2008; Xie, Niu, Kim, Li, & Yang, 2020). For instance, Chernyshova et al. observed this intermediate on Cu surfaces using *in-situ* Raman spectroscopy and proposed that the initial step of CO<sub>2</sub> reduction is the electron transfer forming COO<sup>-</sup>, with C and O binding to the surface (Chernyshova, Somasundaran, & Ponnurangam, 2018). As \*COOH is considered to be a key intermediate for CO formation, there is another step that is \*COO<sup>-</sup> accepting one proton to form \*COOH (Birdja et al., 2019; Xie et al., 2020).

It could also be a concerted proton coupled electron transfer (PCET) process, which means accepting one electron and proton at the same time forming a  $^*\text{COOH}$  intermediate (Birdja et al., 2019; Xie et al., 2020). On Ag surfaces, Firet et al. observed that at low overpotential  $^*\text{COOH}$  is the main intermediate, whereas two continuous steps of electron transfer and proton transfer also exist at high overpotential (Firet & Smith, 2016).

Kinetic research, e.g. based on the Tafel slope can provide information on the RDS, however, there are conflicting reports on whether the RDS is PCET or ET or the value is 65 mV/dec or 120 mV/dec (Marco Dunwell, Luc, Yan, Jiao, & Xu, 2018). This discrepancy may be explained by the different reaction mechanisms on different metals. For instance,  $^*\text{OHCO}$  is reported to be the key intermediate for formate formation, however, on Sn/SnO<sub>2</sub> surfaces, Baruch et al. observed tin surface-bounded carbonate as an important intermediate for CO<sub>2</sub> reduction to formate (Baruch et al., 2015). They have also found similar behaviour on In/In<sub>2</sub>O<sub>3</sub> electrode (Detweiler et al., 2014). The proposed mechanisms for CO<sub>2</sub>RR to CO and formate are summarized and shown in **Figure 1.2** (Xie et al., 2020).

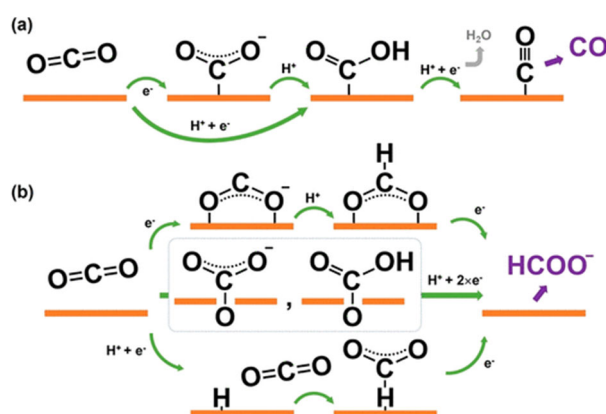


Figure 1.2. Proposed mechanism for (a) CO and (b) HCOO<sup>-</sup> formation. Reprinted with permission from Ref (Xie et al., 2020). Copyright (2020) American Chemical Society.

On the other hand, whether CO<sub>2</sub> gas is the source of CO<sub>2</sub> reduction is still under debate. The most prominent research is from Dunwell et al., they proposed that the CO<sub>2</sub> participating reaction stems from the local HCO<sub>3</sub><sup>-</sup> equilibrium but not directly from CO<sub>2</sub> gas (M. Dunwell et al., 2017). Zhu et al. also observed the same phenomenon on Cu (S. Zhu, Jiang, Cai, & Shao, 2017). Kortlever et al. observed the direct reduction of bicarbonate, which is common on palladium but not on Cu (Kortlever, Tan, Kwon, & Koper, 2013). They assigned a reductive peak in CV that is usually recognized as a CO adsorption peak to be relevant for bicarbonate reduction. To date there is no consensus on which reaction pathway represents the CO<sub>2</sub> activation step, it is possible that on different metals the CO<sub>2</sub> activation step is different and results in different products (Sebastián-Pascual et al., 2019; Xie et al., 2020).

### 1.2.3 CO to C<sub>1</sub> and C<sub>2+</sub> products

C<sub>1</sub> products including methane and methanol are considered to be produced from CO intermediate though the mechanism regarding a large number of proton transfer steps remains unclear. This is due to the high overpotential and low FE of producing methane and methanol and they have rarely been reported in the literature (K. P. Kuhl et al., 2014). According to

theoretical studies, several intermediates have been proposed including  $^*CHO$  as a precursor for  $^*OCH_3$  and then for methanol formation, or  $^*COH$  for methane formation (Cheng, Xiao, & Goddard, 2017; Nie, Esopi, Janik, & Asthagiri, 2013; Peterson, Abild-Pedersen, Studt, Rossmeisl, & Nørskov, 2010). These potential reaction paths have been summarized as shown in **Figure 1.3** (Xie et al., 2020).

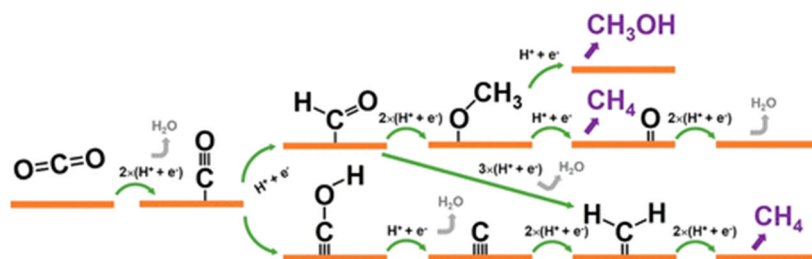


Figure 1.3. Proposed mechanism for methane and methanol formation. Reprinted with permission from Ref (Xie et al., 2020). Copyright (2020) American Chemical Society.

CO reduction to  $C_{2+}$  products is more complex. So far there are little numbers of reports about the mechanism other than for  $C_2H_4$  formation. This is because of the relatively high selectivity for  $C_2H_4$  on various Cu electrodes. However, many pathways and intermediates with more divisions have been proposed as summarized in **Figure 1.4** (Xie et al., 2020). Basically, they can be classified as two categories: the pH dependent pathway that is connected with  $CH_4$  production; and the pH independent pathway, also known as  $^*CO$  dimerization pathway (K. J. Schouten, Qin, Perez Gallent, & Koper, 2012). These two pathways were both observed to be active on Cu (K. J. Schouten et al., 2012). In particular,  $C_2H_4$  can be produced on Cu(100) at a lower overpotential than on Cu(111), as the latter is more selective for  $CH_4$  (K. J. Schouten et al., 2012). This supports that on Cu(100) there is a distinct pathway for  $C_2H_4$  production, which does not share the same intermediate with  $CH_4$ , therefore they proposed it to be a  $^*CO$  dimerization pathway (Gattrell, Gupta, & Co, 2006; K. J. P. Schouten, Kwon, van der Ham, Qin, & Koper, 2011). The pH dependent pathway deviates on whether  $^*CO$  forms  $^*CH_2$  or  $^*CHO$  before forming the C-C bond (Cheng et al., 2017; Alejandro J. Garza, Alexis T. Bell, & Martin Head-Gordon, 2018; Goodpaster, Bell, & Head-Gordon, 2016; Hori et al., 1997). The  $^*CO$  dimerization pathway deviates on whether one CO is from gas phase or both are adsorbate (Calle-Vallejo & Koper, 2013; Cheng et al., 2017). There is various speculation about the steps after the formation of the  $^*CO$  dimer (Calle-Vallejo & Koper, 2013). Pérez-Gallent et al. claimed the observation of a hydrogenated  $^*CO$  dimer in LiOH with *in-situ* FTIR (Perez-Gallent, Figueiredo, Calle-Vallejo, & Koper, 2017). Aside from that, there is hardly any experimental proof of existence for intermediates that are proposed by theoretical studies.

CO as an important intermediate has been most frequently observed in either IR or Raman spectroscopy (Gunathunge et al., 2017; A. Wuttig et al., 2016). Although on Au or Ag, CO is released as product, there have been reports about CO adsorption on Au (M. Dunwell et al., 2017), whereas Ag seems to not adsorb CO easily. The CO affinity on Cu is moderate so that CO can remain adsorbed and further get reduced to  $C_{2+}$  products (Bagger et al., 2017). Investigating the behaviour of CO on Cu can be used to explain the different selectivity and give information on the reaction mechanism to  $C_{2+}$  products.

Heyes et al. claim that besides the typical CO adsorption band at  $2070\text{ cm}^{-1}$  H adsorption shows a peak at  $2090\text{ cm}^{-1}$ , based on D isotope experiments in  $\text{NaClO}_4$  (Heyes, Dunwell, & Xu, 2016). Furthermore, they observed the displacement of CO by H adsorption, but not the opposite. However, there is no other report supporting this assignment. Gunathunge et al. also observed bands in this region during applying potentials to more negative potentials, however the authors assigned bands at both lower and higher wavenumbers to CO adsorption (Gunathunge et al., 2017). Their explanation is that CO accumulates with increasing negative potentials, and Cu undergoes surface reconstruction at high CO coverage. Wuttig et al. observed a hysteresis of CO desorption when scanning the potential forward and backward, this phenomenon was attributed to a possible reconstruction of Cu (A. Wuttig et al., 2016). They found that surface adsorbed CO is in dynamic exchange to solution CO, which signifies the moderate affinity of CO to Cu surface. The authors concluded that although CO adsorption is pH independent,  $\text{C}_{2+}$  production is highly dependent on the number of available CO converting active sites and the amount of surface bound CO, which is influenced both by pH and potential. Malkani et al. investigated the CO adsorption on OD-Cu in KOH electrolyte and compared it to polycrystalline Cu (Malkani, Dunwell, & Xu, 2018). A peak at  $2058\text{ cm}^{-1}$  that is absent on polycrystalline Cu was observed. They think this is consistent to the literature that CO mainly bound to Cu (100), which is considered as a pathway for producing  $\text{C}_{2+}$  products with a lower overpotential. These reports suggest that the CO dimerization mechanism is indeed one of the pathways for  $\text{C}_2\text{H}_4$  production, and that the  $\text{*CO}$  coverage is of great importance to  $\text{C}_{2+}$  production (Y. Huang, Handoko, Hirunsit, & Yeo, 2017; Montoya, Shi, Chan, & Norskov, 2015; K. J. Schouten et al., 2012).

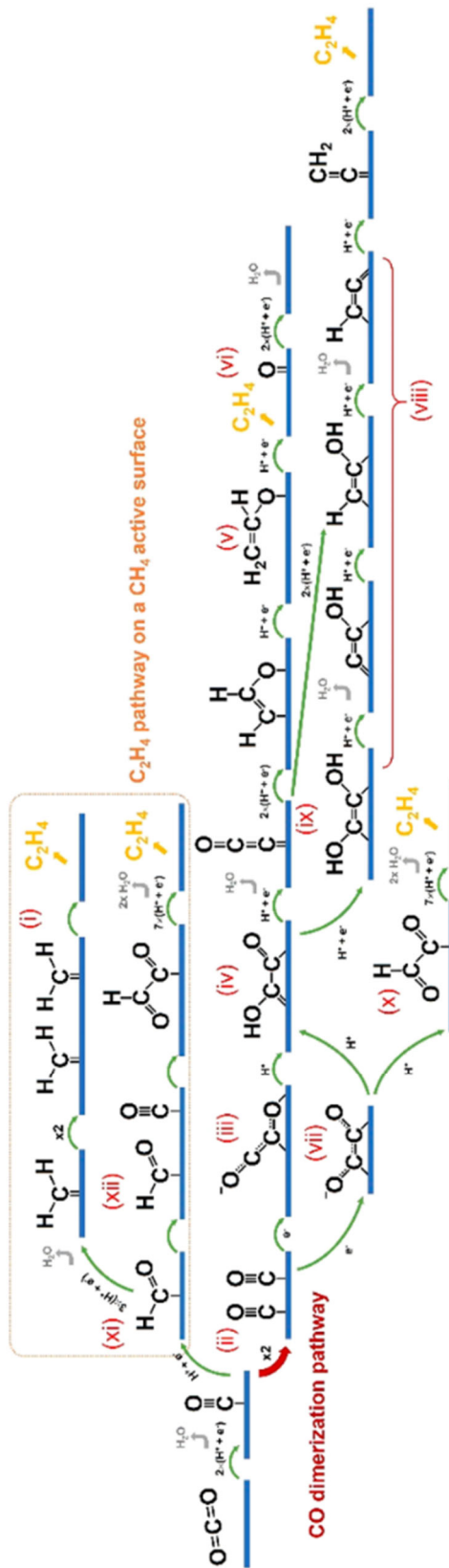


Figure 1.4. Proposed mechanism for C<sub>2</sub>H<sub>4</sub> formation. Reprinted with permission from Ref (Xie et al., 2020). Copyright (2020) American Chemical Society.

## 1.2.4 Electrode morphology effects

As in other catalytic reactions, the electrodes' morphology affects the catalytic reaction activity (Xie et al., 2020). In CO<sub>2</sub>RR the morphology also modifies the products selectivity (Aran-Ais, Gao, & Roldan Cuenya, 2018; Kas et al., 2020). For instance, as mentioned above, the different facets of Cu(100) or Cu(111) show different selectivity for C<sub>2</sub>H<sub>4</sub> or CH<sub>4</sub> (Hori, Takahashi, Koga, & Hoshi, 2003). Cu nanocubes were reported to be selective for C<sub>2</sub>H<sub>4</sub> production which can be attributed to the exposed Cu(100) facet (Roberts, Kuhl, & Nilsson, 2015). Nanostructuring often brings more active sites, however in the work of Reske et al (Reske, Mistry, Behafarid, Roldan Cuenya, & Strasser, 2014), when nanoparticle size was below 5 nm, the selectivity for hydrocarbon products decreased. This is due to the lower mobility of surface adsorbed CO and H for further reduction reaction. Nevertheless, mesoporous structures are reported to suppress HER and therefore promote CO<sub>2</sub>RR on various catalysts (Hall, Yoon, Wuttig, & Surendranath, 2015; Anna Wuttig, Yaguchi, Motobayashi, Osawa, & Surendranath, 2016). Specifically, the dendritic Cu foam catalyst has been investigated frequently (Dutta, Rahaman, Luedi, Mohos, & Broekmann, 2016; Sen, Liu, & Palmore, 2014). Dutta et al. reported a Cu foam catalyst that has above 50% of C<sub>2</sub> products FE (Dutta et al., 2016). A similar Cu foam was reported to be more selective for formic acid (Sen et al., 2014). Klingan et al. investigated the reaction determinants in CO<sub>2</sub>RR on Cu foam catalysts (Klingan et al., 2018). The Cu foam they reported shows relatively good CO and ethylene selectivity which can be affected by the ECSA (electrochemical active surface area) of the electrodes.

## 1.2.5 Oxide-derived Cu catalyst

Since Kanan and coworkers first reported about the excellent oxide-derived (OD) catalysts for CO<sub>2</sub>/CORR including OD-Au, Sn and Cu (Y. Chen & Kanan, 2012; Y. Chen et al., 2012; C. W. Li, Ciston, & Kanan, 2014; C. W. Li & Kanan, 2012), there has been a variety of research focusing on the main function of oxides (Arán-Ais, Scholten, Kunze, Rizo, & Roldan Cuenya, 2020; Favaro et al., 2017; Mandal et al., 2018; Pander et al., 2018; Velasco-Vélez et al., 2018). Soon after the discovery of OD-Cu catalyst, Ib Chorkendorff and coworkers probed the active sites of this catalyst with a CO temperature desorption experiment and high resolution TEM (Verdaguer-Casadevall et al., 2015). They found that grain boundaries play an important role in binding and stabilizing CO. As CO is widely recognized as an important intermediate towards C<sub>2+</sub> products, the stabilization of CO on the surface facilitates further reducing of CO to C<sub>2+</sub> products. This hypothesis was further investigated by Feng et al., they adopted TEM to measure the grain boundaries surface density for OD-Au and OD-Cu nanoparticles and found that the CO partial current density increases on these catalysts with more grain boundaries whereas HER was not influenced (Feng, Jiang, Fan, & Kanan, 2015, 2016).

On the other hand, subsurface oxygen is considered to be essential for CO<sub>2</sub> reduction. Favaro et al. proposed that subsurface oxygen could bind the physisorbed CO<sub>2</sub> molecule and convert to chemisorbed CO<sub>2</sub>, which helps to decrease the CO<sub>2</sub> activation energy (Favaro et al., 2017). Xiao et al. further proposed a mechanism with metal atoms embedded in an oxide matrix for both easier CO<sub>2</sub> activation and lower overpotential for CO dimerization (Xiao, III, Cheng, & Liu, 2017). They think that Cu<sup>+</sup> working together with Cu is the active species for efficient CO<sub>2</sub> reduction activity. In contrast, according to the work of Garza et al., subsurface oxygen is not necessary for CO<sub>2</sub> reduction (A. J. Garza, A. T. Bell, & M. Head-Gordon, 2018). In addition,



Soon et al. conducted a DFT study and found that the surface oxide layer is more stable than subsurface oxygen for Cu(111) (Soon, Todorova, Delley, & Stampfl, 2006). This is different to what Favaro et al. has proposed. In the other work of Crumlin and coworkers they proposed surface oxygen is more stable than subsurface oxygen for Ag (Ye et al., 2019).

Although it is believed that Cu metal is the active species and Cu oxide could not survive under catalytic potentials, there is other research claiming that they observe  $\text{Cu}^+$  species even under high overpotentials for a long time. Ex-situ experiments are not so much helpful in these circumstances due to the fact that defect-rich OD-Cu could easily get reoxidized once taken out of the solution. Mistry et al. adopted  $\text{O}_2$  plasma treated Cu oxide catalysts to investigate this question. Using cross-sectional scanning transmission electron microscopy, surprisingly they found that the  $\text{Cu}^+$  signal exists through the whole time of the experiment (H. Mistry et al., 2016). By comparing with  $\text{H}_2$  plasma treated Cu catalyst, they proposed that surface roughness is not decisive in the  $\text{C}_{2+}$  production, but  $\text{Cu}^+$  species are.

In situ XPS has been adopted for monitoring the oxidation state of the catalyst during  $\text{CO}_2$  reduction. In the recent study of Beatriz and coworkers, pulsed  $\text{CO}_2$  electrolysis was used and they found that the defects and  $\text{Cu}^+$  species work synergistically to reach higher  $\text{C}_{2+}$  selectivity (Arán-Ais et al., 2020). Juan-Jesus et al. systematically investigated the role of the Cu oxidation state, they performed XAS together with product distribution studies, and found that the CuO oxide surface is covered with a carbonate layer which deactivates the catalyst by restraining effective charge transfer (Velasco-Vélez et al., 2018). In their study,  $\text{Cu}^+$  is as active as Cu metal.

Due to the different catalyst morphologies and reaction conditions of different studies, and whether the reaction under investigation is CORR or  $\text{CO}_2\text{RR}$ , it is understandable that there are conflicting results. Other perspectives including local pH and low coordinated atoms also have been reported, but these might come together with morphology change and will not be discussed further. To date, the function of OD-Cu is still a controversial topic. Nevertheless, the outstanding activity of OD-Cu for  $\text{CO}_2\text{RR}$ , especially for  $\text{C}_{2+}$  products, it is still of great importance for future  $\text{CO}_2\text{RR}$  research.

## 1.3 Raman spectroscopy and SERS

This section about Raman spectroscopy is mainly based on ref (Ferraro, Nakamoto, & Brown, 2003; Hollas, 2004; E. Smith & Dent, 2005).

### 1.3.1 Basic theory of Raman spectroscopy

The energy states of a diatomic molecule are shown in **Figure 1.5**. The rotation energy spacings are smallest, and the vibration energy levels are within two electronic excitation energy levels. Infrared (IR) absorption and Raman scattering are both vibrational spectroscopies. For IR and Raman, wavenumber is used more often than wavelength as an energy unit, IR and Raman process happens within the energy range of  $10^2$  to  $10^4 \text{ cm}^{-1}$ .

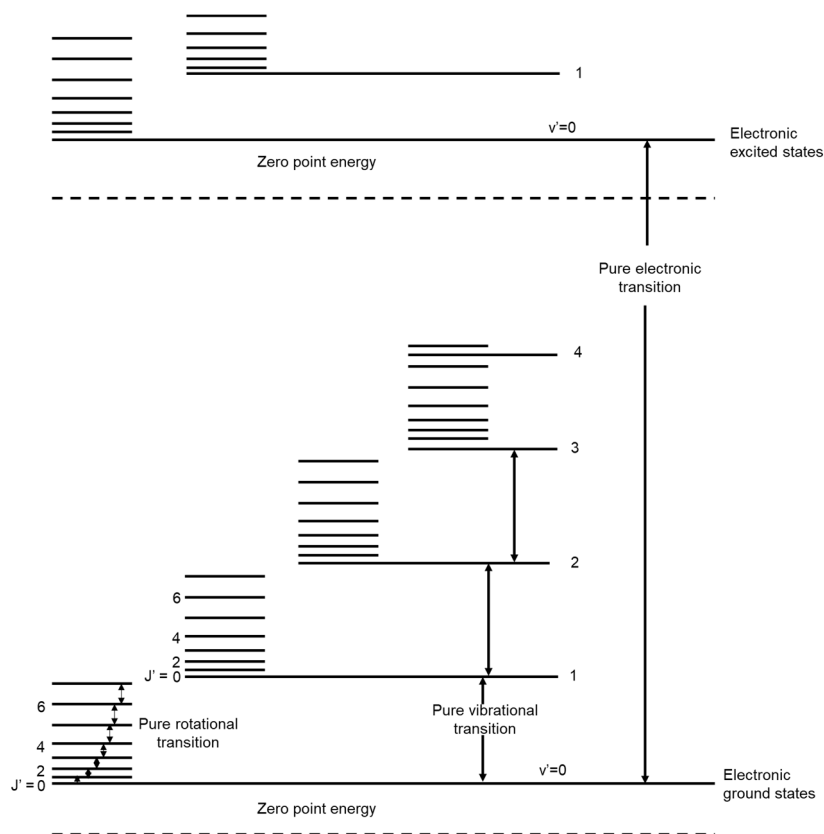


Figure 1.5. Energy levels of a diatomic molecule. (The actual spacings of electronic levels are much larger, and those of rotational levels are much smaller, than those shown in the figure.) Remade based on ref (Ferraro et al., 2003).

The vibration of a diatomic molecule can be considered as a spring, which obeys Hook's law. However, the energy is quantized.

$$E_v = h\nu \left( v + \frac{1}{2} \right), \quad \text{Eq. 1.1}$$

Where  $v=0, 1, 2, \dots$  are the energy levels;  $\nu$  is the vibration frequency, it is defined by Eq. 1.2:

$$\nu = \frac{1}{2\pi} \left( \frac{K}{\mu} \right)^{\frac{1}{2}}, \quad \text{Eq. 1.2}$$

Where  $K$  is the force constant;  $\mu$  is the reduced mass of nuclei, it can be calculated by Eq. 1.3:

$$\mu = \frac{m_1 m_2}{m_1 + m_2}, \quad \text{Eq. 1.3}$$

Therefore, the lighter the atom is, the higher the vibrational frequency, i.e. the band appears at higher wavenumber. For instance, the vibration of C-H is close to  $3000 \text{ cm}^{-1}$ , whereas the C-O bond shows band at close to  $2000 \text{ cm}^{-1}$ .

The potential energy curve for harmonic oscillator is a parabola with the energy levels equally spaced, and the energy at  $v=0$  is not zero but has a value of  $\frac{1}{2}h\nu$ , which is called zero-point energy. Whereas the real vibration of molecules is closer to an anharmonic oscillator, the spacings between energy levels decrease with increasing energy levels. With a consideration of anharmonicity, the potential energy states can be described with Morse curve as shown in **Figure 1.6**. Furthermore, for a harmonic oscillator, only transitions with  $\Delta v=\pm 1$  can happen, whereas overtones with  $\Delta v=\pm 2, \pm 3, \dots$  also has weak signals.

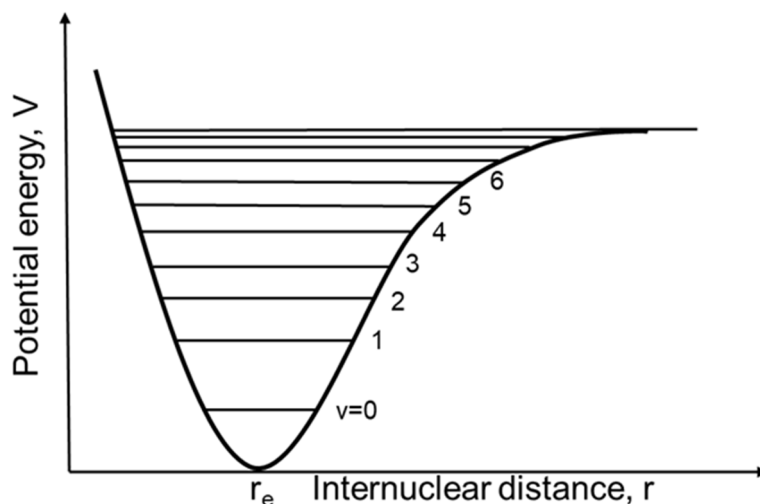


Figure 1.6. Morse curve and energy levels of a diatomic molecule. Remade based on ref (Ferraro et al., 2003).

As a simplified form of **Figure 1.6**, the energy levels are just shown as straight lines with equal spacings as shown in **Figure 1.7**. IR absorption is an absorption of energy that matches with the difference of the two vibrational energy levels, whereas scattering needs a higher energy absorption and excite the molecule into a virtual energy state that is determined by the laser light energy. It should be noted that, the excitation energy is usually much higher than the difference of vibration energy levels, therefore in reality the virtual states should be much higher and the spacings between the vibration energy levels are much smaller. Rayleigh scattering denotes the scattered light with the same energy to the incident light. When the scattered light energy differs to the incident light, it is Raman scattering. Compared to Rayleigh scattering, Raman scattering is much weaker. The difference in the energy of the incident light and the scattered light is called the Raman shift. Raman scattering includes Stokes and anti-Stokes scattering. When the light excites the molecule from the fundamental vibration energy level and back to a higher energy states, the Raman scattering is Stokes scattering; when the molecule was at the first vibration energy state and the scattered light return to the fundamental energy level, it is called anti-stokes scattering. According to Maxwell-Boltzmann equation,

most molecules are resting at the fundamental vibration energy level, therefore stokes scattering is more abundant than anti-stokes scattering.

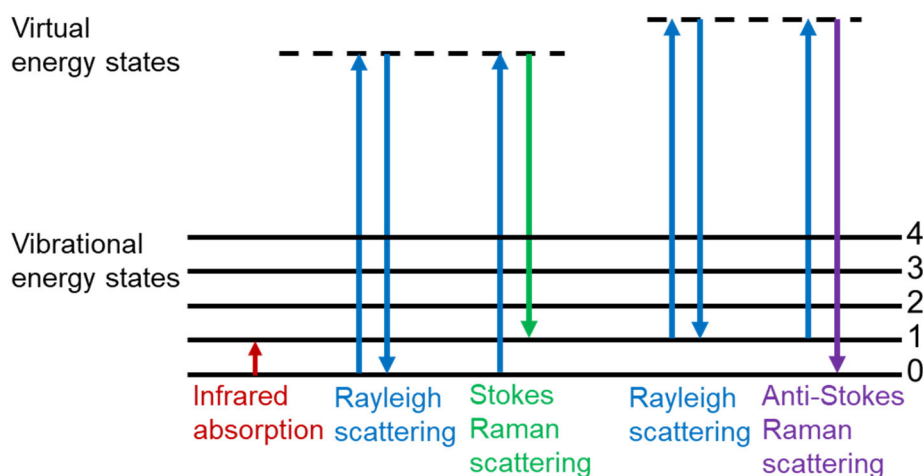


Figure 1.7. Scheme showing IR absorption, Rayleigh scattering, stokes and anti-stokes Raman scattering. Remade based on ref (Ferraro et al., 2003).

### 1.3.2 Raman selection rules.

Raman selection rules are different to IR which requires a change in the dipole moment for a transition to occur, whereas Raman is sensitive to a change of the polarizability. As a result, they often show different and complementary spectra. As an example, the linear  $\text{CO}_2$  molecule is discussed. According to  $3N-5$  rule,  $\text{CO}_2$  has 4 modes of vibration including symmetrical and anti-symmetrical stretching as well as two bending modes as shown in **Figure 1.8**. Since the symmetrical stretching mode causes no change to the dipole moment, it is thus IR inactive, however, it causes a clear change in the polarizability and is thus Raman active. The anti-symmetrical stretching and the bending modes only cause a temporal and symmetrical change of the polarizability, so in total they result in no change to polarizability, making the symmetric stretching mode the only one visible in Raman. Accordingly,  $\text{CO}_2$  shows bands at  $667$  and  $2350 \text{ cm}^{-1}$  in IR spectra and one band at  $1340 \text{ cm}^{-1}$  in Raman spectra. Although in real Raman measurements,  $\text{CO}_2$  also shows a peak at  $1286 \text{ cm}^{-1}$  corresponding to the second harmonic of the bending mode vibration ( $2 \nu_2$ ) (Davis & Oliver, 1972).  $\text{CO}$  as a diatomic molecule with different atoms has only one vibrational mode that is the symmetrical stretching mode. This vibration mode is both Raman and IR active. An overview is given in **Figure 1.9**.

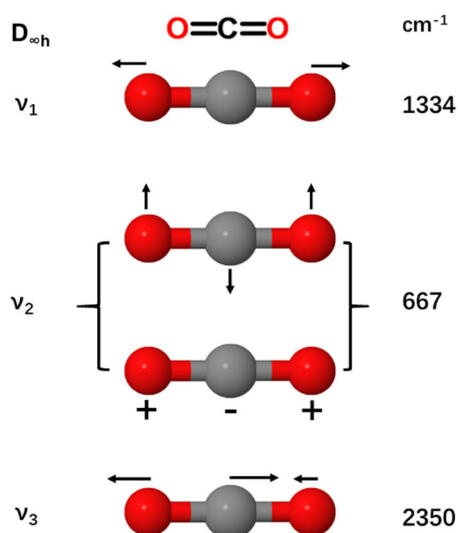


Figure 1.8. Normal vibration modes of CO<sub>2</sub> molecule.

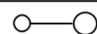

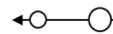
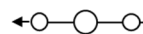
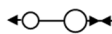
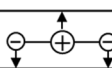
Molecule vibration				
				
Change of dipole moment	$\neq 0$	$= 0$	$\neq 0$	$\neq 0$
IR active	yes	no	yes	yes
Change of polarizability	$\neq 0$	$\neq 0$	$= 0$	$= 0$
Raman active	yes	yes	no	no

Figure 1.9. Selection rules for Raman and IR spectra. Remade based on ref (E. Smith & Dent, 2005).

### 1.3.3 Isotope labelling

Isotope labelling is a useful tool for vibrational spectroscopy, since a change of the mass causes a clear shift in the spectra. In CO<sub>2</sub>RR research, carbon isotope labelling is used frequently. As an example, <sup>13</sup>CO has a band at around 2005 cm<sup>-1</sup> that is normally at 2050 cm<sup>-1</sup> for <sup>12</sup>CO, revealing a shift of 45 cm<sup>-1</sup>, which can be estimated using equation Eq. 1.4 based on a simple harmonic oscillator model (Westheimer, 1961).  $\lambda$  is the wavenumber of the vibrational mode,  $\mu$  is the reduced mass of the unlabeled molecule, and \* denotes the molecule which is labeled with isotope. Similarly, when labeling water with D, the H-O-H bending mode vibration band at 1640 cm<sup>-1</sup> shifts down to around 1200 cm<sup>-1</sup>.

$$\frac{1}{\lambda} \sqrt{\frac{\mu^*}{\mu}} = \frac{1}{\lambda^*}, \quad \text{Eq. 1.4}$$

### 1.3.4 Raman spectrometer

Historically, the excitation light source for Raman was used to be low pressure mercury arc. With the invention of Lasers (Light amplifier by stimulated emission of radiation), Raman scattering could be better observed and since then developed much faster. This is mainly due to the advantage of Lasers having strong, coherent monochromatic light in a wide range of wavelengths. Our Raman instrument is equipped with a 473 nm (YAG), a 532 nm (YAG) and a 633 nm (He-Ne) laser. A scheme of our instrument is shown in **Figure 1.10**. It is a microscope incorporated confocal Raman spectrometer. The laser beam comes from the objective and reaches the sample, the scattered light goes back from the objective to a notch filter, where the Rayleigh scattering light is blocked, then the Raman scattering light is diffracted by the grating and read by the CCD detector.

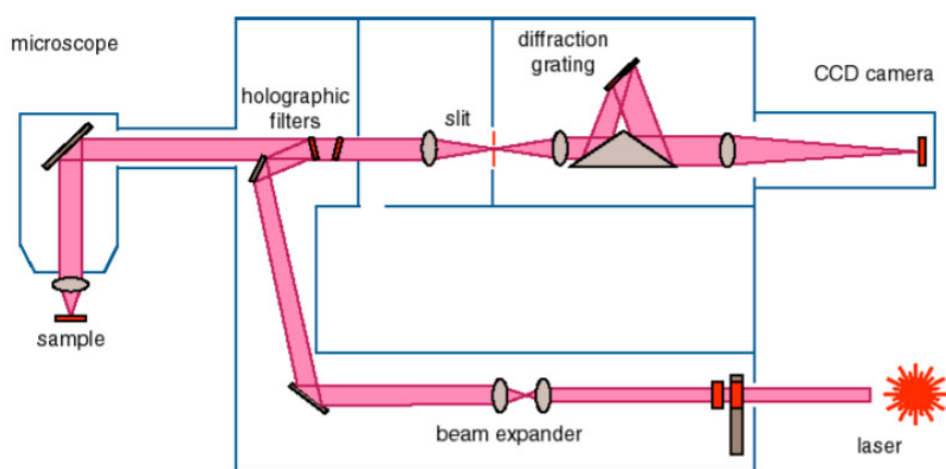


Figure 1.10. Scheme of Raman spectroscopy instrument. (Source: Renishaw Raman spectrometer.)

### 1.3.5 SERS

Despite the promising applications of Raman spectroscopy, the low detection sensitivity limits its practical use. This is solved by the discovery of surface enhanced Raman scattering (SERS) effect. SERS was first discovered in 1974 by Fleischmann, Hendra and McQuillan (Fleischmann, Hendra, & McQuillan, 1974). They were using an electrochemical protocol to create a high surface area Ag electrode, on which the pyridine in the electrolyte was adsorbed and later they observed a surprisingly high Raman signal, though they did not realize it was a surface enhancement effect. Jeanmaire and Van Duyne in America and Albrecht and Creighton in UK both reported in 1977 that the effect is dependent on the size of the structure (Albrecht & Creighton, 1977; Jeanmarie & Duyne, 1977). Until then, SERS has been widely investigated and applied in different fields due to its extremely high sensitivity with an enhancement factor of  $10^5 - 10^6$ . SERS is most prominent on coinage metals (Cu, Ag, Au), because of the effective surface plasma resonance (SPR) phenomenon (Wu, Li, Ren, & Tian, 2008). However, the SPR effect is quenched when the excitation energies are higher than 2.2 eV (563 nm) for Cu and Au and 3.8 eV (326 nm) for Ag. This explains why Ag has a high SERS using the 532 nm laser, whereas for Cu the 633 nm laser source is chosen. Due to the difference in the electronic band

structures, the SPR is less prominent in the visible range for other transition metals. However, creating nanostructures can modify the electronic band structure and therefore enables SERS also for those metals. Tian et al. developed roughening methods for Pt, Ru, Rh, Pd, Fe, Co and Ni electrodes which facilitated them for SERS (Tian, Ren, & Wu, 2002).

### **1.3.5.1 SERS mechanisms: electromagnetic and chemical enhancement mechanism**

The Raman intensity is proportional to the electric field and the molecular polarizability, therefore there are generally two kinds of enhancement mechanisms, the electromagnetic effect (EM) and the chemical enhancement (CE) (Langer et al., 2020). EM is mainly explained by surface plasmonic resonances that causes an increase of local electric field. CE results from the chemisorption of molecules. The chemical bond between the substrate and the molecule enables charge transfer between them, which causes an increased polarizability. EM enhancement is more prevalent than CE in most systems. CE is typically a relatively weak effect, whereas in electrochemical systems, it is necessary to put more emphasis on CE since it may affect the species observed and the interaction between adsorbates and the surface during an electrochemical process.

### **1.3.5.2 Electrochemical SERS**

As mentioned above, SERS was first discovered in electrochemical processes. This may not be a coincidence since electrochemical research at that time was going into the microscopic level with the need to understand the mechanistic details occurring at electrochemical interfaces. Today, this demand is more urgent when it comes to electrocatalytic research due to the urgent need for developing efficient catalysts. Moreover, investigating electrochemical SERS processes also promotes the comprehension of the SERS mechanism itself (Wu et al., 2008).

EC-SERS is more complex than other SERS systems (Wu et al., 2008). In electrochemical systems, double layer structures are formed in the electrochemical interface due to the electric field, and it is changing with potential and reactant concentrations. Now, in EC-SERS system, light illuminates and alters the double layer structure and the electrode in turn can influence the local optical field on the surface (Wu et al., 2008). The influence of the electric potential to the double layer structure differs between different electrode materials since the potential of zero charge (pzc) varies for different electrodes. When the potential is more positive than the pzc, the interaction of the anions with electrode becomes stronger, meanwhile cations will leave the surface, and vice versa. Furthermore, the potential also influences the Raman intensity, which can be explained by photo-driven CT mechanisms (Wu et al., 2008). Only when the potential matches the CT transfer energy between the surface and the adsorbed molecules resonance Raman scattering is observed. Higher or lower potentials result in less prominent Raman intensities. The complexity of EC-SERS systems may to some extent hinder the comprehension of EC systems, however, it also brings plenty of possibilities. For instance, the change of electrode potentials, electrode materials, electrode morphology and the electrolyte species are factors that can be adjusted and investigated. A proper experimental design will definitely help to gain new insights in both electrochemical reactions and the SERS effect.

## 1.4 Scope and organisation of this thesis

The main purpose of this thesis is to investigate the electrochemical CO<sub>2</sub> reduction mechanism mainly on Cu foam in aqueous electrolyte. This is implemented by *operando* SERS, which is a useful tool in detecting the reaction intermediates.

The thereby obtained results are presented in four chapters:

- 1) **Chapter 2** establishes the methodology of *operando* SERS on the CO<sub>2</sub>RR process on Cu-foam materials. A proper data analysis procedure is developed, based on which the adsorption of intermediates during the CO<sub>2</sub>RR process are investigated.
- 2) **Chapter 3** discusses the role of oxide and bicarbonate and the interaction between them. With the help of carbon isotope labelling, the existence of hydroxycarbonate intermediates is detected, which may help to explain the extraordinary activity for C<sub>2</sub> products on Cu oxide.
- 3) **Chapter 4** investigates the different role of Ag and Cu foam, and the reason for the improved CO selectivity on mixed CuAg foams; a study of the CO production mechanism on the CuAg surface is presented and discussed.
- 4) **Chapter 5** focuses on the reaction factors of mass transport, which are investigated in detail by monitoring the local pH with Raman spectroscopy. Reactions in different conditions including a flow cell setup and use of D<sub>2</sub>O electrolyte are investigated as well.

Each chapter starts with a specific introduction within the research topic of that chapter, followed by the results with discussion, and the materials and methodology are documented at the end of the respective chapter.



## 2. New aspects of *operando* Raman spectroscopy applied to electrochemical CO<sub>2</sub> reduction on Cu foams

*A major fraction of the here shown results has been published in*

### **New aspects of *operando* Raman spectroscopy applied to electrochemical CO<sub>2</sub> reduction on Cu foams.**

Jiang S, Klingan K, Pasquini C, Dau H. The Journal of chemical physics. 2019 Jan 28;150(4):041718.

Copyright (2019) AIP Publishing.

In the published study, the authors contributed as follows: Jiang, S. performed all experiments and analyzed the data; Pasquini, C. designed the electrochemical *Operando* Raman cell; Klingan, K. and Dau, H. supervised research; all authors participated in writing, discussion and revision of the article.

### **2.1 Introduction**

Vibrational spectroscopy, specifically surface-enhanced Raman spectroscopy (SERS), can be readily coupled to an electrochemistry experiment and thereby becomes a promising experimental tool in CO<sub>2</sub>RR research, given the sensitivity to identify adsorbate species and their bonding to the surface (Handoko, Wei, Jenndy, Yeo, & Seh, 2018; Heidary, Ly, & Kornienko, 2019; J. Li & Gong, 2020; X. Li, Wang, Li, Sun, & Xie, 2020; Shangqian Zhu, Li, Cai, & Shao, 2019). *Operando* SERS with coinage metals coincidentally match with the need to investigate CO<sub>2</sub> reduction process on Cu, Ag and Au. Au and Ag are selective catalysts for CO production (Bagger et al., 2017). Cu on the other hand is the only metal that could further reduce CO to C<sub>2</sub> products (Nitopi et al., 2019). However, the product distribution is typically diverse with each product being low in FE (Kendra P. Kuhl et al., 2012). With certain modifications, for instance morphology design, the selectivity for C<sub>2</sub>H<sub>4</sub> or CH<sub>4</sub> production may be improved (Aran-Ais et al., 2018; Gao, Arán-Ais, Jeon, & Roldan Cuenya, 2019; Vasileff, Xu, Jiao, Zheng, & Qiao, 2018). It is of interest to explore the origin of the improved selectivity with *in-situ* techniques, hence guide future catalyst design.

Nevertheless, *operando* Raman spectroscopy has not been used very frequently for the detection of surface-adsorbed molecules in aqueous CO<sub>2</sub> reduction, possibly related to specific challenges involved in *operando* SERS (Yilin Deng & Yeo, 2017; Heidary et al., 2019). The technique requires suitably structured “rough” surfaces, SERS background signals may distort the spectral information, intense gas evolution at higher overpotentials can impede the measurements, and a variety of potential species may show similar Raman peaks that may complicate the interpretation of the Raman spectra seriously.

CO as an important intermediate for multi-carbon products is an exception and has been most frequently observed in *operando* Raman experiments (Y. Deng et al., 2018; Oda, Ogasawara, & Ito, 1996; Ross et al., 2017; B. D. Smith & Irish, 1997; A. Wuttig et al., 2016). Waegele's group used *operando* Raman to examine the potential dependent CO peak trend (Gunathunge et al., 2017). They claim that the change of the CO Raman peak shape reflects Cu surface reconstructions induced by increase of CO coverage with increasing negative potential during the CO<sub>2</sub> reduction process. In another work they have found two kinds of binding modes of CO to Cu: bridge bonded and atop bonded CO at 1850 and 2000 cm<sup>-1</sup> in IR spectra. The bridge-bonded CO adsorption is observed to be electrochemically inert in alkaline electrolyte. Chang et al. observed similar phenomena with Raman (X. Chang, Zhao, & Xu, 2020). They systematically investigated the relation of these two binding modes with solution local pH and C<sub>2</sub> product activity. These pioneering works truly advanced in acquiring information on key CO<sub>2</sub>RR steps, whereas there is potential for detecting other reaction intermediates and exploring possible reaction pathways of CO<sub>2</sub>RR by *operando* SERS.

In this chapter, the issue of complex background phenomena in *operando* SERS has been addressed and first steps in the investigation of the adsorbed reaction species at the surface of a Cu foam electrode during electrochemical CO<sub>2</sub> reduction has been undertaken. Additionally, the chemical state of the Cu electrode surface has been identified, specifically the potential-dependence of oxide formation. A highly porous electrodeposited Cu foam was employed, because of its interesting CO<sub>2</sub>RR properties, which has previously been well-characterized regarding structural parameters and the CO<sub>2</sub>RR product spectrum. Here it has been shown that the interesting Cu-foam catalysts can be used as a SERS-active surface in their "native" as-synthesized form.

## 2.2 Results and discussion

### 2.2.1 The dendritic structure

Template prepared Ag or Au nanostructures are the most investigated substrates for Surface enhanced Raman scattering research. Compared to Ag and Au, Cu has less prominent SERS enhancement. With the interest of Cu as an electrocatalyst for CO<sub>2</sub> reduction, higher SERS on Cu is needed for the detection of reaction intermediates. This can be achieved by increasing the roughness of the Cu substrate, higher roughness often has more defects, which also can potentially increase the number of active sites. Electrodeposition for preparing SERS substrates is fast and reproducible. Here, a Cu foam catalyst with a dendritic structure is electro-deposited according to literature procedures (Klingan et al., 2018). Briefly, a flat Cu foil (10x10 mm<sup>2</sup>) is negatively polarized in galvanostatic mode in a three-electrode cell containing 0.2 mM CuSO<sub>4</sub> for a certain time (10/20 s). Compared to a flat Cu foil surface, the Cu foam catalyst has a thick layer of porous structure due to the hydrogen bubble formed in situ during deposition. Varying deposition time and current can regulate the thickness of the Cu foam. A series of height profiles at 0 to 50 μm taken with a microscope at different sample conditions are shown in **Figure 2.1a**, the sample deposited with 1 A, 20 s is the thickest, which is twice as thick as the sample deposited with 0.5 A 10 s. At the same height, the pore structure has roughly the same diameter, whereas with increasing time, the pore grows larger with a wider opening as shown with circle

indicator in **Figure 2.1a**. According to previous study, comparing to Cu foil of 1 cm<sup>2</sup>, Cu foam (0.5 A, 20 s) has an ECSA of 62 cm<sup>2</sup> (Klingan et al., 2018).

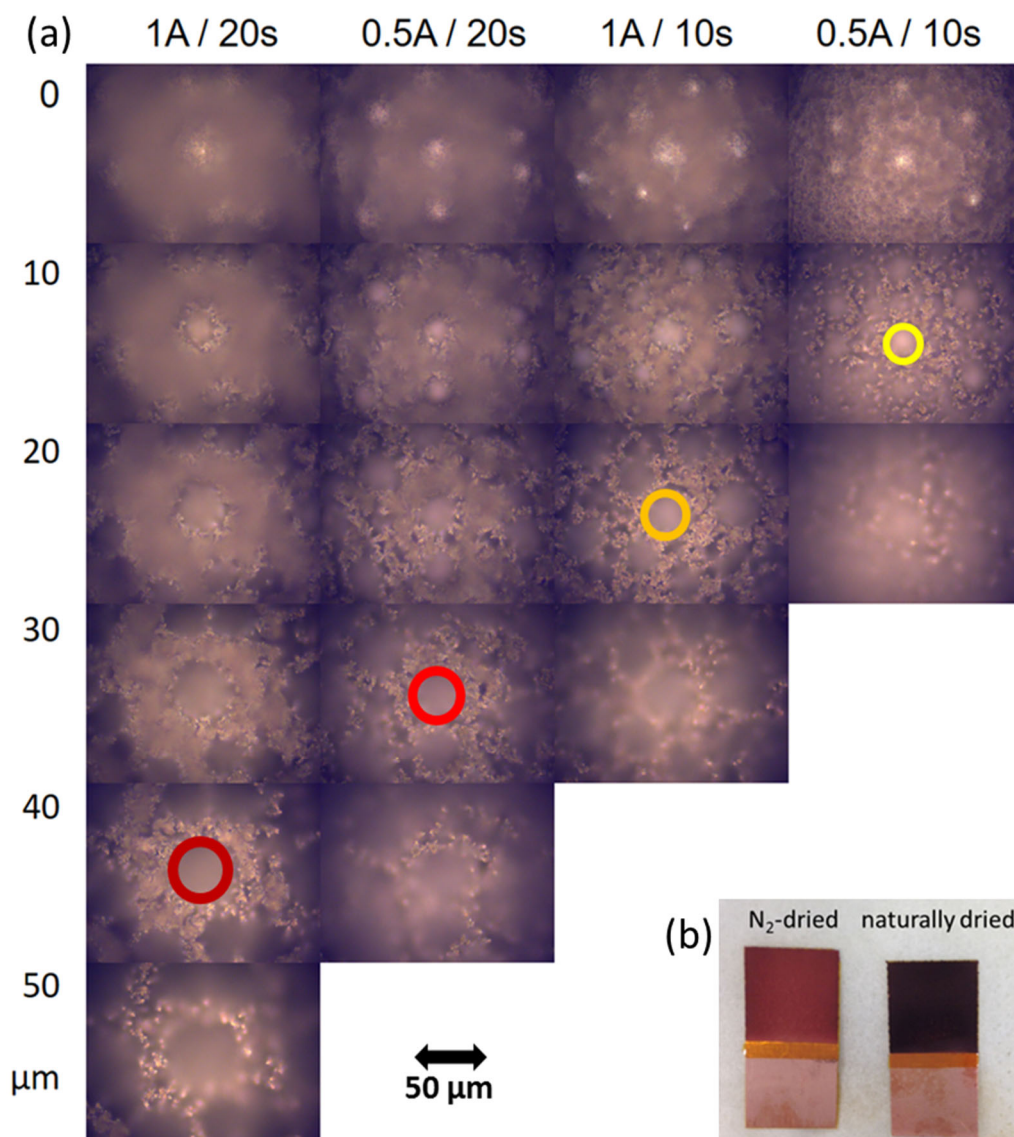


Figure 2.1. (a) Microscopic pictures of height profiles at 0 to 50 μm of Cu foam under different deposition conditions; (b) photo of N<sub>2</sub> gas dried Cu foam electrode and the one naturally dried in air, which shows that different treatment of the electrode will end up with different color.

Although metallic Cu is deposited, after exposing it to the air, an oxide layer is naturally formed on the electrode. The treatment of Cu foam after deposition is found to have an impact on the formation of oxide. As shown in **Figure 2.1b**, after deposition and rinsing with water, the Cu foam naturally dried in the air for several minutes showed dark red color, whereas the Cu foam dried with N<sub>2</sub> gas (1 minute) kept the original red color and can last for a relatively long time (1 day) until it gets darker as well, which denotes a slower process of oxidation of metallic Cu. This suggests that the water layer accelerated the oxidation process which may be related to the rough mesoporous structure. Indeed, keeping the catalyst with the surface water layer and store for longer time has even more prominent effect as will be discussed in **Chapter 3**.

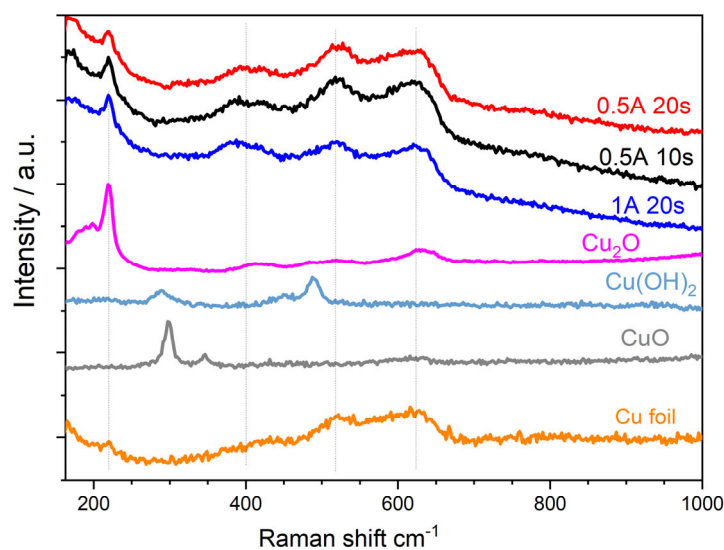


Figure 2.2. Raman spectra of dry Cu foams with different deposition conditions in comparison to reference compounds including  $\text{Cu}_2\text{O}$ ,  $\text{Cu}(\text{OH})_2$ ,  $\text{CuO}$  and  $\text{Cu}$  foil. All spectra are measured with 633 nm laser.

The Raman spectra of the dry samples show three broad peaks at 370-430, 490-550, 560-650  $\text{cm}^{-1}$  and a narrow sharp peak at 220  $\text{cm}^{-1}$  as can be seen in **Figure 2.2**. Reference compounds including  $\text{Cu}_2\text{O}$ ,  $\text{Cu}(\text{OH})_2$ ,  $\text{CuO}$  and  $\text{Cu}$  foil have also been measured for comparison. Samples with different thicknesses all show the same broad bands. These bands are also visible on  $\text{Cu}$  foil, which comes from the natural oxide formed on  $\text{Cu}$  surface. Unfortunately, it is hard to define the real composition due to the amorphous nature of the catalyst. In literature, the reported Raman shift are often overlapping or conflicting for different copper oxides assignments, especially when it comes to nanostructured morphology. **Table 2.1** listed the bands of reference  $\text{Cu}$  oxides in comparison to the bands of the  $\text{Cu}$  foam. Compared to the peaks observed on  $\text{Cu}$  foam, huge resemblance to  $\text{Cu}_2\text{O}$  can be seen, however,  $\text{CuO}$  band at 633  $\text{cm}^{-1}$  and  $\text{Cu}(\text{OH})_2$  bands at 488  $\text{cm}^{-1}$  are also in this range and cannot be excluded. It is also possible that only a thin layer of  $\text{CuO}$  or  $\text{Cu}(\text{OH})_2$  that shows no strong Raman signal.

Table 2.1. Raman bands of  $\text{Cu}$  oxide reference compounds compared to the bands observed in this work.

Compounds	Raman shift / $\text{cm}^{-1}$				
$\text{Cu}_2\text{O}$	150	220	410	520	625
$\text{CuO}$		300	348		633
$\text{Cu}(\text{OH})_2$		290	450	488	
$\text{Cu}$ foam	150	220	370-430	490-550	560-650

Under OCP (open circuit potential) in electrochemical cell with  $\text{CO}_2$  saturated bicarbonate

electrolyte, there is no structural change observed compared to the dry sample. Under the same condition, a spectrum measured with the blue 473 nm laser is shown in **Figure 2.3** in comparison to the one taken with the red 633 nm laser. It can be seen that using 473nm laser although with a high laser power, the oxide peaks are not evident, except peaks at 150 and 645  $\text{cm}^{-1}$ . This suggests that underneath the oxide layer there is still metallic Cu that has a SERS effect using the 633nm laser, which enabled the observation of clear oxide bands. This is explained in **Chapter 1** that Cu has SPR effect when the excitation energies are lower than 2.2 eV (563 nm). In addition, with the blue laser, peaks from solution species are also visible, which suggests that 473 nm laser is a better choice when measuring solution species and avoiding influence of surface adsorbate.

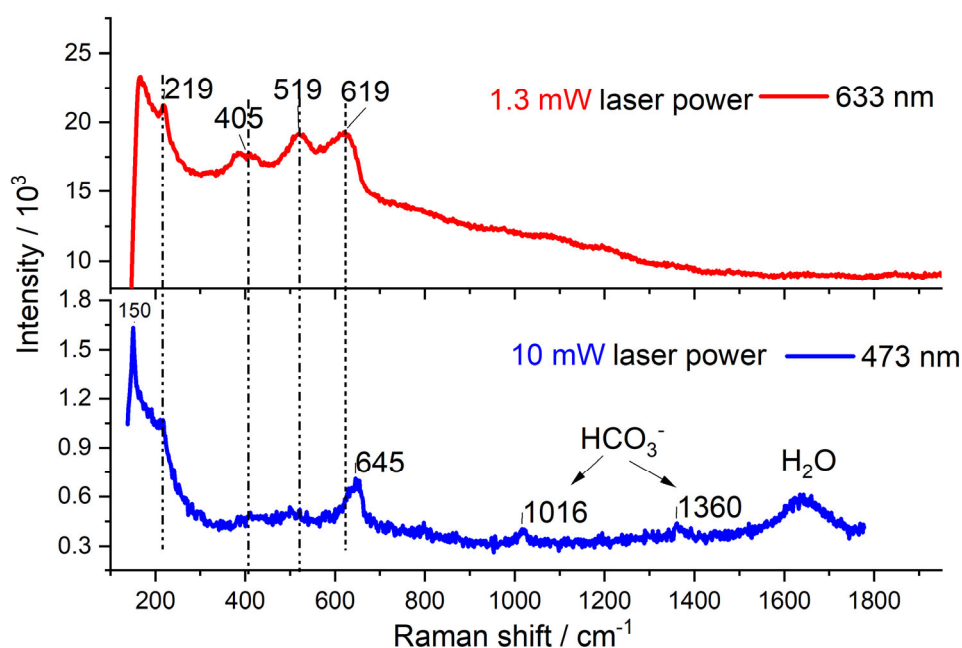


Figure 2.3. Raman spectra of Cu foam under OCP measured with 633 nm laser (1.3 mW) and 473 nm laser (10 mW). Due to SERS with the 633nm laser, oxide bands are more visible.

### 2.2.2 Operando SERS spectra and SERS background

The product distribution of these high surface area Cu foams has been investigated in literature, it differs distinctly from the product distribution of a flat Cu metal surface: formation of hydrogen and methane is strongly suppressed (per surface area), whereas carbon monoxide and even more so ethylene is formed with especially high partial current densities. Limitation of the proton transport and alkalization at the foam surface may explain this selectivity shift to some extent, as will be discussed in **Chapter 5**. In this chapter, the surface adsorbed species are investigated by *operando* Raman spectroscopy to get an insight of the reaction mechanism.

For different deposition conditions, the product distributions are quite similar, 18.5% faradaic efficiency for  $\text{C}_2\text{H}_4$  was obtained with 0.5 A, 20 s Cu foam. Due to the similar behavior of different Cu foam, here only the Cu foam deposited with 0.5 A, 20 s has been investigated. Using a home-built Raman cell, where the catalyst i.e. the working electrode faces the water immersive objective, Raman spectra can be acquired under electrochemical reaction conditions.

A photo of the Raman cell and a scheme of it are shown in **Figure 2.4**. A Pt ring works as the counter electrode and a miniature stick saturated Ag/AgCl electrode works as the reference electrode. The electrolyte is 0.1 M KHCO<sub>3</sub> with CO<sub>2</sub> gas continuously purging in the cell. To exploit the SERS effect, the 633 nm laser is used, and in order to have a homogeneous detection area and to reduce potential radiation damage the streamline mode was used which has a line focus of 100 μm length 10 μm width with 1.3 mW laser power.

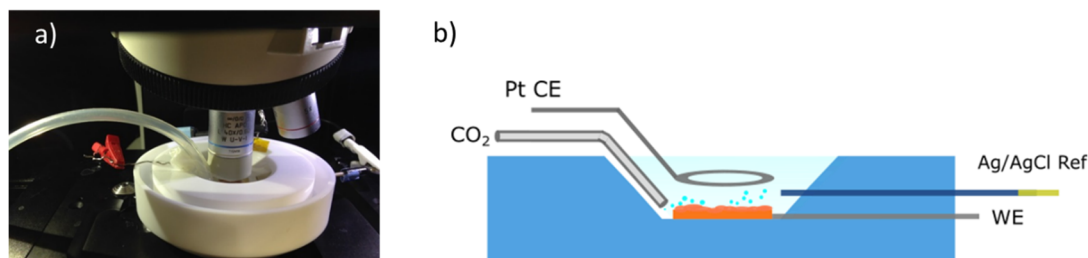


Figure 2.4. (a) A photo of *in-situ* Raman cell; (b) a scheme of the Raman cell.

Due to the high overpotential of CO<sub>2</sub> reduction, only when potential goes above  $-0.5 V_{RHE}$ , gas chromatography (GC) can detect some products (Klingan et al., 2018). However, SERS is sensitive to low amounts of surface adsorbed species. Accordingly, there is a possibility that the rising of certain intermediates bands can be observed at lower overpotentials. Moreover, considering that the usual cyclic voltammetry measurements are done in the range of 0 to  $-0.9 V_{RHE}$ , this range was chosen for the *operando* Raman measurements. Within this work, a protocol of a series of constant potentials was employed to reach steady state conditions. Firstly, a CA (Chronoamperometry) series on a fresh catalyst with surface oxide layer was performed from 0  $V_{RHE}$  until  $-0.9 V_{RHE}$  with 100 mV intervals and each potential for 2 mins, which is labeled as series 1. Next with the same reduced Cu catalyst but quickly exchanging to fresh electrolyte, a second CA series scanning forwards from  $-0.1$  to  $-0.9 V_{RHE}$  and backwards to  $-0.1 V_{RHE}$  was performed, which are labeled as series 2 and 3 respectively. The raw data are shown in **Figure 2.5**. Many peaks can be observed with changing potential, which suggest that the Cu foam works well as a SERS substrate without any modification. In addition to the sharp Raman peaks, there is a broad background beneath the spectra, which is changing with potential. This may distort the direct interpretation of the data; therefore, a proper data analysis procedure is necessary. Firstly, the background was subtracted. The background was fitted by Renishaw software, it usually consists of a curve with polynomial order of 6 to 8. The background spectra of **Figure 2.5** are shown in Appendix 8.1.

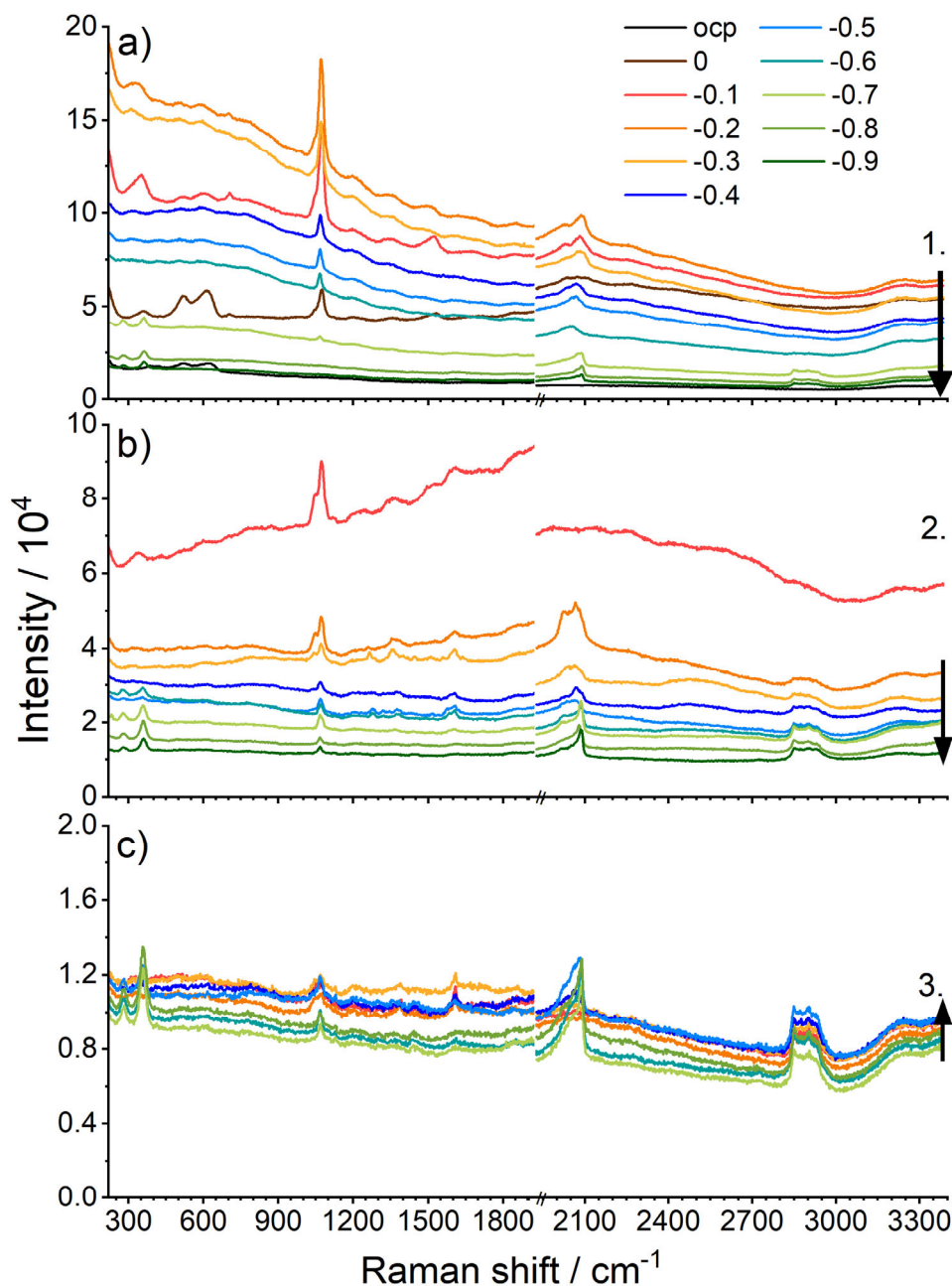


Figure 2.5. *Operando* Raman spectra of Cu foam in  $\text{CO}_2$ -saturated  $\text{KHCO}_3$  buffer (0.1 M, pH 6.8) at various electrochemical potentials, before background subtraction and normalization. a) Reduction of  $\text{Cu}_x\text{OH}_y$  to metallic copper and electrochemical  $\text{CO}_2$  reduction from 0 to  $-0.9 V_{\text{RHE}}$  (Series 1, as described in the main text). b) After oxide reduction, potentials from  $-0.1$  to  $-0.9 V_{\text{RHE}}$  were applied (Series 2). c) Backward scan from  $-0.8$  to  $-0.1 V_{\text{RHE}}$  (Series 3). Arrows indicate the scan direction of the electric potential. The legend in panel a) provides the applied potentials (vs. RHE) and the respective line color; the black line labeled by "OCP" corresponds to conditions of an "open-circuit potential" meaning that no potential was applied at the "floating" working electrode. The spectra are not offset against each other. Reprinted from ref (Jiang, Klingan, Pasquini, & Dau, 2019), with the permission of AIP Publishing.

In order to investigate the trend of background intensity with applied potential, the background intensity at the same point of series 1, 2 and 3 was plotted against the electric potential in **Figure 2.6**. The background intensity in series 1 experienced the biggest change; it increased in the beginning and peaked at  $-0.2 V_{RHE}$ , then kept decreasing. In contrast, when starting from the reduced state, the background intensity kept decreasing (series 2). It can be speculated that in series 1 both potential and Cu oxidation states play a role for the SERS background. However, in series 3, when going from negative to positive potential, the background intensity did not change considerably. The reason of no obvious change in background intensity of series 3 can be related to the history of the electrode, for instance irreversible reaction or modification of the surface.

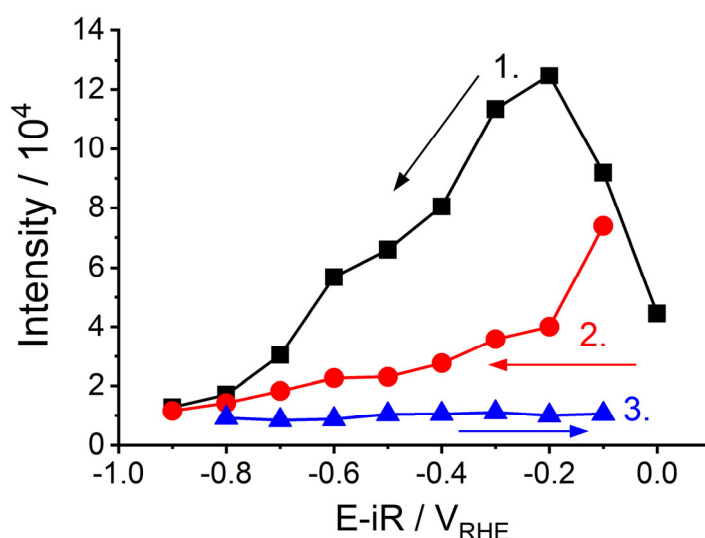


Figure 2.6. Intensity of the SERS background (averaged values of region 1) versus electrochemical potential of a Cu foam in 0.1 M  $KHCO_3$  (pH 6.8). The black symbols correspond to Series 1 (increasingly negative potentials), the red symbols to Series 2 (second series of increasing negative potentials), and the blue symbols to Series 3 (increasingly positive potentials). The background intensities relate to the data shown in Figure 2.5. Reprinted from ref (Jiang, Klingan, Pasquini, & Dau, 2019), with the permission of AIP Publishing.

Apparently, the background intensity is changing with potential, which may interrupt the real peak trend. Therefore, a further step for data analysis for *operando* SERS spectra is proposed. After background subtraction, the background is used to normalize the curve. The spectra after analysis of **Figure 2.5** are shown in **Figure 2.7**. It can be seen in **Figure 2.7** that besides the sharp Raman peaks; there is also a series of oscillation bumps appears roughly every  $100 \text{ cm}^{-1}$ . In order to trace the origin of this phenomena, a spectrum of a piece of plain white paper was taken, no peaks but only these regular bumps are observed (see Appendix 8.2). Therefore, it can be speculated that the appearance of these regular bumps is an artefact of the detector system when there is high signal. It is possible to remove them by subtracting the spectra of paper, whereas here it is not applied. In the following section, the validation of the proposed analysis method for *operando* Raman data and the origin of the SERS background will be discussed.



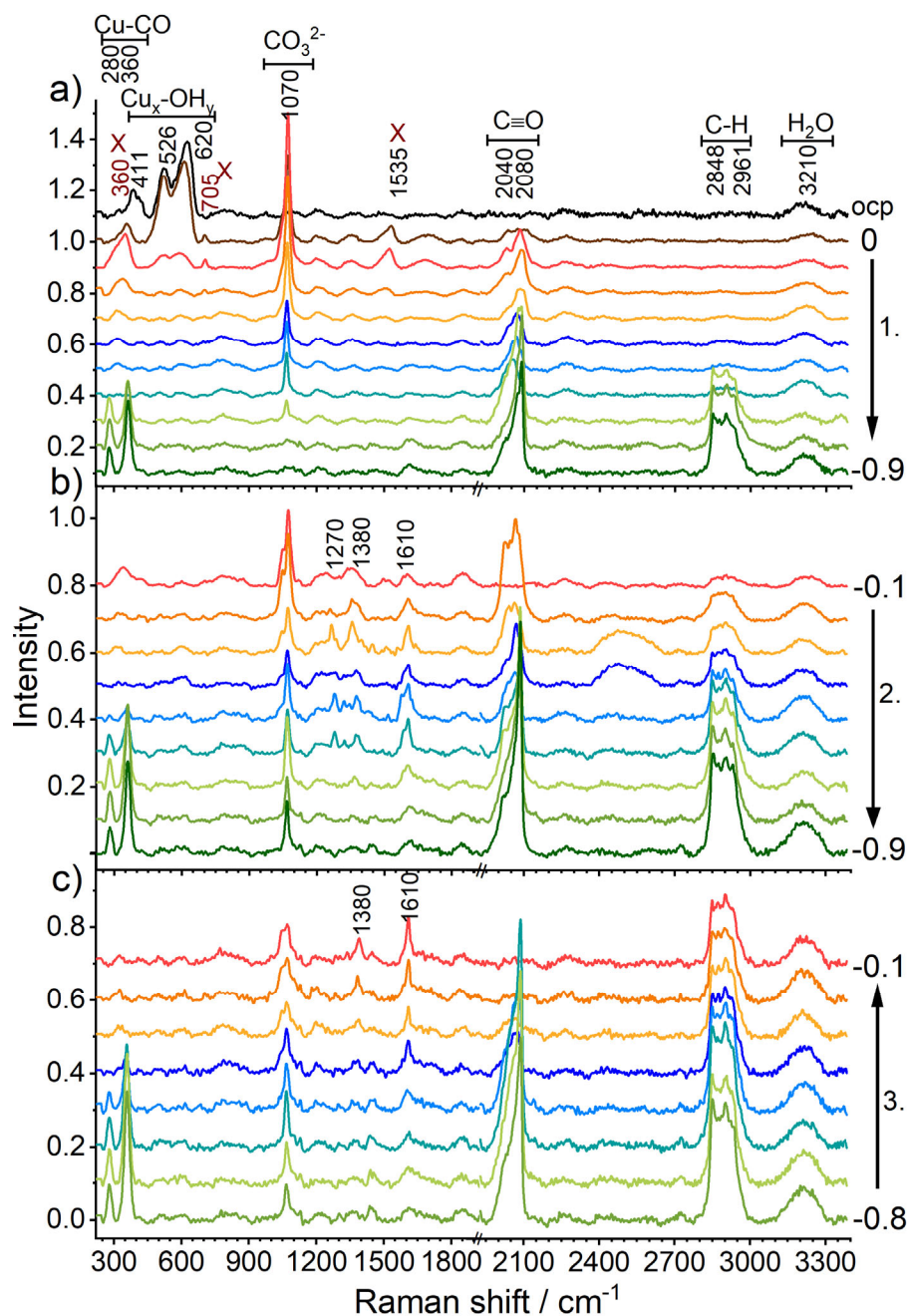


Figure 2.7. *Operando* Raman spectra of Cu foam in CO<sub>2</sub>-saturated KHCO<sub>3</sub> buffer (0.1 M, pH 6.8) at various electrochemical potentials, after background subtraction and normalization. The data of Figure 2.5 was processed by background subtraction and normalization to the intensity of the SERS background; for clarity of the graphical presentation, a vertical offset was applied. a) Reduction of Cu<sub>x</sub>OH<sub>y</sub> to metallic copper and electrochemical CO<sub>2</sub> reduction by potentials ranging from 0 to -0.9 V<sub>RHE</sub> (Series 1). b) After oxide reduction, potentials from -0.1 to -0.9 V<sub>RHE</sub> were applied (Series 2). c) Backward scan from -0.8 to -0.1 V<sub>RHE</sub> (Series 3). The water band at 3210 cm<sup>-1</sup> corresponds to the broad spectrum of O-H stretching vibrations which becomes visible as a separate band only after removal of a smooth background; it likely results from bulk water molecules and thus is not informative in the context of the present study. Reprinted from ref (Jiang, Klingan, Pasquini, & Dau, 2019), with the permission of AIP Publishing.

## 2.2.3 Origin of SERS background and validation of the data analysis method

### 2.2.3.1 SERS effect related to Cu oxide

The origin of the background can be related to the chemical and electromagnetic effect that cause the SERS effect. Lin et al. use plasmonic photoluminescence to restore the background (Lin et al., 2017). Nevertheless, the analysis procedure report in this chapter is simpler and more practical for extracting the “background-clean” spectra.

From the background intensity trend, it can be speculated that two factors are influencing the background, which can be both the catalyst oxidation states and the applied potential. To clarify how these two factors work and to signify the validity of here presented data analysis method, cyclic voltammetry (CV) was performed from completely reduced potential ( $-0.4 V_{\text{RHE}}$ ) to an oxidizing potential ( $1 V_{\text{RHE}}$ ) then back to negative potential and record the Raman spectra (roughly every 50 mV). **Figure 2.8a** and **2.8b** show the raw Raman data; **Figure 2.8c** and **2.8d** show the data after background subtraction and normalization of the forward scan and backward scan, respectively. In the raw data there is hardly any trend visible but chaotic curves with background high or extremely low. Especially the spectra at oxidizing potentials are low in intensity and the peaks are hardly visible. This suggests that the oxide decreases SERS effect and background intensity is influenced by the SERS intensity.

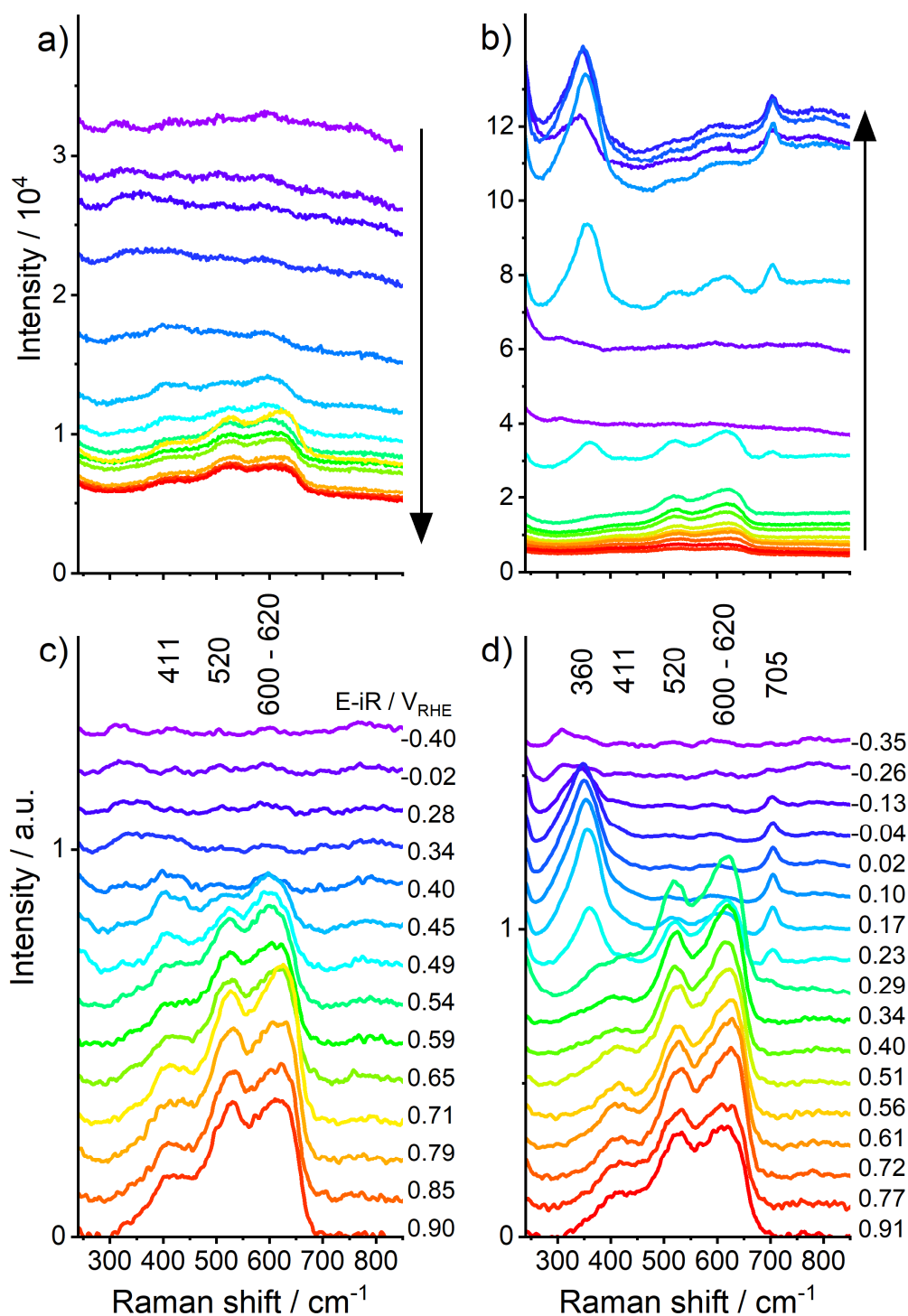


Figure 2.8. *Operando* Raman spectra at various electrochemical potentials of a Cu foam during a CV with  $1 \text{ mV s}^{-1}$  ( $0.1 \text{ M KHCO}_3$  buffer, pH 8.8). In a) and c), forward-scan from negative to positive potentials. In b) and d), backward-scan from positive to negative potentials. The top row of spectra, in a) and b), shows the unprocessed data; the spectra are not offset against each other. The arrows indicate the direction of major changes in the Raman intensity during the scan of the electric potential. The bottom row of spectra, in c) and d), shows background-subtracted and normalized spectra; a vertical offset was applied for visual clarity. Reprinted from ref (Jiang, Klingan, Pasquini, & Dau, 2019), with the permission of AIP Publishing.

In **Figure 2.9**, the intensity trend of the oxide peak at  $620\text{ cm}^{-1}$  and the peak at  $360\text{ cm}^{-1}$  that appeared after Cu oxide reduction were plotted, **Figure 2.9a** shows the one in the dataset after background subtraction without normalization and **Figure 2.9b** shows the data after both background subtraction and normalization. With increasing potential to the positive direction, in **Figure 2.9a** the oxide peak intensity kept increase until around  $0.2\text{ V}_{\text{RHE}}$  and then suddenly decrease again, which is contradictory to the fact that the oxide content should only increase or remain constant. This is corrected by the normalization, the  $620\text{ cm}^{-1}$  peak intensity remained at the same level until  $1.0\text{ V}_{\text{RHE}}$ . Now it can be clearly seen that there is a hysteresis between Cu oxide reduction and oxidation scan. When oxide is being reduced, the peak at  $620\text{ cm}^{-1}$  remains relatively the same intensity before decreasing after potential reached  $0.3\text{ V}_{\text{RHE}}$ , whereas in the oxidizing scan only after  $0.7\text{ V}_{\text{RHE}}$  the oxide peak reached the same intensity. Notably, the peak at  $360\text{ cm}^{-1}$  shows a remarkable intensity in **Figure 2.9a** (plotted with 0.2 factor), whereas after normalization, it shows only comparable or even lower intensity than oxide bands, which is more reasonable considering that the surface adsorbed species can only be lower in amount than the bulk oxide. It can be concluded that background subtraction and appropriate normalization are both important for analyzing *operando* SERS data to draw conclusion on peak trend information.

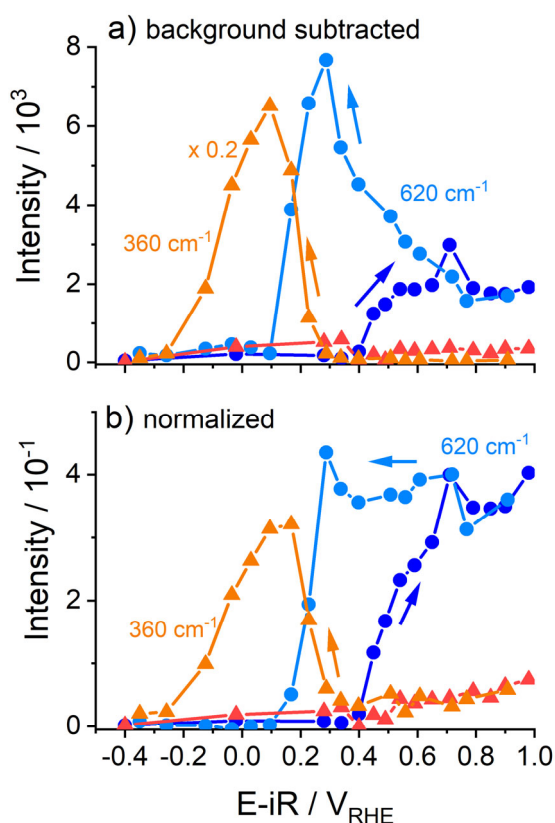


Figure 2.9. Potential dependent Raman intensities at  $620\text{ cm}^{-1}$  (dark and light blue) and at  $360\text{ cm}^{-1}$  (red and orange) of a Cu foam during a CV with  $1\text{ mV s}^{-1}$  in  $0.1\text{ M KHCO}_3$  (pH 8.8). a) Background subtracted intensities. b) Background subtracted and normalized intensities. Arrows indicate the potential scan direction. The intensities relate to the data shown in Figure 2.8. The backward-scan intensities (orange curve) in a) have been multiplied by 0.2. Reprinted from ref (Jiang, Klingan, Pasquini, & Dau, 2019), with the permission of AIP Publishing.

### 2.2.3.2 Thiophenol calibration experiment

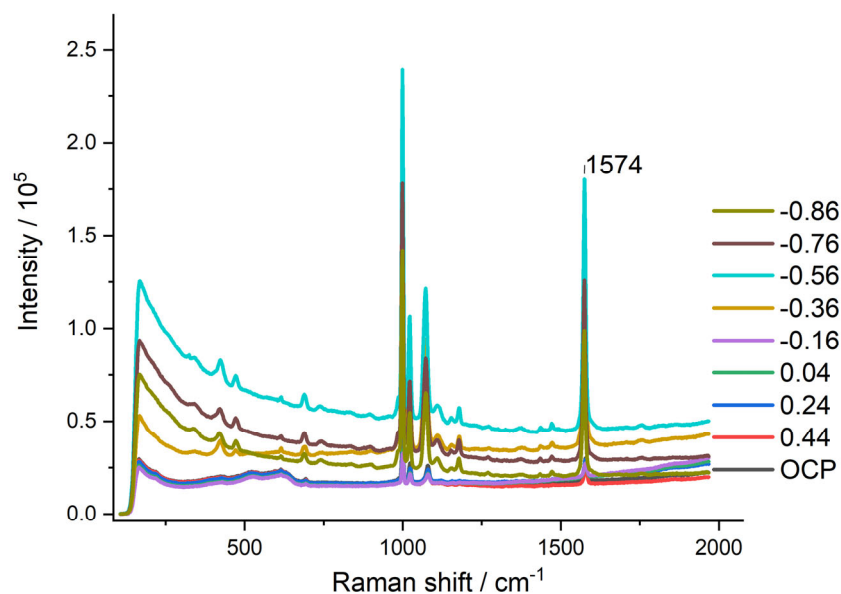


Figure 2.10. *In-situ* Raman spectra of thiophenol (10 mmol/L) adsorption on Cu foam under series of potentials (from 0.44 to -0.86  $V_{\text{RHE}}$ ) performed in 0.1 M  $\text{NaClO}_4$  electrolyte (raw data).

Pyridine and other molecules are normally used for magnifying the SERS effect (Albrecht & Creighton, 1977; Fleischmann et al., 1974; Mahajan et al., 2010). In order to further illustrate the mechanism of SERS background, the adsorption of thiophenol on a Cu foam was examined. After deposition of the Cu foam electrode, a certain amount of thiophenol dissolved in ethanol (10 mmol/L) solution was quickly dropped on the surface of Cu foam to make sure that thiophenol is in contact with Cu metal before Cu oxide forms, then it was left in the air for 3 hours. As shown in **Figure 2.10**, under OCP, Cu oxide peaks appeared, and tiny peaks of thiophenol were visible at 998, 1021, 1072 and 1574  $\text{cm}^{-1}$ . *Via* applying negative potentials until -0.36  $V_{\text{RHE}}$ , Cu oxide was completely reduced and thiophenol peaks were enhanced, at the same time, some new bands appeared at 423, 471, 688  $\text{cm}^{-1}$ , which suggests that SERS effect is prominent on reduced Cu. This can be noted as series 1 similar to the protocol in **Section 2.2.2**, on the reduced Cu foam potential scanning forward and backward were measured and noted as series 2f and 2b (spectra shown in Appendix 8.3). This is to see if there is a potential dependence of SERS effect without the influence of Cu oxide. The peak intensity at 1574  $\text{cm}^{-1}$  vs potential trend for these three series were plotted in **Figure 2.11a**. In the first CA series, the peak intensity experienced the biggest change. After -0.2  $V_{\text{RHE}}$  where Cu oxide layer was reduced, the peak intensity surged an order of magnitude. This is not observed in the second series, but there is still a trend with the maximum appearing at around -0.4  $V_{\text{RHE}}$ . Similar to the trend observed in series 3 in **Figure 2.6**, there is also no big variation in the background intensity when scanning backwards on the reduced Cu. These experiments performed in  $\text{NaClO}_4$  electrolyte where there is no influence from  $\text{CO}_2\text{RR}$ , however the same behavior of SERS intensity change is observed compared to the experiments that was performed in  $\text{CO}_2\text{RR}$ . Therefore, it further proves that the SERS intensity trend does not come from  $\text{CO}_2\text{RR}$  and needs to be corrected before analysis of  $\text{CO}_2\text{RR}$  Raman spectra.

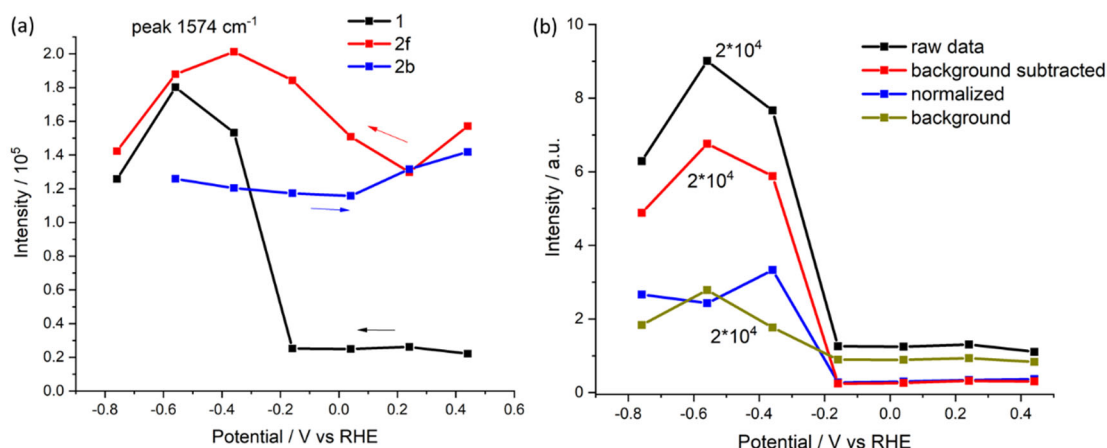
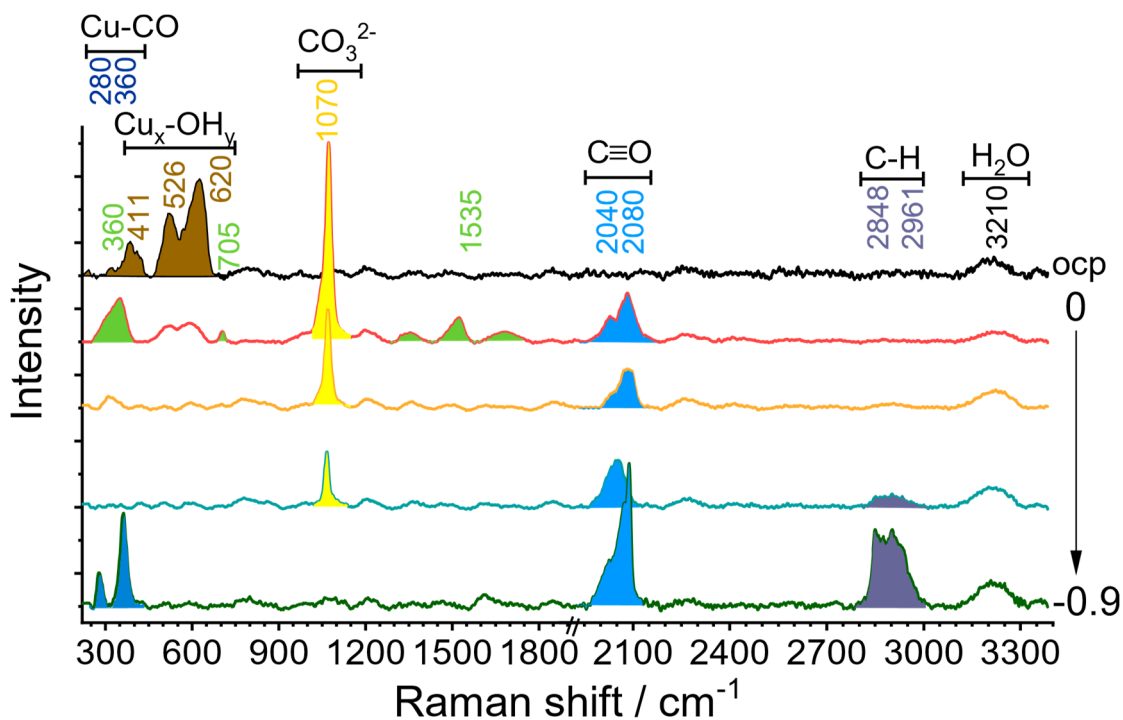


Figure 2.11. (a) Peak at 1574 cm<sup>-1</sup> trend in raw spectra vs potential in two series 1. Fresh Cu electrode scanning forward; 2. Scanning forward and backward on the reduced Cu foam electrode; (b) Peak trend of thiophenol at 1574 cm<sup>-1</sup> in series 1 of raw data (black curve), after subtracting background (red curve), after normalization (blue curve) and the Raman background (grass green curve) trend.

The increase of SERS intensity in series 1 on Cu oxide, further validated the function of oxide content on the SERS effect. It is consistent to literature reporting similar behavior for Ag nanoparticles, where it is shown that after exposing to ozone, Ag changed to Ag<sub>2</sub>O, and the SERS factor decreased 3 orders of magnitude (Han et al., 2011). Furthermore, the peak intensity trend vs potential of peak at 1574 cm<sup>-1</sup> in series 1 in different steps of data analysis were plotted in **Figure 2.11b**. The significant increase of peak intensity resulting from SERS effect can be corrected by normalization. Nevertheless, in the normalized data, the peak intensity still increased after -0.2 V<sub>RHE</sub>. It can be speculated that the stronger binding of thiophenol molecule to Cu after reduction gives a higher intensity, i.e. result of chemistry enhancement mechanism. This is consistent to the SERS enhancement mechanism proposed by Otto et al. (Otto, Billmann, Eickmans, Erturk, & Pettenkofer, 1984).

## 2.2.4 Adsorbed species and corresponding assignments

So far, it has been proven that the validity of the proposed data analysis procedure, therefore the peak intensities in **Figure 2.7** can be investigated in detail. As illustrated in **Scheme 2.1**, the peaks appeared in series 1 can be divided into several subgroups based on their origin from different species, the peaks from the same species are labeled with the same color. It is therefore clear how the peaks change with potentials. In summary, under OCP, only Cu oxide bands were observed. With decreasing potentials, the Cu oxide bands decreased intensity and disappeared after -0.2 V<sub>RHE</sub>, new bands at 350, 705, 1535 cm<sup>-1</sup> appeared simultaneously. The origin of these bands will be discussed in **Chapter 3**. The carbonate peak at 1068 cm<sup>-1</sup> appeared since 0 V<sub>RHE</sub> and weakened at high overpotentials. CO intramolecular band appeared since -0.1 V<sub>RHE</sub> and changes its shape with decreasing potentials. Whereas Cu-CO band appeared only after -0.5 V<sub>RHE</sub> when a broad C-H band also appeared. In the following sections, combining with series 2 and 3, the adsorption of carbonate, CO intermediate and C-H bands will be discussed in detail respectively.



**Scheme 2.1.** Illustration for appearance and disappearance of Raman peaks observed in *operando* Raman experiments shown in Figure 2.7a.

#### 2.2.4.1 Carbonate adsorption

The first peak to be noticed is the carbonate (symmetrical stretching mode of C-O in CO<sub>3</sub><sup>2-</sup>) peak at 1070 cm<sup>-1</sup> (Davis & Oliver, 1972), which appeared at almost all potentials. Surprisingly, bicarbonate (C-OH stretching mode at 1015 cm<sup>-1</sup>) is absent (Davis & Oliver, 1972), given that bicarbonate is more abundant in the CO<sub>2</sub> saturated bicarbonate electrolyte. It is reported that the equilibrium constant of buffer ions might be different on nanostructured surfaces than in the solution (Raciti, Mao, & Wang, 2018; Xiaoyang Shi, Xiao, Chen, & Lackner, 2016; X. Shi, Xiao, Lackner, & Chen, 2016), therefore bicarbonate tends to deprotonate and adsorb on the surface visible as carbonate band.

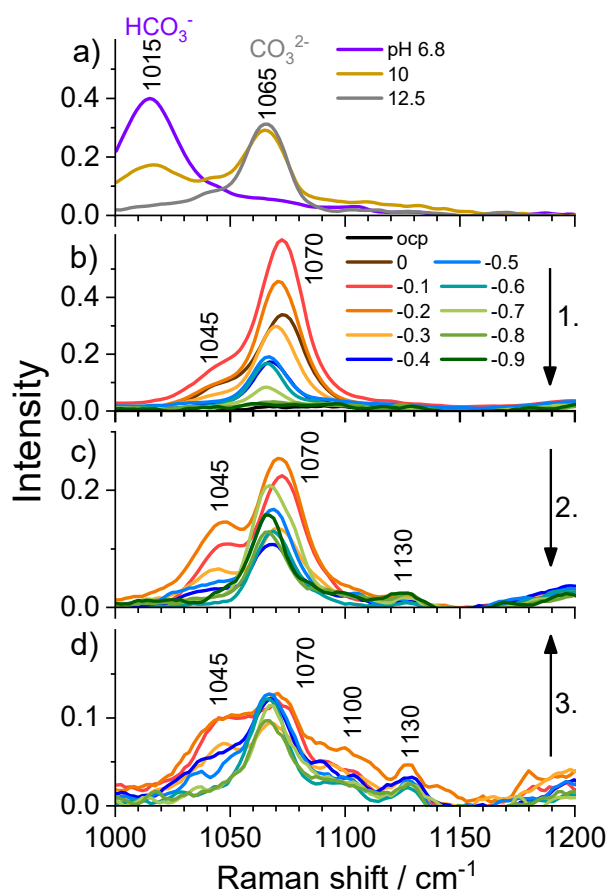


Figure 2.12. Carbonate/bicarbonate ( $\text{CO}_3^{2-}/\text{HCO}_3^-$ ) Raman bands at 1000-1100  $\text{cm}^{-1}$ . a) Solution spectra of dissolved  $\text{KHCO}_3$  (0.1 M) at pH 6.8 (violet,  $\text{HCO}_3^-$ ), pH 10 (gold) and at pH 12.5 (grey,  $\text{CO}_3^{2-}$ ). (b-d) *Operando* Raman spectra of the carbonate region at different potentials in 0.1 M  $\text{KHCO}_3$  (pH 6.8) during b) potential sweep from 0 to  $-0.9 V_{\text{RHE}}$  (Series 1), c) second potential sweep from  $-0.1$  to  $-0.9 V_{\text{RHE}}$  (Series 2), and d) backward scan from  $-0.8$  to  $-0.1 V_{\text{RHE}}$  (Series 3). Arrows indicate the scan direction. The legend in b) provides the applied voltages and the respective line color. All spectra are background subtracted and normalized. Reprinted from ref (Jiang, Klingan, Pasquini, & Dau, 2019), with the permission of AIP Publishing.

The pzc (potential of zero charge) value of Cu is reported to be at around  $-0.4 V_{\text{RHE}}$  (Łukomska & Sobkowski, 2004). Carbonate as an anion species adsorbs stronger when the potential is more positive than the pzc, and it tends to desorb when potential goes lower than the pzc. In **Figure 2.13** the peak area trend of the carbonate peak extracted from **Figure 2.12** was plotted. In the first and second series forward scan, the peak intensity first increases and decreases roughly after  $-0.2 V_{\text{RHE}}$ , which slightly deviate from the reported pzc value. In the third scan when scanning backward, there is no obvious peak intensity change. This might be due to the modification of the electrode after exposing to high potential and  $\text{CO}_2$  reduction process. Aside from the influence of pzc to the peak intensity trend in the same series, the peak intensity of carbonate is much higher in the first series than the other series. This is the opposite to the result of the thiophenol experiment, where it was found that the presence of surface oxides will decrease the intensity of adsorbed species, since the weaker binding result in a lower SERS factor. Here it can be assumed that (bi)carbonate has a high binding affinity to the oxide



therefore when starting from the oxide covered surface, the surface adsorbed carbonate is more abundant compared to the reduced catalyst. In the next chapter, the interaction of carbonate with Cu oxide will be further investigated. Stark effect is also visible, as with decreasing potentials the carbonate peak red shifts from  $1070\text{ cm}^{-1}$  to  $1065\text{ cm}^{-1}$ .

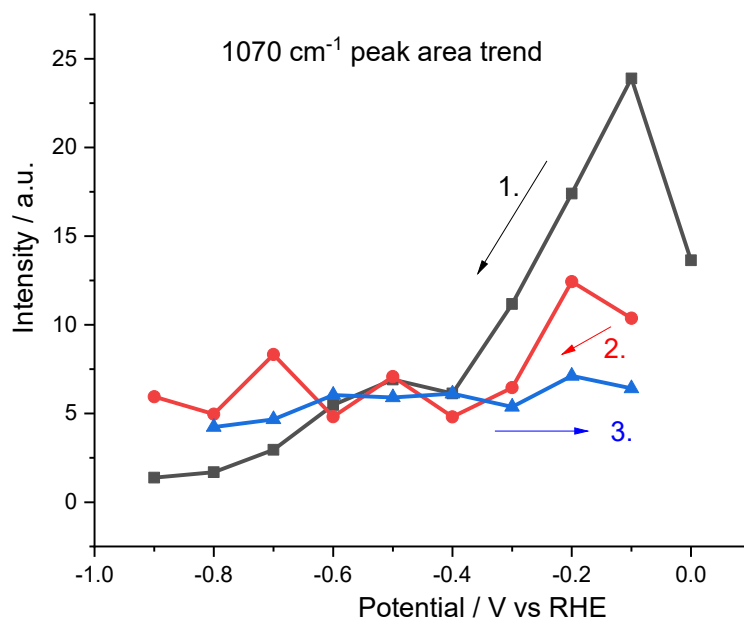


Figure 2.13. Carbonate peak area trend in Figure 2.12. Peak area was fitted with glofit.

#### 2.2.4.2 Adsorbed CO intermediates

CO as an important  $\text{CO}_2\text{RR}$  intermediate is often observed in *operando* experiments (Gunathunge et al., 2017; A. Wuttig et al., 2016; Shangqian Zhu et al., 2019). Here 4 different Raman bands related to CO are observed at about  $280$ ,  $360$ ,  $2040$  and  $2080\text{ cm}^{-1}$ , as shown in **Figure 2.14a, b**. The CO peak intensity vs potential dependence is plotted in **Figure 2.14c, d**. These bands can be assigned to two kinds of CO peaks, the pair of peaks present in the low frequency region are characteristic for Cu-CO vibrations: at  $280\text{ cm}^{-1}$  the frustrated rotational mode of CO and at  $360\text{ cm}^{-1}$  the Cu-CO stretch vibration (Akemann & Otto, 1991, 1993). The two high frequency bands are assignable to CO intramolecular stretching vibrations with different adsorption geometries (Akemann & Otto, 1991, 1993).

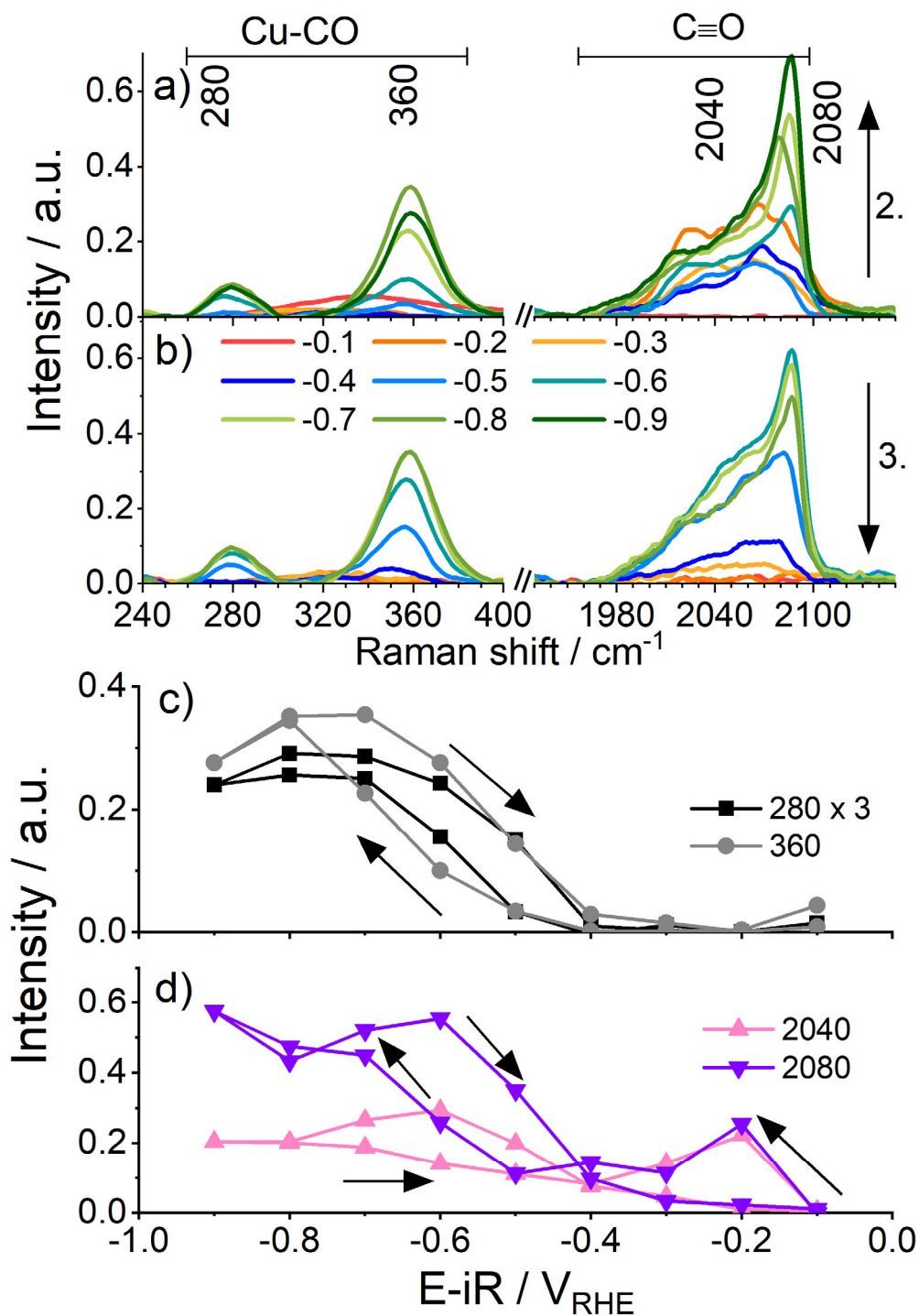


Figure 2.14. Potential-dependent intensities of Cu-CO and intramolecular CO bands (in CO<sub>2</sub>-saturated 0.1 M KHCO<sub>3</sub> buffer, pH 6.8). In (a), forward scan from -0.1 to -0.9 V<sub>RHE</sub> (Series 2 of Figure 2.7). In (b), backward scan from -0.8 to -0.1 V<sub>RHE</sub> (Series 3 of Figure 2.7). The arrows indicate the direction of major changes in Raman intensities when decreasing [in (a)] or increasing [in (b)] the electric potential; the legend in panel (b) provides the applied voltages and respective line color. In (c), potential-dependence of the Raman intensity at 280 cm<sup>-1</sup> and 360 cm<sup>-1</sup> assignable to Cu-CO bands. In (d), potential-dependence of the Raman intensities at 2040 cm<sup>-1</sup> and 2080 cm<sup>-1</sup> assignable to intramolecular CO stretch bands. Reprinted from ref (Jiang, Klingan, Pasquini, & Dau, 2019), with the permission of AIP Publishing.

Intramolecular C≡O stretch bands are already present at a potential as high as -0.2 V<sub>RHE</sub>. Between -0.1 and -0.4 V<sub>RHE</sub>, an asymmetric broad band at around 2040 cm<sup>-1</sup> (ranging from about 1980 to 2100 cm<sup>-1</sup>) (labeled as \*CO<sup>A</sup>) represents the dominating feature; it likely is composed of several overlapping sub-bands. At more positive potentials, an additional sharp band, centered around 2080 cm<sup>-1</sup> (2070-2085 cm<sup>-1</sup>) (labeled as \*CO<sup>B</sup>), becomes clearly visible. The correlated appearance and strength of the sharp 2080 cm<sup>-1</sup> band, on the one hand, and the Cu-CO vibrations at 280 and 360 cm<sup>-1</sup>, on the other hand, is visible in all potential series suggesting that these bands are assignable to the same Cu-CO binding mode. In clear contrast, the broad band of intramolecular C≡O stretch vibrations remains without any obvious counterpart in the region of the Cu-CO vibrations, suggesting assignment to CO adsorption modes that are not associated with detectable Cu-CO vibrations. Gunathunge et al. observed and explained this phenomenon as Cu surface reconstruction (Gunathunge et al., 2017). They proposed that \*CO coverage plays an important role in C-C bond coupling. When CO accumulated to certain amount, it will induce surface reconstruction of the Cu surface, and this may promote CO dimer formation which is considered as a prerequisite for C<sub>2</sub>H<sub>4</sub> production. Largely in line with their results, the following explanation can be proposed: the broad intramolecular CO bands (\*CO<sup>A</sup>) observed at potentials ranging from -0.2 to -0.4 V<sub>RHE</sub> result from binding of CO to the Cu foam surface involving several binding modes, instead of a preferred one. At even more negative potentials, adsorbed \*CO accumulates at the Cu surface until surface reconstruction allows \*CO to occupy undercoordinated defect sites (giving rise to the sharp 2080 cm<sup>-1</sup> band), which results in strong electronic back donation from CO to Cu (appearance of Cu-CO bands, \*CO<sup>B</sup>). It is worth to be further investigated that the mechanistic role of \*CO<sup>A</sup> and \*CO<sup>B</sup> in CO<sub>2</sub> reduction.

Based on electrochemical analyses, recently it has been suggested that a current plateau in cyclic voltammetry (CVs) results from CO<sub>2</sub> reduction and significant \*CO binding to a major fraction of Cu-foam surface sites at potentials more negative than -0.5 V<sub>RHE</sub>, whereas \*CO desorption requires potentials less negative than -0.4 V<sub>RHE</sub> (Klingan et al., 2018). This hypothesis is strongly supported by the herein described hysteresis in the \*CO binding of **Figure 2.14** in line with results for binding of gaseous CO to copper surfaces (A. Wuttig et al., 2016).

#### 2.2.4.3 Adsorbed intermediates with C-H bonds

There were also many intermediates' peaks observed other than CO and carbonate bands. In the region of 2800-3000 cm<sup>-1</sup> appears typical C-H stretch vibration bands. In series 1, **Figure 2.7**, these peaks appeared after -0.4 V<sub>RHE</sub>, whereas when starting from reduced Cu, these peaks appeared earlier at around -0.2 V<sub>RHE</sub>. When scanning back to positive potentials in series 3, these band did not disappear meaning that they are accumulating rather than desorbing from the surface. An enlarged graph of the peaks is shown in **Figure 2.17a**, the broad peak can be distinguished as several subpeaks at 2848, 2874, 2904, 2936 and 2961 cm<sup>-1</sup>.

Since C-H bond exists in various forms like HCOO-, -CHO, -CH<sub>3</sub> and so forth, and they are all possible intermediates in CO<sub>2</sub>RR process given the complexity of this process (Birdja et al., 2019; Nitopi et al., 2019; Xie et al., 2020; W. Zhang et al., 2018; S. Zhu et al., 2017), it is not trivial to assign the peaks unambiguously. According to the previous report, this catalyst produces some amount of formate at low overpotentials, and ethylene at high overpotentials,

and small amounts of ethanol, propanol and ethane (Klingan et al., 2018). At extremely high potentials, methane overrates ethylene and becomes the main product. However, in the context of this experiment, the highest potential is  $-0.9 V_{RHE}$ , therefore no methane was expected which is also not observed (since methane has peaks at  $2917 \text{ cm}^{-1}$ ) (Magnotti, Kc, Varghese, & Barlow, 2015). Based on this, several reference molecules including methanol, ethanol, formic acid and acetate acid were chosen and measured in order to get an overview of the potential species that may contribute to the bands that are observed in operando Raman spectra. In the solution spectra **Figure 2.15** (Peak assignments can be found in Appendix 8.7), all the molecules have several characteristic bands in  $2800\text{-}3000 \text{ cm}^{-1}$  region, except formate band position deviate a bit.

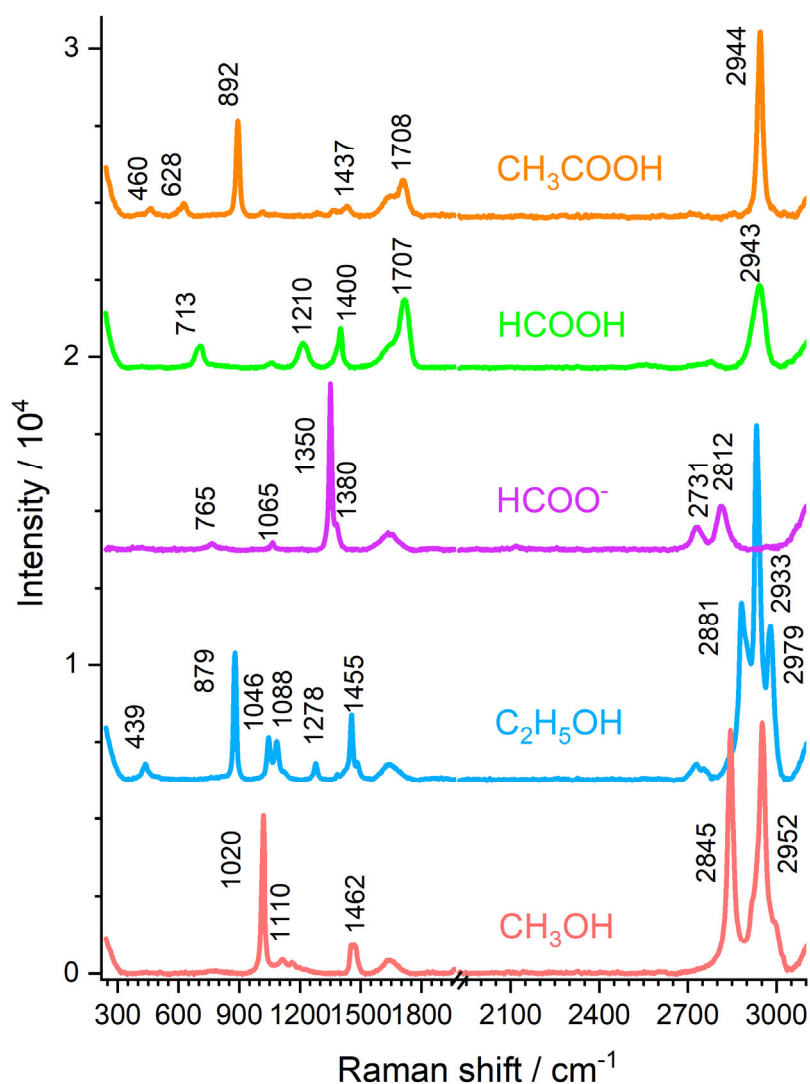


Figure 2.15. Raman spectra of reference solutions including  $\text{CH}_3\text{COOH}$ ,  $\text{HCOOH}$ ,  $\text{HCOO}^-$ ,  $\text{C}_2\text{H}_5\text{OH}$  and  $\text{CH}_3\text{OH}$ . Reprinted from ref (Jiang, Klingan, Pasquini, & Dau, 2019), with the permission of AIP Publishing.

Further experiments were performed under potential. In these experiments a phosphate buffer was used to avoid any  $\text{CO}_2\text{RR}$  products. Cu foam was first reduced to remove surface oxide

layer, then a little amount of each solution containing reference molecule was dropped onto the Cu foam under OCP. The spectra are shown in **Figure 2.16**. The C-H region of these spectra under OCP with molecules (dark lines) are compared to the original solutions' spectra (bright lines) and shown in **Figure 2.17b**. It is clearly seen that in the case of methanol and ethanol, there is no difference between solutions' spectra and on Cu foam surface spectra (detail in **Figure 2.17d**). On the contrary, a broad band raised when formic acid was dropped on Cu foam under OCP. For acetate acid a single peak as in the solution spectra appeared also on Cu foam surface, but redshifted and largely enhanced. This clearly suggest that formic acid and acetate acid could adsorb on the Cu surface. After applying negative potentials, adsorbed formic acid further converts to probably methanol as shown in **Figure 2.17c**.

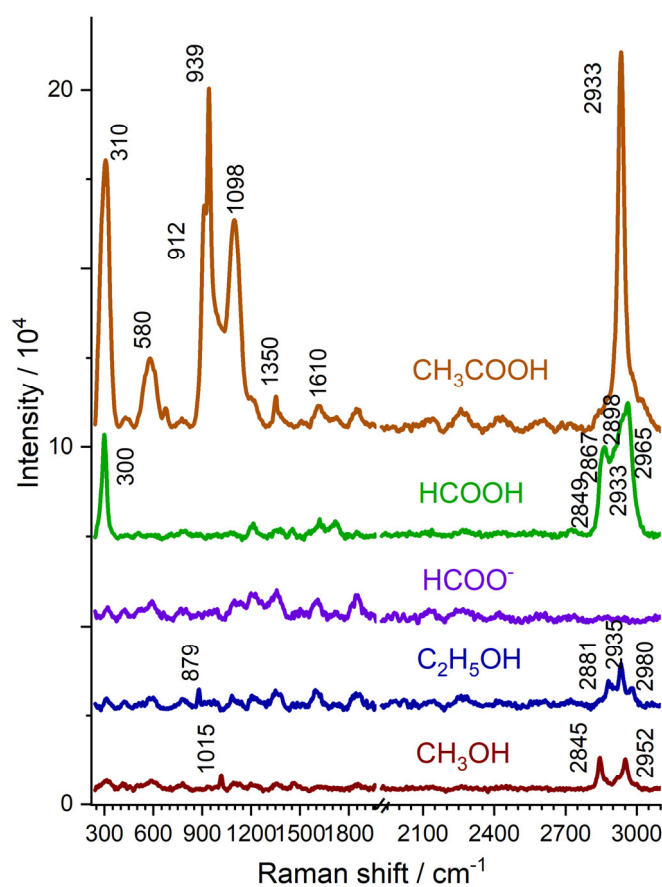


Figure 2.16. Raman spectra of Cu foam surface in 0.1 M KH<sub>2</sub>PO<sub>4</sub>/K<sub>2</sub>HPO<sub>4</sub> with CH<sub>3</sub>COOH, HCOO<sup>-</sup>, HCOOH, C<sub>2</sub>H<sub>5</sub>OH, and CH<sub>3</sub>OH, at OCP. All spectra are background subtracted and displayed with a vertical offset. The spectra were measured with different laser powers and afterwards scaled to 6.7 mW laser power. Reprinted from ref (Jiang, Klingan, Pasquini, & Dau, 2019), with the permission of AIP Publishing.

Currently it is hard to assign certain peaks in C-H bands to distinct intermediates. Similar broad C-H band have been observed on CuS<sub>x</sub> catalysts and have been assigned to adsorbed formate (Y. Deng et al., 2018). The similarities between HCOOH adsorbed on Cu surface to the C-H bands in CO<sub>2</sub> reduction seems point toward assignment to HCOOH (or formate), however the typical vibration peak at 1707 cm<sup>-1</sup> from HCOOH and 892 cm<sup>-1</sup> from acetate are not observed. Thus the assignment C-H bands to formic acid or acetate acid would be in line with the detected

Raman spectra only, if the corresponding band at lower wavenumbers were SERS-silent.

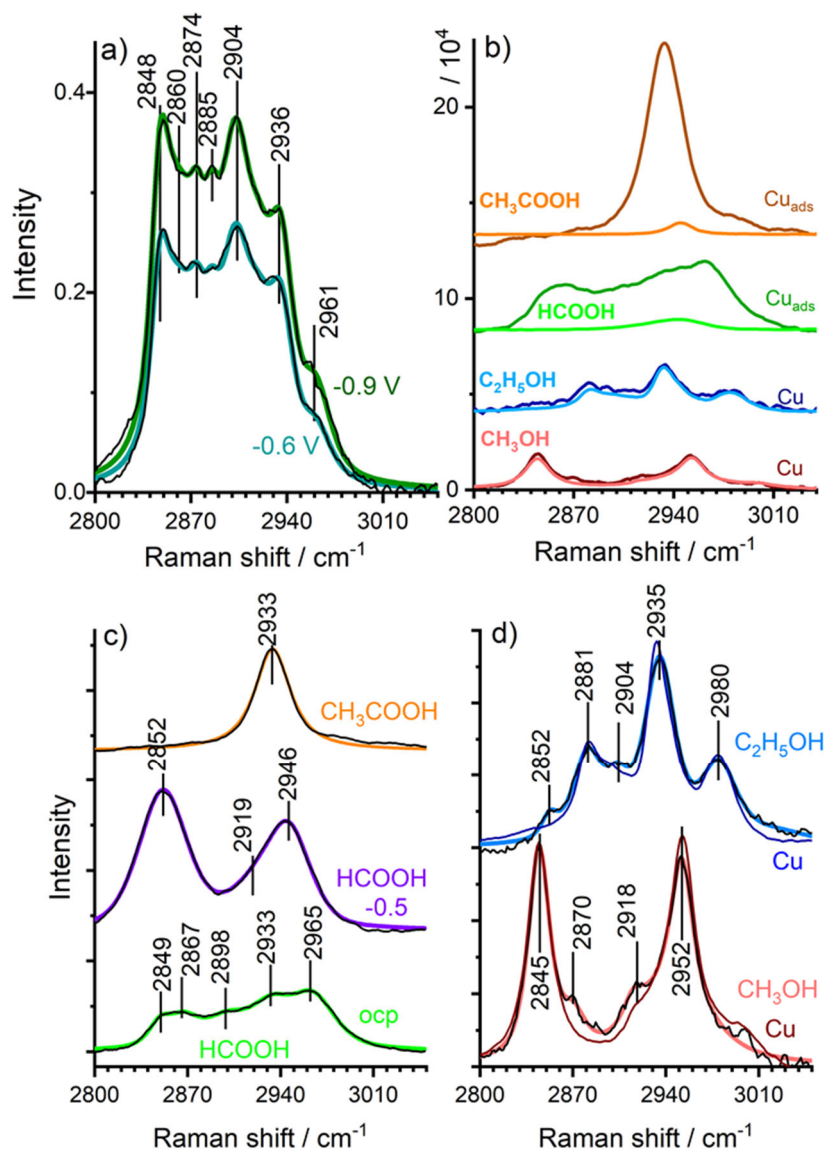


Figure 2.17. Raman spectra of the -CH region. (a) Electrochemical CO<sub>2</sub> reduction in CO<sub>2</sub> saturated 0.1 M KHCO<sub>3</sub> of a Cu foam at -0.6 and -0.9 V<sub>RHE</sub>. (b) Aqueous solutions (bright lines) of CH<sub>3</sub>OH, C<sub>2</sub>H<sub>5</sub>OH, HCOOH, and CH<sub>3</sub>COOH, and solvated in 0.1 M KH<sub>2</sub>PO<sub>4</sub>/K<sub>2</sub>HPO<sub>4</sub> in the presence of a Cu foam at OCP (dark lines). (c, d) Cu foam surface in 0.1 M KH<sub>2</sub>PO<sub>4</sub>/K<sub>2</sub>HPO<sub>4</sub> with (c) CH<sub>3</sub>COOH at OCP and HCOOH at OCP and -0.5 V<sub>RHE</sub>, (d) C<sub>2</sub>H<sub>5</sub>OH and CH<sub>3</sub>OH at OCP (thick colored lines) and in solution (thin colored lines). (a, c, d) Spectra are background subtracted and normalized (black lines- experimental data, colored lines- fitted data). Reprinted from ref (Jiang, Klingan, Pasquini, & Dau, 2019), with the permission of AIP Publishing.

## 2.3 Conclusions

### A. Investigating CO<sub>2</sub>RR by surface-enhanced Raman spectroscopy (SERS)

(1) *SERS activity*. Cu foams with high electrochemical surface area (>30 cm<sup>2</sup> per 1 cm<sup>2</sup> of planar

electrode surface) are both interesting catalysts of CO<sub>2</sub>RR and excellent SERS-active substrates, bearing the advantage of facile synthesis by a simple electrodeposition protocol. They do not require employment of any additional surface modification for electrochemical *operando* SERS, thereby ensuring that the SERS-active material is fully identical to the technologically relevant catalyst material.

(2) *Potential-dependent SERS background signal.* A strong background in the Raman spectra complicates interpretation of specific SERS bands and their intensities seriously. The background intensity depends on the electric potential as well as the 'history' of the surface, e.g., the sequence and duration of previously applied potential steps. The magnitude of the SERS backgrounds correlates with the strength of the Raman enhancement effect. Therefore, aside from background subtraction also appropriate normalization of the Raman intensities is advisable, which possibly has not been considered in previous *operando* SERS studies on CO<sub>2</sub>RR.

(3) *Proposed SERS normalization protocol.* A simple procedure for normalization of the SERS spectra is proposed. In the absence of a verified theory on the relation between SERS background and band intensities, it is assumed that the background and band intensities are proportional, which represents a pragmatic, first-order approach. Accordingly, for normalization the SERS spectra are divided by the intensity of the broad featureless SERS background. This approach results in plausible potential dependencies of Raman band assignable to surface oxides and adsorbed molecular species.

## **B. Detection of adsorbed molecular species for CO<sub>2</sub>-reducing Cu foams.**

(4) *Complete reduction of surface oxides.* The potential dependence of Raman spectra suggests that surface oxides and hydroxides are present on the as-synthesized Cu foam, but exclusively metallic Cu is present at catalytically relevant potentials. Complete reduction of Cu<sub>2</sub>O and possibly mixed oxy-hydroxide phases are observed at about -0.1 V<sub>RHE</sub>.

(5) *Two distinct CO adsorption modes.* There are two basic types of CO adsorption sites. The \*CO<sup>A</sup> type is detectable already at surprisingly positive potentials (below -0.1 V<sub>RHE</sub>) and associated with a broad band of intramolecular CO vibrations (1980-2110 cm<sup>-1</sup>). Likely, a set of several CO adsorption modes contributes, which are jointly characterized by the absence of any detectable Cu-CO vibrations. The \*CO<sup>B</sup> site may be formed by surface reconstruction at potentials below -0.4 V<sub>RHE</sub>. Its spectroscopic signature comprises one sharp intramolecular CO band (2080 cm<sup>-1</sup>) as well as two Cu-CO bands (280 cm<sup>-1</sup> and 360 cm<sup>-1</sup>).

(6) *\*CO desorption hysteresis and possible relation to CO formation rate.* Clear potential-dependent intensity trends of intramolecular \*CO and of Cu-CO bands suggest a hysteresis behavior that supports a previous electrochemical analysis of \*CO adsorption/desorption (Klingan et al., 2018). This hysteresis behavior and indications for saturating \*CO coverage of foam surface sites (see section on time dependence of Raman spectra in **Chapter 5**) lead to the hypothesis that the \*CO desorption characteristics are a co-determinant of the formation rate of externally detectable CO.

(7) *No HCO<sub>3</sub><sup>-</sup> but history-dependent CO<sub>3</sub><sup>2-</sup> adsorption.* There are potential-dependent bands assignable to adsorbed carbonate ions (CO<sub>3</sub><sup>2-</sup>) at 1070 cm<sup>-1</sup> with a pronounced shoulder at 1045 cm<sup>-1</sup> of varying binding strength. Adsorbed HCO<sub>3</sub><sup>-</sup> is not detectable suggesting adsorption-

induced deprotonation. Carbonate adsorption increases on oxide surface and decreases when potentials are more negative than pzc value of Cu.

(8) *Variety of species and adsorption modes of CH<sub>x</sub> reaction products.* Molecular species containing C-H bonds are formed by CO<sub>2</sub> reduction and are clearly detectable as adsorbants on the Cu foam surface as a broad C-H band (2800-3000 cm<sup>-1</sup>) with minimally six resolvable sub-bands. As opposed to \*CO, desorption does not readily occur at non-reducing potentials, but requires buffer exchange. Comparison with references spectra obtained for dissolved molecular species presently do not allow for unambiguous assignment of the adsorbed species, inter alia because of pronounced modifications of the Raman spectra upon adsorption to the Cu surface. Adsorbed formate and methanol intermediates may contribute, but also accumulation of potentially interesting reaction intermediates may be visible in the C-H region of the SERS spectrum. Future computational studies could contribute to identification of the CH<sub>x</sub> product species.

(9) *Complex dependence on catalyst operation history.* For all detected CO<sub>2</sub>RR products, the Raman bands assignable to adsorbed reaction products depend on the previously applied potential sequences. A fully reversible, hysteresis-free potential dependence is generally not observed. The complex history dependence of the adsorbed reaction products requires more attention. On the one hand, it represents a problematic complication, on the other hand, it provides opportunities. By designing suitable potential protocols, valuable insights in the potential dependent kinetics of product formation, adsorption and desorption may be obtainable in future investigations.

## 2.4 Materials and methods

### 2.4.1 Preparation of Cu foams

Cu foams were electrodeposited on polished and cleaned Cu metal foils (2 x 1 cm pieces, 0.1 mm thickness, 99.99+% purity, Goodfellow) by application of a current of -0.5 A/cm<sup>2</sup> for 20 s, from a 0.2 M CuSO<sub>4</sub> / 1.5 M H<sub>2</sub>SO<sub>4</sub> solution in a three-electrode set-up controlled by a SP-300 Biologic potentiostat. More details on Cu foam preparation and their characterization can be found in ref (Klingan et al., 2018).

### 2.4.2 Data collection

Raman spectra were collected with a Renishaw inVia Raman spectrometer coupled with a Leica microscope. Calibration was done using a silicon wafer standard (521 cm<sup>-1</sup>). A water immersion objective (Leica, 40×, numerical aperture of 0.8) was used to focus and collect the incident and scattered laser light. The excitation source was a 633 nm laser (He-Ne laser), which was not focused on a circular spot, but on a line of about 100 μm length (“streamline mode” of the inVia spectrometer), to reduce the laser power per irradiated area. A grating of 1200 lines/mm and a slit size of 20 μm was used. A thin optically transparent Teflon film (0.013 mm, DuPont) protected the objective from damage by acidic or alkaline electrolyte and deposition of organic species. A home-built electrochemical cell made of PTFE was interfaced with the Raman microscope for spectroscopic measurements. The cell was equipped with a saturated Ag/AgCl reference electrode and a Pt-ring counter electrode and controlled by a SP-200



Biologic potentiostat. Ohmic resistances were around 30  $\Omega$  and internally compensated at 85%. Working and counter electrode were spatially separated, but not separated by a specific membrane. Raman spectra were collected in the following ranges: 106 - 1967  $\text{cm}^{-1}$  (range-1) and 1926 - 3384  $\text{cm}^{-1}$  (range-2). 1.3 mW laser power and 30 s data acquisition time was used for each spectral range in the chronoamperometric series and for the cyclic voltammetry experiments.

During all chronoamperometric series the desired potential had been applied for 20 s and 1 min before collecting the range-1 and range-2 spectra, respectively. In other words: 20 s after the potential was applied spectra were collected in range-1 (106 - 1967  $\text{cm}^{-1}$ ) with 30 s acquisition time; 10 s later the range-2 data collection (1926 - 3384  $\text{cm}^{-1}$ ) was started, with 30 s acquisition time.

Electrochemical  $\text{CO}_2$  reduction was performed on an electrodeposited Cu foam surface in 0.1 M  $\text{KHCO}_3$  electrolyte saturated with  $\text{CO}_2$  (pH 6.8), and the electrolyte was continuously purged with  $\text{CO}_2$  throughout the experiment.

An interfering signal artefact was determined by a white paper sheet (0.6 mW laser power, 30 s data acquisition time). The air spectrum was measured with 1.3 mW laser power and 30 s data acquisition time.

Reference spectra were measured for diluted aqueous solutions of 10%  $\text{CH}_3\text{OH}$  (Sigma Aldrich,  $\geq 99.8\%$ ), 10%  $\text{C}_2\text{H}_5\text{OH}$  (Berkel,  $\geq 99.8\%$ ), and 10%  $\text{HCOOH}$  (Sigma Aldrich,  $\geq 98\%$ ), with 6 mW laser power. The spectrum of 1.0 M  $\text{HCOO}^-$  ( $\text{HCOOK}$  in water, Sigma Aldrich,  $\geq 99\%$ ) was collected using 5.6 mW laser power. The 0.1 M  $\text{CH}_3\text{COOH}$  (acetic acid solution, 1 M, Fluka) spectrum was measured with 4.2 mW laser power. All reference spectra were collected for 30 s acquisition time. Thiophenol is purchased from Sigma Aldrich.

Reference molecules were also added at OCP (open-circuit potential, no potential applied) to a Cu foam electrode immersed in 0.1 M  $\text{KH}_2\text{PO}_4/\text{K}_2\text{HPO}_4$ , with a final concentration 10 vol% (for  $\text{CH}_3\text{OH}$ ,  $\text{C}_2\text{H}_5\text{OH}$ ,  $\text{HCOOH}$ ) and about 2 vol% ( $\text{CH}_3\text{COOH}$ ). The spectra of the Cu-foam with adsorbed reference species were collected with 1 mW laser power for 30 s acquisition time. Before comparing the intensities of reference solutions with and without Cu-foam, the Raman spectra have been scaled according to the employed laser power.

### 2.4.3 Data treatment

All spectra were smoothed, and baseline corrected by Renishaw software. Fitting of the baseline is done after SERS peaks were automatically subtracted from the raw data spectra. The baseline consisted of a polynomial function with degrees between 5 and 11, and noise tolerance level around 1.4 - 1.6. The degree of the polynomial function depended strongly on the amount of SERS peaks present. Normalization was done by averaging the intensity of the background curve and this averaged intensity was used to divide the background subtracted and smoothed spectra.

Raman peaks of -CH species were fitted with in-house software "Global Gauss Fit" using 40% Lorentzian and 60% Gaussian character, and iteratively minimizing chi-square values.

# 3. The role of bicarbonate/Cu-oxide interaction in Cu catalyzed CO<sub>2</sub> electro-reduction

## 3.1 Introduction

Oxide derived copper (OD-Cu) showed better selectivity for C<sub>2</sub> products (Lee et al., 2018; C. W. Li et al., 2014; H. Mistry et al., 2016). The mechanism behind the increased efficiency is still a question under debate (Pander et al., 2018; J. Wang, Tan, Zhu, Chu, & Chen, 2021). It is believed that moderate CO surface adsorption facilitates C-C coupling in C<sub>2+</sub> production (Calle-Vallejo & Koper, 2013; Montoya et al., 2015). Verdaguer-Casadevall *et al.* proposed that strong binding sites for CO lie in the grain boundaries of OD-Cu, leading to further reduction of CO to C<sub>2</sub> products (Verdaguer-Casadevall et al., 2015). Other reports claim ‘subsurface oxygen’ can survive even under high catalytic (negative) potentials which could help stabilizing reaction intermediates (Cavalca et al., 2017; C. Liu et al., 2017). It is not clear if this is due to a morphological effect or to a specific -oxo groups involved in the catalytic mechanism. Nevertheless, in recent reports Cu<sup>+</sup> is widely considered as the active phase (Arán-Ais et al., 2020), and the synergistic effect of Cu<sup>+</sup> and Cu<sup>0</sup> may promote both CO<sub>2</sub> activation and the \*CO dimerization (J. Wang et al., 2021).

*Operando* techniques can be used for mechanistic investigations since they give the opportunity to study the catalyst during operation (Heidary et al., 2019; Shangqian Zhu et al., 2019). In case of OD-Cu driven CO<sub>2</sub>RR, the need of *operando* measurements is increased due to the instability of the Cu surface under non-operating conditions. *Operando* Raman spectroscopy is particularly suitable to study reactions on copper since roughened Cu enables the surface enhancement effect (Sharma, Frontiera, Henry, Ringe, & Van Duyne, 2012). Indeed, this amplifies the signal of the molecules adsorbed on the surface of Cu such that even a single molecular layer can be detected (Langer et al., 2020; Schlucker, 2014). With the help of *operando* Raman spectroscopy researchers could trace reaction intermediates and catalyst oxidation states to gain insight on CO<sub>2</sub>RR mechanism (Gunathunge et al., 2017; Iijima, Inomata, Yamaguchi, Ito, & Masuda, 2019; A. Wuttig et al., 2016; Zhao et al., 2020).

Chernyshova *et al.*, using *operando* Raman spectroscopy, proposed that the first step of CO<sub>2</sub> reduction is a single electron transfer to molecular CO<sub>2</sub> forming \*CO<sub>2</sub><sup>-</sup> which adsorbs onto the Cu surface with the C or O atoms (Chernyshova et al., 2018). In a following work, the interaction of the co-adsorbed sodium cation to the proposed \*CO<sub>2</sub><sup>-</sup> intermediate on Cu(111) surface in the presence of an electric field was also investigated by DFT modelling, based on which a specific activation pathway of \*CO<sub>2</sub><sup>-</sup> towards CO or formate has been postulated (Chernyshova & Ponnurangam, 2019). Although, the formation of \*CO<sub>2</sub><sup>-</sup> through molecular CO<sub>2</sub> has been considered energetically disfavoured, the stabilization of \*CO<sub>2</sub><sup>-</sup> may promote this reaction kinetically (Hori, 2008).

On the other hand, it is still unclear whether CO<sub>2</sub> gas or bicarbonate is the first reactant in

CO<sub>2</sub>RR. Dunwell *et al.* investigated the role of bicarbonate in CO<sub>2</sub> reduction on gold by isotope labelling of reactants (M. Dunwell et al., 2017). It was found that the isotope content of the produced CO is largely unaffected (for the initial 20 mins) when only CO<sub>2</sub> gas is marked, which suggests that CO<sub>2</sub> gas is not the C source of the reaction. However, without purging CO<sub>2</sub> gas in the electrolyte medium, the sole bicarbonate could not produce any CO. Therefore, it was concluded that CO<sub>2</sub>(aq) in equilibrium with bicarbonate is the C source in CO<sub>2</sub>RR. A similar result was reported for CO<sub>2</sub>RR on Cu (S. Zhu et al., 2017).

Kortlever *et al.* proposed the direct reduction of bicarbonate on the Cu surface; after using 1 M KHCO<sub>3</sub> without CO<sub>2</sub> gas purging they detected formate as a product of CO<sub>2</sub>RR (Kortlever et al., 2013). This evidence changed the assignment of the first voltametric peak (at around -0.7 V<sub>RHE</sub>) to bicarbonate reduction that had previously been assigned to \*CO adsorption (Hori et al., 1985; Hori et al., 1988). In the same study, different facets showed different activities, in particular highly undercoordinated facet Cu(110) show the highest reduction currents (Kortlever et al., 2013).

Recently, malachite (copper carbonate hydroxide, Cu<sub>2</sub>(OH)<sub>2</sub>CO<sub>3</sub> nanorods have been proposed as the actual active species in Cu driven CO<sub>2</sub>RR (Spodaryk, Zhao, Zhang, Oveisi, & Züttel, 2019). The malachite nanorods, spontaneously formed on copper foil, showed a greater activity than bare copper towards C<sub>2</sub> compounds, suggesting that the copper carbonate hydroxide material could be the actual catalyst of the reaction (Eilert, Roberts, Friebe, & Nilsson, 2016). Whereas in another work, Cu carbonate is observed on Cu<sup>2+</sup> surface, and assumed to block the CO<sub>2</sub> reduction reaction sites due to the poor charge transport (Velasco-Vélez et al., 2018). To date there is no consensus on whether bicarbonate directly participates in the reaction or simply works as a buffer in equilibrium to CO<sub>2</sub>.

In this chapter, *operando* Raman spectroscopy is used to study the electrode/electrolyte interface prior and during CO<sub>2</sub>RR catalysis with the aim to characterize the catalytically active material. It is shown that HCO<sub>3</sub><sup>-</sup> is in equilibrium with the copper oxide layer in the Cu/electrolyte interface. Moreover, the oxide layer can produce an amorphous copper carbonate hydroxide layer similar to the mineral malachite, which might be the origin of the discussed spectral peaks that are observed in **Chapter 2** and possibly the precursor to CO. This puts bicarbonate into a central role for the CO<sub>2</sub>RR and might help explain the higher activity of OD-Cu for CO<sub>2</sub>RR.

## 3.2 Results

### 3.2.1 The origin of peaks at 350, 705, 1530 cm<sup>-1</sup>

Copper electrodes were prepared as described in **Chapter 2** and left under atmospheric condition overnight, a layer of copper oxide is naturally formed on the surface. SERS measurements were performed on a Cu foam electrode after (20 s) and during (2 min) the application of an electric potential. The *operando* SERS spectra specifically from 0 to -0.3 V<sub>RHE</sub> of Cu foam electrode for CO<sub>2</sub> reduction are shown in **Figure 3.1**, 0.1 M KHCO<sub>3</sub> saturated with CO<sub>2</sub> was used as electrolyte. Prior application of any potential, under OCP the only peaks

present are at 405, 520, 620  $\text{cm}^{-1}$ , assigned in **Chapter 2** to a mixture of  $\text{Cu}_2\text{O}$ ,  $\text{CuO}$  and  $\text{Cu}(\text{OH})_2$ , which are naturally formed on the surface of metallic Cu after being exposed to air. After sequential application of increasing negative potentials from 0 to  $-0.3 \text{ V}_{\text{RHE}}$ , peaks at 354-305  $\text{cm}^{-1}$  (A), 705  $\text{cm}^{-1}$  (B), 1070  $\text{cm}^{-1}$  (C) and 1533-1512  $\text{cm}^{-1}$  (D) appeared, a shoulder peak at 1045  $\text{cm}^{-1}$  (C1) and two less prominent peaks at 1340 and 1677  $\text{cm}^{-1}$  (D1 and D2 respectively) are visible. As has been discussed in **Chapter 2**, the peak at 1070  $\text{cm}^{-1}$  is assigned to carbonate symmetrical stretching (Davis & Oliver, 1972). The assignment of other peaks remains unclear, yet their simultaneous appearance suggests that they could belong to the same species. Moreover, these peaks are observed at the oxide reducing potentials and the decrease of peak (B) and (D) seems to occur concurrently to the oxide peak weakening, suggesting a relation between the two phenomena. Interestingly, a Raman peak at 2040-2080  $\text{cm}^{-1}$  usually assigned to adsorbed CO arises (Gunathunge et al., 2017; A. Wuttig et al., 2016), which is not expected at this low overpotential ( $E^\circ_{\text{CO}_2/\text{CO}} = -0.11 \text{ V}_{\text{RHE}}$  (Kendra P. Kuhl et al., 2012)). The peak (A) may comprise two overlapping peak which evolve differently with applied potential: the 354  $\text{cm}^{-1}$  peak dominates at  $-0.1 \text{ V}_{\text{RHE}}$ , with a shoulder at 305  $\text{cm}^{-1}$ , which grows at larger potentials and becomes the dominant peak at  $-0.4 \text{ V}_{\text{RHE}}$ .

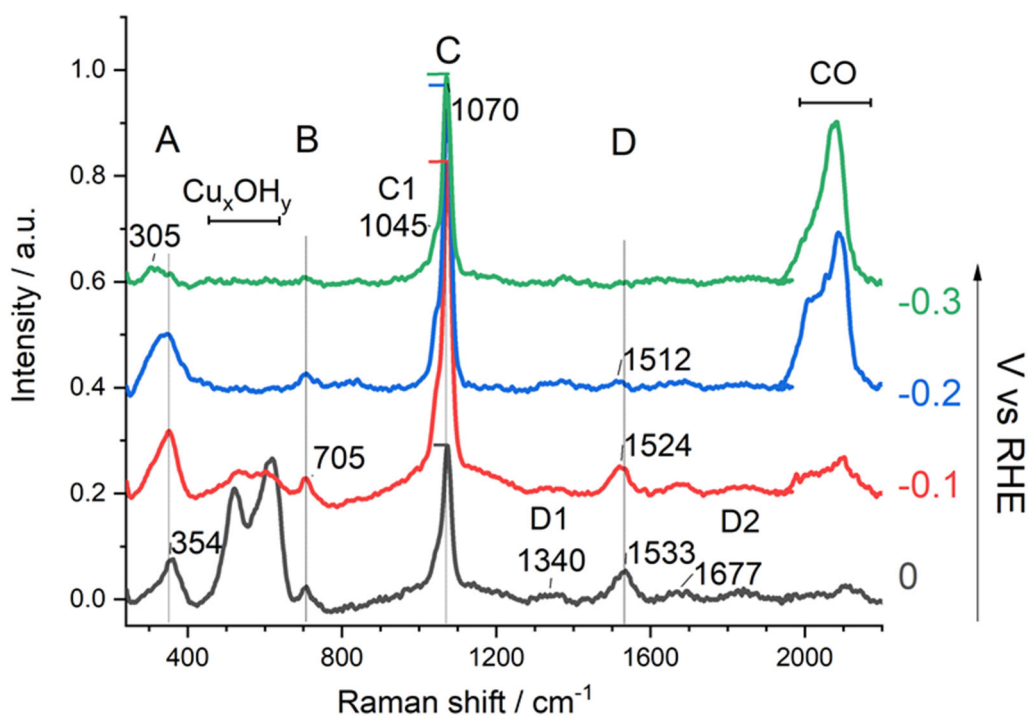


Figure 3.1: *Operando* SERS spectra of Cu foam in  $\text{CO}_2$  saturated 0.1 M  $\text{KHCO}_3$  (pH 6.8) at various potentials (from 0 to  $-0.3 \text{ V}_{\text{RHE}}$ ). Due to peak position shift with increasing negative potentials, the peaks of interest are labelled with (A) for peak at 354-305  $\text{cm}^{-1}$ , (B) for peak at 705  $\text{cm}^{-1}$ , (C) for peak at 1070  $\text{cm}^{-1}$  and (D) for peak at 1512-1533  $\text{cm}^{-1}$ .

As shown in **Figure 3.2**, cyclic-voltammogram of such Cu foam electrode, in a  $\text{CO}_2$  saturated bicarbonate buffer solution, shows unstructured, reversible and irreversible reduction and oxidation peaks. Clearly, this behavior resembles the complex nature of the  $\text{CO}_2\text{RR}$ , oxide reduction and other reactions occurring at this oxide derived Cu surface. The potentials where *operando* Raman spectra were taken are labelled with arrows. It can be seen that the (A)-(D)

peaks observed are exactly located at the reduction peaks in CV. Different concentration of  $\text{CO}_2$  saturated  $\text{KHCO}_3$  electrolyte were adopted to compare the CV curve. It seems that the reduction current also increased in higher concentration of bicarbonate, which suggests that the reduction peaks can be influenced by the concentration of bicarbonate.

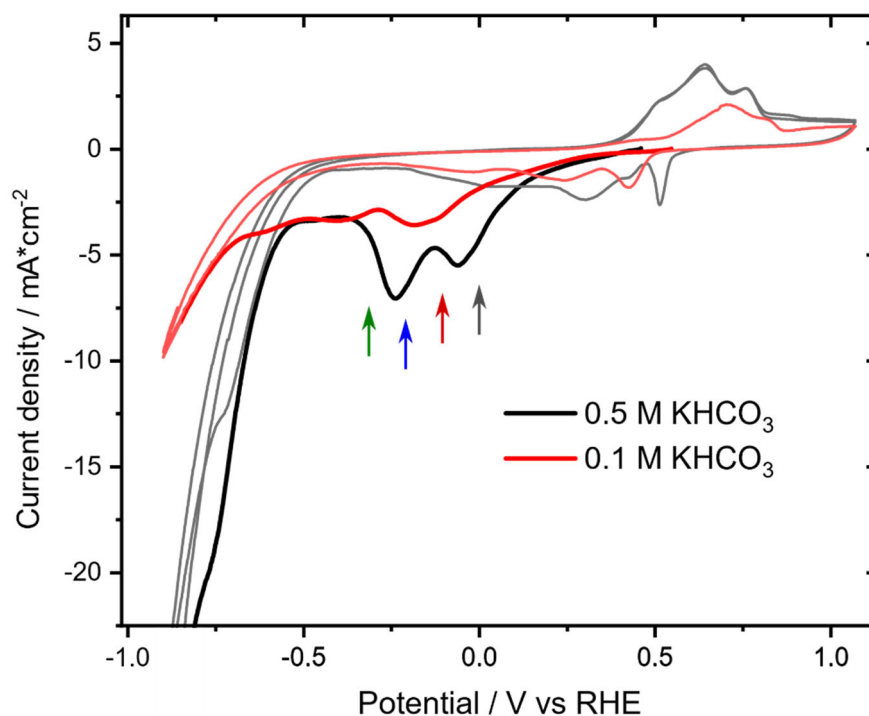


Figure 3.2: Cyclic voltammetry of Cu foam measured in  $\text{CO}_2$  saturated 0.1 M (red) and 0.5 M (black)  $\text{KHCO}_3$ , 10 mV/s. Thicker lines highlight the first sweep from OCP to first vertex. Arrows indicate the potential where *operando* SERS shown in Figure 3.1 was performed, from right to left: 0, -0.1, -0.2, -0.3  $\text{V}_{\text{RHE}}$ .

In the following the relation of the peak (A), (B), (C) and (D) to the  $\text{CO}_2\text{RR}$  is analyzed. As previously mentioned, *operando* Raman or IR spectroscopy have been used by several researchers investigating  $\text{CO}_2$  reduction on Cu catalysts (Chernyshova et al., 2018; M. Dunwell et al., 2017; A. Wuttig et al., 2016; Shangqian Zhu et al., 2019). The peaks at  $705\text{ cm}^{-1}$  and  $1530\text{ cm}^{-1}$  have been assigned to in-plane bending and asymmetric stretching of  $^*\text{CO}_2^-$  intermediate (bound to Cu surface with C,O) produced by a singly reduced  $\text{CO}_2$  molecule (Chernyshova et al., 2018). To further investigate the relation of  $\text{CO}_2$  to this particular assignment, the same *operando* experiment described above was performed without  $\text{CO}_2$  saturation; to this aim  $\text{N}_2$  was purged in the 0.1 M  $\text{KHCO}_3$  electrolyte. The resulting spectra are shown in **Figure 3.3** (dashed lines). It is clear that all four (A-D) peaks become much weaker, which could suggest a relation of these bands to  $\text{CO}_2$ . Though, it should be noted that the removal of  $\text{CO}_2$  alters the bicarbonate buffer equilibrium such that the pH of the solution changes from 6.8 with  $\text{CO}_2$  saturation to 9.16 with  $\text{N}_2$  saturation. The pH change might alter the affinity of the Cu surface with the intermediates or any adsorbed chemical species which might affect the peak magnitude. Later on, this hypothesis will be further discussed.

As mentioned above, it seems that increasing bicarbonate facilitate the reduction peaks in CV.

This may also be the case when  $N_2$  is saturated but not  $CO_2$ . To this end a series of spectra was registered using a higher concentration of bicarbonate to increase the probability of interaction of bicarbonate with the Cu electrode surface. The results, reported in **Figure 3.3** (solid line spectra), show that in  $N_2$  saturated 1 M  $KHCO_3$  (pH of 8.7), the peaks (A)-(D) are visible and present with a pronounced intensity. It can be concluded that bicarbonate itself, in absence of  $CO_2$ , can produce or show, via electro-reduction, the species responsible for peak (A)-(D). The presence of such a species is also observed with 0.5 M  $KHCO_3$  solution ( $N_2$  saturated, pH 8.7), the data are shown in Appendix 8.9. Furthermore, the presence of the CO stretch band indicates that  $CO_2$  gas purging is not required for  $CO_2$  reduction.

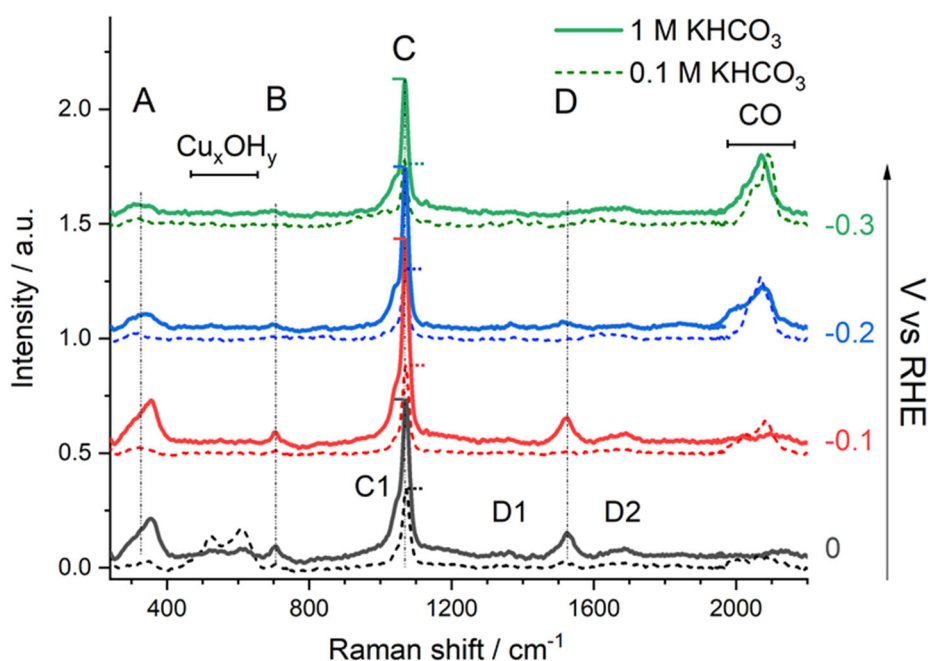


Figure 3.3: Comparison between *Operando* SERS spectra of Cu foam measured in  $N_2$  saturated 0.1 M  $KHCO_3$  (pH 9.16) (solid line) and 1 M  $KHCO_3$  (pH 8.7) (short dash line) at various potentials (from 0 V to  $-0.3 V_{RHE}$ ). (Complete data is also shown in Appendix 8.9).

Selective  $^{13}C$  isotope labelling was performed on the bicarbonate/ $CO_2$  mixture of the electrolyte. This experiment was conducted in the shortest time possible (10 min  $CO_2$  gas saturation prior measurement, plus 8 min measurement time) to avoid isotope mixing due to the equilibrium of the bicarbonate/ $CO_2$  system (see Appendix 8.10 for more details). The labelling of  $KHCO_3$  only (not  $CO_2$  gas) produces a frequency shift of peak (D) from 1533-1505  $cm^{-1}$  to 1497-1474  $cm^{-1}$  as displayed in **Figure 3.4**, the details of peak comparison are shown in **Figure 3.5**. It can be noted that the weaker peaks (D1) and (D2) shift to a similar extent as the main peak (D). Labelling instead solely  $CO_2$  does not cause any shift (see **Figure 3.6**) of peak (D), which again supports that the primary source of such band is bicarbonate ions. The isotopic shift is consistent with C-O vibration from  $^*CO_2^-$  (Chernyshova et al., 2018) or a carbonate anion (M. Dunwell et al., 2017; S. Zhu et al., 2017). Further below, assignment of these bands to a copper carbonate hydroxide species will be proposed. The band at 705  $cm^{-1}$  shows no clear shift as displayed in **Figure 3.5**. The CO band is significantly modified by  $^{12}C/^{13}C$  exchange, but a quantifiable band

shift cannot be resolved because the complexity of the CO band which comprises several sub-bands of varying amplitudes.

There is no clear shift of peak (A) in  $^{13}\text{C}$  labelled electrolyte, see **Figure 3.5a** (another dataset is shown in Appendix 8.10). Due to the absence of isotopic frequency shift when labelling the electrolyte with  $^{13}\text{C}$ , peak (A) is assigned to a Cu-O stretch. Moreover, as described in the following, a similar peak was observed in *operando* SERS recorded with carbon-free neutral pH phosphate buffer, which further supports the assignment to Cu-O vibrations.

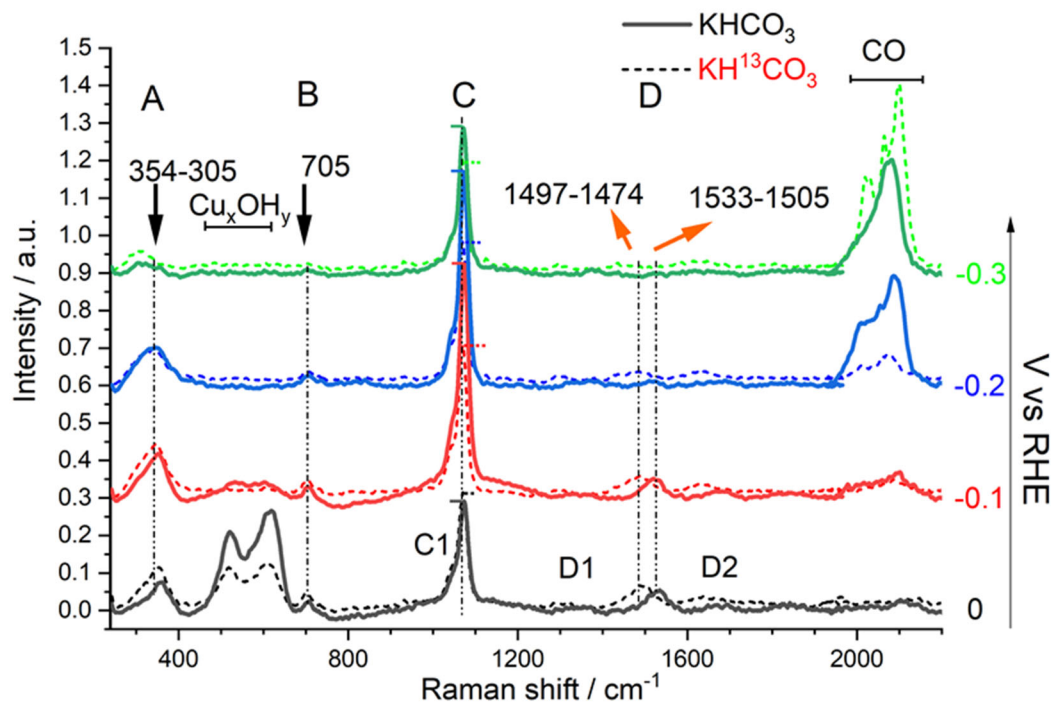


Figure 3.4: Comparison between *operando* SERS spectra of Cu foam measured in  $\text{CO}_2$  saturated 0.1 M  $\text{KHCO}_3$  (solid line) and  $\text{CO}_2$  saturated 0.1 M  $\text{KH}^{13}\text{CO}_3$  (pH 6.8) (short dash line) at various potentials (from 0 V to  $-0.3 V_{\text{RHE}}$ ). Peak comparison is also shown in detail in Figure 3.5.

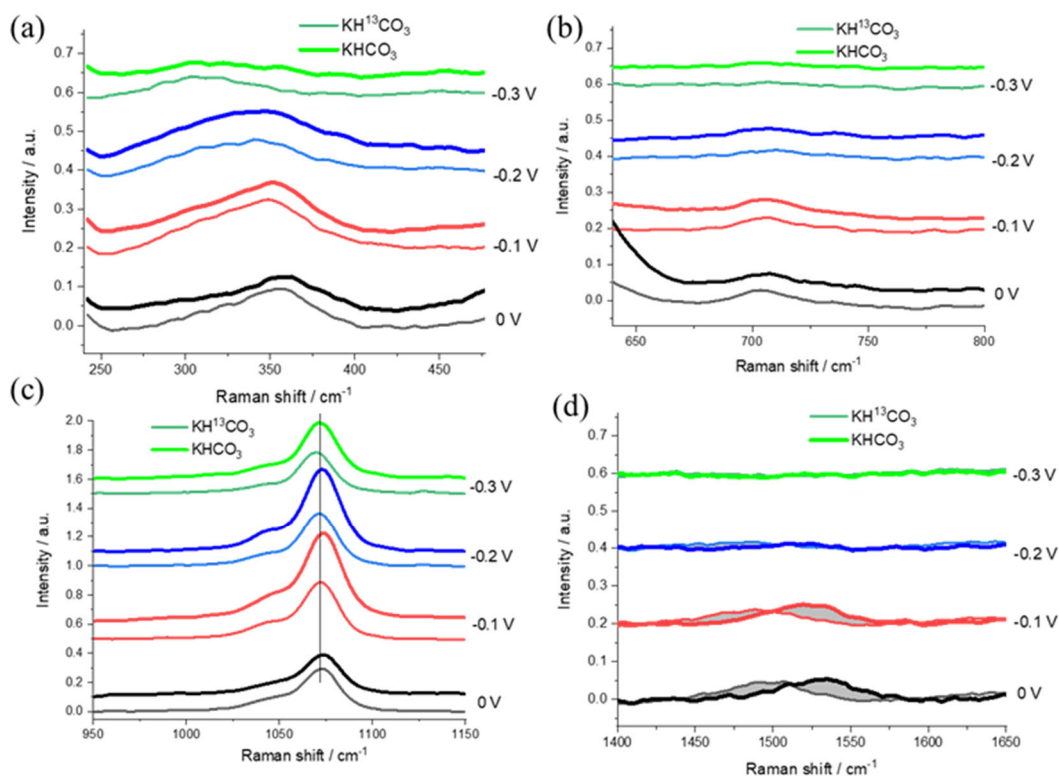


Figure 3.5: Peak comparison between spectra measured in normal solution and KH<sup>13</sup>CO<sub>3</sub> taken from Figure 3.4. (a) Peak at 350 - 309 cm<sup>-1</sup>; (b) peak at 705 cm<sup>-1</sup>; (c) peak at 1070 cm<sup>-1</sup> and (d) peak at 1530-1510 cm<sup>-1</sup>.

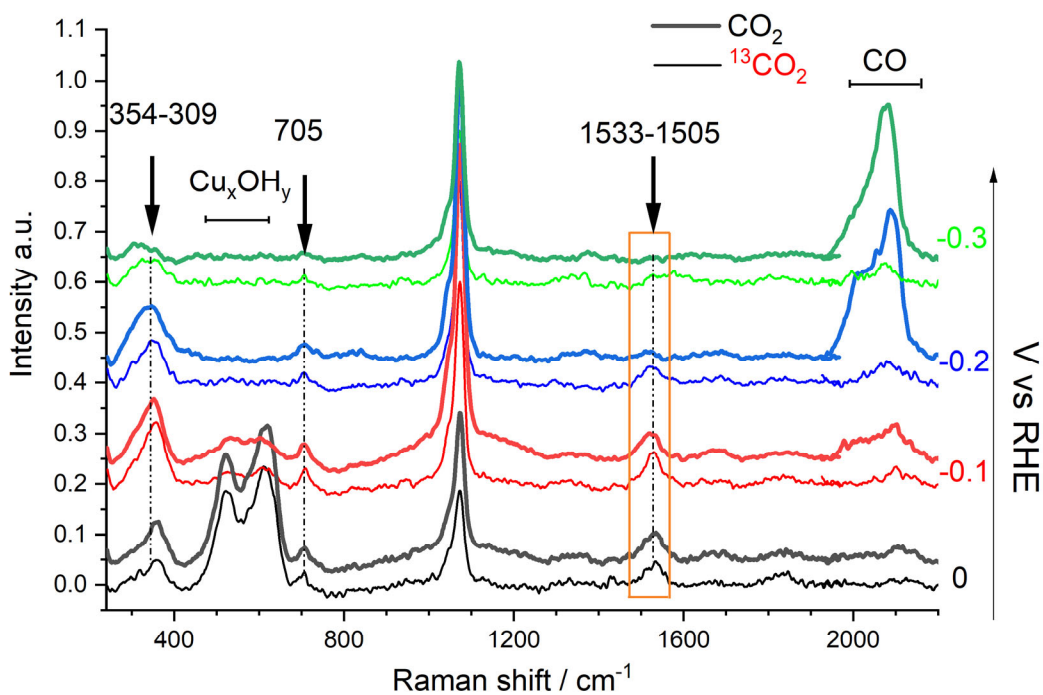


Figure 3.6: Operando Raman spectra of <sup>13</sup>CO<sub>2</sub> saturated KHCO<sub>3</sub> in comparison to normal CO<sub>2</sub> gas saturated KHCO<sub>3</sub>.



To be able to highlight the Cu-O vibration respect to the Cu-C vibrations, the same *operando* Raman experiment described earlier, with N<sub>2</sub> saturated electrolyte, was repeated using phosphate buffer (Kpi, neutral pH) instead of bicarbonate, see **Figure 3.7**. The peak at 310 cm<sup>-1</sup> appeared together with known phosphate adsorption bands (800-1100 cm<sup>-1</sup>). Gediminas *et al.* have investigated phosphate adsorption on Cu, Ag and Au with *in-situ* Raman (Gediminas Niaura, 1997). They observed a peak at around 320 cm<sup>-1</sup> on Cu surface as well as a phosphate band, similar to the spectra in **Figure 3.7**, and suggested that phosphate adsorbs through a bridging oxygen on Cu, Ag and Au surface. To be noted, it is common also for other oxyanion to adsorb on Cu and noble metal surfaces through the oxygen atom (C.A. Melendres a, 2000; Schlaup, 2013). The M-O vibration, in these cases, typically appears in the 250-400 cm<sup>-1</sup> region.

The *operando* SERS recorded in phosphate buffer shows a correlation between potential and phosphate bands. The more negative the potential the stronger is the signal from deprotonated phosphate species (see 987 cm<sup>-1</sup> HPO<sub>4</sub><sup>2-</sup> vs. 1103 cm<sup>-1</sup> H<sub>2</sub>PO<sub>4</sub><sup>-</sup>), suggesting pronounced alkalization at the electrode-electrolyte interface.

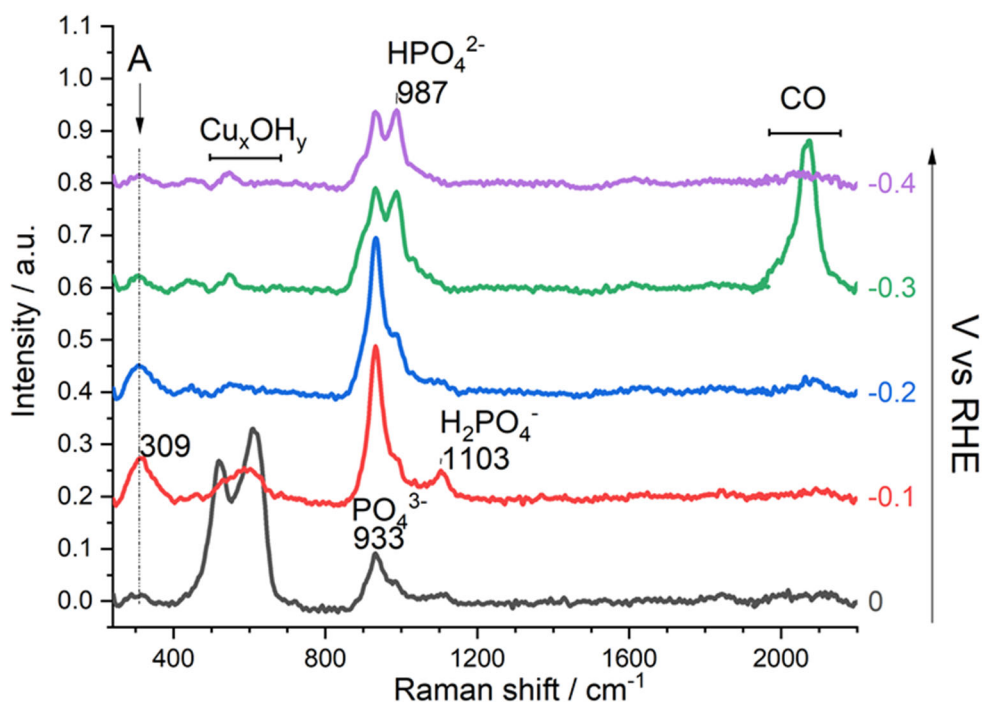


Figure 3.7: *Operando* SERS spectra of Cu foam measured in N<sub>2</sub> saturated 0.1 M potassium phosphate buffer (pH 6.8) at various potentials (from 0 to -0.3 V<sub>RHE</sub>). Complete data see Appendix 8.11.

The results shown so far strongly support the hypothesis that the CO<sub>2</sub>RR intermediate visible in the *operando* SERS are related to carbonate species rather than being created by reduction of dissolved CO<sub>2</sub>. For clarity purposes, the discussion that follows starts with a comparison of the presented results with some literature reports, trying to address inconsistencies, in particular regarding the association of spectroscopic bands to adsorbed CO<sub>2</sub> or carbonate or products of their reduction. Afterwards, the discussion continues with an analysis of what are

thermodynamically and kinetically possible events in the experiments, proposing a new way to interpret the *operando* SERS data, which further below will be supported by additional experiments. This new interpretation can support an adequate discussion of Raman CO<sub>2</sub>RR data, potentially changing the course of a general interpretation in terms of reaction mechanisms in the future.

### 3.2.2 Peak (D) cannot be attributed to adsorbed (bi)carbonate

In the following it is shown that peak (D), at around 1530 cm<sup>-1</sup>, does not originate from vibration of adsorbed (bi)carbonate anions. **Table 3.1** listed and compared the peak positions from results here with other literature reported carbonate bands in these regions, except peak 1045 cm<sup>-1</sup> which is reported as -OH band in azurite and malachite (Frost et al., 2002).

It is clear that dissolved solution species of (bi)carbonate have no bands at around 1530 cm<sup>-1</sup>, however when carbonate adsorb on Au surface, it is reported to have bands at around 1429-1499 cm<sup>-1</sup> which might be a possible explanation for peak (D) (Kazuki Arihara, 2001). Indeed, it is not the first time peak (D) was observed in *operando* vibrational spectra of CO<sub>2</sub>RR in bicarbonate buffer (Baruch et al., 2015; Chernyshova et al., 2018; Detweiler et al., 2014; M. Dunwell et al., 2017; Iijima et al., 2019; Moradzaman & Mul, 2021; L. Wang, Gupta, Goodall, Darr, & Holt, 2017; A. Wuttig et al., 2016). In most cases, it has been assigned to carbonate anion adsorption (M. Dunwell et al., 2017; Iijima et al., 2019; Moradzaman & Mul, 2021; L. Wang et al., 2017; A. Wuttig et al., 2016). Exceptions are some reports that considered the potential correlation of it to CO<sub>2</sub>RR intermediates (Baruch et al., 2015; Chernyshova et al., 2018; Detweiler et al., 2014). On both a tin and an indium oxide surface, Detweiler and Baruch et al. observed a peak at around 1500 cm<sup>-1</sup> by *operando* ATRIR (Baruch et al., 2015; Detweiler et al., 2014). They assigned the one on Sn surface to a surface-bound carbonate (linked via an oxygen from Sn oxide) which is an important intermediate in formate formation (Baruch et al., 2015). One argument against an assignment to an adsorbed carbonate was based on some experiments where peak at 1530 cm<sup>-1</sup> (D) was absent in clear presence of adsorbed carbonate anion band at 1068 cm<sup>-1</sup> (C) (Chernyshova et al., 2018). The same behavior was observed here in the experiment performed in N<sub>2</sub> saturated 0.05 M K<sub>2</sub>CO<sub>3</sub>, where peak (D) was not observed while the band at 1070 cm<sup>-1</sup> band was clearly present (Appendix 8.12). In all the experiment described in this thesis, the correlation between the presence of peak (C) and (D) is never biunivocal, i.e. the band of adsorbed bicarbonate is always present when also peak (D) is, but the contrary is never observed, signifying a special behavior of peak (D). It is believed that peak (C) does not simply originate from carbonate adsorption to a metallic copper surface. There could be two carbonate species contributing to the comparably broad asymmetric vibrational band of peak (C), with one species giving rise also to peak (D). It should be noted that the correlation between the oxide and the appearance of peak (D) is crucial to understand the origin of such band. As treated in the results section, peak (D) always appears after, or in the meanwhile, the disappearance of the oxide bands. In **Table 3.1** two copper carbonate hydroxide are also included.

**Table 3.1.** Summary of Raman shifts (Wavenumber in IR if labelled) for various carbonate species from literature and present study.

Species	Wavenumber / Raman shift (cm <sup>-1</sup> )			
Present study	705	1045	1068	1500-1530
CO <sub>3</sub> <sup>2-</sup> (aq) (Davis & Oliver, 1972)	684		1064	1430, 1380
HCO <sub>3</sub> <sup>-</sup> (aq) (Davis & Oliver, 1972)	632, 672	1017		1360, 1630
Azurite (Frost, Martens, Rintoul, Mahmutagic, & Kloprogge, 2002)	765, 739	1035	1090	1578
Malachite (Frost et al., 2002)	765, 719	1045	1101, 1058	1492
Carbonate on Au (SNIFTIR) (Kazuki Arihara, 2001)				1425-1499
Sn-carbonate (IR) (Baruch, Pander, White, & Bocarsly, 2015)				1500

### 3.2.3 Thermodynamics of the system and formation of metastable material

Mostly *operando* Raman spectroscopy results on CO<sub>2</sub>RR are evaluated on the basis that the rough Cu surface can enhance the signal of adsorbed molecule. However, the measured Raman signals do not necessarily imply that the detected peaks are indeed stemming from individual molecular species adsorbed directly on the metallic copper surface. The surface Raman enhancement effect can extend over several nanometers (Dieringer et al., 2006; J. F. Li, Zhang, Ding, Panneerselvam, & Tian, 2017; Singh et al., 2012; Wei et al., 2009). Several layers of material on the copper surface could be either detectable due to the enhancement effect of the Cu surface or because of their intrinsic Raman properties. Indeed, an estimation of the charge exchanged in the reduction of a monolayer of adsorbed carbonate, results in a 1/30 of the redox charge that is normally observed in the CV. This indicate that a larger quantity of material than a monolayer has to be adsorbed on the Cu surface to produce this current density, see Appendix 8.13 for more details. It can be speculated that metastable materials can be produced at the Cu surface under CO<sub>2</sub>RR operation conditions.

An idea of the possible chemical species that can be formed around the Cu electrode during CO<sub>2</sub>RR can be given by an analysis of the thermodynamics of the system. Pourbaix diagrams show the thermodynamically stable species of a certain system as a function of the applied electric potential or solution redox potential, and pH. Since the system is constituted of a copper electrode, usually covered by a layer of oxide/hydroxide, immersed in a bicarbonate solution, the Pourbaix diagram of Cu/Cu<sub>2</sub>O/azurite/malachite has been chosen, see **Figure 3.8A**.

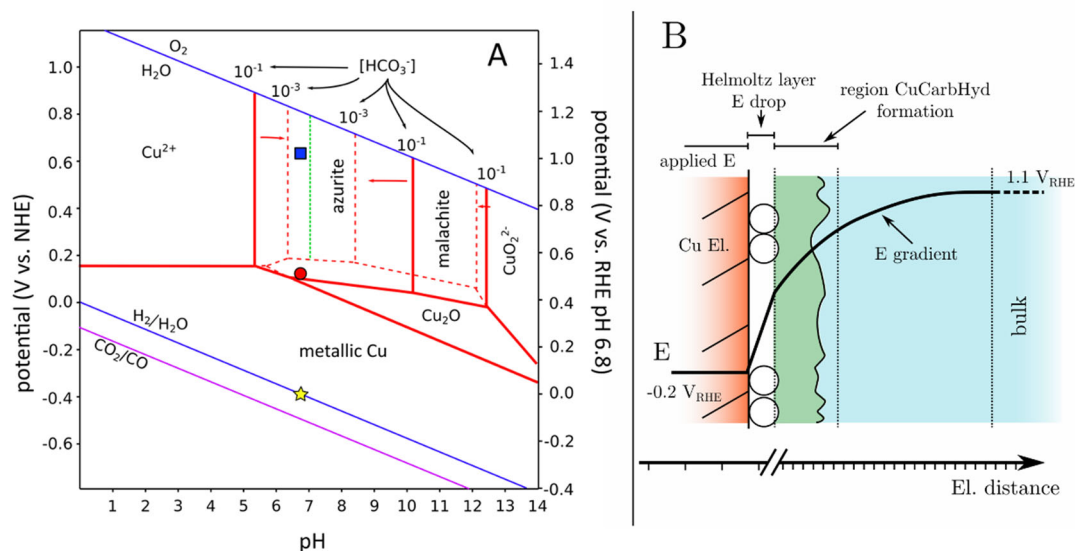


Figure 3.8: (A) Pourbaix diagram of the Cu-HCO<sub>3</sub><sup>-</sup> solution system. The solid red lines represent a HCO<sub>3</sub><sup>-</sup> concentration of 10<sup>-1</sup> M, the dashed line concentration of 10<sup>-3</sup> M, the concentration of dissolved Cu<sup>2+</sup> concentration is assumed to be 10<sup>-6</sup> M, to account for equilibration of the Cu/Cu(OH)<sub>2</sub> with the electrolyte. The violet line represents the equilibrium potential of CO<sub>2</sub>/CO reaction. The green dashed line represents the minimum HCO<sub>3</sub><sup>-</sup> concentration (HCO<sub>3</sub><sup>-</sup> 10<sup>-4.3</sup>) needed to produce an azurite phase at any pH/potential. The blue square corresponds to the potential of a solution of CO<sub>2</sub> saturated solution of 0.1 M KHCO<sub>3</sub> (determined experimentally vs. a reference electrode by a Pt wire immersed in such solution (Allen & Larry., 2001)). The red circle indicates the OCP that is typically observed for the as-prepared Cu foam. The yellow star indicates the zero level of the electric potential when using an RHE scale (0 V<sub>RHE</sub> at pH 6.8). The blue solid lines represent the equilibrium potentials for reduction/oxidation of water. Diagram based on ref (Vink, 1986). (B) Graphical representation of the electrical potential vs. distance from the electrode surface under cell operation; Cu electrode in red, CuCarHyd in green, adsorbed species in the Helmholtz layer are shown as circles. A hypothetical potential profile is schematically shown for application of -0.2 V<sub>RHE</sub>.

In **Figure 3.8A**, the blue square marks the electrochemical potential of the CO<sub>2</sub> saturated 0.1 M bicarbonate solution (ca. 1.1 V<sub>RHE</sub>, experimentally determined, see Appendix 8.14 for detail), while the red circle indicates the Cu foam electrode system position at OCP (ca. 0.5 V<sub>RHE</sub>). The yellow star depicts the electrode potential at 0 V<sub>RHE</sub> (at pH 6.8).

As shown in **Chapter 2 section 2.2.1**, the Cu electrode is coated by a layer of Cu<sub>x</sub>OH<sub>y</sub> that is formed readily in air. Thus, upon exposure to the bicarbonate buffer but prior to applying any

potential, the system can be considered as a phase of Cu (hydr) oxide interfaced with the bicarbonate electrolyte. This system is out of equilibrium (see **Figure 3.8A**, the difference between the red circle at OCP and the blue square), with a spontaneous tendency to convert the  $\text{Cu}_x\text{OH}_y$  into azurite/malachite. This is also true under potentials since this out-of-equilibrium condition applies also during operation (region between yellow star and blue square, **Figure 3.8A**). During the application of a potential at the electrode, a gradient of the electrical potential forms due to the potential difference between negative electrode and the more positive electrolyte bulk (ca.  $+1.1 \text{ V}_{\text{RHE}}$ ). A potential gradient as schematically shown in **Figure 3.8B** is proposed. A large part of the potential gradient is observed in the first layer of adsorbed material (Helmholtz layer). Even at potentials large enough to enable  $\text{CO}_2\text{RR}$  operation, i.e.  $-0.2 \text{ V}_{\text{RHE}}$  (1.3 V difference from the bulk), the electrical potential that results after the first drop can be positive enough to allow, in conjunction with local alkalization, the formation/presence of oxidized species like Cu carbonate hydroxide or  $\text{Cu}_x\text{OH}_y$ .

Clearly the system, if left at OCP, can and will evolve naturally into a copper carbonate hydroxide phase. A Cu electrode (covered with natural (hydr)oxide layer) left in 0.1 M  $\text{KHCO}_3$  for 6 days forms an observable green layer of substance inside the cavity of the Cu foam electrode. The Raman spectrum of such a sample is compared to reference spectra of azurite and malachite in **Figure 3.9A**. For comparison with the already discussed data, the 0  $\text{V}_{\text{RHE}}$  spectrum taken from **Figure 3.1** and a  $^{13}\text{C}$  labelled sample (prepared in 0.1 M  $\text{KH}^{13}\text{CO}_3$  for 6 days), are reported in **Figure 3.9A** as well.

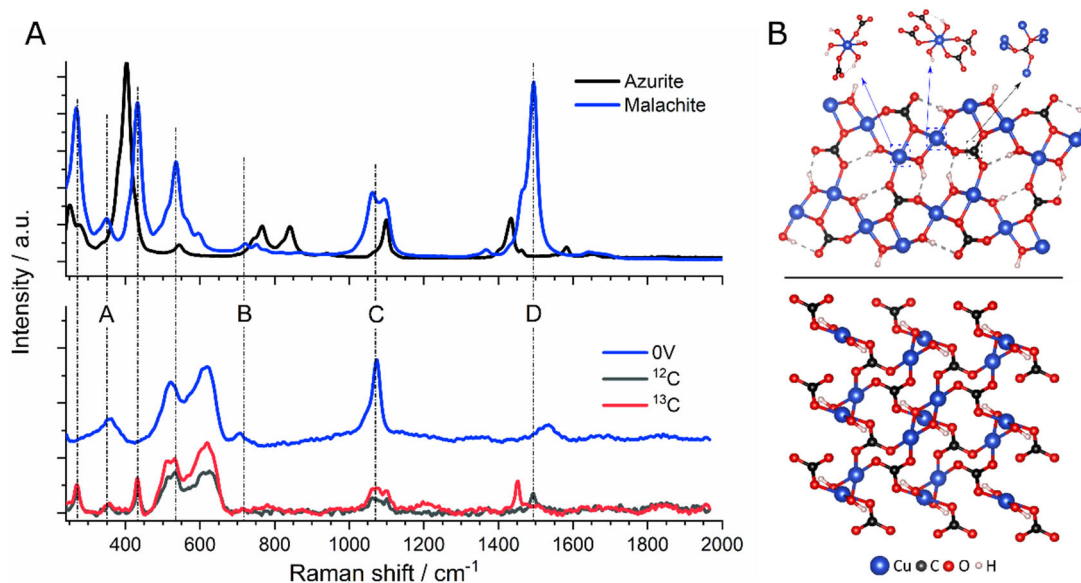


Figure 3.9: (A) Upper panel: reference spectra of azurite and malachite (taken from RRUFF database: azurite, ID R050497, malachite ID R050508); lower panel: SERS spectra of the green material, which is identified as malachite (by putting Cu foam in  $^{12}\text{C}$  or  $^{13}\text{C}$  labelled bicarbonate solution for 6 days) under OCP in 0.1 M  $\text{KHCO}_3$  and  $^{13}\text{C}$  labelled  $\text{KHCO}_3$  solution, in comparison to spectrum of Cu foam measured in  $\text{CO}_2$  saturated 0.1 M  $\text{KHCO}_3$  at 0  $\text{V}_{\text{RHE}}$ . (B) Molecular structure of malachite,  $\text{Cu}_2(\text{OH})_2\text{CO}_3$  (upper panel), and azurite,  $\text{Cu}_3(\text{OH})_2(\text{CO}_3)_2$  (lower panel), remade based on ref (Hurlbut & Klein., 1977).

The Raman spectrum of the green material formed after 6 days exhibits clear similarity with the malachite spectrum: all malachite peaks are detectable in the green material, where additionally also Cu (hydr)oxide peaks are present at wavenumbers below  $700\text{ cm}^{-1}$ , suggesting formation of malachite coexisting with (hydr)oxide phases. The coexisting malachite and the Cu (hydr)oxide likely may be spatially separated, as suggested by the microscope image of Appendix 8.19. Also the spectrum measured at  $0\text{ V}_{\text{RHE}}$  exhibits remarkable similarities with the malachite spectrum. The material formed on the Cu electrode at  $1\text{ V}_{\text{RHE}}$  may not closely resemble the crystalline malachite that is taken as a reference. However, considering the amorphicity of the copper carbonate hydroxide product resulting from conversion of the rough Cu (hydro)oxide layer, some shift in the vibrational frequencies and band amplitudes can be expected. It can be concluded that rather than crystalline malachite, the material formed at  $0\text{ V}_{\text{RHE}}$  may be copper carbonate hydroxide with malachite-derived structural motifs.

To illustrate and support the concept of a malachite-derived structural motifs, the Raman spectra of azurite,  $\text{Cu}_3(\text{OH})_2(\text{CO}_3)_2$ , and malachite,  $\text{Cu}_2(\text{OH})_2\text{CO}_3$  are compared (black and blue lines in **Figure 3.8A**, crystalline structures are also shown in **Figure 3.8B**). Even though the materials are quite similar in structure, some peak frequencies shift by  $100\text{-}200\text{ cm}^{-1}$ . In the same fashion, the amorphous copper carbonate hydroxide that forms in these experiments could exhibit comparable shifts with respect to the crystalline reference materials. Moreover, it should be noted that a shift of  $40\text{ cm}^{-1}$  can be seen in the  $1500\text{ cm}^{-1}$  peak of the  $^{13}\text{C}$  samples compared to the  $^{12}\text{C}$  samples in **Figure 3.7A**, which is comparable with the isotope shift of the Cu electrode reported in **Figure 3.4**. The isotope labelled sample further emphasizes the peak assignment at  $1500\text{ cm}^{-1}$  to anti-symmetrical stretching vibration of carbonate in this kind of structure. No clear shift of the peak at  $350\text{ cm}^{-1}$  is observed, which further support its assignment to Cu-O. Further experiment with a  $\text{D}_2\text{O}$  labelled malachite sample showed only a peak shift at  $430\text{ cm}^{-1}$  to  $420\text{ cm}^{-1}$ , which suggests a component of Cu-OH vibrations (Appendix 8.15).

Due to spectral similarities and to comparable isotope peak shift, the material detected in the measurements (associated with the  $1500\text{ cm}^{-1}$  band) is proposed to be an amorphous malachite-like copper carbonate hydroxide, CuCarHyd. Consequently, following previous assignments (Frost et al., 2002), the following assignment can be done to peak (A-D): (A) to X-Cu-O bending, (B) to in-plane bending of carbonate,  $\nu_4$ ; (C) to C-O symmetric stretching of carbonate,  $\nu_1$ ; (D) to antisymmetric stretching of carbonate,  $\nu_3$ . It should be noted that the shift reported in the  $^{13}\text{C}$  labelling experiments of **Figure 3.4** and **3.7A** is in line with this assignment.

### 3.2.4 *In-situ* formation of CuCarHyd

To support the relation of the spectra to a malachite-like material, examination of the measurements under nitrogen atmosphere (no  $\text{CO}_2$  saturation) performed with different concentration of  $\text{HCO}_3^-$  can be informative. The pH of such solutions is not 6.8 but around 9, due to the absence of  $\text{CO}_2$ . Looking at the Pourbaix diagram, at pH 9 the formation of copper carbonate hydroxide is not as favourable as when the pH is 6.8, making the  $\text{Cu}_2\text{O}$  phase more stable (or more inert due to the lower driving force). Though, at higher concentration of  $\text{HCO}_3^-$  the stability region of  $\text{Cu}_2\text{O}$  is reduced, see dashed vs. solid lines, such that the CuCarHyd becomes the main stable compound in the range  $0$  to  $0.4\text{ V}_{\text{RHE}}$ , i.e. the oxide can be converted

into CuCarHyd. This explains why in **Figure 3.3** the CuCarHyd is seen only in the high bicarbonate concentration experiment (1 M instead of 0.1 M  $\text{KHCO}_3$ ).

The correlation of high pH with the stability of CuCarHyd opens an alternative path for its *in-situ* formation. During the oxide reduction process protons are consumed, causing a substantial variation of the local pH in proximity of the electrode. Such local alkalization could initiate the formation of metastable malachite-like material during operation. The extent of such local pH rise was probed through a series of *operando* Raman spectra using the 473 nm laser which shows no SERS effect, eliminating the signal from the adsorbed species. With this method the local pH under oxide reduction potentials is estimated to be around 9.5, which is even larger than the one obtained with the 1 M bicarbonate solution that showed presence of CuCarHyd in **Figure 3.3**. The results will be shown and discussed in **Chapter 5 section 5.2.2**.

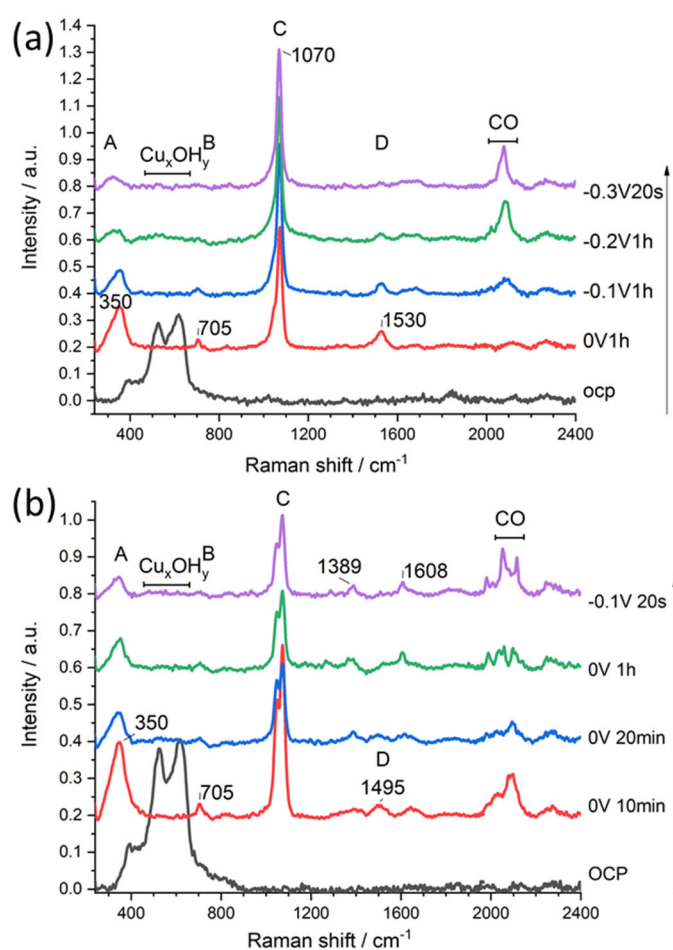


Figure 3.10: (a) Raman spectra of Cu foam measured in  $\text{N}_2$  saturated 0.5 M  $\text{KHCO}_3$  (pH 8.7) at 0, -0.1 and -0.2  $V_{\text{RHE}}$  each potential for 1 hour and -0.3  $V_{\text{RHE}}$  for 20 s. (b) Raman spectra of Cu foam measured in  $\text{CO}_2$  saturated 0.1 M  $\text{KHCO}_3$  (pH 6.8) at 0  $V_{\text{RHE}}$  for 1 hour and -0.1  $V_{\text{RHE}}$  20 s.

A further experiment was performed to support the *in-situ* formation of CuCarHyd material. Applying 0  $V_{\text{RHE}}$  for an hour in  $\text{N}_2$  saturated 0.5 M  $\text{KHCO}_3$  the CuCarHyd peaks are stable and remain at the surface, even applying further -0.1  $V_{\text{RHE}}$  and -0.2  $V_{\text{RHE}}$  each for one hour, the CuCarHyd peaks gradually diminished. Whereas in  $\text{CO}_2$  saturated 0.1 M  $\text{KHCO}_3$ , the

CuCarHyd peaks are only presented at 0  $V_{RHE}$  for the initial 10 mins, then a pair of new bands at 1389 and 1608  $\text{cm}^{-1}$  appeared, which could be from formic acid. There are two major differences between the two electrolytes, the lower concentration of bicarbonate and the lower pH in 0.1 M  $\text{KHCO}_3$ . The high local pH and high concentration of bicarbonate are prerequisite for CuCarHyd *in-situ* formation as discussed above. Furthermore, at low pH it may accelerate the reduction of CuCarHyd. According to the Pourbaix diagram, at 0  $V_{RHE}$  apparently only metallic Cu is stable phase, this suggests that though thermodynamically CuCarHyd is not the stable phase, it is in an equilibrium and a thin layer of CuCarHyd can be *in-situ* formed in the interface under alkaline pH and high bicarbonate concentration.

### 3.2.5 CuCarHyd as CO precursor

As discussed above, even a bare Cu electrode, in presence of  $\text{Cu}_x\text{OH}_y$ , can form a copper carbonate hydroxide layer detectable with SERS. In the experiments that follow, it is further illustrated that if such CuCarHyd material is formed prior or during operation and if it is active towards  $\text{CO}_2\text{RR}$ .

Three kinds of samples were prepared to investigate the source of the carbon necessary to form the CuCarHyd:

- I. Standard type of Cu foam electrode as used also further above (in contact with air);
- II. Cu foam electrode left for 6 days in carbonate solution (malachite enriched); (**Figure 3.11**)
- III. Cu foam electrode left with a water layer on the surface for 4 days in a  $\text{CO}_2$  free environment (hydroxide enriched). (**Figure 3.11**)

*Operando* Raman while scanning CV experiments were used to correlate the formation/consumption of the CuCarHyd layer with the production of CO. The above three types of electrodes were each operated in:

- (i)  $\text{N}_2$  saturated bicarbonate solution;
- (ii) Alkaline electrolyte (0.1 M KOH) without any carbonate/ $\text{CO}_2$ , to assess whether the formation of the CuCarHyd layer happens during or prior to operation.

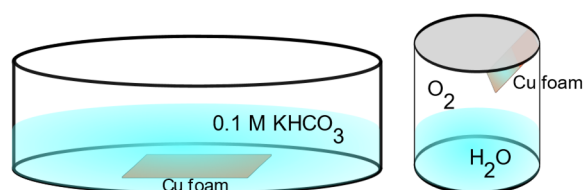


Figure 3.11: Scheme of preparing Malachite sample (left) and hydroxide enriched sample (right).

Cyclic voltammetry was recorded at a low scan rate, 1 mV/s, starting from OCP spanning the range from -0.4 to 1.1  $V_{RHE}$  (-0.6 to 1.5  $V_{RHE}$  in KOH electrolyte). The low scan rate allowed the recording of *operando* Raman spectra (10 s acquisition time), at key points of the CV (every 50-100 mV). To examine the relation of CuCarHyd and the CO peak with potential, two specific measurements were picked and compared. The original Raman spectra and the CV data of Cu foam measured in bicarbonate buffer and the malachite enriched sample measured in KOH are



shown in **Figure 3.12** and **3.13**, the trends are summarized reporting the amplitude of the peaks of interest: the  $1530\text{ cm}^{-1}$  peak, belonging to the CuCarHyd and the  $\sim 2000\text{ cm}^{-1}$  CO peak; respectively squares and circles in **Figure 3.14** and **3.15**.

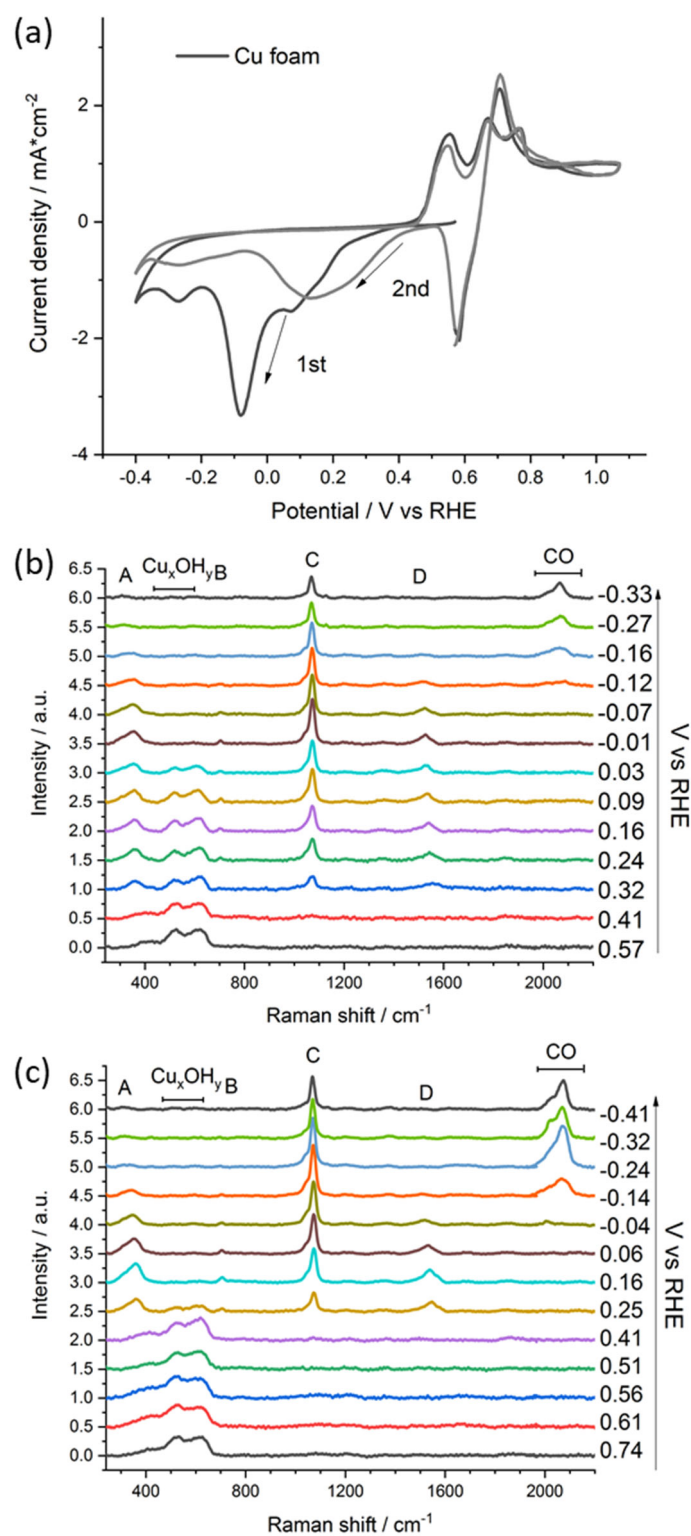


Figure 3.12: (a) CV 1 mV/s data of Cu foam electrode measured in  $\text{N}_2$  saturated 0.5 M  $\text{KHCO}_3$ ; Raman data of the 1<sup>st</sup> (b) and the 2<sup>nd</sup> cycle (c) from positive to negative potentials.

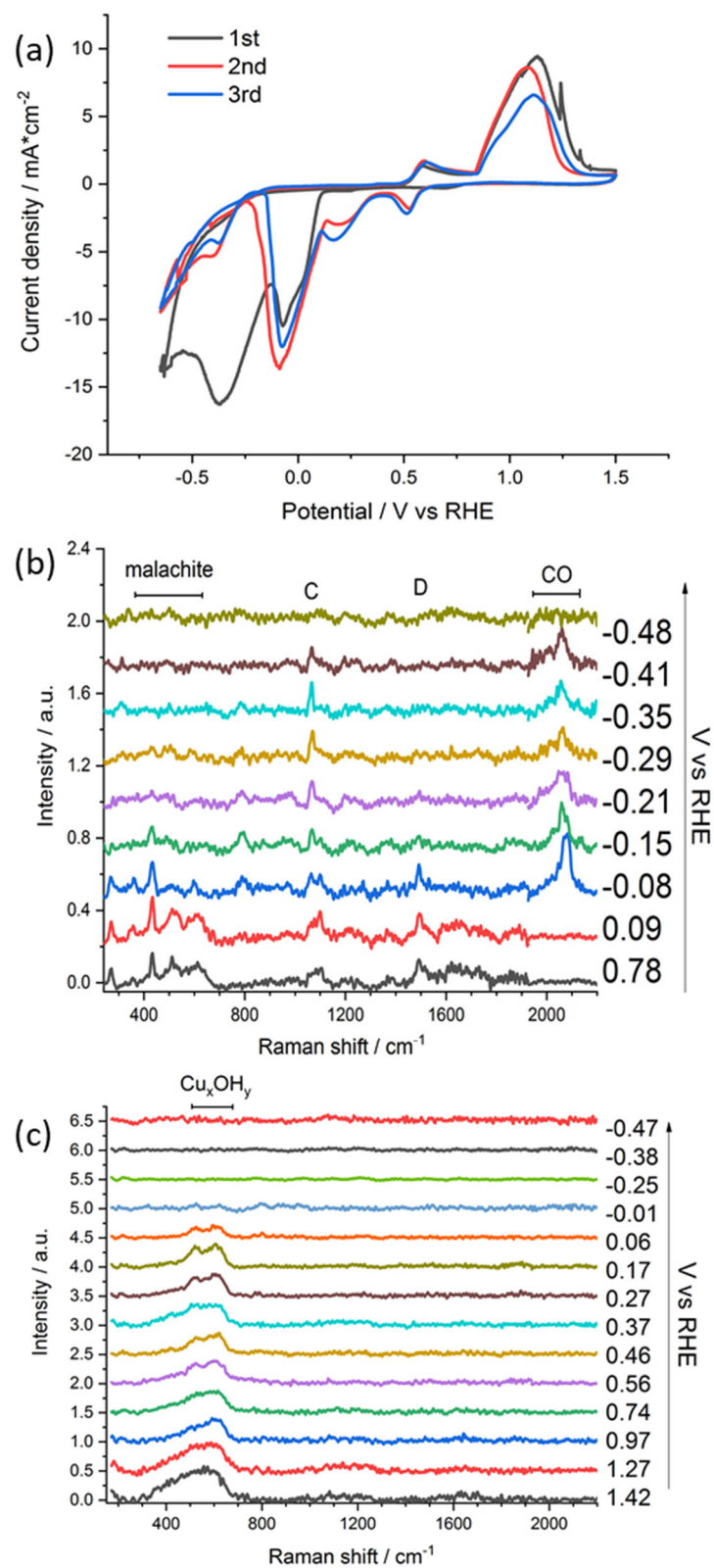


Figure 3.13: (a) CV 1 mV/s data of Cu formed malachite sample measured in  $\text{N}_2$  saturated 0.1 M KOH (pH 13); Raman spectra during 1<sup>st</sup> (b) and 2<sup>nd</sup> cycle (c) from positive to negative potentials (due to low or no SERS, the signal is quite noisy). In the 2<sup>nd</sup> cycle, there is no CO peak observed.

The Raman peak intensities were read and plotted together with CVs as reported in **Figure 3.14** and **3.15**. **Figure 3.14** shows the usual Cu foam sample in N<sub>2</sub> saturated 0.5 M bicarbonate solution, **Figure 3.15** shows the malachite enriched sample in CO<sub>2</sub>-free 0.1 M KOH solution (pH 13) (the concentration of KOH was chosen such that the pH would not be too dissimilar to the N<sub>2</sub> saturated 0.5 M KHCO<sub>3</sub> solution (pH 8.7)).

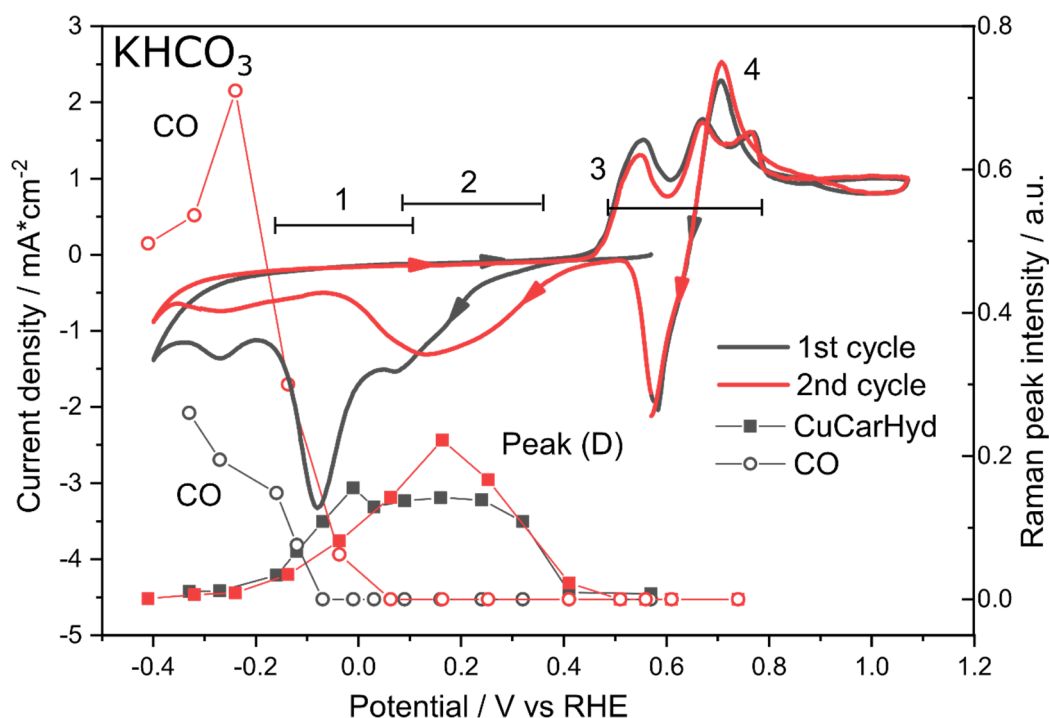


Figure 3.14: First (gray solid line) and second cycle (red solid line) of CV (1 mV/s) of Cu foam electrode measured in N<sub>2</sub> saturated 0.5 M KHCO<sub>3</sub> (pH 8.7) (left y-axis), the scan directions are indicated by arrows; and the peak intensity of peak (D) at 1530 cm<sup>-1</sup> (square symbol solid line curve) and CO peak (empty circle line curve) in the *operando* Raman spectra taken while scanning CV (right y-axis) (an average of 10 mV). Redox wave assignment: 1. 2. reduction of CuCarHyd and hydroxide; 3. oxidation of Cu to Cu<sub>x</sub>OH<sub>y</sub>; 4. pitting corrosion.

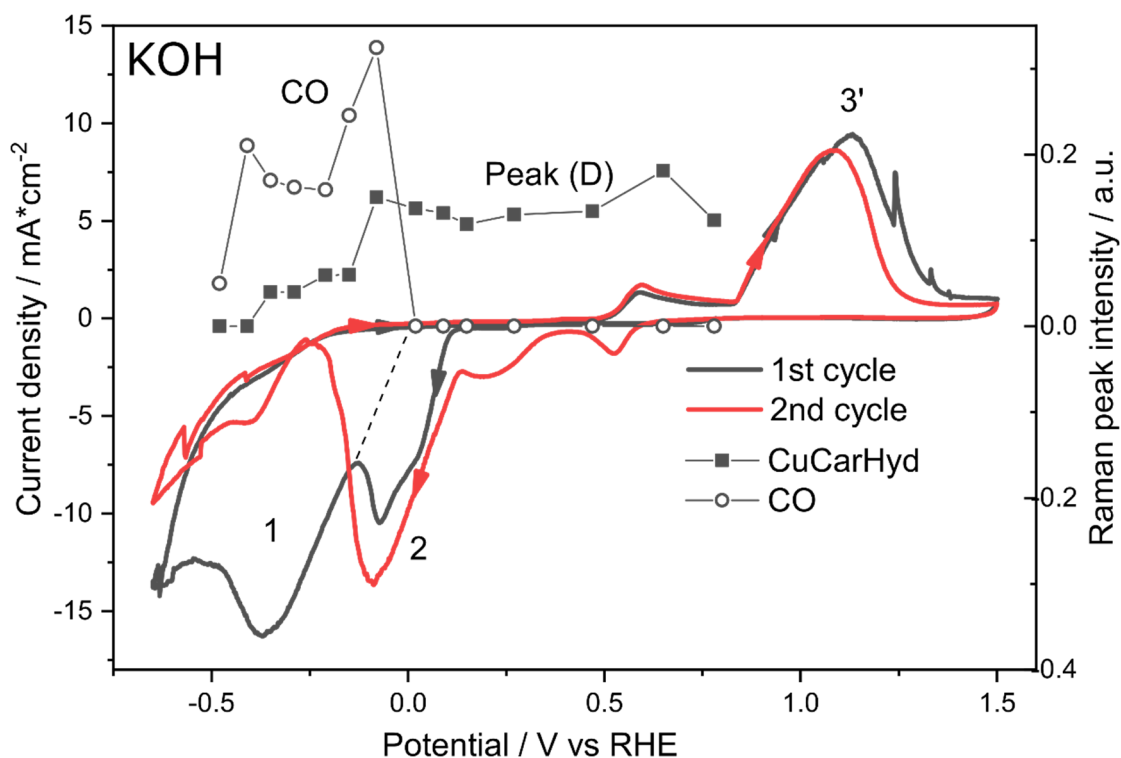


Figure 3.15: First (gray solid line) and second cycle (red solid line) of CV (1 mV/s) of Cu formed malachite electrode measured in  $N_2$  saturated 0.1 M KOH (pH 13) (left y-axis), the scan directions are indicated by arrows; and the peak intensity of peak (D) (square symbol solid line curve) and CO peak (empty circle line curve) in the *operando* Raman spectra taken while scanning 1<sup>st</sup> CV cycle (right y-axis) (an average of 10 mV). The second cycle show no CO and CuCarHyd bands, therefore omitted for clarity. Redox wave assignment: 1. reduction of CuCarHyd (the dashed line indicates the underlying reduction wave under 2); 2. reduction of  $Cu_xOH_y$ ; 3. oxidation of Cu to  $Cu_xOH_y$

The first thing to notice is that in both system the first and second cycle are remarkably different in the cathodic regime. In **Figure 3.15** the waves look shifted due to the large charge exchanged, the onset potentials remain similar. In the first cycle the large reduction peak, with an onset around  $-0.1 V_{RHE}$ , is completely irreversible in **Figure 3.15** but only partially in **Figure 3.14**. This means the reaction consumes the material already present on the electrode, that is not reformed (completely in **Figure 3.15** but only partially in **Figure 3.14**) in the subsequent oxidation/reduction waves. This will be clarified later. In **Figure 3.15** the irreversibility of the cathodic wave **1** is even more accentuated, suggesting an assignment to CuCarHyd reduction. Furthermore, in **Figure 3.16** (b) the first cycle of the cyclic voltammograms of the three different sample preparations measured in  $CO_2$  free 0.1 M KOH are compared. The two reduction peaks in the first cycle of the CVs of malachite are again attributed to the reduction of Cu carbonate hydroxide and Cu hydroxide, while in the hydroxide enriched sample and Cu foam sample, there are only one reduction peak which is attributed to the reduction of Cu hydroxide. Therefore the assignment of the CV redox waves can be speculated as indicated in the figures (labels 1 to 4 in **Figure 3.14** and 1 to 3 in **Figure 3.15**). Briefly, cathodic wave **1** and wave **2** is attributed to the reduction of CuCarHyd and hydroxide; the anodic waves **3** from

0.5 to 0.9  $V_{\text{RHE}}$  to the oxidation of Cu to  $\text{Cu}_x\text{OH}_y$  and the back anodic wave 4 is attributed to pitting corrosion, in line with previous assignments (Sánchez et al., 1990).

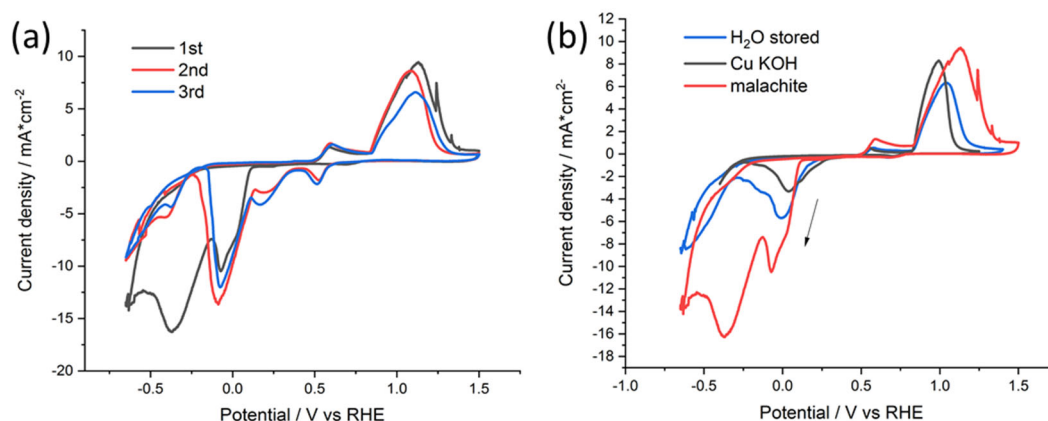


Figure 3.16: (a) 1<sup>st</sup>, 2<sup>nd</sup> and 3<sup>rd</sup> cycle of CV of malachite enriched sample measured in  $\text{N}_2$  saturated 0.1 M KOH (pH 13); (b) CV 1st cycle comparison between Cu foam, hydroxide enriched, and malachite enriched sample measured in  $\text{N}_2$  saturated 0.1 M KOH (pH 13).

Verification on the origin of such waves and clues on the relevance for  $\text{CO}_2\text{RR}$  can be given by the analysis of the Raman spectra collected during the CV. In bicarbonate buffer, all three samples showed both CuCarHyd peaks and CO peak in the first and second cycle as summarized in **Table 3.2** (original Raman data shown also in Appendix 8.17). Whereas in KOH buffer, only malachite enriched sample showed both CuCarHyd and CO peaks in the first cycle (Minor CO peak are observed temporarily for hydroxide enriched sample and Cu foam). This is a clear sign that CuCarHyd is *in-situ* formed but does not exist on Cu foam. It can be *in-situ* synthesized in bicarbonate buffer.

**Table 3.2:** Summary of Raman results of CO peak and peak (D) at  $1530\text{ cm}^{-1}$  of three samples measured in  $\text{N}_2$  saturated KOH and  $\text{N}_2$  saturated  $\text{KHCO}_3$ .

Electrolyte		$\text{N}_2$ saturated 0.5 M $\text{KHCO}_3$			$\text{N}_2$ saturated 0.1 M KOH		
		Cu	Hydroxide enriched Cu	Malachite	Cu	Hydroxide enriched Cu	Malachite
1530	1st	✓	✓	✓	×	×	✓
	2nd	✓	✓	✓	×	×	×
CO	1st	✓	✓	✓	×	×	✓
	2nd	✓	✓	✓	×	×	×

In **Figure 3.14** (usual Cu foam cycled in  $\text{CO}_2$ -free bicarbonate solution) the assumed copper carbonate hydroxide bands (peak (D) at  $1530\text{ cm}^{-1}$ ) appears always from about  $0.4 V_{\text{RHE}}$  and starts decaying from  $-0.1 V_{\text{RHE}}$  in the first cycle and from  $0.1 V_{\text{RHE}}$  in the second cycle. In the same range of potentials, while the CuCarHyd decays, the magnitude of the CO peak rises,

indicating a correlation between the two phenomena. It is interesting to see that the amplitude of the CuCarHyd peak resemble quite well (preceding it by few mV) the magnitude of the cathodic current.

In **Figure 3.15** (malachite enriched sample in CO<sub>2</sub>-free KOH), the CuCarHyd peak is present from the beginning of the voltammogram, as expected, and it stays quite constant until the onset potential of the reduction of the copper carbonate hydroxide at ca. -0.1 V<sub>RHE</sub> where it starts decaying to reach about zero at around -0.45 V<sub>RHE</sub>; concurrently the CO peak rises from 0 to its maximum amplitude at around -0.1 V<sub>RHE</sub>. Again, the rising of the CO peak is associated with the disappearance of the CuCarHyd signal.

The fact that in **Figure 3.15**, the formation of CO in a system where the C source is only the malachite, it suggests that this material is able, itself, to produce the CO species at very low potentials respect to the CO<sub>2</sub>RR. The experiment summarized in **Figure 3.14**, instead, shows that such a material, able to produce CO, can be formed *in-situ* starting from oxidized Cu foam electrode in a solution of bicarbonate in absence of CO<sub>2</sub>. This is evident by the fact that the CuCarHyd signal appears starting from zero amplitude, it disappears fully at negative potentials and reappears after the oxidation cycle. A further confirmation that the material is a CuCarHyd is the fact that in both system the CuCarHyd peaks disappear and CO forms at the same potential (at -0.1 to -0.2 V<sub>RHE</sub>). It is proposed that a common route of CO formation though Cu carbonate hydroxides, which are initially present in the malachite enriched Cu foam but transiently formed at the standard Cu surface in the presence of a carbonate electrolyte.

As discussed further above, it is assumed that the formation of the copper carbonate hydroxide by the conversion of copper (hydro)oxides is supported by a high local pH at the electrode surface during the (hydro)oxide reduction (cathodic wave **2** in **Figure 3.14**). Moreover, it can be assumed that CuCarHyd under operation conditions is formed by a non-equilibrium process involving the electric-potential gradient between negative electrode and solution potential (see **Figure 3.8B**). CuCarHyd can withstand more negative potentials compared to the oxide (see 1<sup>st</sup> vs 2<sup>nd</sup> cycle cathodic currents in **Figure 3.15**). The observation that the CuCarHyd is the last species that is detected going towards catalytic potentials and immediately prior CO production, suggests that the CuCarHyd could be an essential reaction intermediate of the CO<sub>2</sub>RR.

### 3.2.6 CO Intensity relates to (hydro)oxide content

Similar CV/Raman experiments were performed also for hydroxide enriched sample (Appendix 8.17) together with malachite enriched sample and Cu foam, with the aim to vary the amount of CuCarHyd formed and correlate it with the produced CO that is adsorbed at the catalyst electrode. The CO peak area trend vs. potential of the first cycle of CV/Raman is plotted for all three samples in **Figure 3.17**. It can be seen that the malachite enriched sample produces the most CO whereas the hydroxide enriched sample produced an intermediate CO quantity when compared to the standard Cu foam.

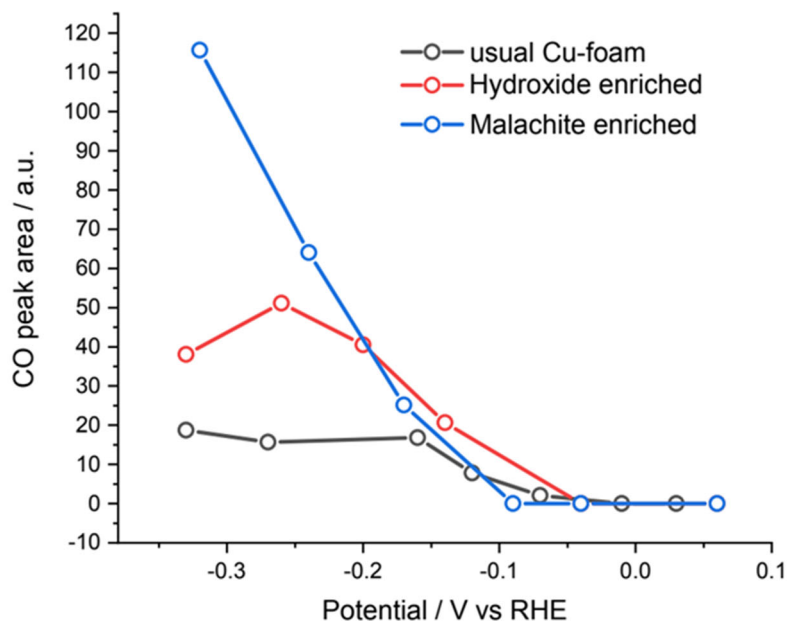


Figure 3.17: CO peak area trend vs potential of Raman data during first cycle of CV 1 mV/s in  $N_2$  saturated 0.5 M  $KHCO_3$  for Cu foam, hydroxide enriched Cu foam and Cu formed malachite sample.

### 3.2.7 CO presence at low overpotential relates to (hydro) oxide

In order to further illustrate the role of oxide for formation of CuCarHyd and CO, long time experiments on “oxide” and *in-situ* “reduced Cu” surface were performed. The “oxide” is just the Cu foam catalyst used before with naturally formed surface oxide layer, and the “reduced Cu” is prepared by cycling 4 times and scanning 3 times linear sweeping voltammetry between -0.1 to -0.9  $V_{RHE}$  before measurements. The electrochemical data and the complete Raman spectra for long-time measurements are shown in Appendix 8.18. **Figure 3.18** shows the comparison between Raman spectra of “oxide” surface and “reduced Cu” surface. When starting from oxide a peak at around 2000-2100  $cm^{-1}$  appeared at low overpotential and carbonate peak intensity is much higher. It should be noted that on oxide surface CuCarHyd bands appeared in the beginning and disappeared after 0  $V_{RHE}$ . The assignment of peak at around 2060  $cm^{-1}$  to CO but not H adsorption was further proved by the measurement in  $D_2O$  electrolyte (Appendix 8.18). Plotting the Cu-CO and CO bands intensity in **Figure 8.30, 31** in Appendix versus potential (**Figure 3.19**), it can be seen that on the oxide surface, CO band keeps increasing until the highest negative potential, whereas on reduced Cu surface, the CO peak intensity reduced after -0.6  $V_{RHE}$ . This suggests that starting from oxide CO production shows lower overpotential, and CO can adsorb on the surface and accumulate. This is of great importance to high selectivity for  $C_{2+}$  products. It has been proposed that \*CO coverage is decisive for  $C_2H_4$  production, when \*CO accumulate to a certain amount at appropriate potential they might form CO dimer and further to  $C_2H_4$  (Y. Huang et al., 2017). In line with this the lower overpotential for CO production may also help decrease  $C_2H_4$  production overpotential.

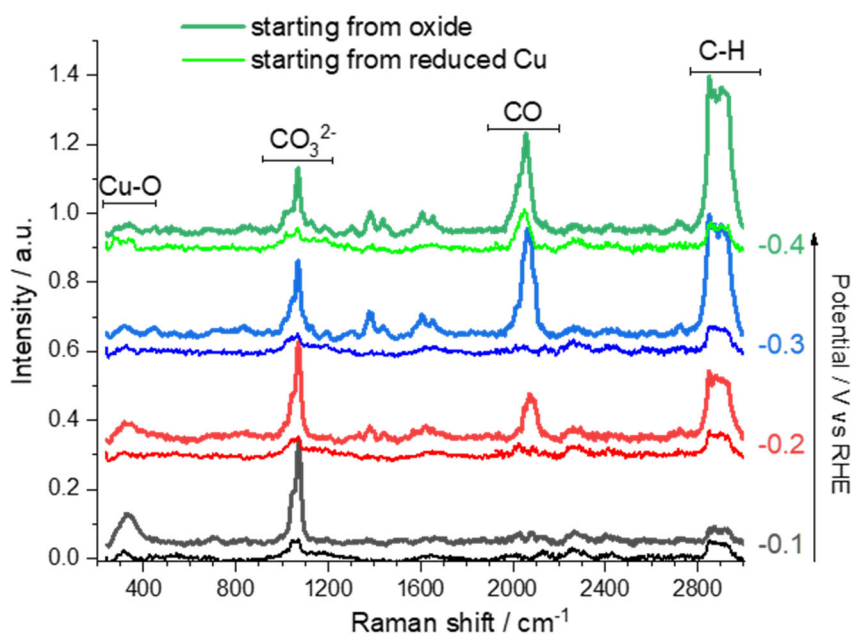


Figure 3.18: Long time measurement (protocol scheme shown in Appendix 8.18) for Cu foam electrode starting from oxide and starting from reduced state.  $\text{CO}_2$  gas was constantly purged to 0.1 M  $\text{KHCO}_3$  electrolyte, spectra was taken in the end of each potential.

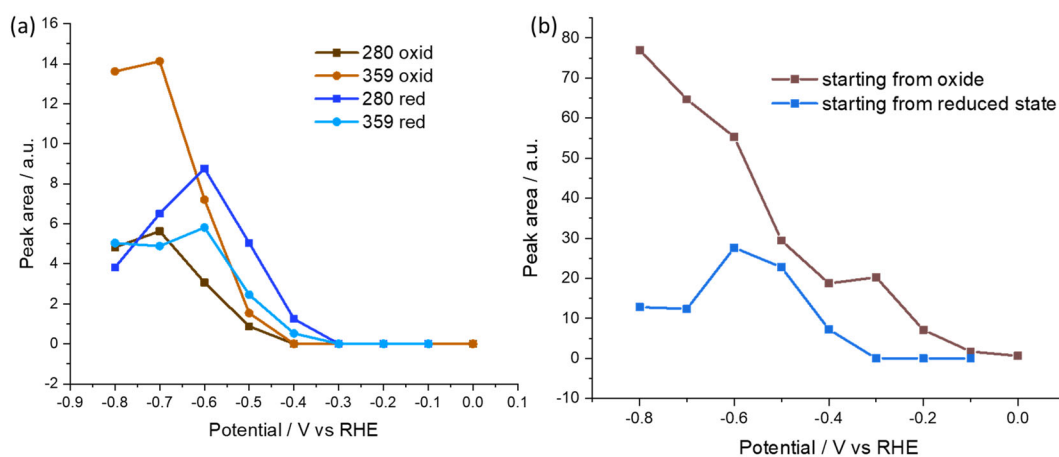


Figure 3.19: CO peak area trend vs potentials for peak at (a) 280 and 359  $\text{cm}^{-1}$  and (b) 2000-2100  $\text{cm}^{-1}$ . Data read from long time measurement for Cu foam electrode starting from oxide and starting from reduced state.

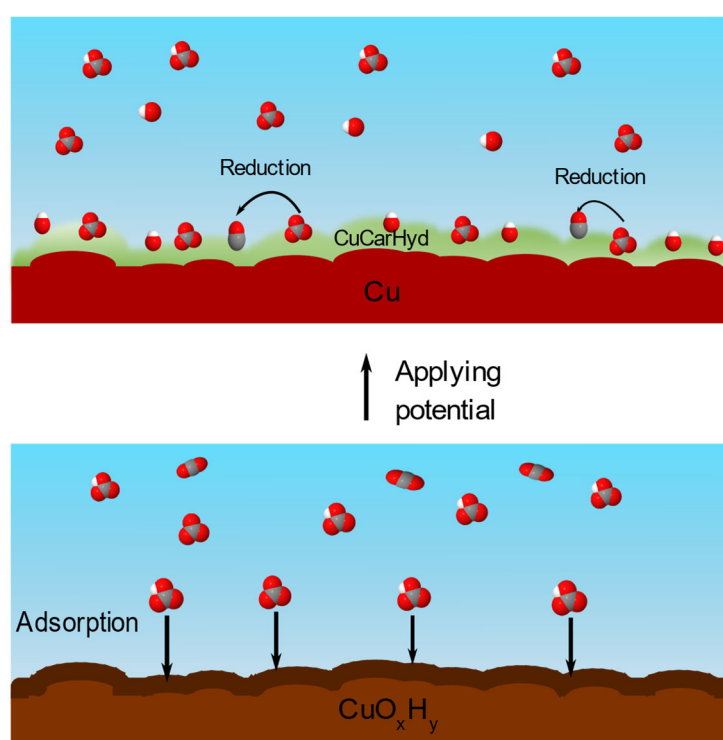
### 3.2.8 Discussion

When designing new catalysts atomically precise control of the active sites is often the goal (Xie et al., 2020), therefore *operando* spectroscopy techniques are used to ideally detect the reaction intermediate adsorbed on the active sites (Handoko et al., 2018). Oxide-derived catalyst is a relatively convenient and bulk transformation strategy, which in turn cause the



tremendous increasement of CO<sub>2</sub>RR activity (C. W. Li et al., 2014; C. W. Li & Kanan, 2012). Therefore, the reaction mechanism may not be easily explained by a specific reaction intermediate. Here a brand-new way of interpretation of the reaction pathways on oxide-derived Cu for CO<sub>2</sub>RR is proposed.

As shown in **Scheme 3.1**, before applying potential due to the affinity of oxide to (bi)carbonate, there is a layer of bicarbonate in the vicinity. Once applying reducing potential, some part of Cu oxide is reduced, meanwhile, hydroxy ion was produced and local pH increases (as will be illustrated in **Chapter 5**), bicarbonate tends to deprotonate and forms carbonate which adsorb on the Cu surface. Since the local potential may be much more positive than the applied potential, the oxide surface together with hydroxyl ion and carbonate anion may form a motif of Cu carbonate hydroxide, which gives the peaks (A-D). With further scanning to negative potentials, the motif of copper carbonate hydroxide could further get reduced to CO.



**Scheme 3.1.** Proposed reaction process of oxide Cu foam electrode interfacing with bicarbonate buffer under OCP and under reducing potentials.

The origin of these bands and the new hypothesis has been investigated in detail in the previous sections, it is also based on the high signal of peak (A-D) in *operando* Raman spectra, it can be speculated that molecular intermediates like  $^*CO_2^-$  may not be able to show such high signal. Nevertheless, the active material formed in the interface may be only several atomic layer, so it may not block the electron conduction as reported earlier in another work (Velasco-Vélez et al., 2018). The biggest advantage of this active material is that it is not necessary to be prepared on purpose, it is naturally formed on the oxide surface interfacing with bicarbonate electrolyte and can be consumed and reformed in a sustainable way.

This may help explain in previous reports that bicarbonate is crucial for CO<sub>2</sub>RR (M. Dunwell et al., 2017; Marco Dunwell, Yan, & Xu, 2018; S. Zhu et al., 2017), here it is proved to be actively participating the reaction. In addition, high local pH was observed to suppress the HER therefore facilitate the CO<sub>2</sub>RR, here it can be concluded that according to Pourbaix diagram, high pH is also optimized for the formation of copper carbonate hydroxide as well.

Benefiting from the new findings, protocols based on pulse potentials or introducing more hydroxyls can be assumed to promote CO<sub>2</sub>RR extensively by forming and restoring oxide and therefore CuCarHyd. Indeed, there have been reports about both strategies and the reason behind it remain unclear then (He et al., 2020; Kimura et al., 2020). Now it may be explained well by the findings here. In other reports subsurface oxygen or Cu<sup>+</sup> residues were detected at even highly negative potentials which were used to explain the high C<sub>2+</sub> production selectivity. Whether the material reported here is also present at high overpotentials may not be easily affirmed. Nevertheless, the low overpotential of CO formation can result in higher \*CO coverage which may promote \*CO dimer formation and indirectly promote C<sub>2+</sub> production.

### 3.3 Conclusions

In this chapter, a scrupulous investigation was performed to elucidate the role of bicarbonate in the formation of intermediates of CO<sub>2</sub>RR catalyzed by Cu foam electrodes. Via isotope labelling and comparison with reference compounds various literature peak assignments to reaction intermediates were critically analyzed and new assignments proposed. The new findings motivate new perspectives regarding the catalytically active material and the basic mode of catalysis in CO<sub>2</sub>RR at Cu electrodes, as summarized in the following.

***Formation of Cu carbonate hydroxides.*** It is shown that CuCarHyd does not need to be synthesized explicitly, but it is spontaneously produced once the electrode (coated with Cu<sub>x</sub>OH<sub>y</sub>) is immersed in bicarbonate solution (**Figure 3.1, 3.3, 3.4, 3.12**). The presence of the copper carbonate hydroxide at catalytic potentials can be rationalized by local alkalization in combination with electrical potential gradients (**Figure 3.8B**), which could enable the formation of metastable materials over a large range of potentials (**Figure 3.8A**). The presence of oxidized species at highly reducing potentials (up to -1.0 V<sub>RHE</sub>) indeed has been reported before for Cu-based CO<sub>2</sub>RR systems, where Cu oxide residues were found to persist (Cavalca et al., 2017; Phil De Luna et al., 2018; Eilert et al., 2017). Here it is proposed that CuCarHyd are present at low overpotentials and may present at catalytic potentials, as a metastable material, partially consumed and re-synthesized in a cyclic fashion.

***CO formation not starting from CO<sub>2</sub> but from carbonate ions of CuCarHyd.*** The hypothesis of a CuCarHyd being the actual catalytic material of the CO<sub>2</sub>RR, has been considered before (Eilert et al., 2016; Henckel et al., 2020; Spodaryk et al., 2019). Here it is shown that in carbonate-free and CO<sub>2</sub>-depleted electrolyte, the carbonate ions present in a CuCarHyd layer can be reduced to CO (**Figure 3.12 - 3.15**) and that increasing CuCarHyd amount increases the Raman signal of the produced CO (**Figure 3.17**). These experiments do not only support a crucial role of CuCarHyd. They also suggest that CO<sub>2</sub>RR at the Cu foam electrodes does not

start from CO<sub>2</sub>, as mostly assumed, but from carbonate ions, in line with the Raman spectra detected for <sup>13</sup>C isotope labelling of either CO<sub>2</sub> or carbonate (**Figure 3.4 – 3.6**).

**Possible role of Cu oxides.** The CuCarHyd likely is produced by the reaction of Cu oxide/hydroxide with dissolved bicarbonate/carbonate ions. This hypothesis on the genesis of the CuCarHyd that promote CO formation resonates with previously studies where Cu oxide has been proposed to favour CO<sub>2</sub>RR (C. J. Chang et al., 2019; Phil De Luna et al., 2018; Jung et al., 2019; Lee et al., 2018; C. W. Li et al., 2014; H. Mistry et al., 2016; Velasco-Vélez et al., 2018; J. Wang et al., 2021). For example, in a recent report high catalytic activity was observed for Cu electrode that were positively polarized for a brief period of time thereby reactivating maximal CO<sub>2</sub>RR (Kimura et al., 2020); the positive polarization could restore the layer of oxide needed to react with bicarbonate to produce the CuCarHyd. In summary, the promoting role of Cu oxide in CO<sub>2</sub>RR could relate to Cu oxide being a precursor to CuCarHyd.

**Passivating role of CuCarHyd.** It has been reported that CuCarHyd material could hinder the CO<sub>2</sub>RR (Velasco-Vélez et al., 2018), whereas the findings here suggests a promoting role. Passivation behaviour may arise from especially extended malachite formation on Cu electrode, as it is observed for Cu foams with high abundance of CuCarHyd operating in carbonate buffer (see Appendix 8.19).

**Alternative twist of CO<sub>2</sub>RR mechanism.** The above results on copper carbonate hydroxide layers suggest a basic mode of CO<sub>2</sub>/carbonate reduction at Cu electrodes that contrast previous mechanistic models. The active material could be amorphous CuCarHyd covering the metallic Cu electrode partially or completely. The CO<sub>2</sub>RR leading to CO may start from carbonate ions of the CuCarHyd, by electron transfer to the metallic electrode. The kinetic competence of the step is indicated by CO formation already at surprisingly low overpotentials, as low as -0.1 V<sub>RHE</sub>, though CO desorption likely requires higher overpotentials (Klingan et al., 2018). It should be noted that the here suggested CuCarHyd-facilitated CO<sub>2</sub>RR may also relate the high catalytic activity of Cu-based materials towards C<sub>1+n</sub>>C<sub>1</sub> products (Phil De Luna et al., 2018; Y. Huang et al., 2017; Jung et al., 2019; W. Zhang et al., 2020), since the copper carbonate hydroxide structure could promote the C<sub>1</sub>-C<sub>1</sub> intermediate interaction due to the high density of carbonate moieties in the structure.

### 3.4 Materials and methods

A Cu foam electrode was electrodeposited as mentioned in **Chapter 2**. Briefly, the Cu foam electrode was deposited via electroreduction from a 0.2 M CuSO<sub>4</sub> solution at -0.5 A for 20 s. After deposition, the electrode was rinsed with MilliQ water and dried in air. Raman spectra were acquired by a Renishaw in Via confocal Raman spectrometer. A 633 nm laser was used as the scattering source with a power of 1.3 mW; the laser was focused (by a cylindrical lens) to a streamline on the Cu surface resulting on a spot of 100 μm long and 10 μm wide. A water immersive objective was used with 40× magnification ratio and N.A. 0.8.

*Operando* Raman experiments were performed in a home-built Raman cell, in which the working electrode faces the objective. A Pt ring (that surrounds the objective) was used as counter electrode, and a miniature Ag/AgCl electrode as the reference electrode. Potential vs Ag/AgCl is converted to RHE scale by  $V_{\text{RHE}} = V_{\text{ref}} + 0.2 \text{ V} + 0.059 \text{ V} \times \text{pH}$ . After mounting the catalyst in the cell, 10 mL electrolyte was purged with CO<sub>2</sub> or N<sub>2</sub> for 10/20 min respectively and subsequently poured into the cell, which then was left purging throughout the experiment. Spectra under open circuit potential (OCP) were always acquired first, the OCP for all the measurement was always around 0.5 V<sub>RHE</sub>. Usually, two ranges of spectra were acquired separately, 106-1967 cm<sup>-1</sup> and 1926-3384 cm<sup>-1</sup>, and after data analysis (see later) individually plotted together. 5 accumulations were averaged to one spectrum and the exposure time was 5 s for each accumulation. Raman data while scanning CV 1mV/s was acquired with 2 accumulations for a shorter time. Data analysis has been reported in **Chapter 2**, in summary the background was subtracted and its averaged amplitude was used for normalization. The figures finally shown in the text were plotted with an offset for clarity.

KHCO<sub>3</sub>, K<sub>2</sub>CO<sub>3</sub> and KH<sup>13</sup>CO<sub>3</sub>(98% <sup>13</sup>C) were purchased from Sigma Aldrich and used without further treatment. All chemicals were used without further treatment. Phosphate buffer was prepared by mixing 0.1 M KH<sub>2</sub>PO<sub>4</sub> and K<sub>2</sub>HPO<sub>4</sub> (Carl Roth) solution until pH reaching 7. All buffers were prepared with MilliQ water (>18 MΩ • cm). N<sub>2</sub> gas (purity 99.8%), CO<sub>2</sub> gas (purity 99.995%) and <sup>13</sup>CO<sub>2</sub> gas (99.0% <sup>13</sup>C) were purchased from Linde gas. D<sub>2</sub>O (99.8% D) was purchased from Carl Roth.

## 4. *Operando* Raman research on bimetallic CuAg catalysts for CO<sub>2</sub> reduction to CO

*The results of the first part (section I) of this chapter have been published in:*

### **Electrodeposited AgCu Foam Catalysts for Enhanced Reduction of CO<sub>2</sub> to CO.**

Kottakkat T, Klingan K, Jiang S, Jovanov ZP, Davies VH, El-Nagar GA, Dau H, Roth C. ACS applied materials & interfaces. 2019 Apr 1;11(16):14734-44.

Copyright (2019) American Chemical Society.

The author contributions to have been as follows: Kottakkat, T. prepared samples and performed electrochemical experiments as well as GC measurements for gas products; Jiang, S. performed all Raman measurements and analyzed the Raman data; Jovanov, Z. P. performed GC measurements for liquid products; El-Nagar, G. A. and Kottakkat, T. performed SEM measurements; Davies, V. H. supported the GC measurements; Dau, H. and Roth, C. supervised research; Kottakkat, T. and Klingan, K. developed the publication focus and wrote major parts of the paper; all authors participated in writing, discussion and revision of the article.

Of all results of the above study, exclusively the results obtained by Shan Jiang are presented in this chapter.

### **4.1 Introduction**

Electrocatalytic reduction of CO<sub>2</sub> has been widely investigated on various metal catalysts (Bagger et al., 2017; Xie et al., 2020). Due to different surface properties, the product distributions of CO<sub>2</sub>RR vary (Bagger et al., 2017). On the contrary to Cu which is able to produce C<sub>2+</sub> products, Au and Ag can solely produce CO with high selectivity. Nevertheless, H<sub>2</sub> as a side product cannot be fully avoided. Recently, nanostructured electrodes of noble metals have been widely investigated and applied in electrocatalytic reactions (Hemma Mistry et al., 2016; Seh et al., 2017; Strasser, Gliech, Kuehl, & Moeller, 2018; Xie et al., 2020). Most of these materials could be also applied to the CO<sub>2</sub>RR processes. Wuttig et al. developed mesoporous Ag and Au catalysts to selectively catalyse the reduction of CO<sub>2</sub> to CO and proposed that nanostructuring helps to suppress HER, therefore further improving the CO selectivity (Hall et al., 2015; Anna Wuttig et al., 2016; Yoon, Hall, & Surendranath, 2016).

Alloying is another useful strategy for improving the CO<sub>2</sub>RR activity (Vasileff et al., 2018). For instance, doping Cu with little amounts of Ag can avoid the high cost of using pure Ag and increase the activity of Cu at the same time. However, this modification often causes a change of the product selectivity depending on the surface structure of the catalyst and the ratio between Cu to Ag on the surface. Huang et al. developed a series of bimetallic nanoparticles by varying the ratio of Ag and Cu (J. Huang, Mensi, Oveisi, Mantella, & Buonsanti, 2019). The Faradaic efficiency (FE) for C<sub>2</sub>H<sub>4</sub> improves more than three times than pure Cu catalyst. Taking advantage of the different selectivity of Cu and Ag, a tandem catalyst is developed by Lum et

al. (Lum & Ager, 2018). Due to the high selectivity of CO on Ag, CO coverage is flourished, which further promotes C<sub>2+</sub> production on Cu with a high FE. This precise control of the surface structure is thus a promising strategy for developing catalyst suitable for industry scale processes.

In addition, despite the high cost of Ag and Au, they are of great interest for mechanistic studies of the CO production. To date, there is still no comprehensive model describing the reaction mechanism on CO evolving catalyst (Sebastián-Pascual et al., 2019; Xie et al., 2020). This might be related to the unsolved question of the CO<sub>2</sub> activation. COOH\* is considered as the main intermediate for CO production, whereas the reaction steps towards COOH\* remain unclear (Firet & Smith, 2016; Rosen et al., 2015).

Furthermore, considering the different surface properties of various metal catalysts, whether there is a common mechanism for CO<sub>2</sub> activation remains a question. For instance, according to Ye et al.'s theoretical study, there are two different pathways for CO<sub>2</sub> activation on Cu and Ag surfaces (Ye et al., 2019). They were among the first who proposed the important role of subsurface oxygen for CO<sub>2</sub> activation on Cu based on theoretical calculations (Favaro et al., 2017). They found that the oxygen atoms tend to stay on the surface of Ag, leading to a different reaction mechanism. A chemisorbed species (O=CO<sub>2</sub><sup>δ-</sup>) is proposed to be the key intermediate for CO<sub>2</sub> activation on Ag. In their recent work they further investigated a AgCu catalyst, combining DFT with APXPS and they found that in these bimetallic catalysts, Ag tends to be more abundant on the surface (Ye et al., 2020). However, when the material is exposed to CO<sub>2</sub> with surface adsorbed O, subsurface Cu atoms tend to replace some surface Ag atoms, which may help to stabilize and activate CO<sub>2</sub> on the surface.

Those studies focused on the activation of gaseous CO<sub>2</sub>, and bicarbonate is reported to be not participating in the CO<sub>2</sub> reduction (A. Wuttig, Yoon, Ryu, & Surendranath, 2017). However, Dunwell et al. pointed out that in the study the analysis of the dependence of bicarbonate neglected the influence of changing pH with varying concentrations of bicarbonate (Marco Dunwell, Luc, et al., 2018). With a consideration of the changing pH, and after correction of the potential scale to vs RHE, there is a clear dependence of the CO partial current on the bicarbonate concentration, which suggests that bicarbonate indeed plays a role in the CO<sub>2</sub>RR process. Nevertheless, in another work they could only prove that bicarbonate is in equilibrium with CO<sub>2</sub> that further participates in the reaction (M. Dunwell et al., 2017).

*In-situ* Raman/IR was employed to investigate the origin of the high CO selectivity on Ag. Smith and co-workers used *in-situ* Raman and attributed an intermediate band to the adsorption of \*OCHO, claiming that this intermediate inhibits HCOO<sup>-</sup> production and therefore promotes CO production (D. Bohra et al., 2019). Further research based on *operando/in-situ* techniques are promising in helping solve these questions.

In this work, an Ag modified Cu dendritic structure was used to investigate the reaction mechanism of CO<sub>2</sub> reduction. Alloying Cu with Ag modified the surface properties of Cu and resulted in an improved CO selectivity. The CO production mechanism was further investigated with *operando* Raman spectroscopy with carbon isotope experiment.

## 4.2 Results and discussion

CuAg foams were deposited according to the protocol reported by Kottakkat et al. (Kottakkat et al., 2019). The method is modified based on the deposition procedure for Cu foams as used in **Chapter 2**. Basically, 50 mmol (CuAg50) of  $\text{AgNO}_3$  was added to the original Cu sulphate solution to make CuAg alloy. The final Cu/Ag ratio in the deposited foam is around 2:1. As a reference, a pure Ag foam was also prepared using a 20 mM Ag nitrate solution. The CuAg foam has a similar morphology as the Cu foam as shown in **Figure 4.1**. The porous structure was retained; fresh samples show a grey colour which comes from Ag. After exposing to reducing potentials, the colour of the catalyst changed to reddish. According to Kottakkat's study, CuAg foams have a higher roughness factor than Cu foams (Kottakkat et al., 2019). The product distribution was investigated with gas chromatography. Unlike Cu foams, which have a relatively high selectivity for  $\text{C}_2\text{H}_4$ , CuAg foam catalysts show an enhanced selectivity for CO, which is of great importance for practical industry production. Due to the low amounts of Ag used in this catalyst but comparable CO selectivity to Ag and Au, CuAg is a better choice. However, the reaction mechanism for the high CO selectivity on this bimetallic catalyst is still unclear.

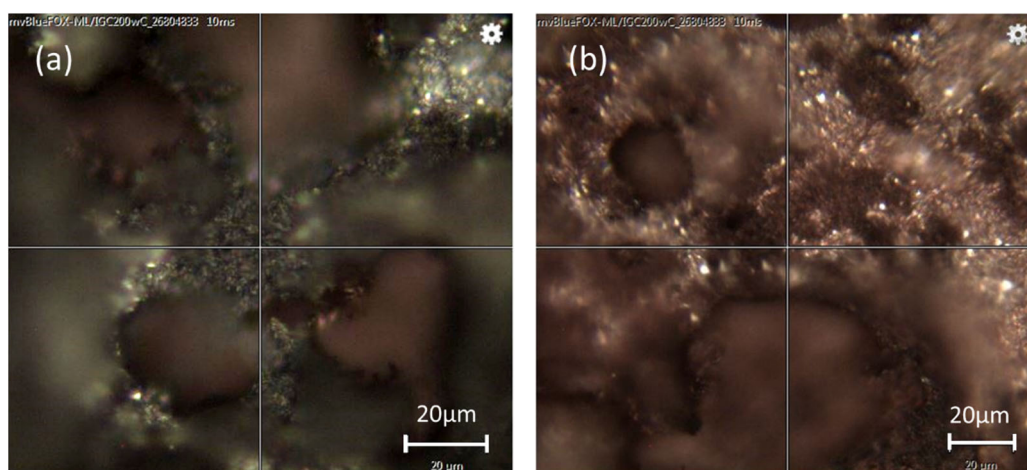


Figure 4.1. Microscope pictures of CuAg foam (a) under OCP and (b) after reduction

### 4.2.1 CO selectivity on CuAg foams

Bimetallic catalysts with Cu and Ag for  $\text{CO}_2$  reduction have been reported before, however, CO is not always the main product. Therefore, it is worth to explore the main reason of varying product selectivity for different catalysts. Here, *operando* Raman experiments on CuAg foams were performed aiming to investigate the different selectivity between Cu and CuAg foam catalysts. The same experiment as in **Chapter 2, Figure 2.1** series1 was performed on a fresh CuAg foam, the data was analysed in the same way; the resulting spectra are shown in **Figure 4.2**. Under OCP, three broad bands at around 430, 527, 604  $\text{cm}^{-1}$  from Cu oxide again are present. A sharp peak at 419  $\text{cm}^{-1}$  can also be observed and has been assigned to AgO (Han et al., 2011). Under 0  $V_{\text{RHE}}$  a peak at 2138  $\text{cm}^{-1}$  appeared but vanished for higher potentials. It can be assigned to CO adsorbed on partially oxidized Ag according to literature (Ichinohe, Wadayama, & Hatta, 1995). With increasing negative potentials, the oxide bands gradually disappeared. CO bands

are present at  $2080\text{ cm}^{-1}$  through all potentials, which is different from Cu as has been discussed in **Chapter 2**. On pure Cu foam surface, there is a transition from a broad band at low ( $2040\text{ cm}^{-1}$ ) and high ( $2080\text{ cm}^{-1}$ ) wavenumbers to a sharp band at high wavenumber, whereas on CuAg, this trend is not observed. In addition, two Cu-CO bands at  $280$  and  $360\text{ cm}^{-1}$  are also absent on CuAg. This suggests that the incorporation of Ag may influence the CO affinity.

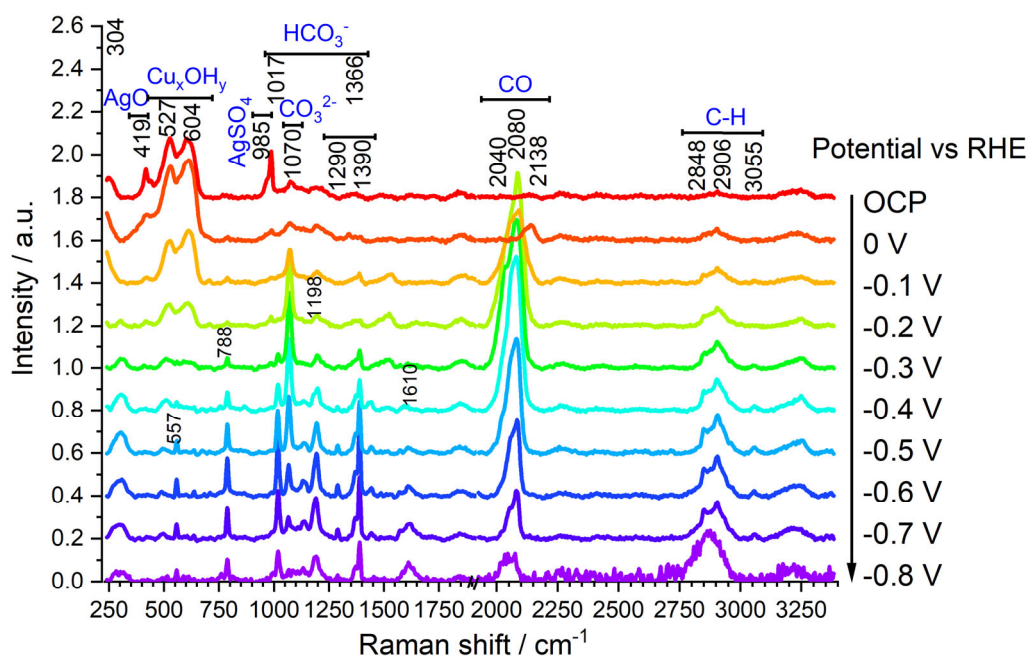


Figure 4.2. *Operando* Raman spectra of CuAg50 in  $0.1\text{ M KHCO}_3$ , pH 6.8. Potentials are given with reference to RHE. The arrow indicates the scan direction. The spectra are background subtracted, normalized, and offset. The noise level in the spectrum of  $-0.8\text{ V}_{\text{RHE}}$  is enhanced due to intense gas evolution. Reprinted with permission from ref (Kottakkat et al., 2019) Copyright (2019) American chemical society.

The presence of Ag within the Cu foam drastically changes the potential dependency of the CO peak area compared with Cu foam catalyst as shown in **Figure 4.3** (Cu foam data was taken from **Figure 2.3a** in **Chapter 2**). It should be noted that the higher CO intensity on CuAg is related to the higher SERS intensity on Ag than Cu. On the Cu foam, only at potentials above  $-0.6\text{ V}_{\text{RHE}}$  where Cu-CO bands appeared the CO peak increased to its maximum. This potential is much lower on Ag:  $-0.2$  to  $-0.4\text{ V}_{\text{RHE}}$ . Below  $-0.4\text{ V}_{\text{RHE}}$  the CO peak intensity keeps decreasing, which suggests that CO is released as a product and cannot accumulate at high potentials. The presence of Ag apparently modified the CO adsorption properties, which facilitated the release of CO ending up with an elevated selectivity to CO for the CuAg catalyst.

Next to the CO peaks there are plenty of new peaks visible which are absent on the Cu foam surface.  $\text{COOH}^*$  is considered as an important intermediate for CO production. According to Firet et al.'s *in-situ* IR results,  $\text{COOH}^*$  presents peaks at  $1288$  and  $1386\text{ cm}^{-1}$  (Firet & Smith, 2016), which also appeared in the spectra shown in **Figure 4.2**. At high overpotentials, peaks at  $557$ ,  $788\text{ cm}^{-1}$  and  $1198\text{ cm}^{-1}$  appear, the origin of which remains unclear. Since the Cu catalyst has a large product distribution, it is possible that after alloying with Ag some



intermediates which do not contribute to the final products appear due to some branched reaction paths.

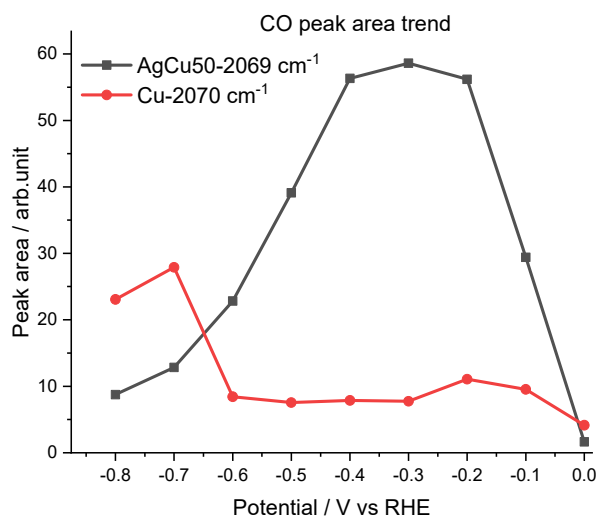


Figure 4.3. Potential dependence of the integrated peak area for the intramolecular CO stretching bands at around 2070  $\text{cm}^{-1}$ . Reprinted with permission from ref (Kottakkat et al., 2019) Copyright (2019) American chemical society.

In order to further illustrate how pure Ag behaves during  $\text{CO}_2$  reduction, *operando* Raman experiments on Ag foams were performed. In **Figure 4.4** it can be seen that on Ag foams there is no CO intramolecular band, the Ag-CO band is also absent. This is consistent to literature and due to the fact that Ag has a lower CO binding energy than Cu (Bagger et al., 2017; X. Liu et al., 2017), therefore CO does not adsorb on Ag surfaces. This again supports the speculation for CuAg catalysts that the main difference in the CO peak trend can be attributed to the presence of Ag that modifies the properties of surface active sites. Aside from the CO peak feature difference, two pairs of interesting peaks at 1436 (A) and 1608 (B)  $\text{cm}^{-1}$ , and 2717 (C) and 2814 (D)  $\text{cm}^{-1}$  were observed, which were not observed in Cu foam spectra. In the following, the origin of these bands will be further explored.

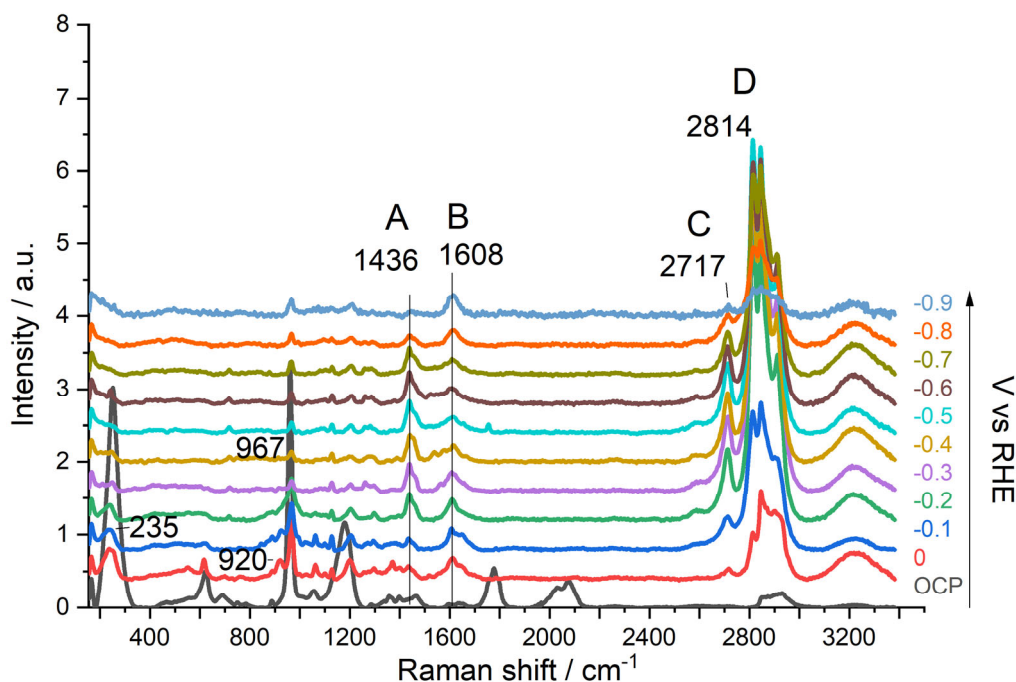


Figure 4.4. *Operando* Raman spectra of an Ag foam measured in 0.1 M KHCO<sub>3</sub> saturated with CO<sub>2</sub> pH 6.8 at various potentials. The arrow indicates the scanning direction.

## 4.2.2 CO production pathway on CuAg foams

In addition to the difference in the CO adsorption property on Cu and CuAg foams, which may help to release CO as a product in case of CuAg, the reaction steps for CO<sub>2</sub> reduction to CO may also differ on Cu and Ag surfaces. To answer this question, a long-time experiment was performed to further illustrate the surface properties of Cu, Ag and CuAg electrodes. Long-time measurements are meaningful in this case since the most frequent intermediate(s) will accumulate more than the less popular intermediates. Instead of applying each potential for 2 min on fresh catalyst, the catalyst was first reduced by scanning CV 4 times, LSV 3 times, then -0.1 V<sub>RHE</sub> was applied for 4 min, -0.2 V<sub>RHE</sub> for 6 min and -0.3 to -0.8 V<sub>RHE</sub> each for 10 min. Raman spectra were acquired every 2 min. The last spectrum of each potential was plotted in the final spectra.

The result of the long-time measurement for the Ag foam is shown in **Figure 4.5**. Like in the short time measurement in **Figure 4.4**, CO intramolecular band did not appear, and two pairs of peaks at 1436 and 1608 cm<sup>-1</sup>, and 2717 and 2814 cm<sup>-1</sup> also appeared in the long-time measurement. The other tiny peaks which appeared in **Figure 4.4** cannot be clearly distinguished. The same long-time experiment spectrum of the Cu foam is shown in Appendix **Figure 8.31**. Bands at 1436 and 1608 cm<sup>-1</sup> were not observed. In **Chapter 5**, it will be shown that in flow cell measurements on Cu, bands at 1389 and 1598 cm<sup>-1</sup> are observed instead. These bands were tentatively assigned to formate.

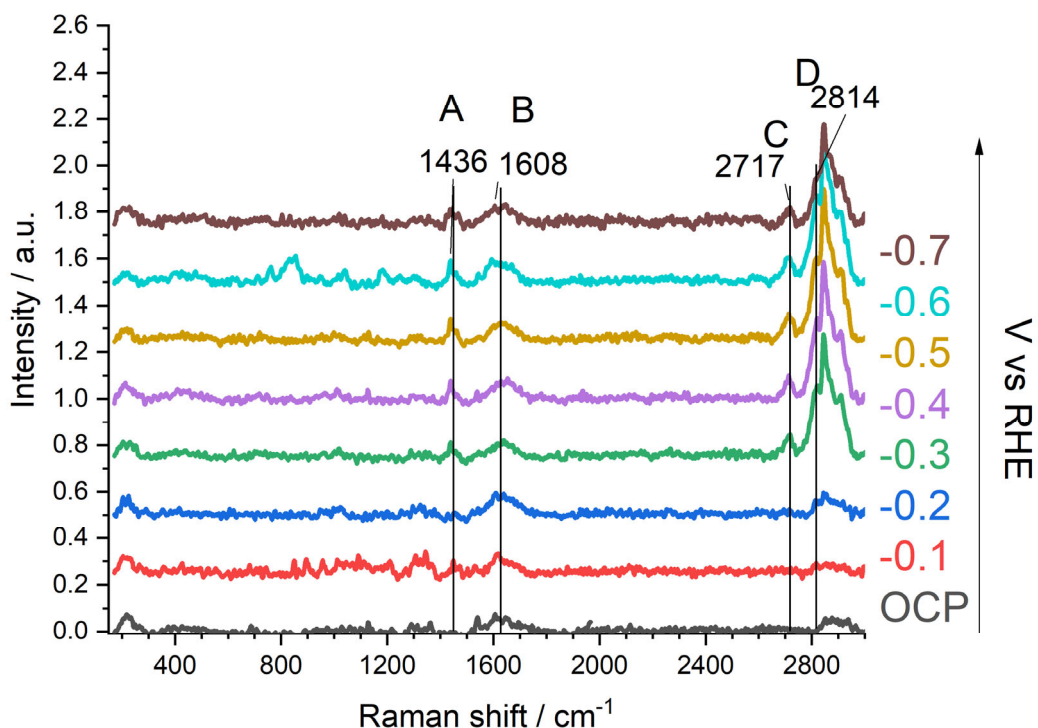


Figure 4.5. Long-time measurement of *operando* Raman spectra of an Ag foam measured in 0.1 M  $\text{KHCO}_3$  saturated with  $\text{CO}_2$  (pH 6.8) at various potentials. The arrow indicates the scanning direction.

**Figure 4.6** shows the result of a long-time measurement on a CuAg foam. The Cu-CO and CO intramolecular bands appeared at high overpotential with a lower intensity than on Cu foam. It should be noted that this is different from the short time measurement where Cu-CO bands were absent as shown in **Figure 4.2**. It could be caused by surface reconstruction during the long-time measurement. In addition, peaks at 1436, 1608, 2717 and 2814  $\text{cm}^{-1}$  also appeared besides the normal C-H band that appeared on the Cu foam surface. These two pairs of peaks suggest that Ag incorporation clearly altered the surface properties of Cu. CuAg foam apparently has both Cu and Ag features.

Nevertheless, there is the possibility that Cu and Ag form separate phases in CuAg foam. It is reported that in the dynamic catalytic reaction process, Cu and Ag tend to reconstruct while Cu atoms go towards the surface and Ag atoms sink into the bulk (Ye et al., 2020). Here, the possibility that Cu and Ag separated into two phases and “worked” individually cannot be fully excluded. Nevertheless, the product analysis showed that Cu was influenced by Ag and enhanced CO selectivity was achieved. Further structure sensitive element analysis method can be adopted to illustrate this problem.

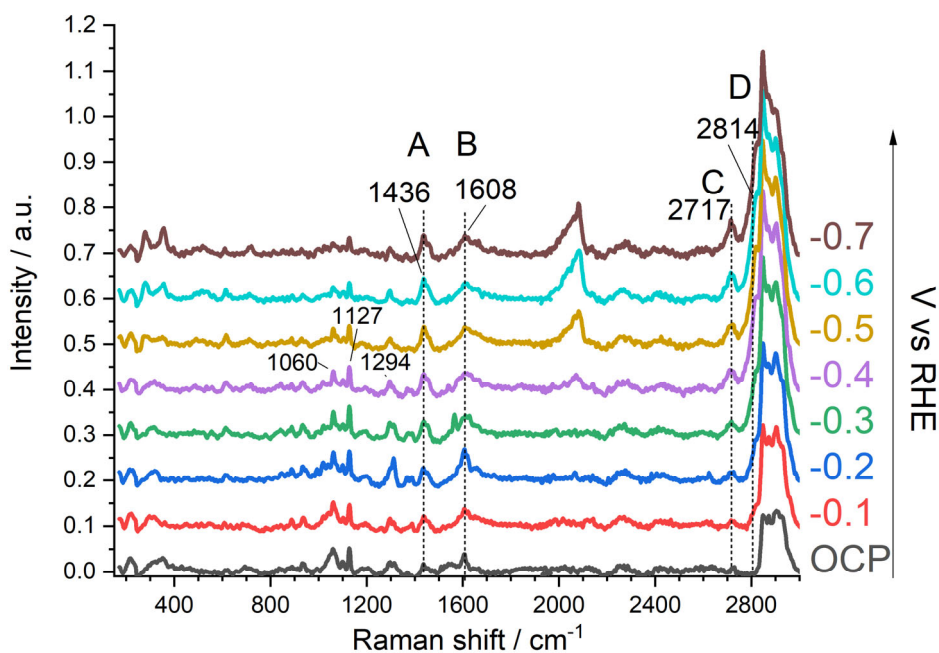


Figure 4.6. Long-time measurement of *operando* Raman spectra of a CuAg50 foam measured in 0.1 M KHCO<sub>3</sub> saturated with CO<sub>2</sub> pH 6.8 at various potentials. The arrow indicates the scanning direction.

Bohra et al. observed peaks at 1436 and 1603 cm<sup>-1</sup> on an Ag electrode in Li<sub>2</sub>B<sub>4</sub>O<sub>7</sub> electrolyte with *in-situ* Raman spectroscopy (D. Bohra et al., 2019). They assigned the peak at 1436 cm<sup>-1</sup> to bidentate adsorbed on the Ag, and 1603 cm<sup>-1</sup> to the vibration band of water. They proposed that this bidentate structure help prevent HCOO<sup>-</sup> production yet promotes CO production. However, in their study there is no isotope experiment to support this assignment. Since the water band overlaps with the C=O vibration region, it is not clear whether the 1603 cm<sup>-1</sup> band truly stems from water vibrations. Besides that, bicarbonate also has vibration bands in this region, thus, there is a possibility that the 1436 cm<sup>-1</sup> peak is from carbonate adsorption, and that at 1603 cm<sup>-1</sup> is from bidentate vibration instead. As has been discussed in **Chapter 3**, bicarbonate is interacting with the oxide in CO<sub>2</sub>RR on Cu, accordingly, it cannot be excluded that bicarbonate also actively participates in CO<sub>2</sub> reduction on Ag and CuAg catalysts. Due to the different surface properties, it is possible that carbonate adsorbs on Cu and Ag surfaces with a different geometry, therefore the bands were proposed from Cu hydroxycarbonate did not appear, but new bands from carbonate symmetrical vibration are prevalent on Ag.

In order to explore this possibility, a <sup>13</sup>C isotope experiment was performed, the result is shown in **Figure 4.7**. First thing to notice is that in 0.5 M KH<sup>13</sup>CO<sub>3</sub> electrolyte without CO<sub>2</sub> saturation, peaks (A) to (D) are still present similar to the result in **Chapter 3**. This clearly suggest that bicarbonate itself is the source for these two pairs of peaks. Comparing this data to the one taken in normal CO<sub>2</sub> saturated KHCO<sub>3</sub> solution in **Figure 4.4**, the peaks (A-D) all show no clear shift. This could be explained by the symmetrical stretching vibration of bicarbonate and bidentate structure adsorbing on Ag surface with two oxygen atoms. Indeed, in some reports about CO<sub>2</sub> photoreduction, these two structures have been observed and assigned exactly to peak (A) and (B) (Xiaodong Li et al., 2019). As it is discussed in Zhang et al.'s theoretical study,

though high energetic barrier to be produced, the bidentate intermediate is a thermodynamically stable intermediate on Ag surfaces, but CO is the primary product from the \*COOH intermediate which is kinetically the favoured pathway (X.-G. Zhang, Jin, Wu, & Tian, 2018). This means the bidentate intermediate is important in a way that block further reduction to HCOOH but promotes CO selectivity.

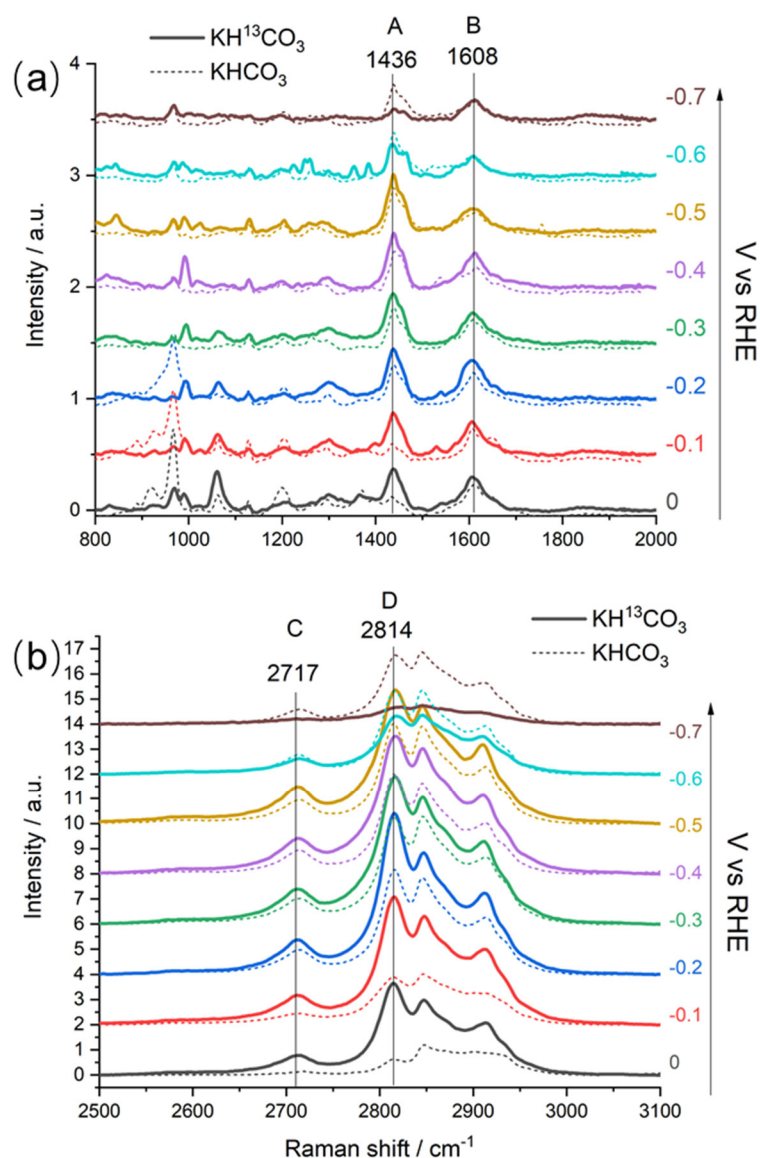


Figure 4.7. Raman spectra of an Ag foam measured in N<sub>2</sub> saturated 0.5 M KH<sup>13</sup>CO<sub>3</sub> electrolyte in comparison to the spectra of Figure 4.4: (a)range-1; (b)range-2.

Herein, the C-H peaks at 2717 and 2814 cm<sup>-1</sup> can be assigned to formate bands, given the fact that these bands are only observed in formate solution spectra as shown in **Figure 2.15**. It should be noted that in literature, these two bands in formate solution spectra are assigned to C-H vibrations, if there should be a shift when <sup>13</sup>C is labelled is unclear (Ito & Bernstein, 1956). The possibility that little amounts of formate are produced aside from CO cannot be excluded.

In summary, the high selectivity for CO on CuAg foam could be explained in the following

perspectives. The Ag component in CuAg may help release CO as the main product. Furthermore, the appearance of similar peaks that are observed on Ag foams suggests that on CuAg surfaces bicarbonate and bidentate structures also adsorb in a way that may block formate production and thereby promote CO production.

### 4.3 Conclusions

In conclusion, *operando* Raman spectroscopy was used to investigate the enhanced CO selectivity on bimetallic catalyst CuAg foams. The CO binding on CuAg shows a different trend compared to Cu foams, which gives an explanation to the low overpotential for CO production on the CuAg foam. Possible reaction intermediates are observed on Ag foam, which may help blocking the formate production, in the meantime promoting the CO production. Similar behaviour was observed for the CuAg foam, which also supports that although Ag content is less than Cu, it played a dominant role in deciding the reaction products.

### 4.4 Materials and methods

Raman spectra were collected with a Renishaw inVia Raman spectrometer coupled with a Leica microscope. Calibration was done using a silicon wafer standard ( $521\text{ cm}^{-1}$ ). A 633 nm laser (He-Ne laser, 0.95 mW power) focusing on a line ( $\sim 100\text{ }\mu\text{m}$  length) was used as an excitation source. A home-built electrochemical cell made of PTFE was interfaced with the objective for spectroscopic measurements. The desired potential was applied for 20 s before collecting the spectra to ensure steady-state conditions. The acquisition time for each spectrum was 30 s. All spectra were smoothed, and baseline corrected by Renishaw software. The baseline consisted of a polynomial function with degrees between 5 and 11, and noise tolerance level around 1.4–1.6. The degree of the polynomial function depended strongly on the amount of SERS peaks present. Normalization was done by averaging the intensity of the background curve and this averaged intensity was used to divide the background subtracted and smoothed spectra. Peak area analysis was performed by in-house software “gloFit”.

$\text{KHCO}_3$  and  $\text{KH}^{13}\text{CO}_3$  (98%  $^{13}\text{C}$ ) were purchased from Sigma Aldrich. All chemicals were used without further treatment. All buffers were prepared with MilliQ water ( $>18\text{ M}\Omega \cdot \text{cm}$ ).  $\text{N}_2$  gas (purity 99.8%) and  $\text{CO}_2$  gas (purity 99.995%) were purchased from Linde gas.

## 5. Mass transport and local pH gradient on Cu foam electrode during CO<sub>2</sub> reduction reaction

*The first part (section I) of this chapter has been published in:*

### **Reactivity determinants in electrodeposited Cu foams for electrochemical CO<sub>2</sub> reduction.**

Klingan K, Kottakkat T, Jovanov ZP, Jiang S, Pasquini C, Scholten F, Kubella P, Bergmann A, Roldan Cuenya B, Roth C, Dau H. ChemSusChem. 2018 Oct 11;11(19):3449-59.

Copyright (2018) Wiley-VCH Verlag GmbH & Co. KGaA, Weinheim.

The author contributions in the above publications has been as follows: Klingan, K prepared the samples, performed electrochemical experiments, and headed the *operando* XAS experiments; Jiang, S., Pasquini, C., and Kubella, P. contributed to the XAS experiments; Kottakkat, T. performed GC measurements for gas products; Jovanov, Z. P. performed GC measurements for liquid products; Pasquini, C. designed the electrochemical *operando* Raman cell; Jiang, S. performed all Raman measurements and analysed the Raman data; Scholten, F. and Bergmann, A. performed *in-situ* XPS measurements; Kubella, P. performed SEM measurements; Klingan, K., Cuenya, B.R., Roth, C. and Dau, H. supervised the research; Klingan, K. and Dau, H. developed the publication focus and wrote major parts of the paper; all authors participated in writing, discussion and revision of the article.

Of all results of the above study, exclusively the results obtained by Shan Jiang are presented in this chapter.

### **5.1 Introduction**

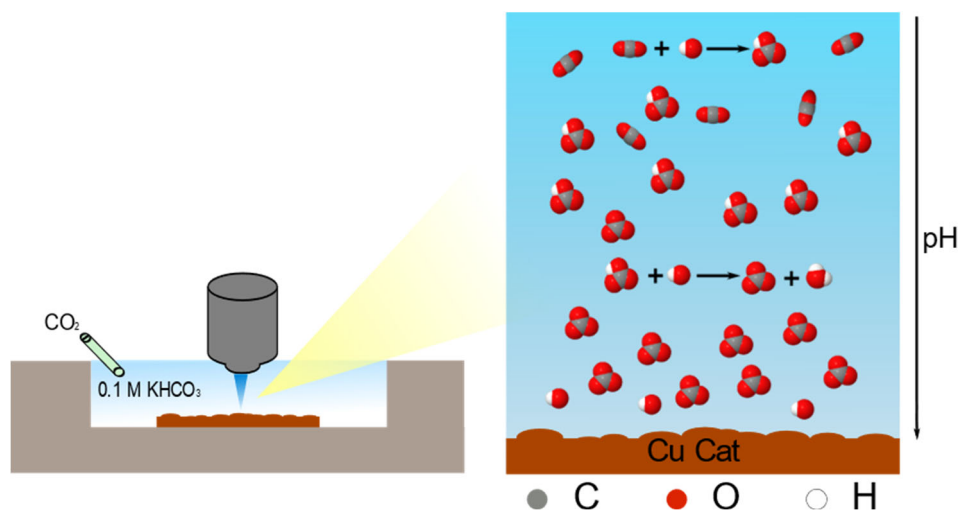
The electrochemical reduction of CO<sub>2</sub> has a broad spectrum of products (Kendra P. Kuhl et al., 2012). Products separation is costly and therefore is one obstacle for practical application. How to improve the product selectivity is thus a critical topic. To this end, the identity of ionic species and buffering strength of the electrolyte should be taken into consideration when designing a catalyst system (Aran-Ais et al., 2018; Gao et al., 2019; Marcandalli, Goyal, & Koper, 2021; Pupo & Kortlever, 2019). Specifically, the local proton concentration (i.e. pH) in the electrochemical reaction interface is an important factor that influences the electrochemical reaction (Bohra, Chaudhry, Burdyny, Pidko, & Smith, 2019; Marco Dunwell, Yan, et al., 2018; Marco Dunwell, Yang, et al., 2018; Varela, Kroschel, Reier, & Strasser, 2016). In CO<sub>2</sub>RR system, the equilibria between CO<sub>2</sub>/HCO<sub>3</sub><sup>-</sup>, HCO<sub>3</sub><sup>-</sup>/CO<sub>3</sub><sup>2-</sup> and H<sub>2</sub>CO<sub>3</sub>/HCO<sub>3</sub><sup>-</sup> always exist in bicarbonate buffer and exists once saturating the electrolyte with CO<sub>2</sub> gas when non-buffering electrolyte (e.g. KOH) or other buffer system (e.g. Kpi) is employed (here only aqueous solvent is considered). These equilibria are sensitive to pH changes. As a side reaction, hydrogen evolution reaction is unavoidable in all CO<sub>2</sub>RR processes, which consumes protons faster than

CO<sub>2</sub>RR and increases local pH. In non-buffering system and bicarbonate buffer, the elevated local pH can be compensated partially by the CO<sub>2</sub> buffering effect. However as is well known that it is a slow process due to slow hydration kinetics of the CO<sub>2</sub>-bicarbonate system: CO<sub>2</sub>(aq)+OH<sup>-</sup>↔HCO<sub>3</sub><sup>-</sup> (t<sub>1/2</sub> = 19 s at near-neutral pH) (Schulz, Riebesell, Rost, Thoms, & Zeebe, 2006). Consequently, local alkalization on the one hand causes insufficient CO<sub>2</sub> for CO<sub>2</sub>RR, while on the other hand it will help to inhibit further hydrogen evolution reactions (Divya Bohra et al., 2019; Varela et al., 2016; Anna Wuttig et al., 2016). Therefore, it is a trade off when choosing a certain buffer.

Moreover, local pH change will also affect C<sub>1</sub> and C<sub>2</sub> product selectivity. As mentioned in **Chapter 1**, on Cu(111) both CH<sub>4</sub> and C<sub>2</sub>H<sub>4</sub> formation pathway is pH dependant, whereas on Cu(100) surface C<sub>2</sub>H<sub>4</sub> can be produced with lower overpotential, and this pathway is pH independent (K. J. Schouten et al., 2012). This pH independent pathway is through the formation of CO dimer (K. J. P. Schouten et al., 2011). Based on this promising reaction mechanism, there have been many theoretical studies (Calle-Vallejo & Koper, 2013; Goodpaster et al., 2016; Montoya et al., 2015). The C<sub>2</sub>H<sub>4</sub> production overpotential is reported to be affected by the \*CO coverage which also supports the CO dimer reaction mechanism (Y. Huang et al., 2017). Since hydrogen adsorption is competing for the active site with CO, local alkalization seems to naturally promote CO dimer formation.

Hori et al. first discussed the local pH change in 1989, where they adopted various buffering capacities and tested CO<sub>2</sub>RR products (Hori et al., 1989). In concentrated KHCO<sub>3</sub> and phosphate buffer, the selectivity for CH<sub>4</sub> is promoted, whereas in diluted KHCO<sub>3</sub> buffer and non-buffering capabilities (KCl, K<sub>2</sub>SO<sub>4</sub> and KClO<sub>4</sub>), C<sub>2</sub>H<sub>4</sub> production is favoured. Gupta et al. proposed a mathematical model based on which they have thoroughly calculated the local pH during CO<sub>2</sub> electrochemical reduction in different buffer capacities at different current densities and thicknesses of diffusion layers (Gupta, Gattrell, & MacDougall, 2005). According to their results, the local pH can be up to 6 units higher than the bulk pH. Raciti et al. further used the same model to calculate the local concentration of CO<sub>2</sub> and OH<sup>-</sup> on Cu nanowire electrodes under electrochemical CO<sub>2</sub>RR (Raciti et al., 2018). They found that the diffusion layer is thicker by increasing the length of nanowire. Combined with their experimental results they successfully illustrated that a certain extent of local alkalization helps to inhibit the hydrogen evolution rate and lift the C<sub>2</sub> product selectivity at the same time. Dunwell et al. were the first who experimentally detected this local pH increase on planar Au electrodes by *in-situ* ATR-SEIRAS and correlated it to the changes of overpotential (Marco Dunwell, Yang, et al., 2018). It was proposed that operating at low current densities is necessary in order to acquire precise electrokinetic data. It is a pioneering work for future studies with *in-situ* techniques for determining local reactant concentration.





**Scheme 5.1.** Local pH determination setup and local pH gradient scheme.

Here *in-situ* Raman spectroscopy is adopted to investigate this problem on a Cu dendritic structure in 0.1 M  $\text{KHCO}_3$  electrolyte (**Scheme 5.1**). The Raman bands of carbonate and bicarbonate bands are clearly separated and therefore a clear trend can be observed. The Cu dendritic structure has never been investigated for this purpose, which is of great importance since the product distribution is quite diverse. The rough surface may cause severe mass transport limitations which might have both advantages and disadvantages. A flow cell was used to improve mass transport and to investigate the impact of the flowing electrolyte. The effect of local pH increase to  $\text{CO}_2\text{RR}$  mechanism is further discussed.

## 5.2 Results and discussion

### 5.2.1 Local pH gradient determination with *in-situ* Raman spectroscopy

As mentioned above the local pH change can be compensated by  $\text{CO}_2$  buffering effect following these equilibria:  $\text{CO}_2 + \text{H}_2\text{O} \leftrightarrow \text{H}_2\text{CO}_3$ , ( $K_1 = 2.63 \times 10^{-3}$ );  $\text{H}_2\text{CO}_3 \leftrightarrow \text{H}^+ + \text{HCO}_3^-$ , ( $K_2 = 2.5 \times 10^{-4}$ ); and  $\text{HCO}_3^- \leftrightarrow \text{H}^+ + \text{CO}_3^{2-}$ , ( $K_3 = 4.69 \times 10^{-11}$ ). Therefore, at a certain local pH the local concentrations of carbonate and bicarbonate anions are determined. This relationship gives the opportunity to use Raman spectroscopy to indirectly detect local pH by detecting the carbonate and bicarbonate concentrations which are proportional to their bands' intensities.

In order to build the relationship between pH and the Raman bands' intensities of carbonate and bicarbonate, a series of standard solutions with various pHs were prepared and measured. The lowest pH is 6.8 ( $\text{CO}_2$  saturated 0.1 M  $\text{KHCO}_3$  solution), followed by 8.8 (0.1 M  $\text{KHCO}_3$  solution), then solution pHs from 9 to 12.5 were adjusted by adding aliquots of KOH. The results are shown in **Figure 5.1**. The symmetrical C-O stretching vibration in the carbonate anion shows a peak at  $1065 \text{ cm}^{-1}$ , whereas the peaks at  $1015$  and  $1363 \text{ cm}^{-1}$  stem from C-OH stretching and symmetric C-O stretching motions in the bicarbonate anion, respectively (Davis & Oliver, 1972). As the solution pH increases from 6.8 to 11, the band ratio between bicarbonate and carbonate decreases until the pH reaches a value above 11 at which the bicarbonate band completely vanished and only the carbonate band remained. The direct relation of band intensity to pH is derived from **Figure 5.1** and plotted in **Figure 5.2**. The ratio of carbonate to bicarbonate can be calculated by the sum of two bicarbonate bands intensity dividing the

carbonate band intensity, which result in a trend with changing pH (green curve in **Figure 5.2**), this clear trend enabled us to use it as a calibration curve and estimate the local pH in CO<sub>2</sub>RR under catalytic potentials.

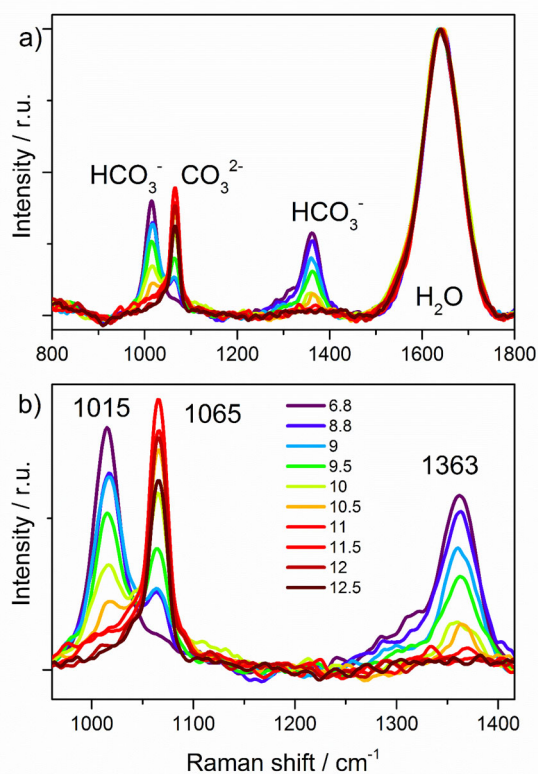


Figure 5.1. Raman spectra of 0.1 M KHCO<sub>3</sub> at different pH values. The pH was adjusted by addition of KOH. The solution was excited with a 473 nm laser. The spectra have been smoothed and normalized to the H<sub>2</sub>O peak. HCO<sub>3</sub><sup>-</sup> shows Raman peaks at 1015 and 1363 cm<sup>-1</sup>, CO<sub>3</sub><sup>2-</sup> at 1065 cm<sup>-1</sup>. Reprinted with permission from ref (Klingan et al., 2018). Copyright (2018) Wiley-VCH Verlag GmbH & Co. KGaA, Weinheim.

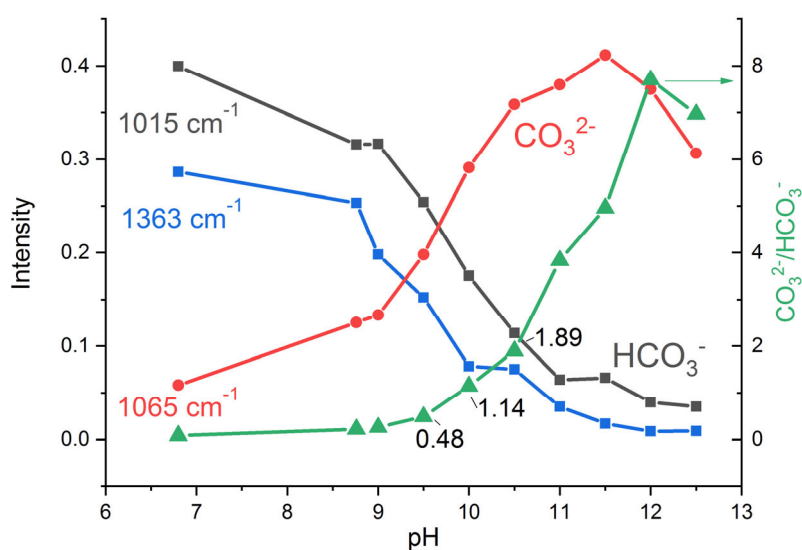


Figure 5.2. Maximum intensity trends of HCO<sub>3</sub><sup>-</sup> (1015 (grey) and 1363 (blue) cm<sup>-1</sup>) and CO<sub>3</sub><sup>2-</sup> (1065 cm<sup>-1</sup> (red)) Raman bands of 0.1 M KHCO<sub>3</sub> at different pH values.

The surface enhanced Raman scattering effect makes detecting molecules adsorbed on a metal surface possible even at extremely low concentrations. However, the peak intensity ratios may not properly reflect the real concentration ratio between the species due to the potentially different preference for being absorbed on a metal surface. In order to detect the real solution composition, the 473 nm laser was used at high power to avoid SERS when measuring *in-situ* local pH changes on the Cu foam.

In order to estimate the thickness of the diffusion layer and to depict gradual pH changes close to the surface, the pH near the surface and in the solution that is at distances away from the surface are all of interest. This was achieved with the depth scan mode of the Raman spectrometer. **Figure 5.3** shows the pictures taken under microscope of Cu foam under OCP, where the focusing point is on the surface of the Cu foam, at a distance of 20  $\mu\text{m}$  and 40  $\mu\text{m}$  above the surface. It can be seen that at a distance of 40  $\mu\text{m}$ , the microscope loses focus completely and the morphology of the Cu foam electrode is hard to recognize. This ensures that at a distance of above 40  $\mu\text{m}$  the focus point is in the solution above the surface but not on the Cu electrode surface.

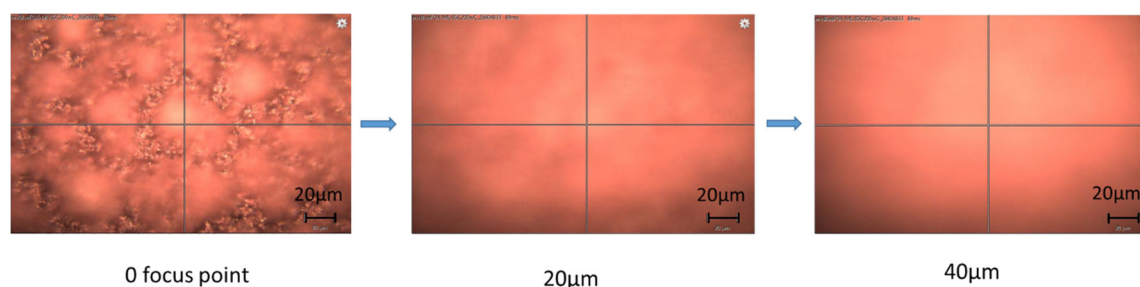


Figure 5.3. Microscopic pictures of Cu foam electrode with focusing point on the surface, at a distance of 20  $\mu\text{m}$  and 40  $\mu\text{m}$  above the surface.

Every 20  $\mu\text{m}$  a spectrum was taken until 200  $\mu\text{m}$ , for clarity reason only the spectra at a distance of 0  $\mu\text{m}$  and 200  $\mu\text{m}$  at different potentials are shown in **Figure 5.4** (rest spectra are shown in Appendix 8.20). The catalyst was reduced before starting the measurement in order to avoid any influence from oxide reduction current. Spectra under OCP was taken as a reference, it is expected that  $\text{CO}_2$  is homogeneously distributed and there is no difference between 0  $\mu\text{m}$  and 200  $\mu\text{m}$  spectra, only bicarbonate peaks at 1015 and 1356  $\text{cm}^{-1}$  present. After a potential of  $-0.6 V_{\text{RHE}}$  was applied for 3min the current reached a plateau and a series of spectra were taken. From **Figure 5.4b** it can be seen that a small carbonate peak in 0  $\mu\text{m}$  spectrum appeared, whereas there is no clear change in 200  $\mu\text{m}$  spectrum. After applying  $-0.7 V_{\text{RHE}}$ , the spectra at 0  $\mu\text{m}$  shows a much higher peak of carbonate than bicarbonate, even at 200  $\mu\text{m}$ , carbonate peak is still prominent. Consistent with a theoretical study (Raciti et al., 2018), alkalization truly exists at high overpotentials during  $\text{CO}_2\text{RR}$  on Cu surfaces; at  $-0.7 V_{\text{RHE}}$  the diffusion layer could be as thick as 200  $\mu\text{m}$ .

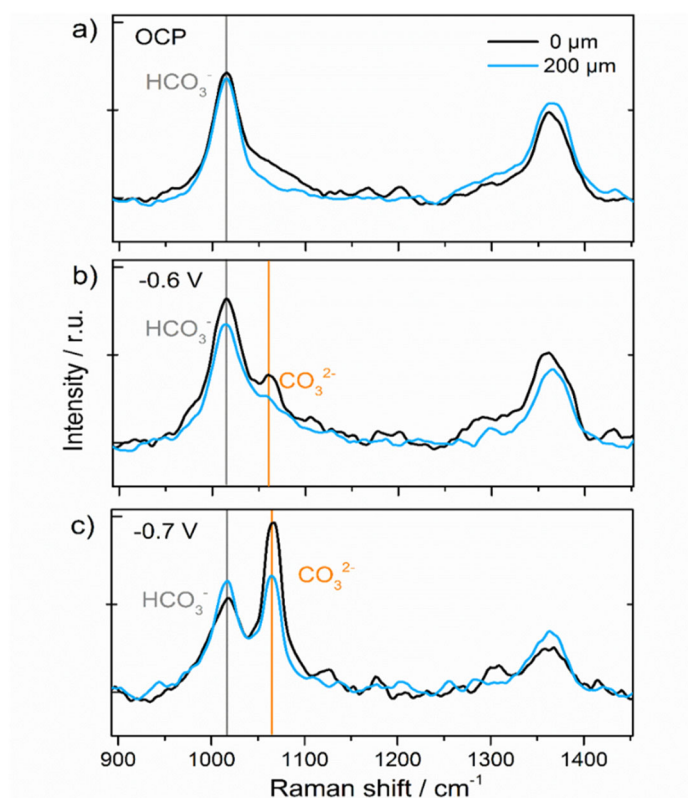


Figure 5.4. *Operando* Raman spectra of solution species at (a) OCP, (b)  $-0.6 V_{\text{RHE}}$ , and (c)  $-0.7 V_{\text{RHE}}$  in  $\text{CO}_2$  saturated  $0.1 \text{ M KHCO}_3$  (bulk pH 6.8) on Cu foam electrode surface  $0 \mu\text{m}$  (black line) and  $200 \mu\text{m}$  away from the surface (blue line). The spectra have been smoothed and normalized to the  $\text{H}_2\text{O}$  peak. Reprinted with permission from ref (Klingan et al., 2018). Copyright (2018) Wiley-VCH Verlag GmbH & Co. KGaA, Weinheim.

In order to determine the pH quantitatively, the spectra measured under reaction conditions were compared to the standard solution spectra with known pH. The results are shown in **Figure 5.5**. At  $-0.6 V_{\text{RHE}}$  the pH is about 9.0 close to the surface and about 7.8 at  $200 \mu\text{m}$  away. At  $-0.7 V_{\text{RHE}}$  this pH dramatically increases to around 10 on the surface and 9.5 at a distance of  $200 \mu\text{m}$ . This result is comparable to Gupta et al.'s result, where they calculated that within a diffusion layer of  $100 \mu\text{m}$ , at a current of  $5 \text{ mA/cm}^2$  the pH on the surface can be around 9.8 (Gupta et al., 2005). Although in the system studied here at  $-0.7 V_{\text{RHE}}$  the current is only around  $2 \text{ mA/cm}^2$ , the catalyst used here has a higher roughness factor and without stirring in the system the diffusion layer could be thicker than  $200 \mu\text{m}$  as shown above. It is thus understandable that a pH as high as 10 was detected here.

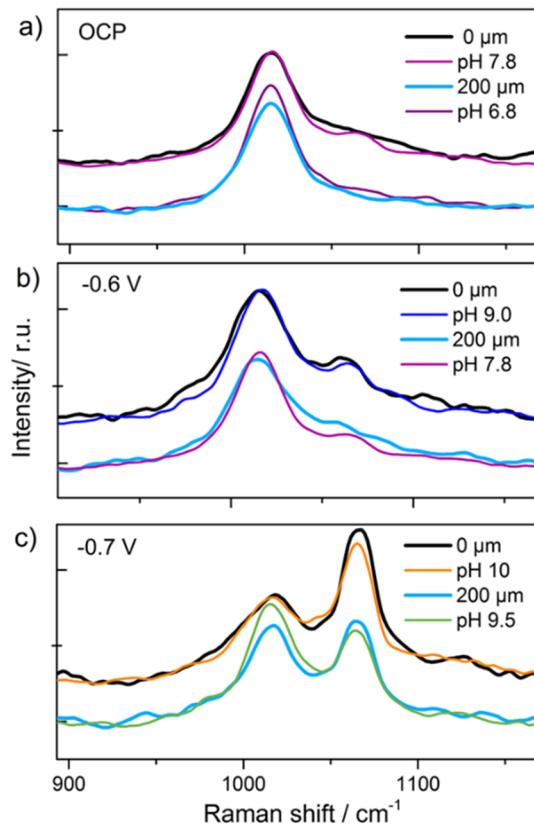


Figure 5.5. Local pH changes estimated from bicarbonate/carbonate equilibrium on Cu foam. Comparison between *operando* Raman spectra on Cu foam directly at the electrode surface (0  $\mu\text{m}$ ) and 200  $\mu\text{m}$  far away from the surface at (a) OCP, (b)  $-0.6\text{ V}_{\text{RHE}}$ , and (c)  $-0.7\text{ V}_{\text{RHE}}$  with reference spectra at different pH values (experimental data from Figure 5.1, except pH 7.8 which is the average of pH 6.8 and 8.8), showing the  $\text{HCO}_3^-$  band at  $1015\text{ cm}^{-1}$  and the  $\text{CO}_3^{2-}$  band at  $1065\text{ cm}^{-1}$ . Reprinted with permission from ref (Klingan et al., 2018). Copyright (2018) Wiley-VCH Verlag GmbH & Co. KGaA, Weinheim.

For this kind of porous structure with a high surface area, it is not trivial to determine the thickness of the interface layer. The mass transport for electrolyte species certainly is more limited compared to planar electrodes, therefore on planar electrodes local alkalization should be less prominent. To prove that, the same experiment on Cu foil was performed and the results are shown in **Figure 5.6**. At  $-0.6\text{ V}_{\text{RHE}}$  there is no big difference between 0  $\mu\text{m}$  and 200  $\mu\text{m}$ , and the estimated pH is 7.8. When the potential goes to  $-0.7\text{ V}_{\text{RHE}}$ , the pH is around 9.5 at 0  $\mu\text{m}$ , and at a distance of 200  $\mu\text{m}$ , the pH is just 8.8, which is less alkaline as in the Cu foam system. This suggests a thinner diffusion layer compared to the Cu foam electrode. On Cu foil surface, HER competes over  $\text{CO}_2\text{RR}$ ; therefore, it is understandable that also in this case local alkalization exists.

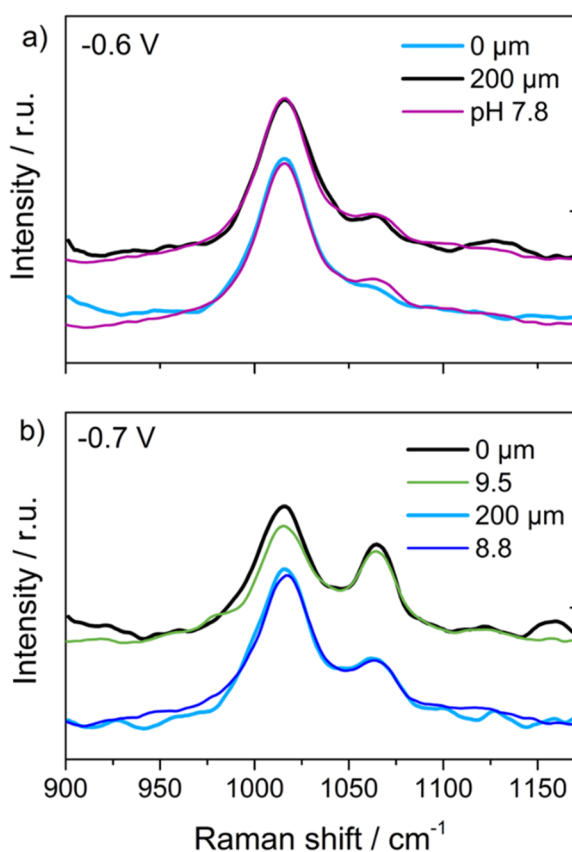


Figure 5.6. Local pH changes estimated from bicarbonate/carbonate equilibrium on Cu foil. Comparison between *operando* Raman spectra on Cu foil surface (0  $\mu\text{m}$ ) and 200  $\mu\text{m}$  far away from the surface at (a)  $-0.6 V_{\text{RHE}}$ , and (b)  $-0.7 V_{\text{RHE}}$  with reference spectra at different pH values (experimental data from Figure 5.1, except pH 7.8 which is the average of pH 6.8 and 8.8), showing the  $\text{HCO}_3^-$  band at  $1015 \text{ cm}^{-1}$  and the  $\text{CO}_3^{2-}$  band at  $1065 \text{ cm}^{-1}$ . Reprinted with permission from ref (Klingan et al., 2018). Copyright (2018) Wiley-VCH Verlag GmbH & Co. KGaA, Weinheim.

## 5.2.2 Local pH during redox potentials

Local pH change exists in various electrochemical processes, not only the catalytic reactions but also the electrodeposition process and the redox reactions of the electrode itself (Monteiro & Koper, 2021). In  $\text{CO}_2\text{RR}$  research, the local pH change due to  $\text{CO}_2\text{RR}$  has been investigated, but the local pH change during the electrode oxide reduction process is often neglected. Cu oxide has been reported to have enhanced  $\text{CO}_2\text{RR}$  activity, the main reason behind it is still unknown. The resultant grain boundaries created after oxide reduction or the remained subsurface oxygen are the two most acknowledged explanations for the enhanced activity. However, if the oxide content is high enough, the consistent oxide reduction reaction is a source for *in-situ* producing a locally alkaline environment, which may bear a huge effect for the product selectivity. In **Chapter 3**, the interaction of carbonate anions in the electrolyte with oxide during  $\text{CO}_2\text{RR}$  is investigated, a hydroxycarbonate was observed as intermediate that forms mostly under alkaline pH. The data presented here shows that the local pH is truly increased in this process.

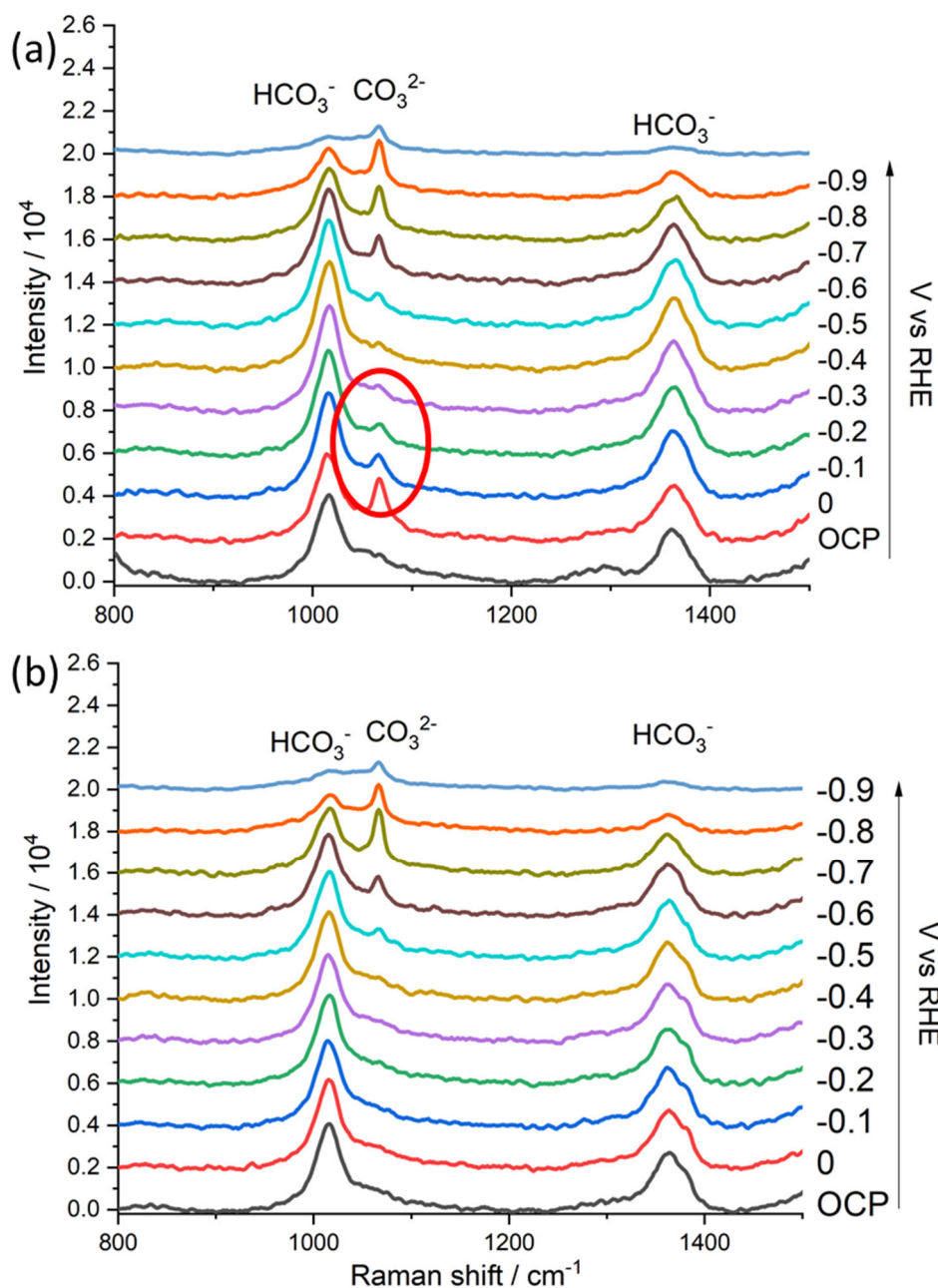


Figure 5.7. Solution spectra taken with the 473nm laser under various potentials (from 0 to -0.9  $V_{\text{RHE}}$ ). (a) The first CA series on fresh Cu foam electrode with surface oxide; (b) second CA series with the reduced catalyst directly after measuring first CA series. The data were smoothed without normalization, the low signal at high overpotential is due to severe bubble formation.

The same CA series experiments (**Chapter 3 Figure 3.1**) in CO<sub>2</sub> saturated 0.1 M KHCO<sub>3</sub> were performed again using the 473 nm laser where there is no SERS effect as it has been discussed before, therefore only solution species can be detected. Since the trend with increasing potentials on the Cu surface is examined, spectra were taken exclusively focusing on the surface (0  $\mu\text{m}$ ). Two series of measurement have been done, firstly on the Cu foam catalyst covered with surface oxide at potentials from 0 to -0.9  $V_{\text{RHE}}$ , then with this reduced catalyst a second series of potentials was applied in the same range. **Figure 5.7** shows the results. It can be seen

that when starting from oxide, at 0  $V_{\text{RHE}}$  the carbonate bands rise immediately and gradually decrease with increasing overpotentials, and again increase when  $\text{CO}_2\text{RR}$  starts at higher overpotentials as it has been discussed above. However, when starting from reduced catalyst, the spectra at low overpotentials did not show carbonate bands, only again when potentials go above  $-0.5 V_{\text{RHE}}$  carbonate bands appear. This is better illustrated in **Figure 5.8a, 8b**, where the peak intensity of carbonate and bicarbonate band read from **Figure 5.7** were plotted against potentials. It should be noted that at high overpotentials all three peaks decrease, which is due to an intensity decrease of the whole spectra caused by noisy data. Thus the real pH change is better illustrated by the total trend of the  $\text{CO}_3^{2-}/\text{HCO}_3^-$  ratio. In general, with both oxide and reduced catalyst, by increasing overpotentials, the ratio between carbonate band and bicarbonate band increase after  $-0.5 V_{\text{RHE}}$  due to an increase of local pH. Nevertheless, **Figure 5.8a** shows an additional rise at around 0 to  $-0.2 V_{\text{RHE}}$  corresponding to the reduction of oxide, which is absent in **Figure 5.8b**. This suggests the relation of local pH change to the oxide reduction process at relevant potentials. The ratio of  $\text{CO}_3^{2-}/\text{HCO}_3^-$  finally reached 1.18 at  $-0.9 V_{\text{RHE}}$  in the first CA series, which is slightly higher than the second CA series. This might be the result of accumulated local alkalization from oxide reduction.

The  $\text{CO}_2/\text{HCO}_3^-$ ,  $\text{HCO}_3^-/\text{CO}_3^{2-}$  and  $\text{H}_2\text{CO}_3/\text{HCO}_3^-$  equilibria are sensitive to pH. Therefore, under Cu oxide reducing potentials, when local pH is increased, the concentration of  $\text{CO}_2$  near the electrode surface is low;  $\text{HCO}_3^-$  and  $\text{CO}_3^{2-}$  are more prevalent than  $\text{CO}_2$ . It may also explains why carbonate rather than  $\text{CO}_2$  participates the reaction and produce CO under copper oxide reduction potentials as has been discussed in **Chapter 3**.



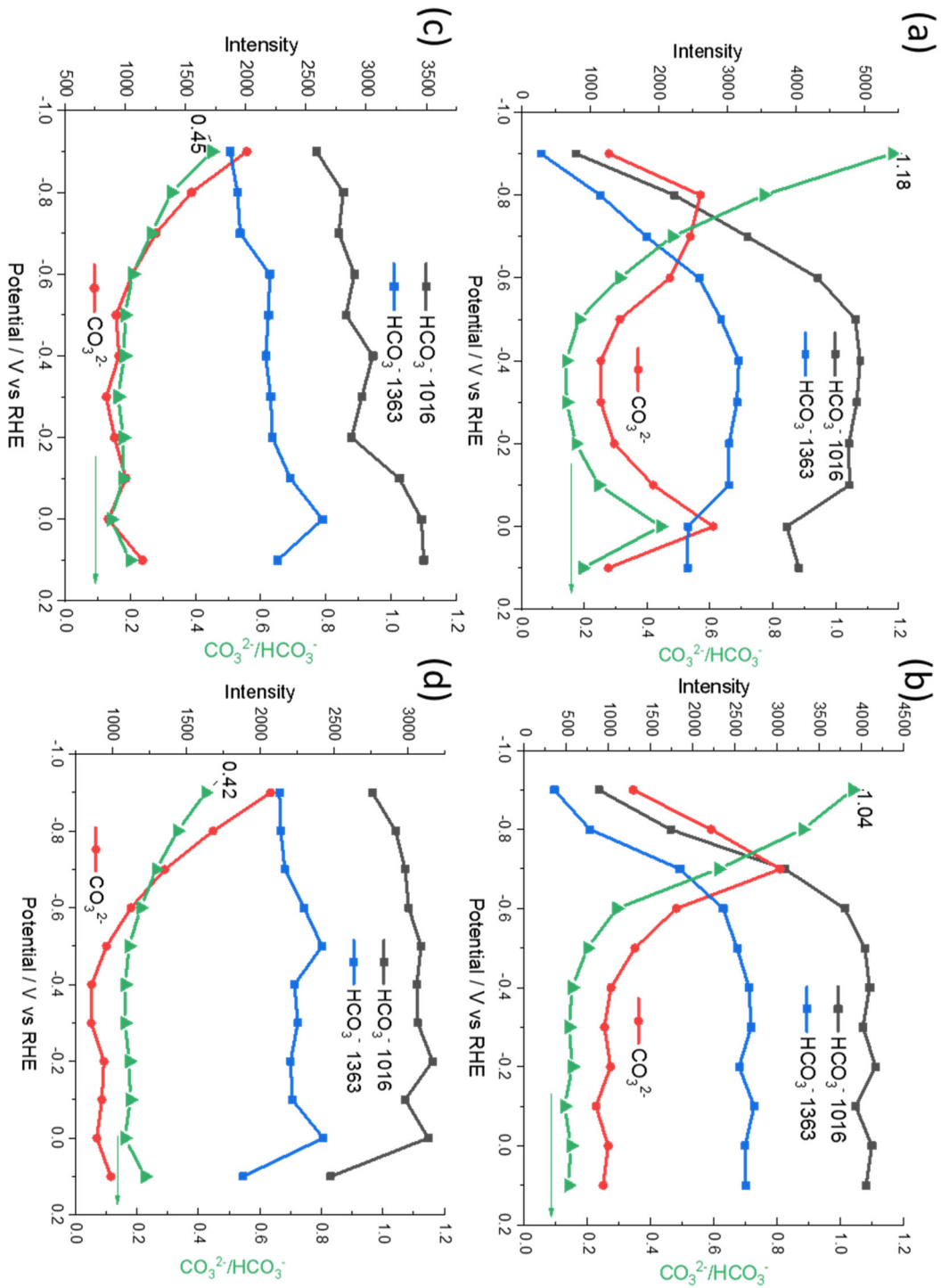


Figure 5.8. Local  $\text{HCO}_3^-/\text{CO}_3^{2-}$  concentration of CA starting from oxide and starting from reduced Cu in normal Raman cell ((a) on Cu oxide and (b) on reduced Cu) and in flow cell (flow rate 10mL/min) ((c) on oxide and (d) on reduced Cu). (0.1  $V_{\text{RHE}}$  data point denotes data measured under OCP but not at 0.1  $V_{\text{RHE}}$ ).

### 5.2.3 Local pH in flow cell

Considering the severe change of local pH and the potential influence on the product selectivity and activity of CO<sub>2</sub>RR, various strategies have been developed in order to improve the mass transport. Gas diffusion electrodes and flow cells are two effective strategies. A gas diffusion electrode is an electrode like graphite paper that allows CO<sub>2</sub> gas pass through from the backside, which assures enough CO<sub>2</sub> for the reaction and facilitates its better mixing with the electrolyte (Liu, Smith, & Burdyny, 2019; Weng, Bell, & Weber, 2018). In flow cell this is realized by flowing electrolyte, which also helps to decrease the thickness of the diffusion layer and promotes mass transport (Weekes, Salvatore, Reyes, Huang, & Berlinguette, 2018). To investigate the effect of flowing electrolyte to the local pH, a lab-made flow cell was developed.

The same experiment as for the standard Raman cell (**Figure 5.7**) was performed in flow cell to compare the local pH gradient, the spectra are shown in Appendix 8.21. In **Figure 5.8** the local concentrations of bicarbonate and carbonate were extracted (c, d) and compared to normal cell (a, b). As it has been discussed above, in the normal cell there are two periods of pH increase when starting from the oxide. When measuring in the flow cell as shown in **Figure 5.8c**, although starting from oxide, there is no pH increase at reduction potentials (0 to -0.2 V<sub>RHE</sub>), which means that the OH<sup>-</sup> produced during the oxide reduction is quickly compensated by the flow of fresh buffer. On the other hand, going through the same series of potentials on reduced catalyst, the local pH remained the same and slowly increased after -0.4 V<sub>RHE</sub> and reached maximum at -0.9 V<sub>RHE</sub> (**Figure 5.8d**). At the same potentials the currents are comparable (in flow cell the current density is a bit higher, see Appendix 8.22), however, in the flow cell the maximum value for CO<sub>3</sub><sup>2-</sup>/HCO<sub>3</sub><sup>-</sup> is around 0.45 at -0.9 V<sub>RHE</sub>, whereas in normal cell this value is reached at around -0.7 V<sub>RHE</sub>. This suggests that in flow cell the local alkalization is significantly alleviated. Specifically, according to the calibration curve in **Figure 5.2**, the pH at -0.9 V<sub>RHE</sub> is 0.5 units lower in the flow cell than in the standard cell. Nevertheless, it is necessary to note that even when flow cell is used, the local pH still increases especially at high overpotentials (above -0.6 V<sub>RHE</sub>); the local alkalization problem is alleviated but it still exists. Similarly, in two recent studies on determination of local pH in flow cell and on gas diffusion electrode, mass transport limitation was also observed and was raised to be a critical issue that cannot be neglected (Lu et al., 2020; Z. Zhang et al., 2020).

In order to illustrate the impact of local pH to reactions intermediates in a flow cell, a series of Raman spectra were taken with the 633 nm laser with a flow rate of 10 mL/min as shown in **Figure 5.9**. First thing to notice is that in flow cell data acquisition at extreme high overpotentials is enabled, the spectra are less noisy compared to the ones acquired in a normal cell. Peak at 1526 cm<sup>-1</sup> disappears already at -0.1 V<sub>RHE</sub>, after which new bands at 1391 and 1595 cm<sup>-1</sup> appear. Presumably, they are from bicarbonate vibrations or vibrational bands of formic acid products (Pan et al., 2020; S. Zhu et al., 2017). Correlating to the resolved local alkalization at oxide reducing potentials, the earlier disappearance of peak at 1526 cm<sup>-1</sup> proves that the relation of its occurrence to local high pH as discussed in **Chapter 3**.

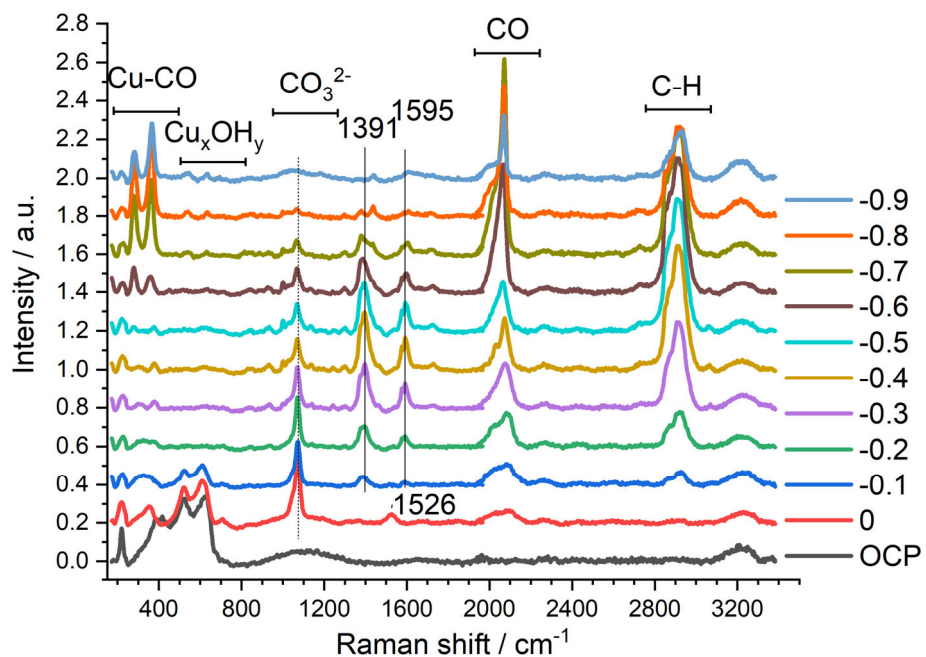


Figure 5.9. *Operando* SERS spectra measured in CO<sub>2</sub> saturated 0.1 M KHCO<sub>3</sub> (pH 6.8) in the flow cell at a flow rate of 10 mL/min. Potentials were applied from bottom to up as indicated with an arrow.

#### 5.2.4 Local pH in D<sub>2</sub>O electrolyte

Compared to H<sub>2</sub>O prepared electrolyte, in D<sub>2</sub>O prepared electrolyte the reaction rate of D<sup>+</sup> is slower, which might result in a lower HER activity (Bigeleisen & Wolfsberg, 1958; W. Zhang & Burgess, 2012). A less prominent local alkalization can be speculated. Whereas isotope effect may also cause slower reaction rate between OD<sup>-</sup> and CO<sub>2</sub>, which results in a higher local pH. CO<sub>2</sub> (aq) + OH<sup>-</sup> ↔ HCO<sub>3</sub><sup>-</sup> is a slow reaction. In water solution the reaction rate is  $t_{1/2} = 19$  s (Schulz et al., 2006). This slow buffering effect may be magnified in D<sub>2</sub>O electrolyte. It is worth to investigate whether less active HER or slower CO<sub>2</sub> buffering effect plays a more important role in determining the local pH change in CO<sub>2</sub>RR. Determining local pH in D<sub>2</sub>O electrolyte provides the opportunity to answer this question.

In D<sub>2</sub>O electrolyte, the symmetrical vibration of C, O in bicarbonate remain at the same position, whereas the C-OH band shifts from 1015 cm<sup>-1</sup> to 981 cm<sup>-1</sup> due to heavier D atom than H (see **Figure 5.10**), which is consistent to literature (Davis & Oliver, 1972). A comparison of D<sub>2</sub>O prepared KHCO<sub>3</sub> solution to normal KHCO<sub>3</sub> solution is shown in the Appendix 8.23. By adjusting the solution pH the carbonate and bicarbonate band intensities again change accordingly as shown in **Figure 5.10**. The first thing to notice is that the bicarbonate band of the symmetrical C-O bending vibration band at 1363 cm<sup>-1</sup> is equal in height to the C-OH band at 981 cm<sup>-1</sup> in D<sub>2</sub>O buffer, whereas in H<sub>2</sub>O prepared buffer the C-OH band intensity is always higher compared to the C-O band. This may be related to the heavier D atom than H, therefore C-OH vibration is weaker than C-O vibration in D<sub>2</sub>O solution. This is also magnified by the sharp carbonate band in alkaline pH solutions in D<sub>2</sub>O electrolyte, which is not observed in H<sub>2</sub>O electrolyte. It should be noted that when measuring the pH of D<sub>2</sub>O solution with normal pH

meter, there is a difference of 0.4, which should be added to the value measured (Covington, Paabo, Robinson, & Bates, 1968). However, this is not done here in **Figure 5.10**.

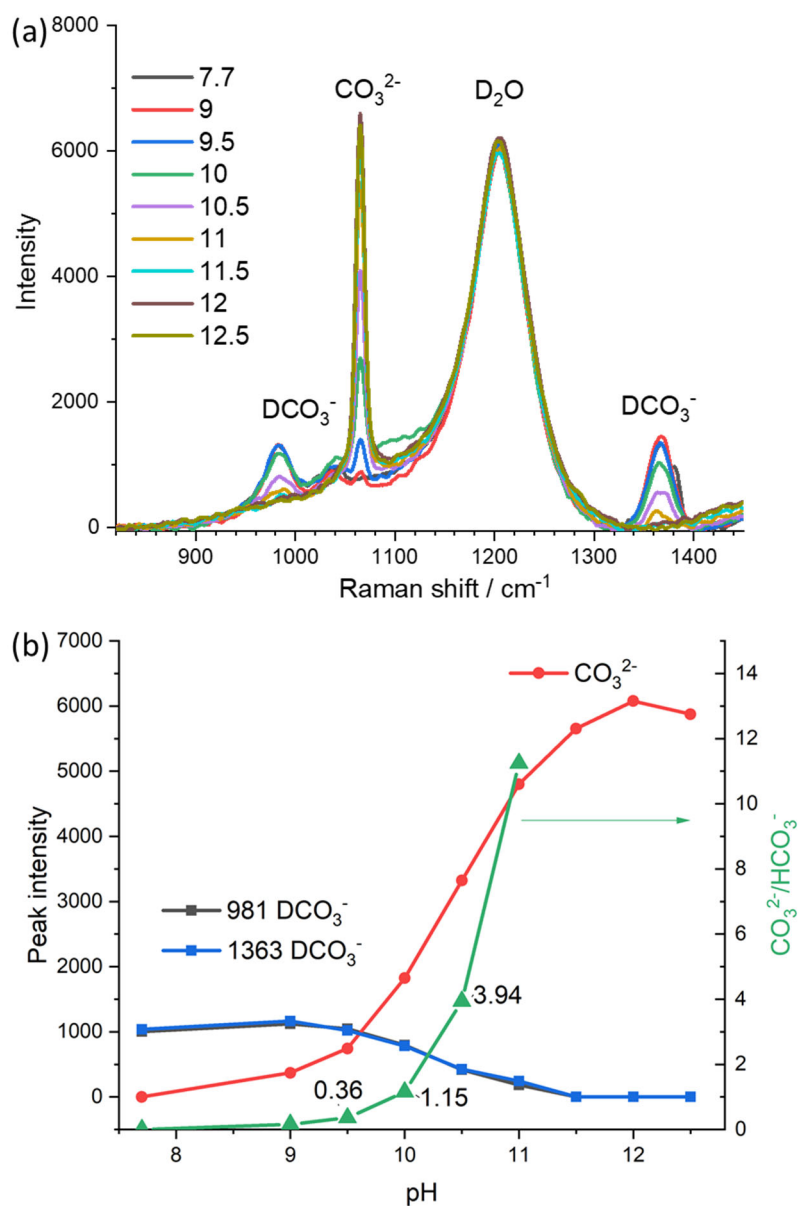


Figure 5.10. (a) Raman spectra of 0.1 M KDCO<sub>3</sub> at different pH values (read by pH meter). The pH was adjusted by addition of KOH. The solution was excited with the 473 nm laser. DCO<sub>3</sub><sup>-</sup> shows Raman peaks at 981 and 1363 cm<sup>-1</sup>, CO<sub>3</sub><sup>2-</sup> at 1065 cm<sup>-1</sup>. (b) Maximum intensity trends of DCO<sub>3</sub><sup>-</sup> (981 (black) and 1363 (blue) cm<sup>-1</sup>) and CO<sub>3</sub><sup>2-</sup> (1065 cm<sup>-1</sup> (red)) Raman bands of 0.1 M KDCO<sub>3</sub> at different pH values.

Already when no potential is applied, a difference of reaction rate of CO<sub>2</sub> in D<sub>2</sub>O electrolyte to H<sub>2</sub>O prepared electrolyte can be observed. In H<sub>2</sub>O prepared electrolyte, after saturating with CO<sub>2</sub> for 10 min, only bicarbonate bands are observed which suggests the saturation of CO<sub>2</sub> as shown in the OCP spectrum in **Figure 5.7**. However, saturating CO<sub>2</sub> to D<sub>2</sub>O prepared 0.1 M KDCO<sub>3</sub> for 10

mins is not enough to obtain a well saturated buffer, this can be seen by the low intensity of bicarbonate band as shown in **Figure 5.11** (OCP 10 mins spectrum). This is not due to slow transportation of  $\text{CO}_2$  to the surface, since there is a strong band at  $1283\text{ cm}^{-1}$  which is from  $\text{CO}_2$  gas, and in solution there is also no carbonate band (sol 10 mins spectrum). It can be explained by the slow reaction of  $\text{OD}^-$  with  $\text{CO}_2$  instead. Only after saturating longer than 30 mins, a clear band from the bicarbonate anion at  $981\text{ cm}^{-1}$  appeared and  $\text{CO}_2$  band decreased (OCP 30 mins spectrum). At least a three times slower reaction rate for  $\text{D}_2\text{O}$  reacting with  $\text{CO}_2$  is estimated.

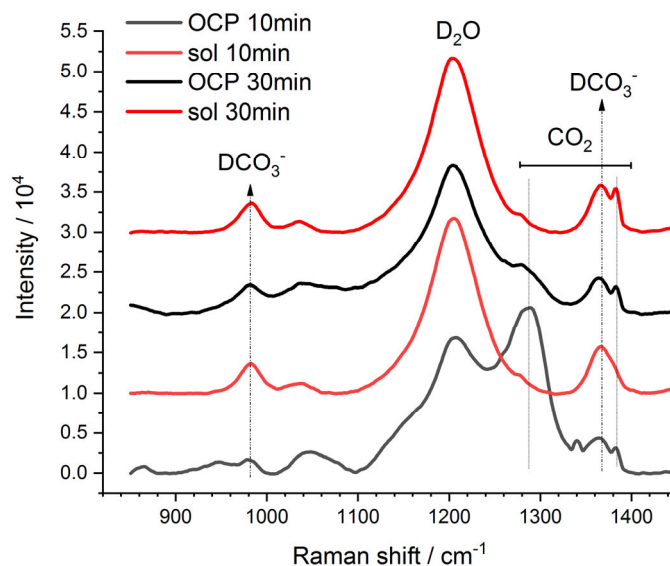


Figure 5.11. Raman spectra of Cu foam surface under OCP and solution above surface after saturating  $\text{CO}_2$  to  $\text{D}_2\text{O}$  prepared 0.1 M  $\text{KHCO}_3$  electrolyte for 10 mins and 30 mins.

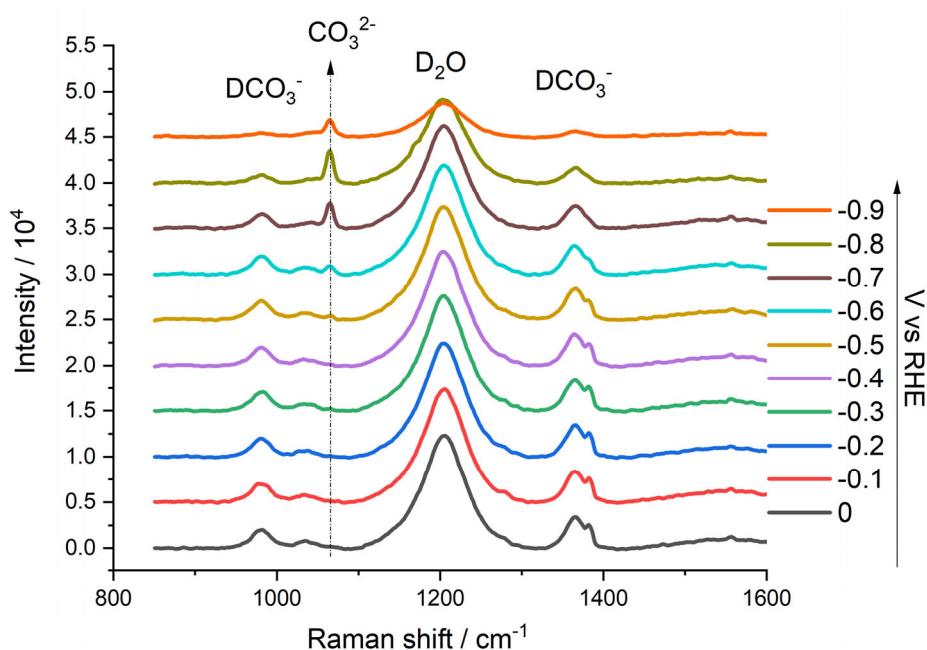


Figure 5.12. Raman spectra on reduced Cu foam surface at various potentials in  $\text{CO}_2$  saturated  $\text{D}_2\text{O}$  prepared 0.1 M  $\text{KHCO}_3$  electrolyte.

With the similar Cu catalyst reduced not in water but in D<sub>2</sub>O prepared electrolyte, the same local pH gradient measurement as in **Figure 5.7** was performed (**Figure 5.12**). After applying potentials, the appearance of a carbonate band at 1065 cm<sup>-1</sup> was observed at high overpotentials, which indicates local alkalization. The peak area trend vs potential of the same experiment measured in H<sub>2</sub>O or D<sub>2</sub>O buffer were plotted and shown in **Figure 5.13**. The current is comparable in D<sub>2</sub>O to H<sub>2</sub>O solution (Appendix 8.24), whereas the local pH is higher in D<sub>2</sub>O electrolyte. Taking the ratio of CO<sub>3</sub><sup>2-</sup>/HCO<sub>3</sub><sup>-</sup> at potential -0.9 V<sub>RHE</sub> as an example, the local pH is above 10 in D<sub>2</sub>O electrolyte (without adding 0.4 for correcting the measurement error of pH meter (Covington et al., 1968)), whereas in H<sub>2</sub>O electrolyte it is below 10 according to the calibration curve for H<sub>2</sub>O and D<sub>2</sub>O electrolyte respectively. This suggest that alkalization is more severe in D<sub>2</sub>O buffer, which further support that the slow reaction rate of buffering effect is more decisive than the activity of HER in determining the local pH. This local alkalization together with the lower HER activity in D<sub>2</sub>O electrolyte both may help increase the CO<sub>2</sub>RR activity and selectivity. Indeed, C<sub>2</sub>H<sub>4</sub> production rate is enhanced in D<sub>2</sub>O electrolyte in one the gas chromatography test (Appendix 8.25), due to the fact that C<sub>2</sub>H<sub>4</sub> production is pH independent, the higher local pH may facilitate \*CO dimer formation.

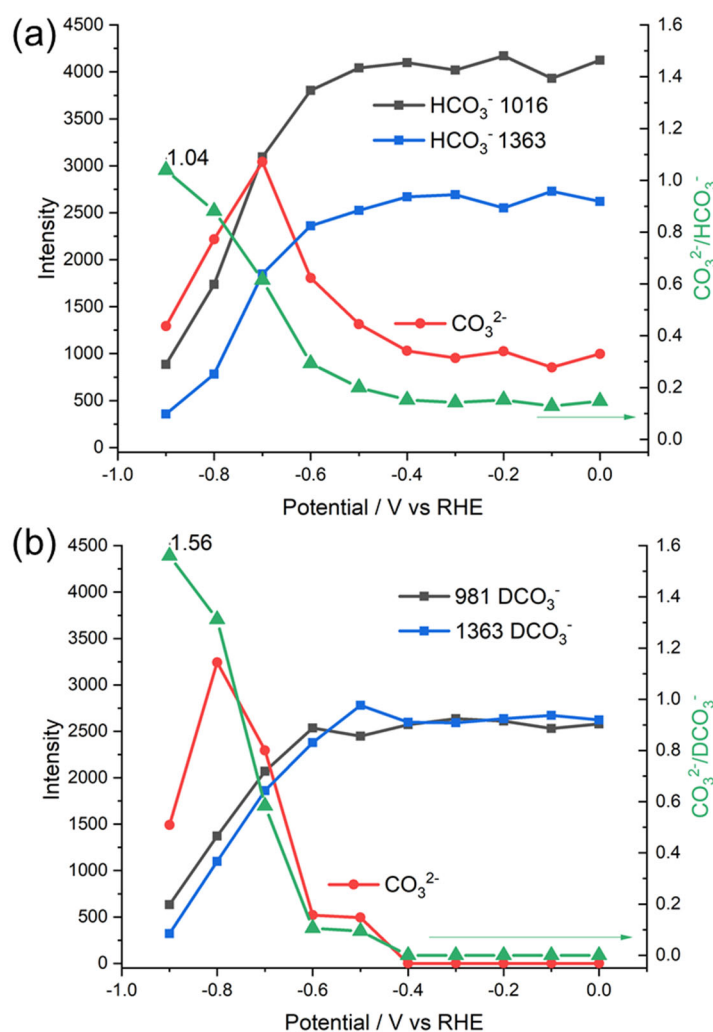


Figure 5.13. Peak intensity trend vs potential of carbonate/ bicarbonate band in H<sub>2</sub>O (a) and D<sub>2</sub>O (b) prepared electrolyte on reduced Cu foam.

## 5.2.5 Further results related to local alkalization

On the basis of the result of local pH measurements, in this section the influence of local alkalization on the CO<sub>2</sub>RR mechanism and the potential link of it to hydroxide formation and bubble formation sites is discussed.

### 5.2.5.1 Local pH alkalization for CO to C<sub>2</sub> product conversion - Time-dependence of Raman spectra

The effect of local alkalization as high as about pH 10 on the surface at high overpotential was demonstrated above. According to literature, the optimum pH for CO<sub>2</sub>RR is around 9-10 at which CO<sub>2</sub> transportation is not fully limited while HER is inhibited (Raciti et al., 2018). In addition, slightly alkaline pH can promote C<sub>2+</sub> production selectivity compared to C<sub>1</sub> products (Varela et al., 2016). Correlating these findings with the product distribution of Cu catalyst, the better selectivity for C<sub>2</sub>H<sub>4</sub> production might be explained. GC results show that Cu foam catalyst starts to give C<sub>2</sub>H<sub>4</sub> products also at about -0.7 V<sub>RHE</sub> where local alkalization starts to manifest. The influence from pH cannot be neglected. The appearance of certain intermediates that is considered as potential-dependent may be pH-dependent instead.

Time-dependent spectra collected over the course of about 20 mins (spectra were taken every 120 s) at a constant potential of -0.5 and -0.7 V<sub>RHE</sub> exhibit clear differences (**Figure 5.14**). At -0.5 V<sub>RHE</sub>, no products can be detected via GC. However, Raman spectroscopy resolves adsorbed surface species, specifically CO (2060-2080 cm<sup>-1</sup>) and -CH<sub>x</sub> species (2800-3000 cm<sup>-1</sup>). At -0.5 V<sub>RHE</sub>, a major fraction of adsorbed species is seen already for data collection starting after 20 s, followed by a slow gradual increase with time.

After switching potential to -0.7 V<sub>RHE</sub>, the CO band changed to a sharp band at 2080 cm<sup>-1</sup> consistent to the trend reported in **Chapter 2**, this variation may be caused by the surface reconstruction of Cu due to the CO adsorption or can be due to the pH increase which may modify the CO adsorption mode. At -0.7 V<sub>RHE</sub> the intensities of the CO and -CH<sub>x</sub> bands are constant over the elapsed time. Thus, it can be speculated that at least regarding the CO bands, no further accumulation of adsorbed CO (\*CO) after applying -0.7 V<sub>RHE</sub> is detectable. This may suggest that all the accessible CO adsorption sites are occupied, so that complete (saturating) \*CO coverage is reached after switching potential to -0.7 V<sub>RHE</sub> for 20 s.

In ref (Klingan et al., 2018), it was estimated from electrochemical data that a very high, presumably saturating level of \*CO is conceivable. Comparison of the \*CO peak at 2040/2080 cm<sup>-1</sup> at -0.5 V<sub>RHE</sub> and -0.7 V<sub>RHE</sub> indeed favors the saturated \*CO adsorption. It is a possible consequence of saturated \*CO coverage that the externally detectable rate of formation of gaseous CO could be limited by the \*CO desorption rate. At present, a putative rate limitation caused by saturated \*CO adsorption and slow \*CO desorption is at the level of a working hypothesis. This hypothesis does not yet involve the additional complexity by different \*CO adsorption sites (discussed in **Chapter 2**) or \*CO desorption rates that are potential-dependent or pH-dependent (A. Wuttig et al., 2016).

Kimura et al. proposed that OH species on Cu surfaces promote CO adsorption (Kimura et al., 2020). CO bands at 2020 and 2060 cm<sup>-1</sup> were observed with ATR-SEIRAS. According to their calculation, the peak at 2020 cm<sup>-1</sup> relates to a CO adsorption mode that is surrounded by surface OH<sub>ads</sub> species. This adsorption mode of CO gets reduced to C<sub>2</sub> products readily. The 2020 cm<sup>-1</sup>

peak was not observed *via* pH increase in the experiments here, the peak at 2080  $\text{cm}^{-1}$  appeared at high potential instead. This discrepancy might result from different experiment protocol and different catalyst morphology or due to the difference between Raman active or IR active bands. It is worth to explore whether the local pH plays a role for Cu surface reconstruction and CO adsorption geometry.

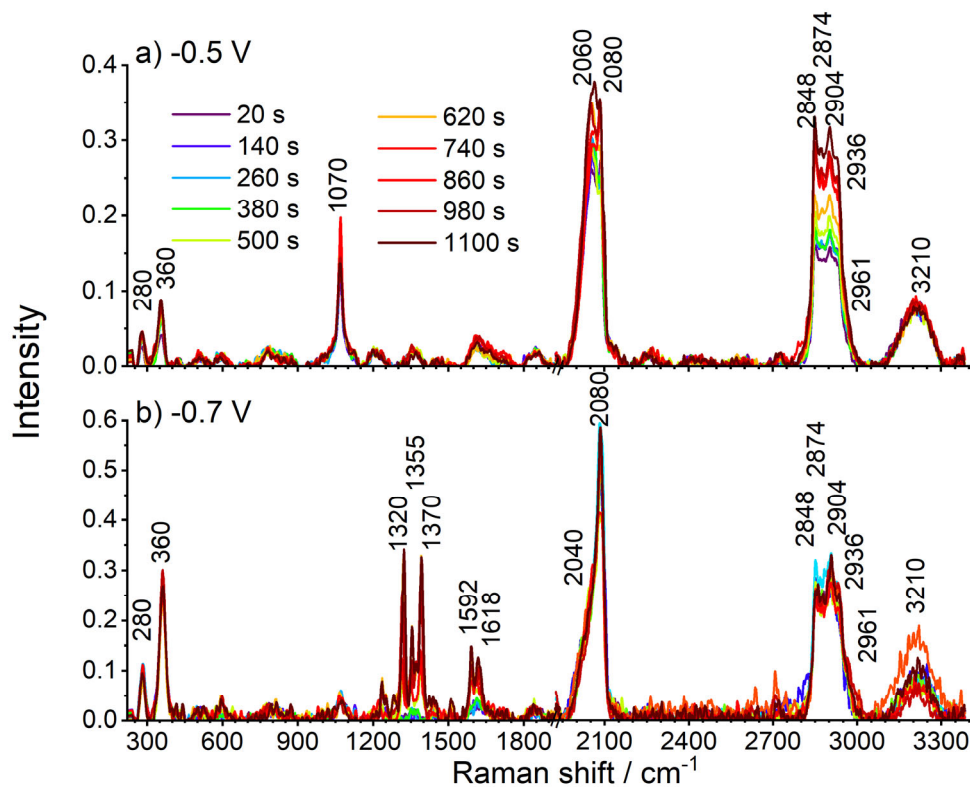


Figure 5.14. *Operando* Raman spectra of Cu foam in  $\text{CO}_2$  saturated carbonate buffer (0.1 M  $\text{KHCO}_3$  pH 6.8) at a)  $-0.5 V_{\text{RHE}}$  and b)  $-0.7 V_{\text{RHE}}$  over the course of 20 min. Spectra were collected every 2 min. All spectra are background subtracted and normalized. The noise level increases with increasing potential due to fierce gas evolution. The time indicated in the legend refers to the starting time of the Raman data collection period. Reprinted with permission from ref (Jiang, Klingan, Pasquini, & Dau, 2019), copyright (2019) AIP Publishing.



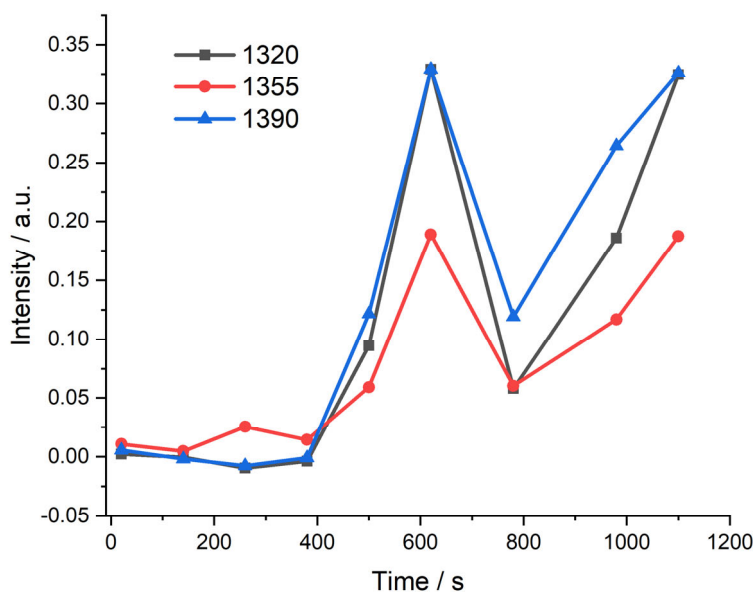


Figure 5.15. Time dependence for peak intensity of 1320, 1355 and 1390  $\text{cm}^{-1}$  bands.

Additional bands at 1320, 1355, and 1390  $\text{cm}^{-1}$  are detected at all times  $\geq 500$  s at  $-0.7 V_{\text{RHE}}$ . All bands in between 1310 and 1630  $\text{cm}^{-1}$  exhibit the same time dependency (**Figure 5.15**). It should be noted that at this high potential, bubbles formation sometimes blocks the view therefore the downward trend between 600 to 800s was due to the removal of bubbles. As observed in spectra taken using the flow cell (**Figure 5.9**), these bands also appeared. Likely, these bands belong to a common reaction intermediate with a carboxyl ( $^*\text{COOH}$ ) and bidentate  $\text{COO}^-$  species, similar to suggestions in ref (S. Zhu et al., 2017). A relation of the bands at 1355  $\text{cm}^{-1}$  and 1370  $\text{cm}^{-1}$  to the carbon dioxide dimer radical described in ref (Sheng et al., 2018) is also conceivable, where bands at similar wavenumbers were detected by FTIR spectroscopy (at 1358 and 1368  $\text{cm}^{-1}$ , but not at 1320  $\text{cm}^{-1}$ ). The observed wavenumbers are common for a carboxylate group ( $-\text{CO}_2^-$  with asymmetric stretch vibration at 1695-1540  $\text{cm}^{-1}$  and symmetric stretch vibration at 1440-1335  $\text{cm}^{-1}$ ) (Suh & Kim, 1998), which may stem, e.g, from adsorbed formate or acetate. To explain the slow formation of these bands, there are two alternative options: (i) The formation rate of this product is exceedingly slow so that detectable amounts are accumulated only after about 10 minutes of  $\text{CO}_2\text{RR}$ ; or (ii) a slow surface modification is required before a major reaction product is bound in a mode that gives rise to a SERS signal. The former option would be more likely for acetate (essentially no acetate formation detectable (Klingan et al., 2018)), the latter more likely for formate (significant formate formation (Klingan et al., 2018)).

### 5.2.5.2 Bubble formation

It is widely investigated that active sites for  $\text{CO}_2\text{RR}$  are morphology specific (Hemma Mistry et al., 2016). The rougher the catalyst the better activity. This relation may be explained by the specific facet exposed in rough catalyst or simply due to severe local pH change caused by the rough structure. In order to signify the effect of the morphology to activity, video microscopy was used to detect the bubble formation location on Cu foam catalyst. This enabled us to observe the potentially active sites for the first time.

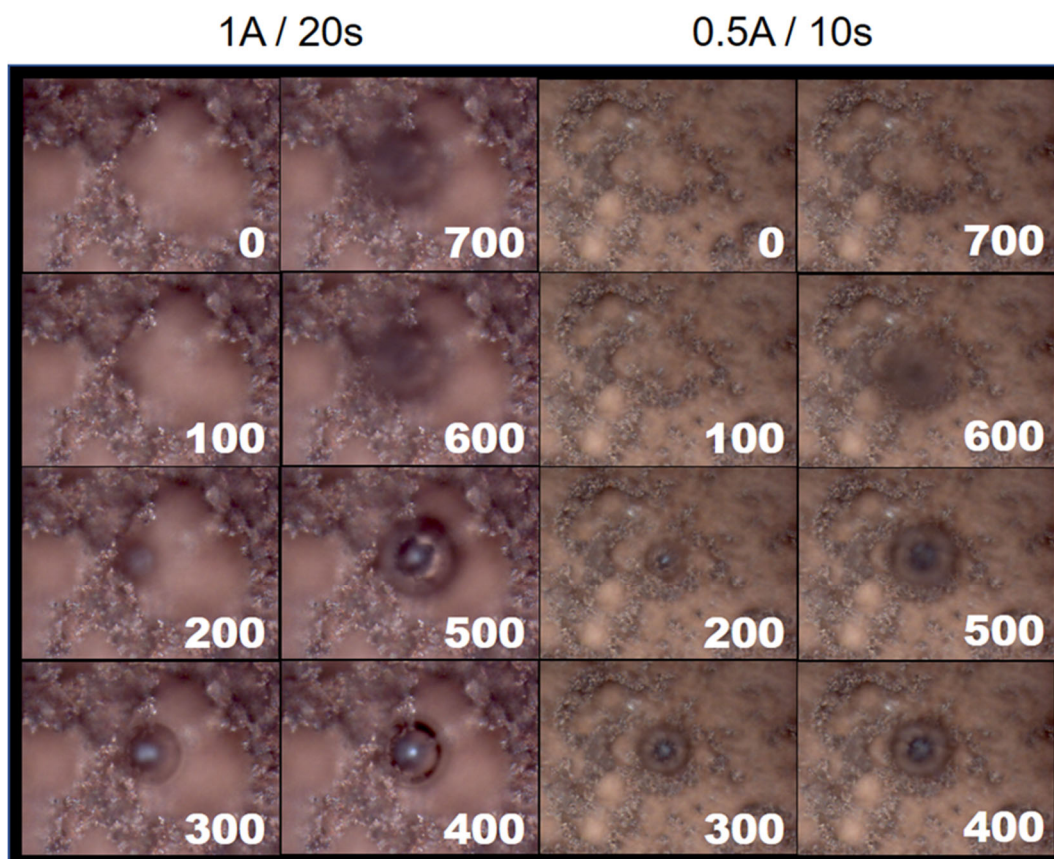


Figure 5.16. Time-dependent bubble formation (0 - 700 s, pictures are taken from the video every 100 s) under  $-0.6 V_{\text{RHE}}$  ( $1.56 \text{ mA/cm}^2$ ) on Cu foam (1 A, 20 s) and  $-0.8 V_{\text{RHE}}$  ( $-3.2 \text{ mA/cm}^2$ ) on Cu foam (0.5 A, 10 s).

Under the microscope the porous structure is well discernible, here two sample thicknesses (1 A, 20 s and 0.5 A, 10 s) are chosen for comparison. As shown in **Chapter 2**, the porous structures are less distributed in thinner catalysts than in thicker catalysts, though the product distributions are similar (Klingan et al., 2018). At a potential of  $-0.6 V_{\text{RHE}}$  for thicker (1 A, 20 s) or  $-0.8 V_{\text{RHE}}$  for thinner catalyst (0.5 A, 10 s) the currents are not so high ( $-1.56$  and  $-3.2 \text{ mA/cm}^2$  respectively) but enough to produce bubbles mildly. A bubble formation process is filmed, and the pictures of frames (every 100 s) are shown in **Figure 5.16**. Surprisingly, for both catalysts, the bubble seems always to arise at the corner of a pore structure, grows gradually, and finally got released from the surface. This is a preliminary result, nevertheless it suggests that the location of the active sites is morphology specific. The reason behind it remains open for further investigations.

### 5.2.5.3 (Hydro)oxide bands at high overpotentials

During  $\text{CO}_2\text{RR}$ , Cu oxide should be completely reduced given the high negative potentials applied. However, it was reported that  $\text{Cu}^+$  remains even at high overpotentials (up to  $-1 V_{\text{RHE}}$ ) and may play an important role for  $\text{C}_{2+}$  product selectivity (H. Mistry et al., 2016). Therefore, searching for evidence of oxide residues or absence has raised researchers' attention. Recently, it is reported that Cu oxide or hydroxide appeared at high overpotentials, which might be related

to the extremely high local pH (X. Chang et al., 2020).

Since the local pH will be affected by the history of potentials applied, longer time measurements will intensify local alkalization. A spectrum of Cu foam after applying  $-0.9 V_{\text{RHE}}$  for an hour is shown in the Appendix 8.26, where a peak at  $530 \text{ cm}^{-1}$  potentially from Cu (hydro)oxide band is observed. This suggests that constantly exposing Cu foam to high overpotentials where local pH remained at high pH, surface oxide can form.

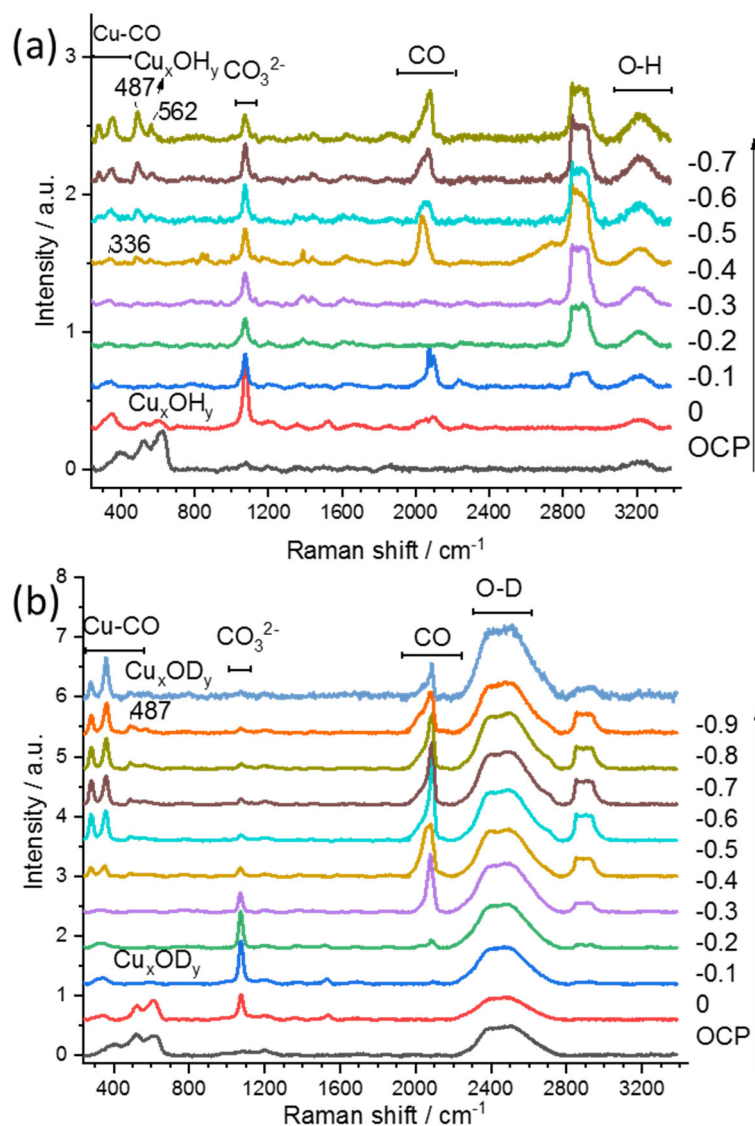


Figure 5.17. Operando SERS spectra measured in  $\text{CO}_2$  saturated (a)  $0.1 \text{ M LiHCO}_3$  (pH 6.8); (b)  $0.1 \text{ M LiDCO}_3$  at various potentials, each potential for 10 mins.

It is reported that different cations also affect  $\text{CO}_2\text{RR}$  activity, compared to  $\text{K}^+$ ,  $\text{Li}^+$  promotes HER and methane formation. This is related to the different hydration ability of different cations (Murata & Hori, 1991; Resasco et al., 2017). Therefore, in  $\text{LiHCO}_3$  electrolyte local alkalization may be severer than in  $\text{KHCO}_3$  electrolyte. However, the experiment to detect the local pH in the  $\text{LiHCO}_3$  buffer failed due to the noisiness of the data being caused by bubble formation during the harsh HER conditions. Nevertheless, two bands at  $487$  and  $562 \text{ cm}^{-1}$  were observed

when 0.1 M LiHCO<sub>3</sub> is used, which suggests a local alkalization (**Figure 5.17a**). It is worth to noticing that Cu-CO band were weak suggesting a different selectivity in LiHCO<sub>3</sub> electrolyte. By changing the buffer to D<sub>2</sub>O prepared buffer, the Cu-CO bands were enhanced as shown in **Figure 5.17b**. In the meantime, no (hydro)oxide band labeled with D<sub>2</sub>O was observed. The tiny 487 cm<sup>-1</sup> peak may be due to little amounts of H impurity.

These results provide another possible explanation for the observance of oxide even at high overpotentials in previous reports (Cavalca et al., 2017; Eilert et al., 2017). It may not be the original oxide residue, but due to the interface layer accumulated more OH<sup>-</sup> and formed Cu oxide/hydroxide *in-situ* (X. Chang et al., 2020). Moreover, it is possible that the local formed (hydr)oxide species play a role in C<sub>2+</sub> product formation by forming more CuCarHyd relating to the discussion in **Chapter 3**. Surface sensitive tools for instance XPS can be employed to further investigate this phenomenon.

### 5.3 Conclusions

In this study, the local pH was investigated with *in-situ* Raman spectroscopy in 0.1 M KHCO<sub>3</sub> buffer on Cu foam surfaces and in solution. By comparing with standard solution spectra, at high overpotentials (above -0.6 V<sub>RHE</sub>) an increase of 2-3 pH units is observed. This is quite severe local alkalization; one reason is the poor buffer of 0.1 M KHCO<sub>3</sub> used in this study. According to literature, lower concentration of bicarbonate gives better C<sub>2</sub>H<sub>4</sub> selectivity (Hori et al., 1997). In section 5.1, the Cu-CO band - the potential intermediate for C<sub>2</sub> products, only appeared at high overpotentials which might be related to the local alkalization. It is reported that the local pH change may cause the morphology change of Cu surface, which then have an impact on intermediates like CO binding to Cu surface. Increasing buffer concentrations may change the product distribution and enhance HER as well, the local pH gradient cannot be directly compared to 0.1 M KHCO<sub>3</sub>. Although it is not possible to detect the pH in Li<sup>+</sup> cation buffer, it still can be speculated that a higher pH exists than in KHCO<sub>3</sub> buffer, given the appearance of (hydro)oxide band at high overpotentials as discussed in section 5.3.

The origin of local alkalization can be the slow reaction of CO<sub>2</sub> buffering or the slow mass transportation of CO<sub>2</sub> to the electrode surface, it is never investigated in detail which factor plays the most important role. Here this question was investigated by using D<sub>2</sub>O electrolyte. In D<sub>2</sub>O electrolyte especially the slow buffering effect of CO<sub>2</sub> (aq) is more severe and might be the main reason for causing the local alkalization.

Flow cell can to some extent help alleviate this phenomenon. As an example, at -0.9 V<sub>RHE</sub> a 0.5-unit lower pH could be achieved in flow cell with a flow rate of 10 mL/min, yet local alkalization still exists. In the future, when designing a catalyst system, the unavoidable local pH change should be considered.

Flow cell and long-time measurement both enabled the observation of carboxylate bands potentially assignable to formate or acetate. The occurrence of these bands depends pronouncedly on the history of previous exposures to electric potential and electrolyte composition. This history-dependence result renders conclusions based on a single potential series problematic. Systematic in-depth studies on the conditions for observing carboxylate (or carbonyl) bands could be fruitful but are beyond the scope of the present investigation.

## 5.4 Materials and methods

Raman spectra were collected with a Renishaw inVia Raman spectrometer coupled with a Leica microscope. Calibration was done using a silicon wafer standard ( $521\text{ cm}^{-1}$ ). A water immersion objective (Leica,  $40\times$ , numerical aperture=0.8) was used to focus and collect the incident and scattered laser light during electrochemical measurements. A  $0.013\text{ mm}$  thin optically transparent Teflon film (DuPont) was used to protect the objective from alkaline solution. The spectra were obtained in the range of  $248\text{-}1869\text{ cm}^{-1}$  using a grating with  $2400\text{ lines mm}^{-1}$  and a slit size of  $20\text{ }\mu\text{m}$ . A  $473\text{ nm}$  laser (YAG laser, 100% power) focusing on a line ( $\sim 30\times 5\text{ }\mu\text{m}$ ) served as an excitation source. The exposing time is  $8\text{ s}$  for each spectrum and 10 accumulations were used. The acquisition time for a spectrum with 10 accumulations was  $80\text{ s}$ . A home-built electrochemical cell made of polytetrafluoroethylene was interfaced with the Raman microscope for spectroscopic measurements. The cell was equipped with an Ag/AgCl reference electrode and a Platinum ring counter electrode and controlled with a SP-200 Biologic potentiostat. To acquire spectra at different distances from the catalyst surface, depth scans were performed at each potential, employing the line-focus option of the inVia Raman spectrometer. The focusing point on the void structure of the catalyst surface was set as zero position. Before measurement, three CVs and one LSV were performed to reduce the surface oxides. The depth scans were performed in  $0.1\text{ M KHCO}_3$  electrolyte saturated with  $\text{CO}_2$ , and the electrolyte was continuously purged with  $\text{CO}_2$  throughout the experiment. The desired potential was applied for  $2\text{ min}$  before collecting the spectra to ensure steady-state conditions. All spectra were smoothed, and baseline corrected by Renishaw software. (Bi)carbonate bands intensity in  $\text{D}_2\text{O}$  local pH data was read after analysing by peak-o-mat.

An aqueous solution of  $0.1\text{ M KHCO}_3$  was prepared by dissolving  $\text{KHCO}_3$  ( $\geq 99.95\%$ , Sigma Aldrich) in milliQ  $\text{H}_2\text{O}$  ( $18.2\text{ M}\Omega\cdot\text{cm}$ ). The solution was saturated with  $\text{CO}_2$  for  $30\text{ min}$  and a reference spectrum was collected with  $5.6\text{ mW}$  laser power for  $30\text{ s}$  at pH  $6.8$ .  $\text{D}_2\text{O}$  is purchased from Roth,  $\text{D}_2\text{O}$  prepared reference electrolyte was saturated with  $\text{CO}_2$  for  $1\text{ hour}$  before measurement.  $\text{LiHCO}_3$  is purchased from Sigma Aldrich.  $\text{LiDCO}_3$  and  $\text{KD}_2\text{CO}_3$  electrolyte are prepared by saturating  $\text{Li}_2\text{CO}_3$  electrolyte with  $\text{CO}_2$  for more than  $1\text{ hour}$ .

Flow cell was made with polylactic acid. The electrolyte was pumped through the cell with a flow rate of  $10\text{ mL/min}$ . A Pt coated FTO glass was used as a counter electrode, and a miniature Ag/AgCl electrode is used as a reference electrode.  $\text{CO}_2$  gas was kept saturating the storage bicarbonate solution.

Bubble formation videos were acquired with a high-speed Lumenera INFINITY camera.

## 6. Summary of key results

The main findings of the studies reported in the previous chapters are listed below, organized by six topics.

### Surface-enhanced Raman spectroscopy (SERS)

- Cu(Ag) foams with high electrochemical surface area ( $>30 \text{ cm}^2$  per  $1 \text{ cm}^2$  of planar electrode surface) are both interesting catalysts of  $\text{CO}_2\text{RR}$  and excellent SERS-active substrates, bearing the advantage of facile synthesis by a simple electrodeposition protocol.
- A strong background in the SERS spectra complicates interpretation of specific SERS bands and their intensities seriously. The magnitude of the SERS backgrounds correlates with the strength of the Raman enhancement effect. The Raman enhancement effect is affected by the electric potential as well as the oxidation state of the surface. Therefore, aside from background subtraction also appropriate normalization of the Raman intensities is necessary.
- A simple procedure for normalization of the SERS spectra is proposed. As a pragmatic, first-order approach, it is assumed that the background and band intensities are proportional. Accordingly, for normalization the SERS spectra are divided by the intensity of the SERS background. This approach results in plausible potential dependencies of Raman bands, which are assignable to surface oxides and adsorbed molecular species.

### Oxide carbonate interaction

- Surface oxides and hydroxides are present on the as-synthesized Cu foam, but exclusively metallic Cu is detectable at catalytically relevant potentials. Complete reduction of Cu oxide and possibly mixed hydroxide phases are observed at about  $-0.1 \text{ V}_{\text{RHE}}$ .
- Adsorbed carbonate ions ( $\text{CO}_3^{2-}$ ) at  $1070 \text{ cm}^{-1}$  are observed with varying intensity with changing potential. On the contrary, adsorbed  $\text{HCO}_3^-$  is not detectable.
- A couple of Raman peaks at  $350$ ,  $705$  and  $1530 \text{ cm}^{-1}$  appear while the oxide bands disappear. Through different concentrations of bicarbonate solution and by applying  $^{13}\text{C}$  isotope experiments, they were found to be correlated with the bicarbonate presence in the electrolyte.
- According to the Pourbaix diagram the local pH under relevant potentials suggests that these peaks can be assigned to a Cu carbonate hydroxide intermediate due to the interaction of Cu oxide and bicarbonate. This is further proved by coupling CVs with the Raman experiment: a malachite enriched sample behaves similar in carbonate free electrolyte to the Cu foam in carbonate electrolyte. Long-time measurements on both oxide and reduced Cu surface further confirms the importance of oxide to the appearance of the Cu carbonate hydroxide intermediate and CO formation at low overpotentials.

### CO formation not starting from $\text{CO}_2$ but from carbonate ions of CuCarHyd

- It is reasonable that this Cu carbonate hydroxide intermediate facilitated the formation of CO at low overpotential. It has been shown that in carbonate-free and CO<sub>2</sub>-depleted solution, the carbonate ions present in a CuCarHyd layer can be reduced to CO and that increasing CuCarHyd amount increases the Raman signal of the produced CO. These experiments do not only support a crucial role of CuCarHyd. They also suggest that CO<sub>2</sub> reduction at the Cu foam electrodes does not start from CO<sub>2</sub>, as mostly assumed, but from carbonate ions, in line with the Raman spectra detected for <sup>13</sup>C isotope labelling of either CO<sub>2</sub> or carbonate.
- It should be noted that the here suggested CuCarHyd-facilitated CO<sub>2</sub>RR may also relate the high catalytic activity of oxide-derived Cu-based materials towards C<sub>1+n</sub>>C<sub>1</sub> products, since the copper carbonate hydroxide structure could promote the C<sub>1</sub>-C<sub>1</sub> intermediate interaction due to the high density of carbonate moieties in the structure.

### **CO adsorption on Cu and CuAg foams**

- CO adsorption can be signified as CO intramolecular bands in the high frequency range and two Cu-CO bands that appear in the low frequency range. CO intramolecular bands appeared at surprisingly low overpotential (below -0.1 V<sub>RHE</sub>) and changes its shape from a broad band (1980-2110 cm<sup>-1</sup>) to a sharp band (2080 cm<sup>-1</sup>) at high overpotentials with the appearance of two Cu-CO bands (280 cm<sup>-1</sup> and 360 cm<sup>-1</sup>). This transition may be due to the change of the adsorption geometry of CO molecules.
- Clear potential-dependent intensity trends of intramolecular \*CO and of Cu-CO bands suggest a hysteresis behavior. This hysteresis behavior and indications for saturating \*CO coverage of foam surface sites lead to the hypothesis that the \*CO desorption characteristics are a co-determinant of the formation rate of externally detectable CO.
- On bimetallic catalyst CuAg foams only CO intramolecular bands were observed in the short-time CA experiment. The intramolecular CO band reached maximum intensity before -0.3 V<sub>RHE</sub> which is much earlier compared to Cu foams. This gives an explanation to the low overpotential for CO production on the CuAg foam.
- On Ag foam and CuAg foam, a pair of bands at 1436 and 1608 cm<sup>-1</sup> are assignable to bicarbonate and a bidentate intermediate respectively. The adsorption of bidentate may help blocking the formate production, in the meantime promoting the CO production.

### **Detection of other adsorbed molecular species for CO<sub>2</sub>-reducing Cu foams.**

- A broad C-H band (2800-3000 cm<sup>-1</sup>) with minimally six resolvable sub-bands is observed. As opposed to \*CO, desorption does not readily occur at non-reducing potentials, but requires buffer exchange. By simple comparison with references spectra obtained for dissolved molecular species, a clear assignment of the adsorbed species is difficult. However, by adding these molecular species under OCP onto the Cu surface, pronounced modifications of the Raman spectra are observed for adsorbed formate and acetate, which suggests a contribution of these species to the C-H bands. Future computational studies could contribute to identification of the CH<sub>x</sub> product species.

- Bands in the region of 1300-1600  $\text{cm}^{-1}$  potentially assignable to formate are observed in both long-time experiment and flow cell measurement. The occurrence of these bands depends pronouncedly on the history of previous exposures to electric potential and electrolyte composition. This renders conclusions based on a single potential series problematic.
- For all detected  $\text{CO}_2\text{RR}$  products, the Raman bands assignable to adsorbed reaction products depend on the previously applied potential sequences. A fully reversible, hysteresis-free potential dependence is generally not observed. The complex history dependence of the adsorbed reaction products requires more attention. On the one hand, it represents a problematic complication, on the other hand, it provides opportunities.

### Local pH detection

- The local pH can be detected with Raman spectroscopy by monitoring the relative peak intensities of bicarbonate and carbonate. By measuring a series of different pH of bicarbonate standard solutions, a clear trend of increasing carbonate/bicarbonate ratio with increasing pH is observed.
- By comparing with standard solution spectra and the resulted calibration curve, at high overpotentials (above  $-0.6 V_{\text{RHE}}$ ) an increase of 2-3 pH units is observed. This is quite severe local alkalization; one reason is the insufficient buffer capacity of 0.1 M  $\text{KHCO}_3$  used in this study.
- Except for high overpotentials, under Cu oxide reducing potentials, a local alkalization was also observed. Correlating to the appearance of Cu carbonate hydroxide bands at these potentials, the Pourbaix diagram with Cu oxide and bicarbonate buffer is considered, appropriate pH and concentration of carbonate result in the formation of a Cu carbonate hydroxide phase.
- The origin of local alkalization was investigated using  $\text{D}_2\text{O}$  electrolyte. In  $\text{D}_2\text{O}$  electrolyte especially the slow buffering effect of  $\text{CO}_2$  (aq) is more severe and might be the main reason for the local alkalization.
- Flow cells can to some extent help to alleviate local alkalization. As an example, at  $-0.9 V_{\text{RHE}}$  a 0.5-unit lower pH compared to the value measured in normal cell could be achieved in a flow cell with a flow rate of 10 mL/min, yet local alkalization still exists. In the future, when designing a catalyst system, the unavoidable local pH change should always be considered.
- The severe local alkalization caused reoxidation of the Cu surface even at extremely negative potentials. Long time operation under  $-0.9 V_{\text{RHE}}$  and measurement in 0.1 M  $\text{LiHCO}_3$  electrolyte both enabled the observation of bands assignable to hydroxide.



## 7. References

- Akemann, W., & Otto, A. (1991). Vibrational Modes of CO Adsorbed on Disordered Copper Films. *Journal of Raman Spectroscopy*, 22, 797-803.
- Akemann, W., & Otto, A. (1993). The effect of atomic scale surface disorder on bonding and activation of adsorbates: vibrational properties of CO and CO, on copper. *Surface Science*, 287/288, 104-109.
- Albrecht, M. G., & Creighton, J. A. (1977). Anomalously Intense Raman Spectra of Pyridine at a Silver Electrode. *Journal of the American Chemical Society*, 99(15), 5215-5217.
- Allen, J. B., & Larry, a. R. F. (2001). Electrochemical methods fundamentals and applications. *John Wiley & Sons*.
- Arán-Ais, R. M., Scholten, F., Kunze, S., Rizo, R., & Roldan Cuenya, B. (2020). The role of in situ generated morphological motifs and Cu(i) species in C<sub>2+</sub> product selectivity during CO<sub>2</sub> pulsed electroreduction. *Nature Energy*, 5(4), 317-325.
- Aran-Ais, R. M., Gao, D., & Roldan Cuenya, B. (2018). Structure- and Electrolyte-Sensitivity in CO<sub>2</sub> Electroreduction. *Acc Chem Res*, 51(11), 2906-2917.
- Armaroli, N., & Balzani, V. (2016). Solar Electricity and Solar Fuels: Status and Perspectives in the Context of the Energy Transition. *Chem. Eur.J.*, 22, 32-57.
- Bagger, A., Ju, W., Varela, A. S., Strasser, P., & Rossmeisl, J. (2017). Electrochemical CO<sub>2</sub> Reduction: A Classification Problem. *Chemphyschem*, 18(22), 3266-3273.
- Bartholomew, R. J., & Irish, D. E. (1999). Raman spectral study of 'neat' formic acid and aqueous and organic solutions of formic acid. *Journal of Raman Spectroscopy*, 30, 325-334.
- Baruch, M. F., Pander, J. E., White, J. L., & Bocarsly, A. B. (2015). Mechanistic Insights into the Reduction of CO<sub>2</sub> on Tin Electrodes using in Situ ATR-IR Spectroscopy. *ACS Catalysis*, 5(5), 3148-3156.
- Bigeleisen, J., & Wolfsberg, M. (1958). Theoretical and experiential aspects of isotope effects in chemical kinetics. *Advance in Chemical Physics*, 1, 15-76.
- Birdja, Y. Y., Pérez-Gallent, E., Figueiredo, M. C., Göttle, A. J., Calle-Vallejo, F., & Koper, M. T. M. (2019). Advances and challenges in understanding the electrocatalytic conversion of carbon dioxide to fuels. *Nature Energy*, 4(9), 732-745.
- Bohra, D., Chaudhry, J. H., Burdyny, T., Pidko, E. A., & Smith, W. A. (2019). Modeling the electrical double layer to understand the reaction environment in a CO<sub>2</sub> electrocatalytic system. *Energy & Environmental Science*, 12(11), 3380-3389.
- Bohra, D., Ledezma-Yanez, I., Li, G., de Jong, W., Pidko, E. A., & Smith, W. A. (2019). Lateral Adsorbate Interactions Inhibit HCOO<sup>-</sup> while Promoting CO Selectivity for CO<sub>2</sub> Electrocatalysis on Silver. *Angew Chem Int Ed Engl*, 58(5), 1345-1349.
- Bushuyev, O. S., De Luna, P., Dinh, C. T., Tao, L., Saur, G., van de Lagemaat, J., . . . Sargent, E. H. (2018). What Should We Make with CO<sub>2</sub> and How Can We Make It? *Joule*, 2(5), 825-832.
- C.A. Melendres a, F. Hahn b, G.A. Bowmaker c. (2000). Oxyanion adsorption and competition at a gold electrode. *Electrochimica Acta*, 46, 9-13.
- Calle-Vallejo, F., & Koper, M. T. (2013). Theoretical considerations on the electroreduction of CO to C<sub>2</sub> species on Cu(100) electrodes. *Angew Chem Int Ed Engl*, 52(28), 7282-7285.
- Cavalca, F., Ferragut, R., Aghion, S., Eilert, A., Diaz-Morales, O., Liu, C., . . . Nilsson, A. (2017). Nature and Distribution of Stable Subsurface Oxygen in Copper Electrodes During Electrochemical

- CO<sub>2</sub> Reduction. *The Journal of Physical Chemistry C*, 121(45), 25003-25009.
- Centi, G., Quadrelli, E. A., & Perathoner, S. (2013). Catalysis for CO<sub>2</sub> conversion: a key technology for rapid introduction of renewable energy in the value chain of chemical industries. *Energy & Environmental Science*, 6(6), 1711.
- Chang, C. J., Hung, S. F., Hsu, C. S., Chen, H. C., Lin, S. C., Liao, Y. F., & Chen, H. M. (2019). Quantitatively Unraveling the Redox Shuttle of Spontaneous Oxidation/Electroreduction of CuO<sub>x</sub> on Silver Nanowires Using in Situ X-ray Absorption Spectroscopy. *ACS Cent Sci*, 5(12), 1998-2009.
- Chang, X., Zhao, Y., & Xu, B. (2020). pH Dependence of Cu Surface Speciation in the Electrochemical CO Reduction Reaction. *ACS Catalysis*, 10(23), 13737-13747.
- Chang, Y.-T., Yamaguchi, Y., Miller, W. H., & III, H. F. S. (1987). An Analysis of the Infrared and Raman Spectra of the Formic Acid Dimer (HCOOH)<sub>2</sub>. *J Am Chem Soc*, 109(24), 7245-7253.
- Chen, C., Khosrowabadi Kotyk, J. F., & Sheehan, S. W. (2018). Progress toward Commercial Application of Electrochemical Carbon Dioxide Reduction. *Chem*, 4(11), 2571-2586.
- Chen, X., Chen, J., Alghoraibi, N. M., Henckel, D. A., Zhang, R., Nwabara, U. O., . . . Gewirth, A. A. (2020). Electrochemical CO<sub>2</sub>-to-ethylene conversion on polyamine-incorporated Cu electrodes. *Nature Catalysis*, 4(1), 20-27.
- Chen, Y., & Kanan, M. W. (2012). Tin oxide dependence of the CO<sub>2</sub> reduction efficiency on tin electrodes and enhanced activity for tin/tin oxide thin-film catalysts. *J Am Chem Soc*, 134(4), 1986-1989.
- Chen, Y., Li, C. W., & Kanan, M. W. (2012). Aqueous CO<sub>2</sub> reduction at very low overpotential on oxide-derived Au nanoparticles. *J Am Chem Soc*, 134(49), 19969-19972.
- Chen, Z., Fan, T., Zhang, Y.-Q., Xiao, J., Gao, M., Duan, N., . . . Luo, J.-L. (2020). Wavy SnO<sub>2</sub> catalyzed simultaneous reinforcement of carbon dioxide adsorption and activation towards electrochemical conversion of CO<sub>2</sub> to HCOOH. *Applied Catalysis B: Environmental*, 261, 118243.
- Cheng, T., Xiao, H., & Goddard, W. A., 3rd. (2017). Full atomistic reaction mechanism with kinetics for CO reduction on Cu(100) from ab initio molecular dynamics free-energy calculations at 298 K. *Proc Natl Acad Sci U S A*, 114(8), 1795-1800.
- Chernyshova, I. V., & Ponnuram, S. (2019). Activation of CO<sub>2</sub> at the electrode-electrolyte interface by a co-adsorbed cation and an electric field. *Phys Chem Chem Phys*, 21(17), 8797-8807.
- Chernyshova, I. V., Somasundaran, P., & Ponnuram, S. (2018). On the origin of the elusive first intermediate of CO<sub>2</sub> electroreduction. *Proc Natl Acad Sci U S A*, 115(40), E9261-E9270.
- Chu, S., Cui, Y., & Liu, N. (2016). The path towards sustainable energy. *Nat Mater*, 16(1), 16-22.
- Covington, A. K., Paabo, M., Robinson, R. A., & Bates, R. G. (1968). Use of the Glass Electrode in Deuterium Oxide and the Relation between the Standardized pD (paD) Scale and the Operational pH in Heavy Water. *Analytical Chemistry*, 40(4), 700-706.
- Davis, A. R., & Oliver, B. G. (1972). A Vibrational-Spectroscopic Study of the Species Present in the CO<sub>2</sub>-H<sub>2</sub>O System. *Journal of Solution Chemistry*, 1(4), 329-339.
- De Luna, P., Hahn, C., Higgins, D., Jaffer, S. A., Jaramillo, T. F., & Sargent, E. H. (2019). What would it take for renewably powered electrosynthesis to displace petrochemical processes? *Science*, 364(6438).
- De Luna, P., Quintero-Bermudez, R., Dinh, C.-T., Ross, M. B., Bushuyev, O. S., Todorović, P., . . . Sargent, E. H. (2018). Catalyst electro-redeposition controls morphology and oxidation state for selective carbon dioxide reduction. *Nature Catalysis*, 1(2), 103-110.

- Deng, Y., Huang, Y., Ren, D., Handoko, A. D., Seh, Z. W., Hirunsit, P., & Yeo, B. S. (2018). On the Role of Sulfur for the Selective Electrochemical Reduction of CO<sub>2</sub> to Formate on CuS<sub>x</sub> Catalysts. *ACS Appl Mater Interfaces*, 10(34), 28572-28581.
- Deng, Y., & Yeo, B. S. (2017). Characterization of Electrocatalytic Water Splitting and CO<sub>2</sub> Reduction Reactions Using In Situ/Operando Raman Spectroscopy. *ACS Catalysis*, 7(11), 7873-7889.
- Detweiler, Z. M., White, J. L., Bernasek, S. L., & Bocarsly, A. B. (2014). Anodized indium metal electrodes for enhanced carbon dioxide reduction in aqueous electrolyte. *Langmuir*, 30(25), 7593-7600.
- Dieringer, J. A., McFarland, A. D., Shah, N. C., Stuart, D. A., Whitney, A. V., Yonzon, C. R., . . . Van Duyne, R. P. (2006). Surface enhanced Raman spectroscopy: new materials, concepts, characterization tools, and applications. *Faraday Discuss*, 132, 9-26.
- Dinh, C.-T., Burdyny, T., Kibria, M. G., Seifitokaldani, A., Gabardo, C. M., Arquer, F. P. G. d., . . . Sargent, E. H. (2018). CO<sub>2</sub> electroreduction to ethylene via hydroxide-mediated copper catalysis at an abrupt interface. *Science*, 360, 783-787.
- Dunwell, M., Lu, Q., Heyes, J. M., Rosen, J., Chen, J. G., Yan, Y., . . . Xu, B. (2017). The Central Role of Bicarbonate in the Electrochemical Reduction of Carbon Dioxide on Gold. *J Am Chem Soc*, 139(10), 3774-3783.
- Dunwell, M., Luc, W., Yan, Y., Jiao, F., & Xu, B. (2018). Understanding Surface-Mediated Electrochemical Reactions: CO<sub>2</sub> Reduction and Beyond. *ACS Catalysis*, 8(9), 8121-8129.
- Dunwell, M., Yan, Y., & Xu, B. (2018). Understanding the influence of the electrochemical double-layer on heterogeneous electrochemical reactions. *Current Opinion in Chemical Engineering*, 20, 151-158.
- Dunwell, M., Yang, X., Setzler, B. P., Anibal, J., Yan, Y., & Xu, B. (2018). Examination of near-electrode concentration gradients and kinetic impacts on the electrochemical reduction of CO<sub>2</sub> using surface-enhanced infrared spectroscopy. *ACS Catalysis*, 8(5), 3999-4008.
- Dutta, A., Rahaman, M., Luedi, N. C., Mohos, M., & Broekmann, P. (2016). Morphology Matters: Tuning the Product Distribution of CO<sub>2</sub> Electroreduction on Oxide-Derived Cu Foam Catalysts. *ACS Catalysis*, 6(6), 3804-3814.
- Eilert, A., Cavalca, F., Roberts, F. S., Osterwalder, J., Liu, C., Favaro, M., . . . Nilsson, A. (2017). Subsurface Oxygen in Oxide-Derived Copper Electrocatalysts for Carbon Dioxide Reduction. *J Phys Chem Lett*, 8(1), 285-290.
- Eilert, A., Roberts, F. S., Friebel, D., & Nilsson, A. (2016). Formation of Copper Catalysts for CO<sub>2</sub> Reduction with High Ethylene/Methane Product Ratio Investigated with In Situ X-ray Absorption Spectroscopy. *J Phys Chem Lett*, 7(8), 1466-1470.
- Eisenberg, R., Gray, H. B., & Crabtree, G. W. (2019). Addressing the challenge of carbon-free energy. *Proc Natl Acad Sci U S A*, 117(23), 12543-12549.
- Favaro, M., Xiao, H., Cheng, T., III, W. A. G., Yano, J., & Crumlin, E. J. (2017). Subsurface oxide plays a critical role in CO<sub>2</sub> activation by Cu(111) surfaces to form chemisorbed CO<sub>2</sub>, the first step in reduction of CO<sub>2</sub>. *Proceedings of the National Academy of Sciences*, 114(26), 6706-6711.
- Feng, X., Jiang, K., Fan, S., & Kanan, M. W. (2015). Grain-boundary-dependent CO<sub>2</sub> electroreduction activity. *J Am Chem Soc*, 137(14), 4606-4609.
- Feng, X., Jiang, K., Fan, S., & Kanan, M. W. (2016). A Direct Grain-Boundary-Activity Correlation for CO Electroreduction on Cu Nanoparticles. *ACS Cent Sci*, 2(3), 169-174.
- Ferraro, J. R., Nakamoto, K., & Brown, C. W. (2003). Introductory raman spectroscopy. *Elsevier*.

- Firet, N. J., & Smith, W. A. (2016). Probing the Reaction Mechanism of CO<sub>2</sub> Electroreduction over Ag Films via Operando Infrared Spectroscopy. *ACS Catalysis*, 7(1), 606-612.
- Fleischmann, M., Hendra, P. J., & McQuillan, A. J. (1974). Raman spectra of pyridine adsorbed at a silver electrode. *Chemical Physics Letters*, 26(2), 163-166.
- Formal, F. L., Bouree, W. S., Prevot, M. S., & Sivula, K. (2015). Challenges towards Economic Fuel Generation from Renewable Electricity: The Need for Efficient Electro-Catalysis. *Chimia (Aarau)*, 69(12), 789-798.
- Friedlingstein, P., O'Sullivan, M., Jones, M. W., Andrew, R. M., Hauck, J., Olsen, A., . . . Zaehele, S. (2020). Global Carbon Budget 2020. *Earth System Science Data*, 12(4), 3269-3340.
- Frost, R. L., Martens, W. N., Rintoul, L., Mahmutagic, E., & Klopogge, J. T. (2002). Raman spectroscopic study of azurite and malachite at 298 and 77 K. *Journal of Raman Spectroscopy*, 33(4), 252-259.
- Gao, D., Arán-Ais, R. M., Jeon, H. S., & Roldan Cuenya, B. (2019). Rational catalyst and electrolyte design for CO<sub>2</sub> electroreduction towards multicarbon products. *Nature Catalysis*, 2(3), 198-210.
- Garza, A. J., Bell, A. T., & Head-Gordon, M. (2018). Is Subsurface Oxygen Necessary for the Electrochemical Reduction of CO<sub>2</sub> on Copper? *J Phys Chem Lett*, 9(3), 601-606.
- Garza, A. J., Bell, A. T., & Head-Gordon, M. (2018). Mechanism of CO<sub>2</sub> Reduction at Copper Surfaces: Pathways to C<sub>2</sub> Products. *ACS Catalysis*, 8(2), 1490-1499.
- Gattrell, M., Gupta, N., & Co, A. (2006). A review of the aqueous electrochemical reduction of CO<sub>2</sub> to hydrocarbons at copper. *Journal of Electroanalytical Chemistry*, 594(1), 1-19.
- Ge'nin, F., Quilès, F., & Burneau, A. (2001). Infrared and Raman spectroscopic study of carboxylic acids in heavy water. *Physical Chemistry Chemical Physics*, 3(6), 932-942.
- Gediminas Niaura, A. K. G., and Vincent L. Vilker. (1997). Surface-Enhanced Raman Spectroscopy of Phosphate Anions: Adsorption on Silver, Gold, and Copper Electrodes. *J. Phys. Chem. B*, 101, 9250-9262.
- Goodpaster, J. D., Bell, A. T., & Head-Gordon, M. (2016). Identification of Possible Pathways for C-C Bond Formation during Electrochemical Reduction of CO<sub>2</sub>: New Theoretical Insights from an Improved Electrochemical Model. *J Phys Chem Lett*, 7(8), 1471-1477.
- Gunathunge, C. M., Li, X., Li, J., Hicks, R. P., Ovalle, V. J., & Waegle, M. M. (2017). Spectroscopic Observation of Reversible Surface Reconstruction of Copper Electrodes under CO<sub>2</sub> Reduction. *The Journal of Physical Chemistry C*, 121(22), 12337-12344.
- Gupta, N., Gattrell, M., & MacDougall, B. (2005). Calculation for the cathode surface concentrations in the electrochemical reduction of CO<sub>2</sub> in KHCO<sub>3</sub> solutions. *Journal of Applied Electrochemistry*, 36(2), 161-172.
- Hall, A. S., Yoon, Y., Wuttig, A., & Surendranath, Y. (2015). Mesostructure-Induced Selectivity in CO<sub>2</sub> Reduction Catalysis. *J Am Chem Soc*, 137(47), 14834-14837.
- Han, Y., Lupitsky, R., Chou, T. M., Stafford, C. M., Du, H., & Sukhishvili, S. (2011). Effect of oxidation on surface-enhanced Raman scattering activity of silver nanoparticles: a quantitative correlation. *Anal Chem*, 83(15), 5873-5880.
- Handoko, A. D., Wei, F., Jenndy, Yeo, B. S., & Seh, Z. W. (2018). Understanding heterogeneous electrocatalytic carbon dioxide reduction through operando techniques. *Nature Catalysis*, 1(12), 922-934.
- He, M., Li, C., Zhang, H., Chang, X., Chen, J. G., Goddard, W. A., 3rd, . . . Lu, Q. (2020). Oxygen induced promotion of electrochemical reduction of CO<sub>2</sub> via co-electrolysis. *Nat Commun*, 11(1),

3844.

- Heidary, N., Ly, K. H., & Kornienko, N. (2019). Probing CO<sub>2</sub> Conversion Chemistry on Nanostructured Surfaces with Operando Vibrational Spectroscopy. *Nano Lett*, *19*(8), 4817-4826.
- Henckel, D. A., Counihan, M. J., Holmes, H. E., Chen, X., Nwabara, U. O., Verma, S., . . . Gewirth, A. A. (2020). Potential Dependence of the Local pH in a CO<sub>2</sub> Reduction Electrolyzer. *ACS Catalysis*, *11*(1), 255-263.
- Heyes, J., Dunwell, M., & Xu, B. (2016). CO<sub>2</sub> Reduction on Cu at Low Overpotentials with Surface-Enhanced in Situ Spectroscopy. *The Journal of Physical Chemistry C*, *120*(31), 17334-17341.
- Hoegh-Guldberg, O., Jacob, D., Taylor, M., Guillen Bolanos, T., Bindi, M., Brown, S., . . . Zhou, G. (2019). The human imperative of stabilizing global climate change at 1.5 degrees C. *Science*, *365*(6459).
- Hollas, J. M. (2004). Modern spectroscopy. *John Wiley & Sons*.
- Hori, Y. (2008). Electrochemical CO<sub>2</sub> Reduction on Metal Electrodes. *Modern Aspects of Electrochemistry*, *42*.
- Hori, Y., Kikuchi, K., & Suzuki, S. (1985). Production of CO and CH<sub>4</sub> in electrochemical reduction of CO<sub>2</sub> at metal electrodes in aqueous hydrogencarbonate solution. *Chemistry letters*, 1695-1698.
- Hori, Y., Murata, A., & Takahashi, R. (1989). Formation of Hydrocarbons in the Electrochemical Reduction of Carbon Dioxide at a Copper Electrode in Aqueous Solution. *J. Chem. Soc.*, *85*(8), 2309-2326.
- Hori, Y., Murata, A., Takahashi, R., & Suzuki, S. (1988). Enhanced Formation of Ethylene and Alcohols at Ambient Temperature and Pressure in Electrochemical Reduction of Carbon Dioxide at a Copper Electrode. *Journal of the Chemical Society, Chemical Communications*, 17-19.
- Hori, Y., Takahashi, I., Koga, O., & Hoshi, N. (2003). Electrochemical reduction of carbon dioxide at various series of copper single crystal electrodes. *Journal of Molecular Catalysis A: Chemical*, *199*(1-2), 39-47.
- Hori, Y., Takahashi, R., Yoshinami, Y., & Murata, A. (1997). Electrochemical Reduction of CO at a Copper Electrode. *The Journal of Physical Chemistry B*, *101*(36), 7075-7081.
- Huang, J., Mensi, M., Oveisi, E., Mantella, V., & Buonsanti, R. (2019). Structural Sensitivities in Bimetallic Catalysts for Electrochemical CO<sub>2</sub> Reduction Revealed by Ag-Cu Nanodimers. *J Am Chem Soc*, *141*(6), 2490-2499.
- Huang, Y., Handoko, A. D., Hirunsit, P., & Yeo, B. S. (2017). Electrochemical Reduction of CO<sub>2</sub> Using Copper Single-Crystal Surfaces: Effects of CO\* Coverage on the Selective Formation of Ethylene. *ACS Catalysis*, *7*(3), 1749-1756.
- Hurlbut, C. S., & Klein, a. C. (1977). Manual of mineralogy (after James D. Dana). *Wiley*.
- Ichinohe, Y., Wadayama, T., & Hatta, A. (1995). Electrochemical Reduction of CO<sub>2</sub> on Silver as Probed by Surface-Enhanced Raman Scattering. *Journal of Raman Spectroscopy*, *26*, 335-340
- Iijima, G., Inomata, T., Yamaguchi, H., Ito, M., & Masuda, H. (2019). Role of a Hydroxide Layer on Cu Electrodes in Electrochemical CO<sub>2</sub> Reduction. *ACS Catalysis*, *9*(7), 6305-6319.
- Ito, K., & Bernstein, H. J. (1956). The vibrational spectra of the formate, acetate, and oxalate ions. *Canadian Journal of Chemistry*, *34*(2), 170-178.
- Jeanmarie, D. L., & Duyne, R. P. V. (1977). Part I. Heterocyclic, aromatic, and aliphatic amines adsorbed on the anodized silver electrode. *J. Electroanal. Chem*, *84*, 1-20.
- Jiang, S., Klingan, K., Pasquini, C., & Dau, H. (2019). New aspects of operando Raman spectroscopy applied to electrochemical CO<sub>2</sub> reduction on Cu foams. *The Journal of Chemical Physics*,

150(4), 041718.

- Jung, H., Lee, S. Y., Lee, C. W., Cho, M. K., Won, D. H., Kim, C., . . . Hwang, Y. J. (2019). Electrochemical Fragmentation of Cu<sub>2</sub>O Nanoparticles Enhancing Selective C-C Coupling from CO<sub>2</sub> Reduction Reaction. *J Am Chem Soc*, 141(11), 4624-4633.
- Kas, R., Yang, K., Bohra, D., Kortlever, R., Burdyny, T., & Smith, W. A. (2020). Electrochemical CO<sub>2</sub> reduction on nanostructured metal electrodes: fact or defect? *Chemical Science*, 11(7), 1738-1749.
- Kazuki Arihara, F. K., Takeo Ohsaka, Koichi Tokuda. (2001). Characterization of the adsorption state of carbonate ions at the Au(111) electrode surface using in situ IRAS. *Journal of Electroanalytical Chemistry*, 510, 128-135.
- Kimura, K. W., Casebolt, R., Cimada DaSilva, J., Kauffman, E., Kim, J., Dunbar, T. A., . . . Hanrath, T. (2020). Selective Electrochemical CO<sub>2</sub> Reduction during Pulsed Potential Stems from Dynamic Interface. *ACS Catalysis*, 10(15), 8632-8639.
- Klingan, K., Kottakkat, T., Jovanov, Z. P., Jiang, S., Pasquini, C., Scholten, F., . . . Dau, H. (2018). Reactivity Determinants in Electrodeposited Cu Foams for Electrochemical CO<sub>2</sub> Reduction. *ChemSusChem*, 11(19), 3449-3459.
- Kortlever, R., Tan, K. H., Kwon, Y., & Koper, M. T. M. (2013). Electrochemical carbon dioxide and bicarbonate reduction on copper in weakly alkaline media. *Journal of Solid State Electrochemistry*, 17(7), 1843-1849.
- Kottakkat, T., Klingan, K., Jiang, S., Jovanov, Z. P., Davies, V. H., El-Nagar, G. A. M., . . . Roth, C. (2019). Electrodeposited AgCu Foam Catalysts for Enhanced Reduction of CO<sub>2</sub> to CO. *ACS Appl Mater Interfaces*, 11(16), 14734-14744.
- Kuhl, K. P., Cave, E. R., Abram, D. N., & Jaramillo, T. F. (2012). New insights into the electrochemical reduction of carbon dioxide on metallic copper surfaces. *Energy & Environmental Science*, 5(5), 7050.
- Kuhl, K. P., Hatsukade, T., Cave, E. R., Abram, D. N., Kibsgaard, J., & Jaramillo, T. F. (2014). Electrocatalytic conversion of carbon dioxide to methane and methanol on transition metal surfaces. *J Am Chem Soc*, 136(40), 14107-14113.
- Langer, J., Jimenez de Aberasturi, D., Aizpurua, J., Alvarez-Puebla, R. A., Auguie, B., Baumberg, J. J., . . . Liz-Marzan, L. M. (2020). Present and Future of Surface-Enhanced Raman Scattering. *ACS Nano*, 14(1), 28-117.
- Lee, S. Y., Jung, H., Kim, N. K., Oh, H. S., Min, B. K., & Hwang, Y. J. (2018). Mixed Copper States in Anodized Cu Electrocatalyst for Stable and Selective Ethylene Production from CO<sub>2</sub> Reduction. *J Am Chem Soc*, 140(28), 8681-8689.
- Lewis, N. S., & Nocera, D. G. (2006). Powering the planet: chemical challenges in solar energy utilization. *Proc Natl Acad Sci U S A*, 103(43), 15729-15735.
- Li, C. W., Ciston, J., & Kanan, M. W. (2014). Electroreduction of carbon monoxide to liquid fuel on oxide-derived nanocrystalline copper. *Nature*, 508(7497), 504-507.
- Li, C. W., & Kanan, M. W. (2012). CO<sub>2</sub> reduction at low overpotential on Cu electrodes resulting from the reduction of thick Cu<sub>2</sub>O films. *J Am Chem Soc*, 134(17), 7231-7234.
- Li, F., Men, Z., Li, S., Wang, S., Li, Z., & Sun, C. (2018). Study of hydrogen bonding in ethanol-water binary solutions by Raman spectroscopy. *Spectrochim Acta A Mol Biomol Spectrosc*, 189, 621-624.
- Li, J., & Gong, J. (2020). Operando characterization techniques for electrocatalysis. *Energy &*

- Environmental Science*, 13(11), 3748-3779.
- Li, J. F., Zhang, Y. J., Ding, S. Y., Panneerselvam, R., & Tian, Z. Q. (2017). Core-Shell Nanoparticle-Enhanced Raman Spectroscopy. *Chem Rev*, 117(7), 5002-5069.
- Li, X., Sun, Y., Xu, J., Shao, Y., Wu, J., Xu, X., . . . Xie, Y. (2019). Selective visible-light-driven photocatalytic CO<sub>2</sub> reduction to CH<sub>4</sub> mediated by atomically thin CuIn<sub>5</sub>S<sub>8</sub> layers. *Nature Energy*, 4(8), 690-699.
- Li, X., Wang, S., Li, L., Sun, Y., & Xie, Y. (2020). Progress and Perspective for In Situ Studies of CO<sub>2</sub> Reduction. *J Am Chem Soc*, 142(21), 9567-9581.
- Lin, K. Q., Yi, J., Zhong, J. H., Hu, S., Liu, B. J., Liu, J. Y., . . . Ren, B. (2017). Plasmonic photoluminescence for recovering native chemical information from surface-enhanced Raman scattering. *Nat Commun*, 8, 14891.
- Liu, C., Lourenço, M. P., Hedström, S., Cavalca, F., Diaz-Morales, O., Duarte, H. A., . . . Pettersson, L. G. M. (2017). Stability and Effects of Subsurface Oxygen in Oxide-Derived Cu Catalyst for CO<sub>2</sub> Reduction. *The Journal of Physical Chemistry C*, 121(45), 25010-25017.
- Liu, K., Smith, W. A., & Burdyny, T. (2019). Introductory Guide to Assembling and Operating Gas Diffusion Electrodes for Electrochemical CO<sub>2</sub> Reduction. *ACS Energy Lett*, 4(3), 639-643.
- Liu, X., Xiao, J., Peng, H., Hong, X., Chan, K., & Norskov, J. K. (2017). Understanding trends in electrochemical carbon dioxide reduction rates. *Nat Commun*, 8, 15438.
- Lu, X., Zhu, C., Wu, Z., Xuan, J., Francisco, J. S., & Wang, H. (2020). In Situ Observation of the pH Gradient near the Gas Diffusion Electrode of CO<sub>2</sub> Reduction in Alkaline Electrolyte. *J Am Chem Soc*, 142(36), 15438-15444.
- Łukomska, A., & Sobkowski, J. (2004). Potential of zero charge of monocrystalline copper electrodes in perchlorate solutions. *Journal of Electroanalytical Chemistry*, 567(1), 95-102.
- Lum, Y., & Ager, J. W. (2018). Evidence for product-specific active sites on oxide-derived Cu catalysts for electrochemical CO<sub>2</sub> reduction. *Nature Catalysis*, 2(1), 86-93.
- Magnotti, G., Kc, U., Varghese, P. L., & Barlow, R. S. (2015). Raman spectra of methane, ethylene, ethane, dimethyl ether, formaldehyde and propane for combustion applications. *Journal of Quantitative Spectroscopy and Radiative Transfer*, 163, 80-101.
- Mahajan, S., Cole, R. M., Speed, J. D., Pelfrey, S. H., Russell, A. E., Bartlett, P. N., . . . Baumberg, J. J. (2010). Understanding the Surface-Enhanced Raman Spectroscopy “Background”. *J. Phys. Chem. C*, 114, 7242-7250.
- Malkani, A. S., Dunwell, M., & Xu, B. (2018). Operando Spectroscopic Investigations of Copper and Oxide-Derived Copper Catalysts for Electrochemical CO Reduction. *ACS Catalysis*, 9(1), 474-478.
- Mandal, L., Yang, K. R., Motapothula, M. R., Ren, D., Lobaccaro, P., Patra, A., . . . Venkatesan, T. (2018). Investigating the Role of Copper Oxide in Electrochemical CO<sub>2</sub> Reduction in Real Time. *ACS Appl Mater Interfaces*, 10(10), 8574-8584.
- Marcandalli, G., Goyal, A., & Koper, M. T. M. (2021). Electrolyte Effects on the Faradaic Efficiency of CO<sub>2</sub> Reduction to CO on a Gold Electrode. *ACS Catal*, 11, 4936-4945.
- Martín, A. J., & Pérez-Ramírez, J. (2019). Heading to Distributed Electrocatalytic Conversion of Small Abundant Molecules into Fuels, Chemicals, and Fertilizers. *Joule*, 3(11), 2602-2621.
- Mendoza, N. J., Bonales, L. J., Baonza, V. G., & Caceres, M. (2014). Local hydration pressures in methanol aqueous solution: a Raman spectroscopy analysis. *J Phys Chem B*, 118(33), 9919-9925.

- Mistry, H., Choi, Y. W., Bagger, A., Scholten, F., Bonifacio, C. S., Sinev, I., . . . Roldan Cuenya, B. (2017). Enhanced Carbon Dioxide Electroreduction to Carbon Monoxide over Defect-Rich Plasma-Activated Silver Catalysts. *Angew Chem Int Ed Engl*, *56*(38), 11394-11398.
- Mistry, H., Varela, A. S., Bonifacio, C. S., Zegkinoglou, I., Sinev, I., Choi, Y. W., . . . Cuenya, B. R. (2016). Highly selective plasma-activated copper catalysts for carbon dioxide reduction to ethylene. *Nat Commun*, *7*, 12123.
- Mistry, H., Varela, A. S., Kühl, S., Strasser, P., & Cuenya, B. R. (2016). Nanostructured electrocatalysts with tunable activity and selectivity. *Nature Reviews Materials*, *1*(4), 16009.
- Monteiro, M. C. O., & Koper, M. T. M. (2021). Measuring local pH in electrochemistry. *Current Opinion in Electrochemistry*, *25*, 100649.
- Montoya, J. H., Shi, C., Chan, K., & Norskov, J. K. (2015). Theoretical Insights into a CO Dimerization Mechanism in CO<sub>2</sub> Electroreduction. *J Phys Chem Lett*, *6*(11), 2032-2037.
- Moradzaman, M., & Mul, G. (2021). In Situ Raman Study of Potential-Dependent Surface Adsorbed Carbonate, CO, OH, and C Species on Cu Electrodes During Electrochemical Reduction of CO<sub>2</sub>. *ChemElectroChem*, *8*(8), 1478-1485.
- Murata, A., & Hori, Y. (1991). Product Selectivity Affected by Cationic Species in Electrochemical Reduction of CO<sub>2</sub> and CO at a Cu Electrode. *Bulletin of the Chemical Society of Japan*, *64*(1), 123-127.
- Nakabayashi, T., Kosugi, K., & Nishi, N. (1999). Liquid Structure of Acetic Acid Studied by Raman Spectroscopy and Ab Initio Molecular Orbital Calculations. *J. Phys. Chem. A*, *103*, 8595-8603.
- Nie, X., Esopi, M. R., Janik, M. J., & Asthagiri, A. (2013). Selectivity of CO<sub>2</sub> reduction on copper electrodes: the role of the kinetics of elementary steps. *Angew Chem Int Ed Engl*, *52*(9), 2459-2462.
- Nitopi, S., Bertheussen, E., Scott, S. B., Liu, X., Engstfeld, A. K., Horch, S., . . . Chorkendorff, I. (2019). Progress and Perspectives of Electrochemical CO<sub>2</sub> Reduction on Copper in Aqueous Electrolyte. *Chem Rev*. *119*(12), 7610-7672.
- Nocera, D. G. (2012). The Artificial Leaf. *Acc Chem Res*, *45*(5), 767-776.
- Oda, I., Ogasawara, H., & Ito, M. (1996). Carbon Monoxide Adsorption on Copper and Silver Electrodes during Carbon Dioxide Electroreduction Studied by Infrared Reflection Absorption Spectroscopy and Surface-Enhanced Raman Spectroscopy. *Langmuir*, *12*, 1094-1097.
- Olah, G. A., Prakash, G. K., & Goepfert, A. (2011). Anthropogenic chemical carbon cycle for a sustainable future. *J Am Chem Soc*, *133*(33), 12881-12898.
- Olbert-Majkut, A., Ahokas, J., Lundell, J., & Pettersson, M. (2009). Raman spectroscopy of formic acid and its dimers isolated in low temperature argon matrices. *Chemical Physics Letters*, *468*(4-6), 176-183.
- Otto, A., Billmann, J., Eickmans, J., Erturk, U., & Pettenkofer, C. (1984). The "adatom model" of SERS (Surface enhanced Raman scattering): the present status. *Surface Science*, *138*, 319-338.
- Pan, Z., Wang, K., Ye, K., Wang, Y., Su, H.-Y., Hu, B., . . . Song, S. (2020). Intermediate Adsorption States Switch to Selectively Catalyze Electrochemical CO<sub>2</sub> Reduction. *ACS Catalysis*, *10*(6), 3871-3880.
- Pander, J. E., Ren, D., Huang, Y., Loo, N. W. X., Hong, S. H. L., & Yeo, B. S. (2018). Understanding the Heterogeneous Electrocatalytic Reduction of Carbon Dioxide on Oxide-Derived Catalysts. *ChemElectroChem*, *5*(2), 219-237.
- Perez-Gallent, E., Figueiredo, M. C., Calle-Vallejo, F., & Koper, M. T. (2017). Spectroscopic Observation



- of a Hydrogenated CO Dimer Intermediate During CO Reduction on Cu(100) Electrodes. *Angew Chem Int Ed Engl*, 56(13), 3621-3624.
- Peter, S. C. (2018). Reduction of CO<sub>2</sub> to Chemicals and Fuels: A Solution to Global Warming and Energy Crisis. *ACS Energy Letters*, 3(7), 1557-1561.
- Peterson, A. A., Abild-Pedersen, F., Studt, F., Rossmeisl, J., & Nørskov, J. K. (2010). How copper catalyzes the electroreduction of carbon dioxide into hydrocarbon fuels. *Energy Environ. Sci.*, 3, 1311-1315.
- Pupo, M. M. d. S., & Kortlever, R. (2019). Electrolyte Effects on the Electrochemical Reduction of CO<sub>2</sub>. *Chemphyschem*, 20, 1-11.
- Qiao, J., Liu, Y., Hong, F., & Zhang, J. (2014). A review of catalysts for the electroreduction of carbon dioxide to produce low-carbon fuels. *Chem Soc Rev*, 43(2), 631-675.
- Raciti, D., Mao, M., & Wang, C. (2018). Mass transport modelling for the electroreduction of CO<sub>2</sub> on Cu nanowires. *Nanotechnology*, 29(4), 044001.
- Resasco, J., Chen, L. D., Clark, E., Tsai, C., Hahn, C., Jaramillo, T. F., . . . Bell, A. T. (2017). Promoter Effects of Alkali Metal Cations on the Electrochemical Reduction of Carbon Dioxide. *J Am Chem Soc*, 139(32), 11277-11287.
- Reske, R., Mistry, H., Behafarid, F., Roldan Cuenya, B., & Strasser, P. (2014). Particle size effects in the catalytic electroreduction of CO<sub>2</sub> on Cu nanoparticles. *J Am Chem Soc*, 136(19), 6978-6986.
- Roberts, F. S., Kuhl, K. P., & Nilsson, A. (2015). High selectivity for ethylene from carbon dioxide reduction over copper nanocube electrocatalysts. *Angew Chem Int Ed Engl*, 54(17), 5179-5182.
- Rosen, J., Hutchings, G. S., Lu, Q., Rivera, S., Zhou, Y., Vlachos, D. G., & Jiao, F. (2015). Mechanistic Insights into the Electrochemical Reduction of CO<sub>2</sub> to CO on Nanostructured Ag Surfaces. *ACS Catalysis*, 5(7), 4293-4299.
- Ross, M. B., Dinh, C. T., Li, Y., Kim, D., De Luna, P., Sargent, E. H., & Yang, P. (2017). Tunable Cu Enrichment Enables Designer Syngas Electrosynthesis from CO<sub>2</sub>. *J Am Chem Soc*, 139(27), 9359-9363.
- Sánchez, M. P., Barrera, M., Gonzalez, S., Souto, R. M., Salvarezza, R. C., & Arvia, A. J. (1990). Electrochemical behaviour of copper in aqueous moderate alkaline media, containing sodium carbonate and bicarbonate, and sodium perchlorate. *Electrochimica Acta*, 35(9), 1337-1343.
- Sandberg, R. B., Montoya, J. H., Chan, K., & Nørskov, J. K. (2016). CO-CO coupling on Cu facets: Coverage, strain and field effects. *Surface Science*, 654, 56-62.
- Schlaup, C. H., Sebastian. (2013). In-situ STM study of phosphate adsorption on Cu(111), Au(111) and Cu/Au(111) electrodes. *Surface Science*, 608, 44-54.
- Schlucker, S. (2014). Surface-enhanced Raman spectroscopy: concepts and chemical applications. *Angew Chem Int Ed Engl*, 53(19), 4756-4795.
- Schouten, K. J., Qin, Z., Perez Gallent, E., & Koper, M. T. (2012). Two pathways for the formation of ethylene in CO reduction on single-crystal copper electrodes. *J Am Chem Soc*, 134(24), 9864-9867.
- Schouten, K. J. P., Kwon, Y., van der Ham, C. J. M., Qin, Z., & Koper, M. T. M. (2011). A new mechanism for the selectivity to C<sub>1</sub> and C<sub>2</sub> species in the electrochemical reduction of carbon dioxide on copper electrodes. *Chemical Science*, 2(10), 1902.
- Schulz, K. G., Riebesell, U., Rost, B., Thoms, S., & Zeebe, R. E. (2006). Determination of the rate constants for the carbon dioxide to bicarbonate inter-conversion in pH-buffered seawater systems. *Marine Chemistry*, 100(1-2), 53-65.

- Sebastián-Pascual, P., Mezzavilla, S., Stephens, I. E. L., & Escudero-Escribano, M. (2019). Structure-sensitivity and Electrolyte Effects in CO<sub>2</sub> Electroreduction: From Model Studies to Applications. *ChemCatChem*, *11*(16), 3626-3645
- Seh, Z. W., Kibsgaard, J., Dickens, C. F., Chorkendorff, I., Norskov, J. K., & Jaramillo, T. F. (2017). Combining theory and experiment in electrocatalysis: Insights into materials design. *Science*, *355*(6321).
- Sen, S., Liu, D., & Palmore, G. T. R. (2014). Electrochemical Reduction of CO<sub>2</sub> at Copper Nanofoams. *ACS Catalysis*, *4*(9), 3091-3095.
- Sharma, B., Frontiera, R. R., Henry, A.-I., Ringe, E., & Van Duyne, R. P. (2012). SERS: Materials, applications, and the future. *Materials Today*, *15*(1-2), 16-25.
- Sheng, H., Oh, M. H., Osowiecki, W. T., Kim, W., Alivisatos, A. P., & Frei, H. (2018). Carbon Dioxide Dimer Radical Anion as Surface Intermediate of Photoinduced CO<sub>2</sub> Reduction at Aqueous Cu and CdSe Nanoparticle Catalysts by Rapid-Scan FT-IR Spectroscopy. *J Am Chem Soc*, *140*(12), 4363-4371.
- Shi, X., Xiao, H., Chen, X., & Lackner, K. S. (2016). The Effect of Moisture on the Hydrolysis of Basic Salts. *Chemistry A european journal*, *22*, 18326-18330.
- Shi, X., Xiao, H., Lackner, K. S., & Chen, X. (2016). Capture CO<sub>2</sub> from Ambient Air Using Nanoconfined Ion Hydration. *Angew Chem Int Ed Engl*, *55*(12), 4026-4029.
- Singh, A. K., Khan, S. A., Fan, Z., Demeritte, T., Senapati, D., Kanchanapally, R., & Ray, P. C. (2012). Development of a long-range surface-enhanced Raman spectroscopy ruler. *J Am Chem Soc*, *134*(20), 8662-8669.
- Smith, B. D., & Irish, D. E. (1997). A Surface Enhanced Raman Scattering Study of the Intermediate and Poisoning Species Formed during the Electrochemical Reduction of CO<sub>2</sub> on Copper. *Journal of The Electrochemical Society*, *144*(12), 4288-4296.
- Smith, E., & Dent, G. (2005). Modern Raman spectroscopy: A practical approach. *John Wiley & Sons*.
- Soon, A., Todorova, M., Delley, B., & Stampfl, C. (2006). Oxygen adsorption and stability of surface oxides onCu(111): A first-principles investigation. *Physical Review B*, *73*(16).
- Spodaryk, M., Zhao, K., Zhang, J., Oveisi, E., & Züttel, A. (2019). The role of malachite nanorods for the electrochemical reduction of CO<sub>2</sub> to C<sub>2</sub> hydrocarbons. *Electrochimica Acta*, *297*, 55-60.
- Strasser, P., Gliech, M., Kuehl, S., & Moeller, T. (2018). Electrochemical processes on solid shaped nanoparticles with defined facets. *Chem Soc Rev*, *47*(3), 715-735.
- Suh, J. S., & Kim, J. (1998). Three Distinct Geometries of Surface-Adsorbed Carboxylate Groups. *Journal of Raman Spectroscopy*, *29*, 143-148.
- Tan, X., Yu, C., Ren, Y., Cui, S., Li, W., & Qiu, J. (2021). Recent advances in innovative strategies for the CO<sub>2</sub> electroreduction reaction. *Energy & Environmental Science*, *14*(2), 765-780.
- Tian, Z.-Q., Ren, B., & Wu, D.-Y. (2002). Surface-Enhanced Raman Scattering: From Noble to Transition Metals and from Rough Surfaces to Ordered Nanostructures. *The Journal of Physical Chemistry B*, *106*(37), 9463-9483.
- V. Masson-Delmotte, P. Zhai, Pörtner, H.-O., Roberts, D., Skea, J., Shukla, P. R., . . . (eds.), T. W. (2018). IPCC, 2018: Global Warming of 1.5°C. An IPCC Special Report on the impacts of global warming of 1.5°C above pre-industrial levels and related global greenhouse gas emission pathways, in the context of strengthening the global response to the threat of climate change, sustainable development, and efforts to eradicate poverty. (*World Meteorological Organization, Geneva, 2018*), chapter 1.

- Varela, A. S., Kroschel, M., Reier, T., & Strasser, P. (2016). Controlling the selectivity of CO<sub>2</sub> electroreduction on copper: The effect of the electrolyte concentration and the importance of the local pH. *Catalysis Today*, 260, 8-13.
- Vasileff, A., Xu, C., Jiao, Y., Zheng, Y., & Qiao, S.-Z. (2018). Surface and Interface Engineering in Copper-Based Bimetallic Materials for Selective CO<sub>2</sub> Electroreduction. *Chem*, 4(8), 1809-1831.
- Velasco-Vélez, J.-J., Jones, T., Gao, D., Carbonio, E., Arrigo, R., Hsu, C.-J., . . . Chuang, C.-H. (2018). The Role of the Copper Oxidation State in the Electrocatalytic Reduction of CO<sub>2</sub> into Valuable Hydrocarbons. *ACS Sustainable Chemistry & Engineering*, 7(1), 1485-1492.
- Verdaguer-Casadevall, A., Li, C. W., Johansson, T. P., Scott, S. B., McKeown, J. T., Kumar, M., . . . Chorkendorff, I. (2015). Probing the Active Surface Sites for CO Reduction on Oxide-Derived Copper Electrocatalysts. *Journal of the American Chemical Society*, 137(31), 9808-9811.
- Vink, B. W. (1986). Stability relations of malachite and azurite. *Mineralogical Magazine*, 50(355), 41-47.
- Wang, J., Tan, H. Y., Zhu, Y., Chu, H., & Chen, H. M. (2021). Linking the Dynamic Chemical State of Catalysts with the Product Profile of Electrocatalytic CO<sub>2</sub> Reduction. *Angew Chem Int Ed Engl*.
- Wang, L., Gupta, K., Goodall, J. B. M., Darr, J. A., & Holt, K. B. (2017). In situ spectroscopic monitoring of CO<sub>2</sub> reduction at copper oxide electrode. *Faraday Discuss*, 197, 517-532.
- Wang, Y., Wang, Z., Dinh, C.-T., Li, J., Ozden, A., Golam Kibria, M., . . . Sargent, E. H. (2019). Catalyst synthesis under CO<sub>2</sub> electroreduction favours faceting and promotes renewable fuels electrosynthesis. *Nature Catalysis*, 3(2), 98-106.
- Weekes, D. M., Salvatore, D. A., Reyes, A., Huang, A., & Berlinguette, C. P. (2018). Electrolytic CO<sub>2</sub> Reduction in a Flow Cell. *Acc Chem Res*, 51(4), 910-918.
- Wei, W., Li, S., Millstone, J. E., Banholzer, M. J., Chen, X., Xu, X., . . . Mirkin, C. A. (2009). Surprisingly long-range surface-enhanced Raman scattering (SERS) on Au-Ni multisegmented nanowires. *Angew Chem Int Ed Engl*, 48(23), 4210-4212.
- Weng, L. C., Bell, A. T., & Weber, A. Z. (2018). Modeling gas-diffusion electrodes for CO<sub>2</sub> reduction. *Phys Chem Chem Phys*, 20(25), 16973-16984.
- Westheimer, F. H. (1961). The magnitude of the primary kinetic isotope effect for compounds of hydrogen and deuterium. *Chemical Reviews*, 61(3), 265-273.
- Wu, D. Y., Li, J. F., Ren, B., & Tian, Z. Q. (2008). Electrochemical surface-enhanced Raman spectroscopy of nanostructures. *Chem Soc Rev*, 37(5), 1025-1041.
- Wuttig, A., Liu, C., Peng, Q., Yaguchi, M., Hendon, C. H., Motobayashi, K., . . . Surendranath, Y. (2016). Tracking a Common Surface-Bound Intermediate during CO<sub>2</sub>-to-Fuels Catalysis. *ACS Cent Sci*, 2(8), 522-528.
- Wuttig, A., Yaguchi, M., Motobayashi, K., Osawa, M., & Surendranath, Y. (2016). Inhibited proton transfer enhances Au-catalyzed CO<sub>2</sub>-to-fuels selectivity. *Proceedings of the National Academy of Sciences*, 113(32), E4585-E4593.
- Wuttig, A., Yoon, Y., Ryu, J., & Surendranath, Y. (2017). Bicarbonate Is Not a General Acid in Au-Catalyzed CO<sub>2</sub> Electroreduction. *J Am Chem Soc*, 139(47), 17109-17113.
- Xiao, H., III, W. A. G., Cheng, T., & Liu, Y. (2017). Cu metal embedded in oxidized matrix catalyst to promote CO<sub>2</sub> activation and CO dimerization for electrochemical reduction of CO<sub>2</sub>. *Proc Natl Acad Sci U S A*, 114(26), 6685-6688.
- Xie, C., Niu, Z., Kim, D., Li, M., & Yang, P. (2020). Surface and Interface Control in Nanoparticle Catalysis. *Chem Rev*, 120(2), 1184-1249.

- Yan, Z., Hitt, J. L., Turner, J. A., & Mallouk, T. E. (2020). Renewable electricity storage using electrolysis. *Proc Natl Acad Sci U S A*, *117*(23), 12558-12563.
- Ye, Y., Qian, J., Yang, H., Su, H., Lee, K. J., Etxebarria, A., . . . Crumlin, E. J. (2020). Synergy between a Silver-Copper Surface Alloy Composition and Carbon Dioxide Adsorption and Activation. *ACS Appl Mater Interfaces*, *12*(22), 25374-25382.
- Ye, Y., Yang, H., Qian, J., Su, H., Lee, K. J., Cheng, T., . . . Crumlin, E. J. (2019). Dramatic differences in carbon dioxide adsorption and initial steps of reduction between silver and copper. *Nat Commun*, *10*(1), 1875.
- Yoon, Y., Hall, A. S., & Surendranath, Y. (2016). Tuning of Silver Catalyst Mesostructure Promotes Selective Carbon Dioxide Conversion into Fuels. *Angewandte Chemie International Edition*, *55*(49), 15282-15286.
- Yu, Y., Wang, Y., Lin, K., Hu, N., Zhou, X., & Liu, S. (2013). Complete Raman spectral assignment of methanol in the C-H stretching region. *J Phys Chem A*, *117*(21), 4377-4384.
- Zhang, W., & Burgess, I. J. (2012). Kinetic isotope effects in proton coupled electron transfer. *Journal of Electroanalytical Chemistry*, *668*, 66-72.
- Zhang, W., Hu, Y., Ma, L., Zhu, G., Wang, Y., Xue, X., . . . Jin, Z. (2018). Progress and Perspective of Electrocatalytic CO<sub>2</sub> Reduction for Renewable Carbonaceous Fuels and Chemicals. *Advanced Science*, *5*(1), 1700275.
- Zhang, W., Huang, C., Xiao, Q., Yu, L., Shuai, L., An, P., . . . Yu, Y. (2020). Atypical Oxygen-Bearing Copper Boosts Ethylene Selectivity toward Electrocatalytic CO<sub>2</sub> Reduction. *J Am Chem Soc*, *142*(26), 11417-11427.
- Zhang, X.-G., Jin, X., Wu, D.-Y., & Tian, Z.-Q. (2018). Selective Electrocatalytic Mechanism of CO<sub>2</sub> Reduction Reaction to CO on Silver Electrodes: A Unique Reaction Intermediate. *The Journal of Physical Chemistry C*, *122*(44), 25447-25455.
- Zhang, Z., Melo, L., Jansonius, R. P., Habibzadeh, F., Grant, E. R., & Berlinguette, C. P. (2020). pH Matters When Reducing CO<sub>2</sub> in an Electrochemical Flow Cell. *ACS Energy Letters*, *5*(10), 3101-3107.
- Zhao, Y., Chang, X., Malkani, A. S., Yang, X., Thompson, L., Jiao, F., & Xu, B. (2020). Speciation of Cu Surfaces During the Electrochemical CO Reduction Reaction. *J Am Chem Soc*, *142*(21), 9735-9743.
- Zhou, Y., Che, F., Liu, M., Zou, C., Liang, Z., De Luna, P., . . . Sargent, E. H. (2018). Dopant-induced electron localization drives CO<sub>2</sub> reduction to C<sub>2</sub> hydrocarbons. *Nat Chem*, *10*(9), 974-980.
- Zhu, S., Jiang, B., Cai, W. B., & Shao, M. (2017). Direct Observation on Reaction Intermediates and the Role of Bicarbonate Anions in CO<sub>2</sub> Electrochemical Reduction Reaction on Cu Surfaces. *J Am Chem Soc*, *139*(44), 15664-15667.
- Zhu, S., Li, T., Cai, W.-B., & Shao, M. (2019). CO<sub>2</sub> Electrochemical Reduction As Probed through Infrared Spectroscopy. *ACS Energy Letters*, *4*(3), 682-689.
- Zhuang, T.-T., Liang, Z.-Q., Seifitokaldani, A., Li, Y., De Luna, P., Burdyny, T., . . . Sargent, E. H. (2018). Steering post-C-C coupling selectivity enables high efficiency electroreduction of carbon dioxide to multi-carbon alcohols. *Nature Catalysis*, *1*(6), 421-428.
- Zhuang, T.-T., Pang, Y., Liang, Z.-Q., Wang, Z., Li, Y., Tan, C.-S., . . . Sargent, E. H. (2018). Copper nanocavities confine intermediates for efficient electrosynthesis of C<sub>3</sub> alcohol fuels from carbon monoxide. *Nature Catalysis*, *1*(12), 946-951.

## 8. Appendix

### 8.1 Background spectra

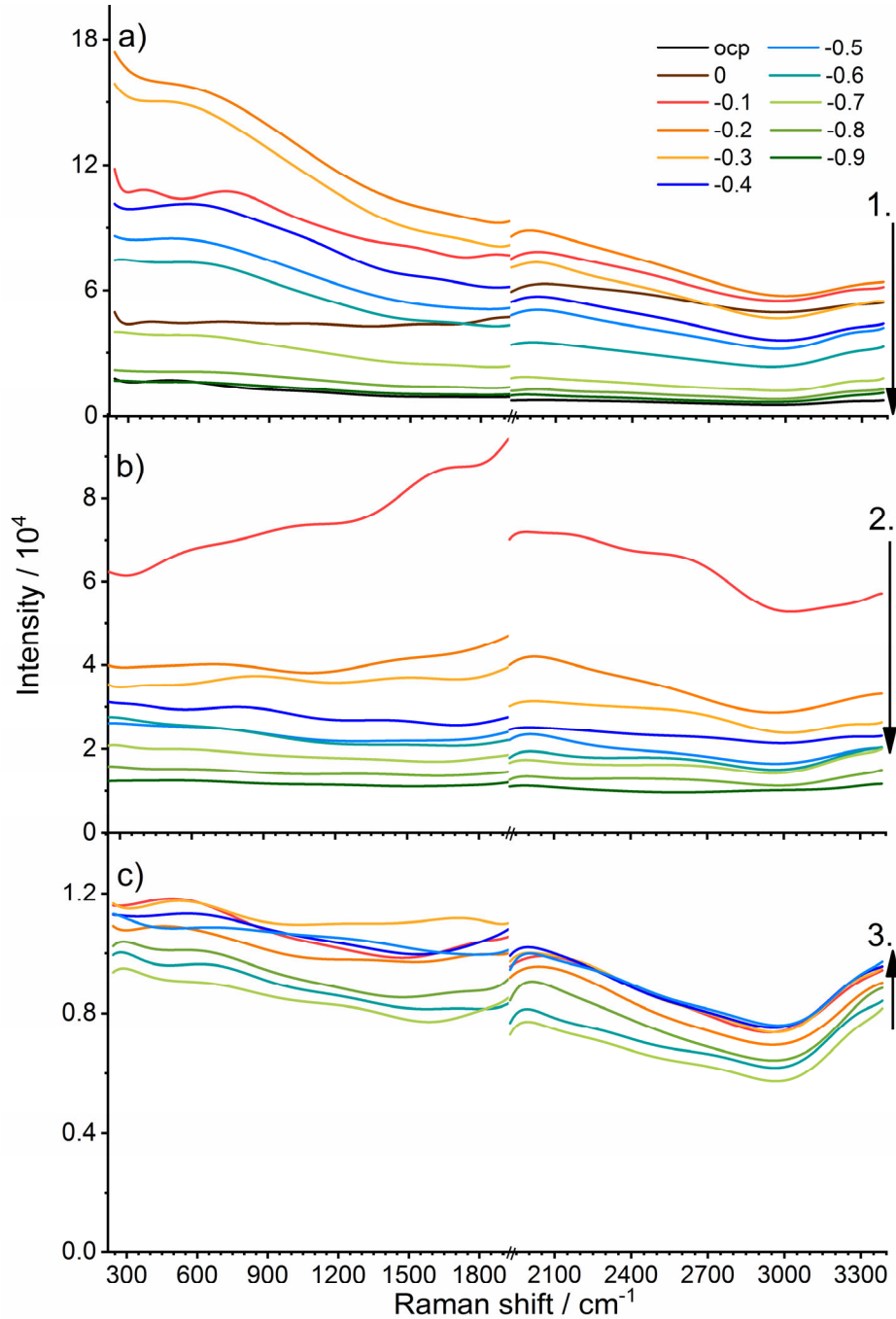


Figure 8.1: Potential-dependent SERS background of a Cu foam in 0.1 M  $\text{KHCO}_3$  at pH 6.8. a) The potential was swept from 0 to  $-0.9 \text{ V}_{\text{RHE}}$  (Series 1: reduction of  $\text{Cu}_x\text{OH}_y$  species of the as-deposited Cu foam). b) Potentials from  $-0.1$  to  $-0.9 \text{ V}_{\text{RHE}}$  were applied (Series 2). c) Backward scan from  $-0.8$  to  $-0.1 \text{ V}_{\text{RHE}}$  (Series 3). The background spectra were determined as described further above; they are NOT offset. Reprinted from ref (Jiang, Klingan, Pasquini, & Dau, 2019), with the permission of AIP Publishing.

## 8.2 Paper artefact

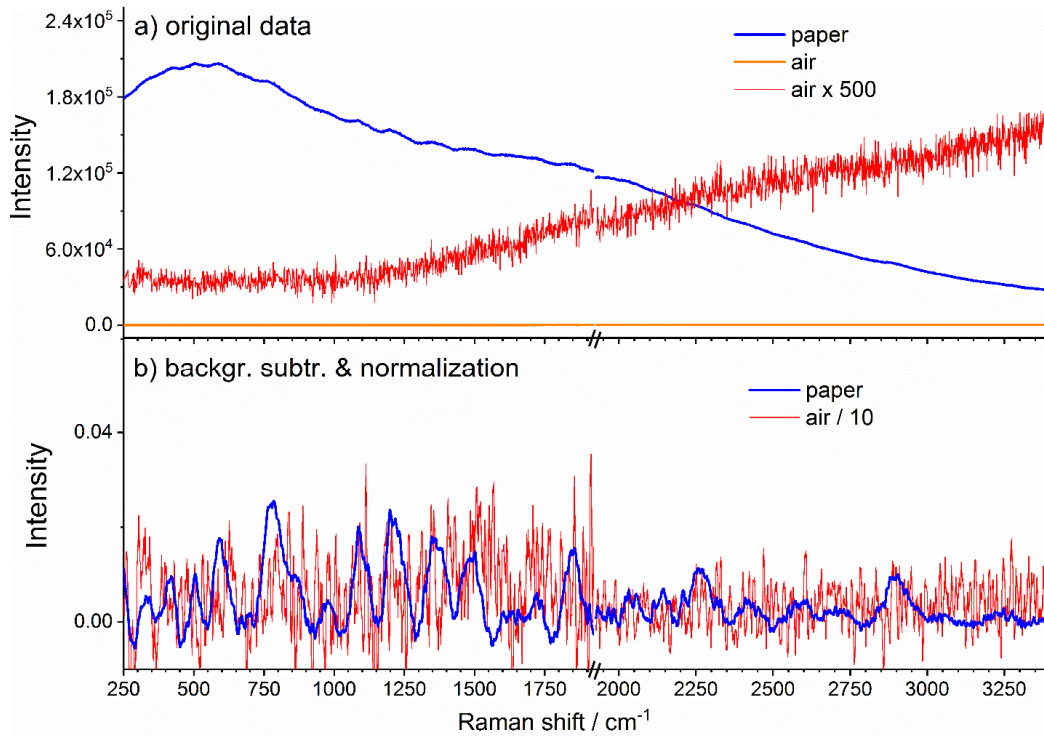


Figure 8.2: a) Raman spectra of a sheet of white paper (in blue), of air (orange), and the air spectrum multiplied by 500 (red). b) Background subtracted and normalized spectra of a paper sheet and of air (signal divided by 10). The interference pattern cannot be found in the air spectrum. Reprinted from ref (Jiang, Klingan, Pasquini, & Dau, 2019), with the permission of AIP Publishing.

Table 8.1: Position of the maxima of the interfering signals (Raman shifts,  $\Delta\omega$  in  $\text{cm}^{-1}$ ) determined from paper after background subtraction and normalization (data in Figure 8.2b). Reprinted from ref (Jiang, Klingan, Pasquini, & Dau, 2019), with the permission of AIP Publishing.

$\Delta\omega / \text{cm}^{-1}$	$\Delta\omega / \text{cm}^{-1}$	$\Delta\omega / \text{cm}^{-1}$	$\Delta\omega / \text{cm}^{-1}$
326	995	1492	1999
420	1101	1628	2126
512	1198	1663	2271
593	1225	1716	2441
788	1365	1854	3249

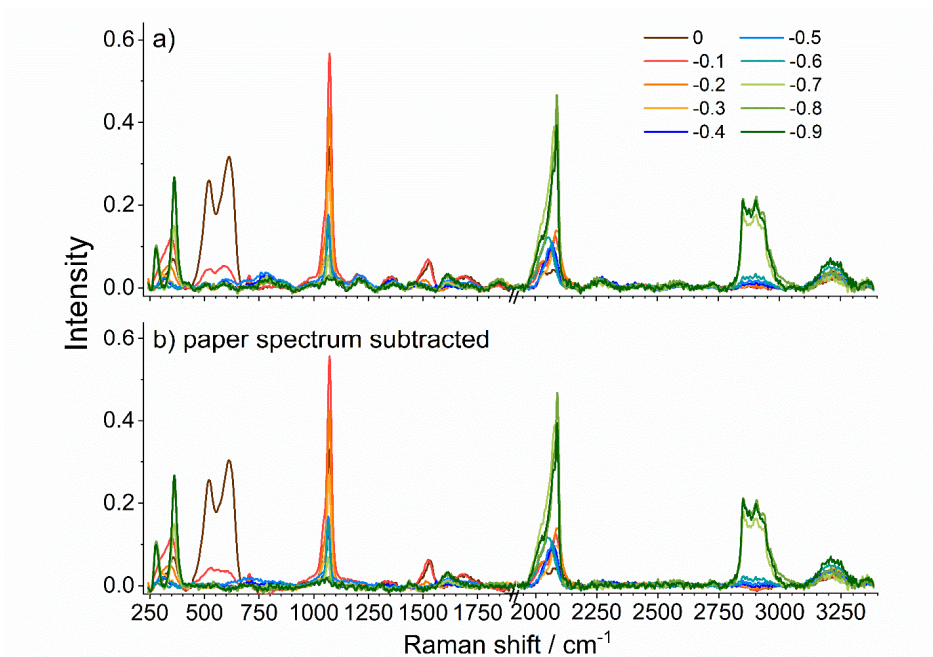


Figure 8.3: *Operando* Raman spectra of Cu foam in CO<sub>2</sub>-saturated carbonate solution (0.1 M KHCO<sub>3</sub>, pH 6.8) at various electrochemical potentials. Reduction behavior of Cu<sub>x</sub>OH<sub>y</sub> to metallic copper and electrochemical CO<sub>2</sub> reduction, 0 to -0.9 V<sub>RHE</sub> (Series 1). a) Background subtracted and normalized spectra. b) Spectrum obtained by subtracting the properly scaled paper spectrum from a). Reprinted from ref (Jiang, Klingan, Pasquini, & Dau, 2019), with the permission of AIP Publishing.

### 8.3 Thiophenol experiment second CA series forward and backward spectra

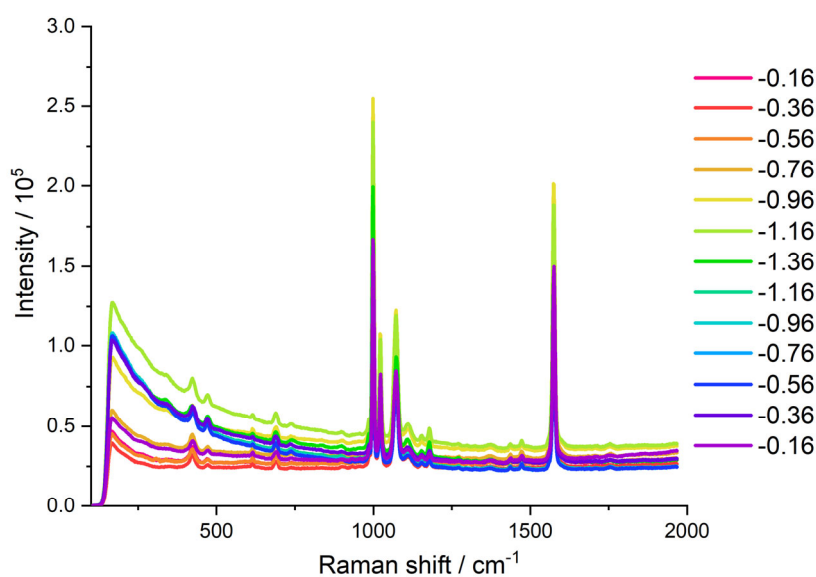


Figure 8.4: The second CA scanning forward from -0.16 to -1.36 V<sub>RHE</sub> and backward, raw spectra.

## 8.4 Second CA series on the same catalyst

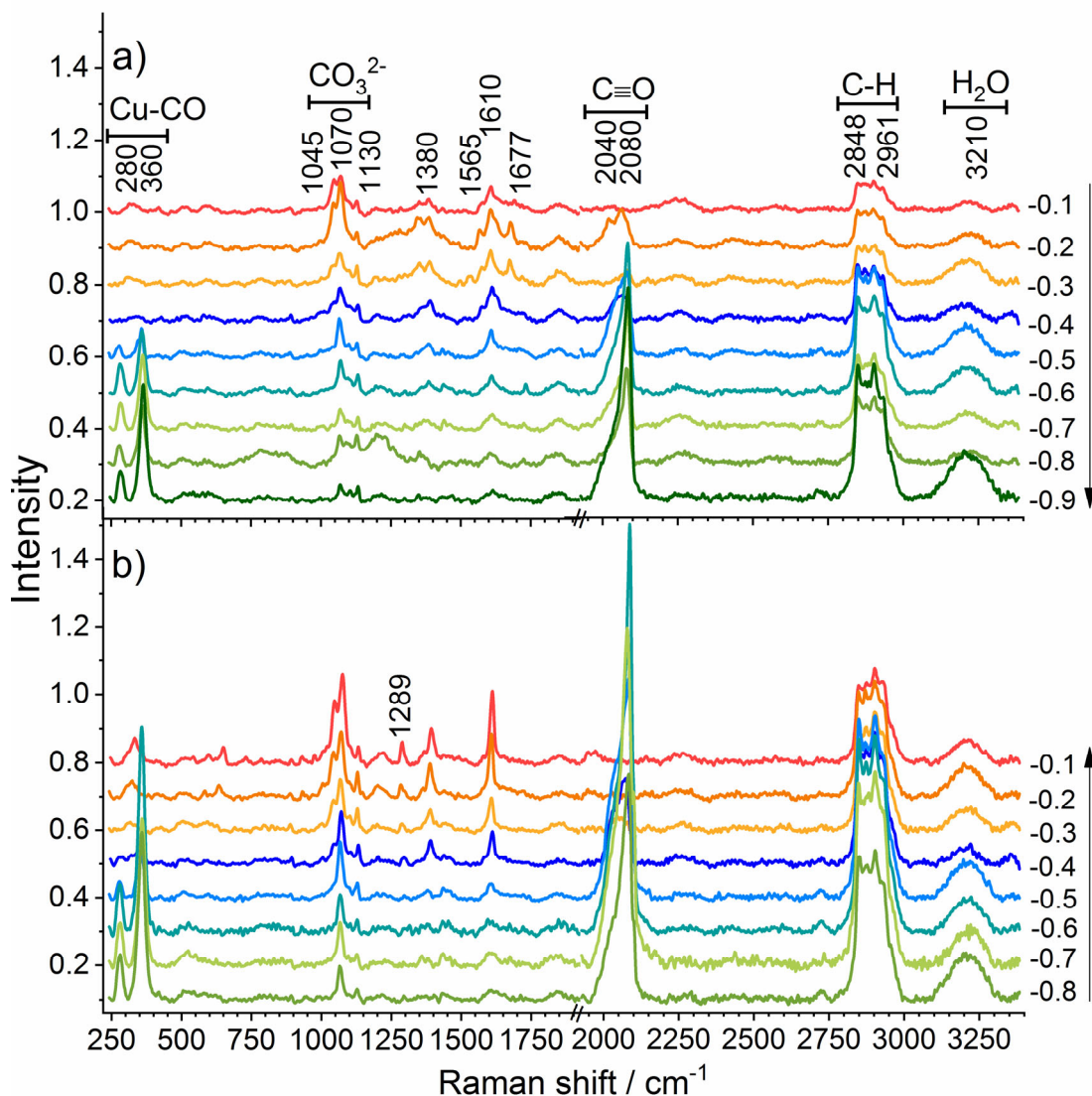


Figure 8.5: *Operando* Raman spectra of Cu foam in CO<sub>2</sub> saturated 0.1 M KHCO<sub>3</sub> (pH 6.8) at different electrochemical potentials after reduction of oxide species (Series 2) and backwards potential series (Series 3). a) Potentials from -0.1 to -0.9 V<sub>RHE</sub>, and b) backward direction from -0.8 to -0.1 V<sub>RHE</sub>. All spectra are background subtracted, normalized, and offset. Arrows indicate the scan direction of the electric potential. As opposed to **Figure 2.7**, the electrolyte was NOT exchanged after series 1. Reprinted from ref (Jiang, Klingan, Pasquini, & Dau, 2019), with the permission of AIP Publishing.



## 8.5 Complete spectra during oxidation reduction CV measurement.

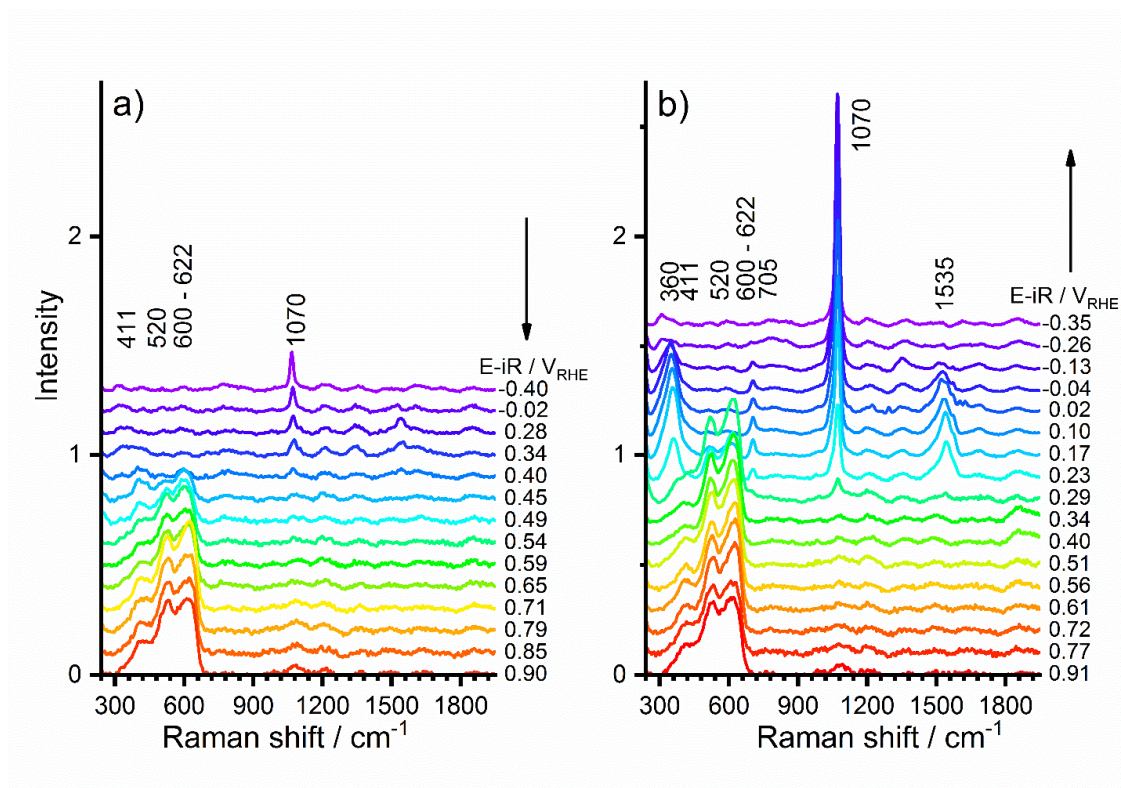


Figure 8.6: *Operando* Raman spectra at different electrochemical potentials during a CV with  $1 \text{ mV s}^{-1}$  in  $0.1 \text{ M KHCO}_3$  solution at pH 8.8 during (a) the forward scan from negative to positive potentials, and (b) the backward scan from positive to negative potentials. Spectra are background subtracted, normalized, and offset. Arrows indicate the potential scan direction. Reprinted from ref (Jiang, Klingan, Pasquini, & Dau, 2019), with the permission of AIP Publishing.

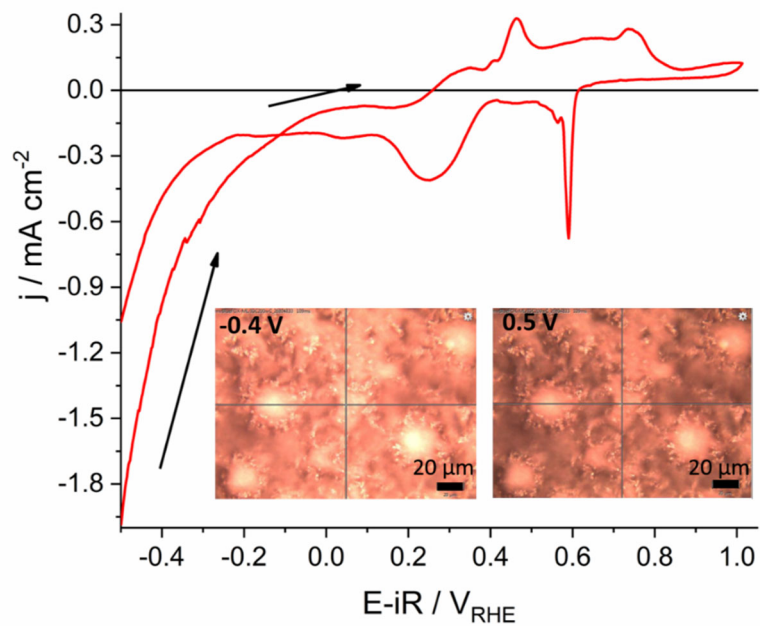


Figure 8.7: CV of a Cu foam with  $1 \text{ mV s}^{-1}$  in  $0.1 \text{ M KHCO}_3$  pH 8.8. Arrows indicate the scan direction. Microscope pictures show the Cu foam at  $-0.4 \text{ V}_{\text{RHE}}$  with a shiny metallic surface and its color change upon oxidation to copper oxide species at  $0.5 \text{ V}_{\text{RHE}}$ . Reprinted from ref (Jiang, Klingan, Pasquini, & Dau, 2019), with the permission of AIP Publishing.

## 8.6 Reproducibility test with carbonate bands

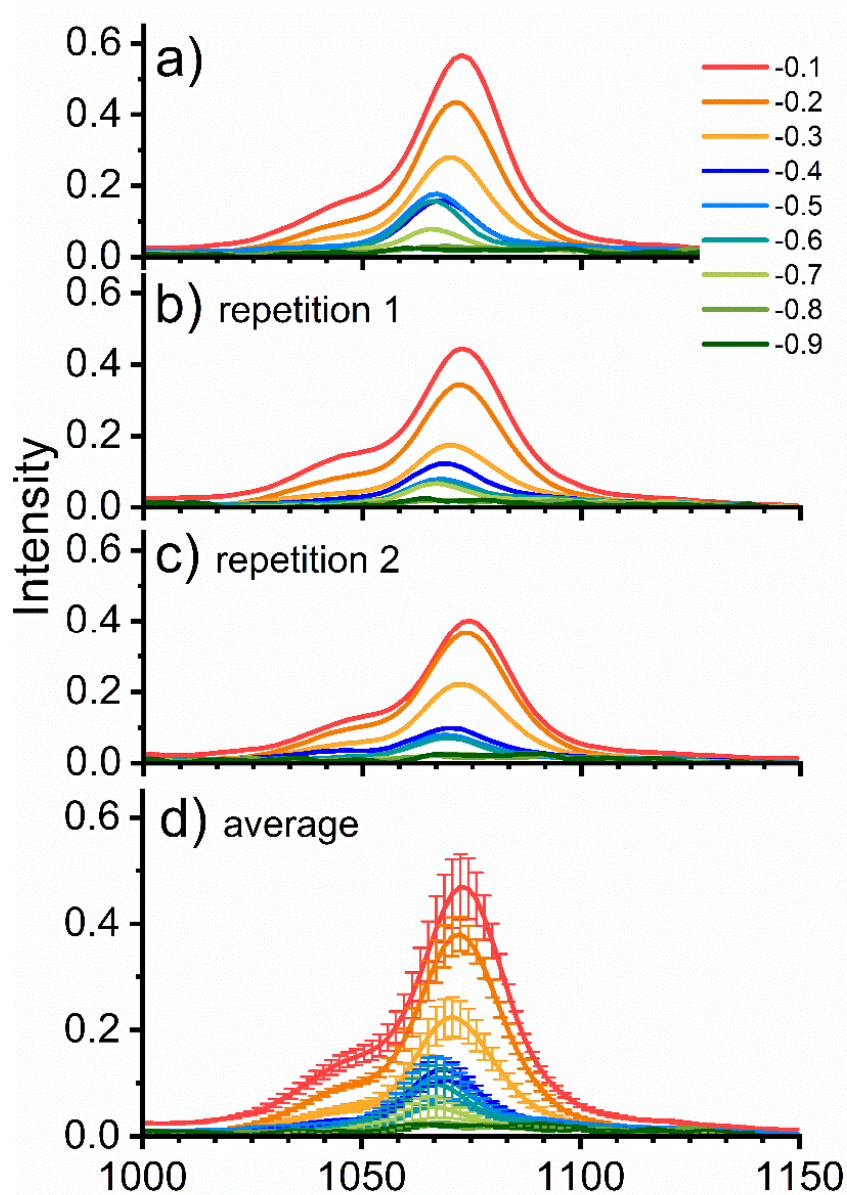


Figure 8.8: Carbonate region: *Operando* Raman spectra of Cu foam in CO<sub>2</sub>-saturated bicarbonate solution (0.1 M KHCO<sub>3</sub>, pH 6.8) at various electrochemical potentials. Background subtracted and normalized spectra. a) Series 1 (data from Figure 2.7), b) repetition, c) 2<sup>nd</sup> repetition, d) averaged data with standard deviations. For each repetition a freshly electrodeposited Cu foam has been used. Reprinted from ref (Jiang, Klingan, Pasquini, & Dau, 2019), with the permission of AIP Publishing.

## 8.7 C-H bands assignment

Table 8.2: Raman shifts ( $\Delta\omega$  in  $\text{cm}^{-1}$ ) of HCOOH, HCOOK,  $\text{C}_2\text{H}_5\text{OH}$ ,  $\text{CH}_3\text{OH}$ , and  $\text{CH}_3\text{COOH}$  solutions. Reprinted from ref (Jiang, Klingan, Pasquini, & Dau, 2019), with the permission of AIP Publishing.

$\Delta\omega / \text{cm}^{-1}$	Species	Mode
439	$\text{C}_2\text{H}_5\text{OH}$	D (CO) (F. Li et al., 2018)
713	HCOOH	B (O-C=O) (Bartholomew & Irish, 1999; Y.-T. Chang, Yamaguchi, Miller, & III, 1987)
765	HCOOK	D(COO) (Ito & Bernstein, 1956)
879	$\text{C}_2\text{H}_5\text{OH}$	Skeletal S(CCO) (F. Li et al., 2018)
892	$\text{CH}_3\text{COOH}$	S(C-C) (Nakabayashi, Kosugi, & Nishi, 1999)
1020	$\text{CH}_3\text{OH}$	S (CO) (Mendoza, Bonales, Baonza, & Caceres, 2014)
1046	$\text{C}_2\text{H}_5\text{OH}$	Skeletal D(CCO)(F. Li et al., 2018)
1065	HCOOK	R(COO) (Ito & Bernstein, 1956)
1088	$\text{C}_2\text{H}_5\text{OH}$	S (CO) (F. Li et al., 2018)
1110	$\text{CH}_3\text{OH}$	D (OCH) (Mendoza et al., 2014)
1210	HCOOH	S (C-O) (Bartholomew & Irish, 1999; Y.-T. Chang et al., 1987)
1278	$\text{C}_2\text{H}_5\text{OH}$	D wag ( $\text{CH}_2$ ) (F. Li et al., 2018)
1350	HCOOK	S(C-O) (Ito & Bernstein, 1956)
1380	HCOOK	R(COO) (Ito & Bernstein, 1956)
1400	HCOOH	B (C-H)(Bartholomew & Irish, 1999)
1455	$\text{C}_2\text{H}_5\text{OH}$	Wag ( $\text{CH}_2$ ) (F. Li et al., 2018)
1462	$\text{CH}_3\text{OH}$	B <sub>as</sub> ( $\text{CH}_2$ ) (Mendoza et al., 2014)
1707	HCOOH	S (C=O) (Bartholomew & Irish, 1999)
1708	$\text{CH}_3\text{COOH}$	S(C=O) (Nakabayashi et al., 1999)
2731	HCOOK	S(C-H) (Ito & Bernstein, 1956)
2812	HCOOK	S(C-H) (Ito & Bernstein, 1956)
2845	$\text{CH}_3\text{OH}$	SS ( $\text{CH}_3$ ) (Yu et al., 2013)
2881	$\text{C}_2\text{H}_5\text{OH}$	S ( $\text{CH}_2$ ) (F. Li et al., 2018)
2933	$\text{C}_2\text{H}_5\text{OH}$	SS ( $\text{CH}_3$ ) (F. Li et al., 2018)
2943	HCOOH	S (C-H) (Olbert-Majkut, Ahokas, Lundell, & Pettersson, 2009)
2944	$\text{CH}_3\text{COOH}$	S( $\text{CH}_3$ )(Nakabayashi et al., 1999)
2952	$\text{CH}_3\text{OH}$	FR ( $\text{CH}_3$ ) (Yu et al., 2013)
2979	$\text{C}_2\text{H}_5\text{OH}$	AS ( $\text{CH}_3$ ) (F. Li et al., 2018)

FR: Fermi resonance mode of  $\text{CH}_3$  bending overtones, S: stretching, SS: symmetric stretching, AS: antisymmetric stretching, D: deformation, Wag: wagging, B: bending.

Table 8.3: Raman shifts ( $\Delta\omega$  in  $\text{cm}^{-1}$ ) of  $\text{CH}_3\text{OH}$ ,  $\text{C}_2\text{H}_5\text{OH}$ ,  $\text{HCOOH}$ ,  $\text{CH}_3\text{COOH}$  at open circuit potential, and  $\text{HCOOH}$  reduction at  $-0.5 \text{ V}_{\text{RHE}}$  on a Cu foam ( in  $0.1 \text{ M KH}_2\text{PO}_4/\text{K}_2\text{HPO}_4$ ). Main bands are bold. Reprinted from ref (Jiang, Klingan, Pasquini, & Dau, 2019), with the permission of AIP Publishing.

$\Delta\omega / \text{cm}^{-1}$ <b><math>\text{CH}_3\text{OH}</math></b>	$\Delta\omega / \text{cm}^{-1}$ <b><math>\text{C}_2\text{H}_5\text{OH}</math></b>	$\Delta\omega / \text{cm}^{-1}$ <b><math>\text{HCOOH}</math></b>	$\Delta\omega / \text{cm}^{-1}$ <b><math>\text{HCOOH}</math></b> $-0.5 \text{ V}_{\text{RHE}}$	$\Delta\omega / \text{cm}^{-1}$ <b><math>\text{CH}_3\text{COOH}</math></b>	$\Delta\omega / \text{cm}^{-1}$ <b><math>\text{CO}_2\text{RR}</math></b>
2845		2849	2852		2848
	2852				
2870		2867			2860, 2874
	2881				2885
		2898			
	2904				2904
2918			2918		
	2935	2933	2946	2933	2936
2952		2965			2961
	2980				

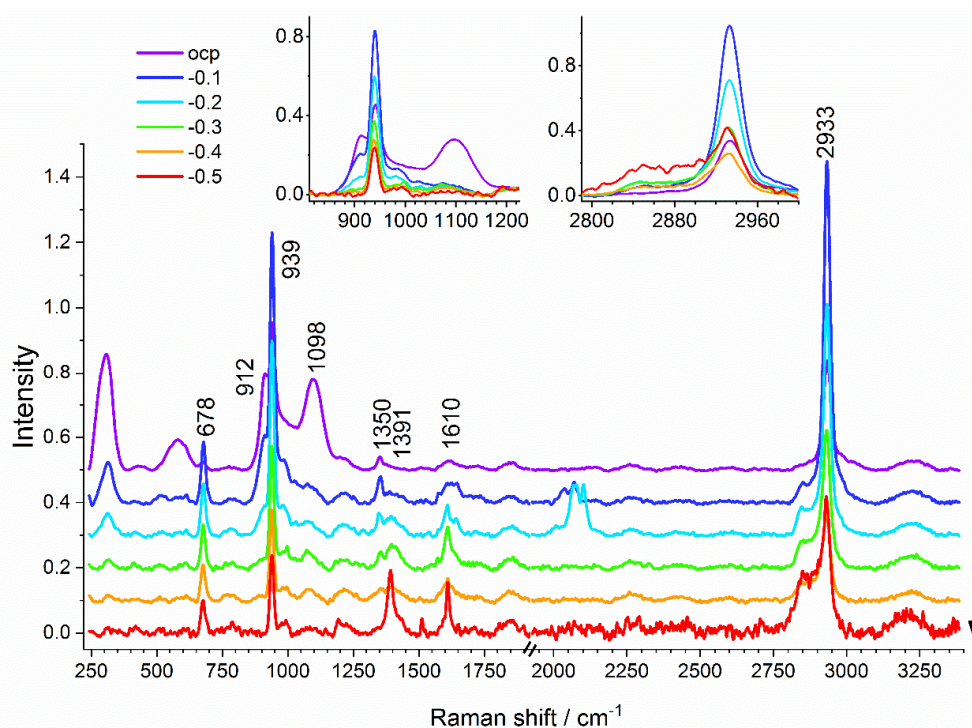


Figure 8.9: *Operando* Raman spectra of a Cu foam in  $0.1 \text{ M KH}_2\text{PO}_4/\text{K}_2\text{HPO}_4$  with acetic acid ( $0.091 \text{ M}$ ) at OCP,  $-0.1$ ,  $-0.2$ ,  $-0.3$ ,  $-0.4$ , and  $-0.5 \text{ V}_{\text{RHE}}$ . All spectra are background subtracted, normalized, and displayed with a vertical offset. The arrow indicates the potential-scan direction. Reprinted from ref (Jiang, Klingan, Pasquini, & Dau, 2019), with the permission of AIP Publishing.

Table 8.4: Raman peaks observed at various potentials (in  $V_{\text{RHE}}$ ) of a Cu foam in 0.1 M  $\text{KH}_2\text{PO}_4/\text{K}_2\text{HPO}_4$  supplemented with acetic acid. Reprinted from ref (Jiang, Klingan, Pasquini, & Dau, 2019), with the permission of AIP Publishing.

$\Delta\omega / \text{cm}^{-1}$ $\text{CH}_3\text{COOH}$	E-iR/ $V_{\text{RHE}}$	Mode
678	all	D( $\text{CO}_2$ ) (Ge'nin, Quilès, & Burneau, 2001)
912	OCP $\rightarrow$ -0.2	S(C-C) (Nakabayashi et al., 1999)
939	all	S(C-C) (Nakabayashi et al., 1999)
1098	OCP	R( $\text{CH}_3$ ) (Ge'nin et al., 2001)
1350	OCP $\rightarrow$ -0.3	S(C-O)+D( $\text{CH}_3$ ) (Ge'nin et al., 2001)
1391	-0.1 $\rightarrow$ -0.4	D( $\text{CH}_3$ )+S(C-O) (Ge'nin et al., 2001)
1610	-0.1 $\rightarrow$ -0.4	S(C=O) (Nakabayashi et al., 1999)
2933	all	S( $\text{CH}_3$ ) (Nakabayashi et al., 1999)

S: stretching, D: deformation, R: rocking, B: bending

## 8.8 Complete data for Figure 3.1, and corresponding electrochemical data

In the main text **Figure 3.1**, only the spectra in the range 0 to -0.3  $V_{\text{RHE}}$  are shown. Here the complete data set with Raman shift range after 2200  $\text{cm}^{-1}$  it shown in **Figure 8.10**. It can be seen that after disappearance of the hydroxycarbonate bands, the CO bands appeared and kept increasing with increasing potential, C-H bands at around 2800-3000  $\text{cm}^{-1}$  were also present after -0.2  $V_{\text{RHE}}$  which also increased with the potential.

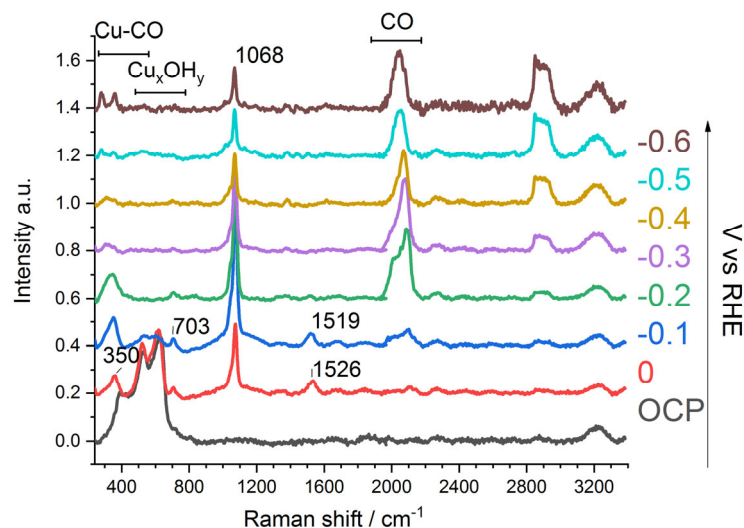


Figure 8.10: Complete data for Figure 3.1. *Operando* SERS spectra of Cu foam in  $\text{CO}_2$  saturated 0.1 M  $\text{KHCO}_3$  (pH 6.8) at various potentials (from 0 to -0.6  $V_{\text{RHE}}$ ).

The corresponding current (vs. time) are shown in **Figure 8.11**. A series of constant potentials was applied with each potential step lasting 2 mins. *Operando* Raman spectra were taken after 20 s at each potential to avoid the rapid change of current in the initial phase.

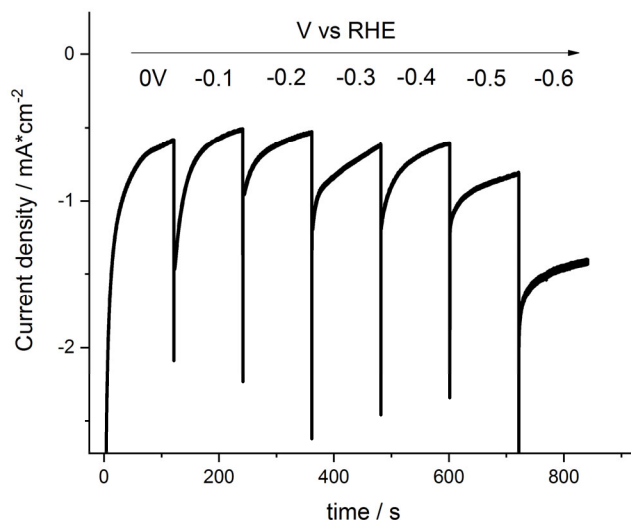


Figure 8.11: Chronoamperometry data of Figure 8.10 of Cu foam measured in CO<sub>2</sub> saturated 0.1 M KHCO<sub>3</sub> (pH 6.8) at various potentials (from 0 to -0.6 V<sub>RHE</sub>).

## 8.9 Complete data for Figure 3.3, Raman spectra with different concentration of bicarbonate electrolyte

Various concentration of bicarbonate solution including N<sub>2</sub> saturated 0.1 M KHCO<sub>3</sub> (pH 9.16), 0.5 M KHCO<sub>3</sub> (pH 8.7), and 1 M KHCO<sub>3</sub> (pH 8.7) were used to investigate the origin of peak (A-D) discussed in the main text. The complete spectra of **Figure 3.3** are shown in **Figure 8.12, 13**. In 0.1 M KHCO<sub>3</sub>, CO peak also appeared though the appearance of peak (D) was not clear. Increasing the concentration of bicarbonate to 0.5 M is enough to see peak (D) with prominent intensity, see **Figure 8.14** (not shown in the main text).

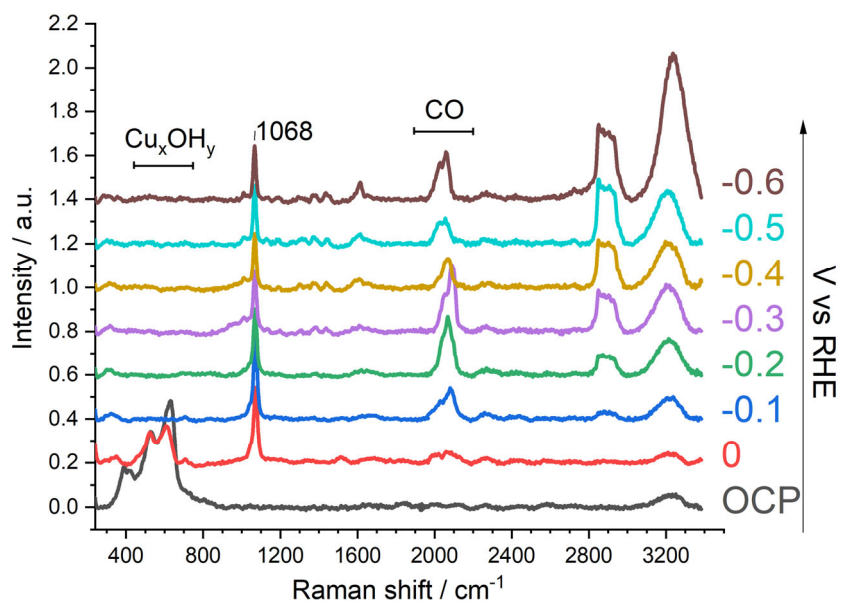


Figure 8.12: Complete data for Figure 3.3 dashed line spectra. *Operando* SERS spectra of Cu foam in  $N_2$  saturated 0.1 M  $KHCO_3$  (pH 9.16) at various potentials (from 0 to  $-0.6 V_{RHE}$ ).

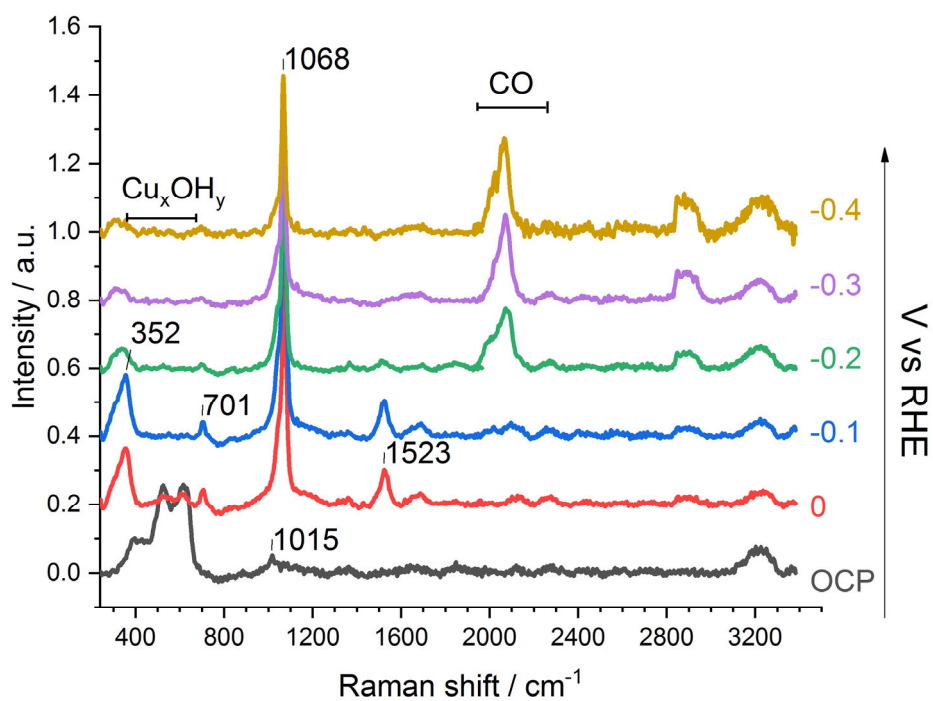


Figure 8.13: Complete data for Figure 3.3 solid line spectra. *Operando* SERS spectra of Cu foam in  $N_2$  saturated 1.0 M  $KHCO_3$  (pH 8.7) at various potentials (from 0 to  $-0.4 V_{RHE}$ ).



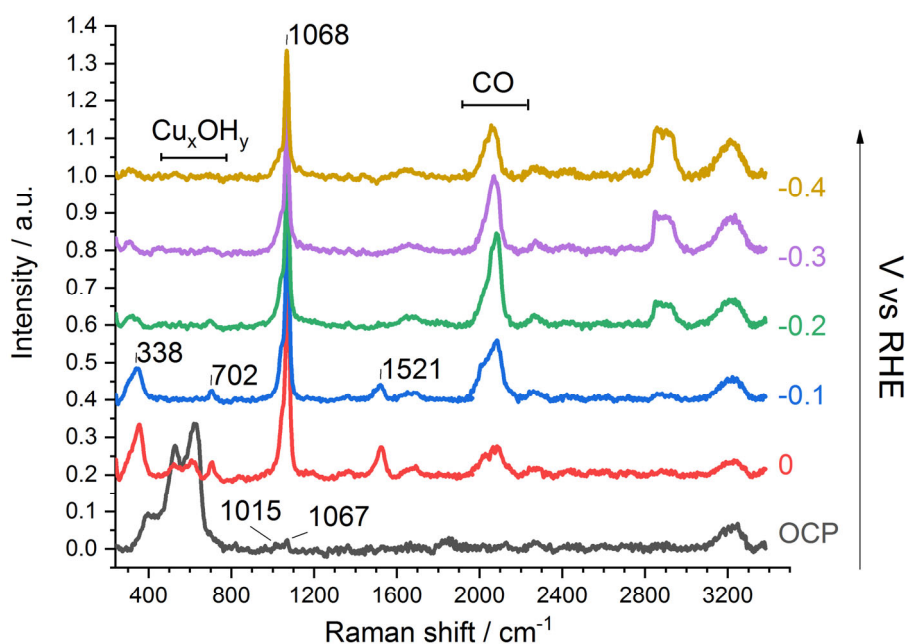


Figure 8.14: Supplementary data for Figure 3.3. *Operando* SERS spectra of Cu foam in  $N_2$  saturated 0.5 M  $KHCO_3$  (pH 8.7) at various potentials (from 0 to  $-0.4 V_{RHE}$ ).

## 8.10 $^{13}C$ isotope experiment

A test experiment was done to check the isotope exchange speed between  $^{12}CO_2$  gas and  $KH^{13}CO_3$  solution. The  $KH^{13}CO_3$  solution was purged with  $^{12}CO_2$  gas while Raman spectra of the solution were taken continuously while the solution composition changed with time. From **Figure 8.15** it can be seen that the peak at  $1326\text{ cm}^{-1}$  of  $H^{13}CO_3^-$  gradually shifts towards  $1364\text{ cm}^{-1}$  which is the natural position of  $HCO_3^-$  band, and the peak at  $1008\text{ cm}^{-1}$  also shifts to  $1011\text{ cm}^{-1}$ . The timescale of this process suggests that more than 30 minutes are needed for all the isotope labelled solution species to exchange with unlabelled gas. For this reason, in the usual experiments, the purging for  $CO_2$  saturation prior measurement lasts only 10 minutes, this is to ensure that the different isotope composition is not altered. In this way a clear distinction can be made whether that the intermediate peaks originate from gas or the solution species.

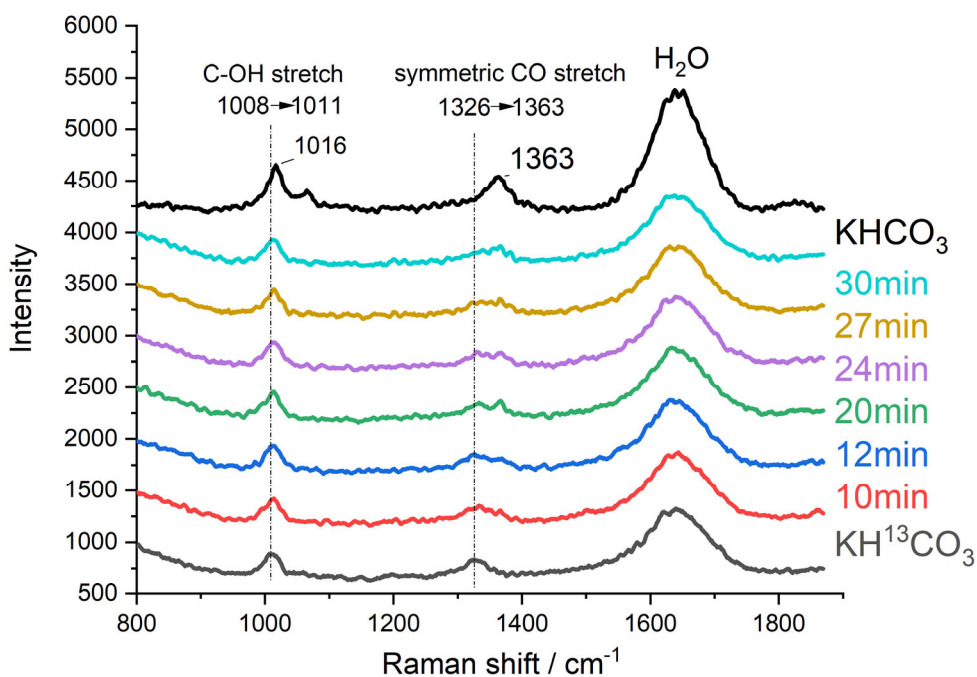


Figure 8.15: Supplementary data for Figure 3.4, saturating  $\text{KH}^{13}\text{CO}_3$  solution with normal  $\text{CO}_2$  gas to trace the isotope change of solution spectra.

A second dataset of *operando* Raman spectra of Cu foam measured in  $\text{CO}_2$  saturated 0.1 M  $\text{KH}^{13}\text{CO}_3$  in comparison to the one taken in normal solution is shown in **Figure 8.16**, the details are shown in **8.17**. As expected, similarly to the data shown in the main text (**Figure 3.4**), in this dataset, only a shift for peak (D) was observed.

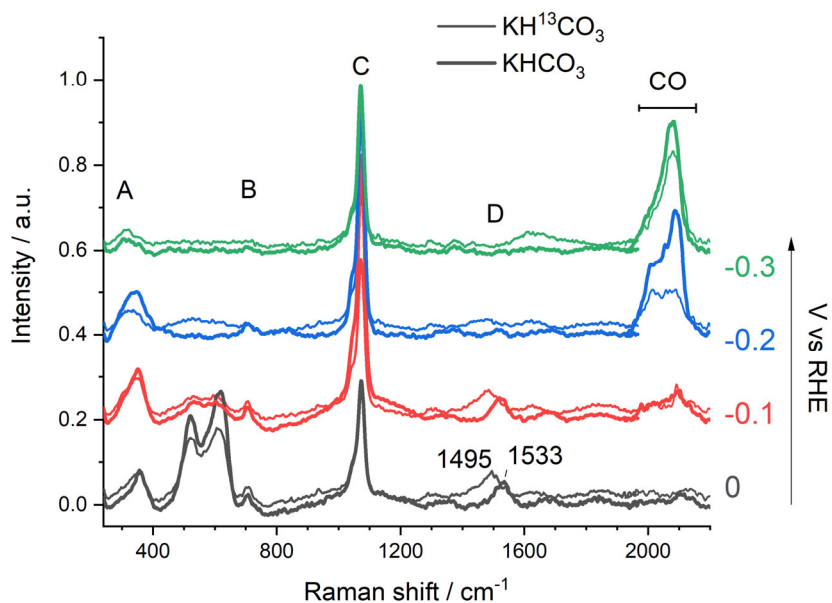


Figure 8.16: Second dataset of *operando* SERS spectra of Cu foam measured in  $\text{CO}_2$  saturated 0.1 M  $\text{KHCO}_3$  (solid line) in comparison to  $\text{CO}_2$  saturated 0.1 M  $\text{KH}^{13}\text{CO}_3$  (pH 6.8) (short dash line) at various potentials (from 0 to  $-0.3 \text{ V}_{\text{RHE}}$ ).

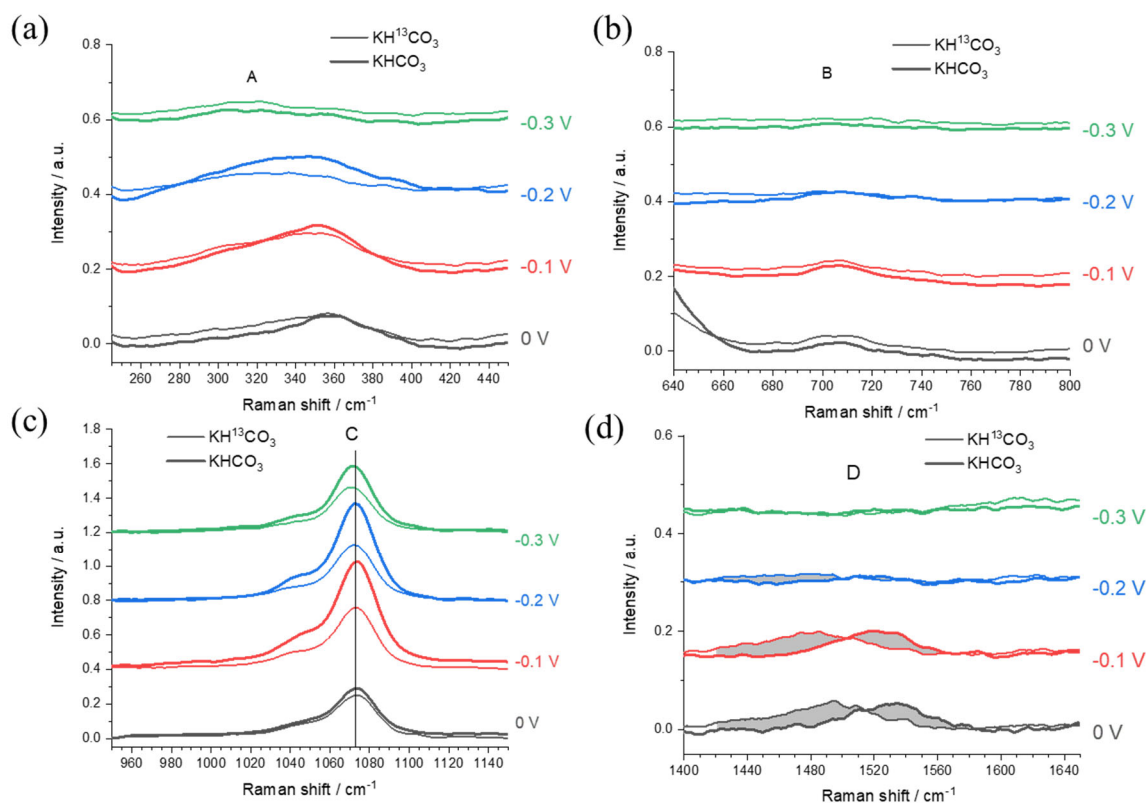


Figure 8.17: Peak comparison between spectra measured in normal solution and  $\text{KH}^{13}\text{CO}_3$  taken from Figure 8.16. (a) Peak at  $350 - 309 \text{ cm}^{-1}$ ; (b) peak at  $705 \text{ cm}^{-1}$ ; (c) peak at  $1070 \text{ cm}^{-1}$  and (d) peak at  $1530\text{-}1510 \text{ cm}^{-1}$ .

## 8.11 CO peak in Kpi buffer

In the experiment performed with Kpi buffer, **Figure 3.7** of the main text, the peak at  $2000 - 2100 \text{ cm}^{-1}$  was unexpected, since no carbon-based species ( $\text{CO}_2$  or  $\text{KHCO}_3$ ) were added to the system intentionally. The same experiment described in **Figure 3.7** / **Figure 8.18** has been repeated to test for reproducibility, results are shown in **Figure 8.19**. Indeed, it can be seen that the unexpected CO peak at  $2000 - 2100 \text{ cm}^{-1}$  appears not always at the same potential and the peak position is not always the same. It has been deduced that the peak is from the minor amount of  $\text{CO}_2$  in solution being reduced or from a small amount of hydroxycarbonate previously/naturally present on the Cu surface (from atmospheric sources). It is interesting to notice that, differently from bicarbonate, in phosphate buffer the adsorbed CO is stable only in a very limited range of potential. This possibly means that as soon it is produced it is detached from the surface, likely replaced by a charged species (like  $\text{K}^+$ ).

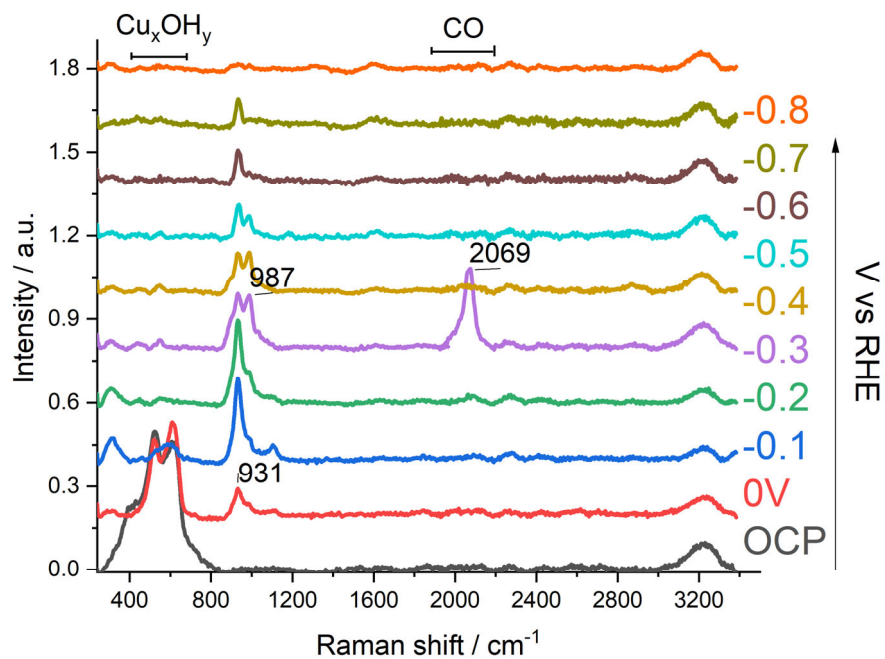


Figure 8.18: Complete data of Figure 3.7, *operando* SERS spectra of Cu foam in  $N_2$  saturated 0.1 M  $KH_2PO_4/K_2HPO_4$  (pH 6.8) at various potentials (from 0 to  $-0.8 V_{RHE}$ ).

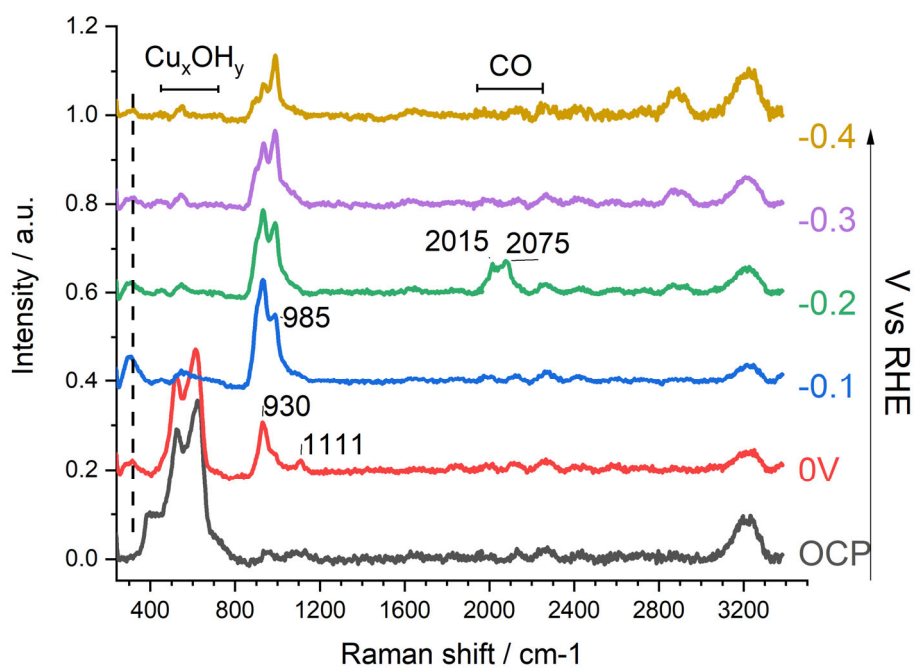


Figure 8.19: Duplicate for Figure 3.7. *Operando* SERS spectra of Cu foam in  $N_2$  saturated 0.1 M  $KH_2PO_4/K_2HPO_4$  (pH 6.8) at various potentials (from 0 to  $-0.4 V_{RHE}$ ).

## 8.12 The different origin of peak (C) and (D)

A supplementary *operando* Raman measurement was conducted, with a different concentration of  $\text{K}_2\text{CO}_3$  electrolyte (to keep the same  $\text{K}^+$  concentration), to further clarify the origin of the peaks C and D. **Figure 8.20** shows that in 50 mM  $\text{K}_2\text{CO}_3$  electrolyte, peak (C) at  $1065\text{ cm}^{-1}$  is always present whereas peak (D) at  $1530\text{ cm}^{-1}$  never appears. This corroborates the different source of these two peaks; peak (C) at  $1065\text{ cm}^{-1}$  can be originated from carbonate adsorption thus it is always found in all the conditions, whereas peak (D) at  $1530\text{ cm}^{-1}$  does not seem to belong to a solution species. In the main text it was proposed that peak (D) is from a hydroxycarbonate that only appears under proper conditions.

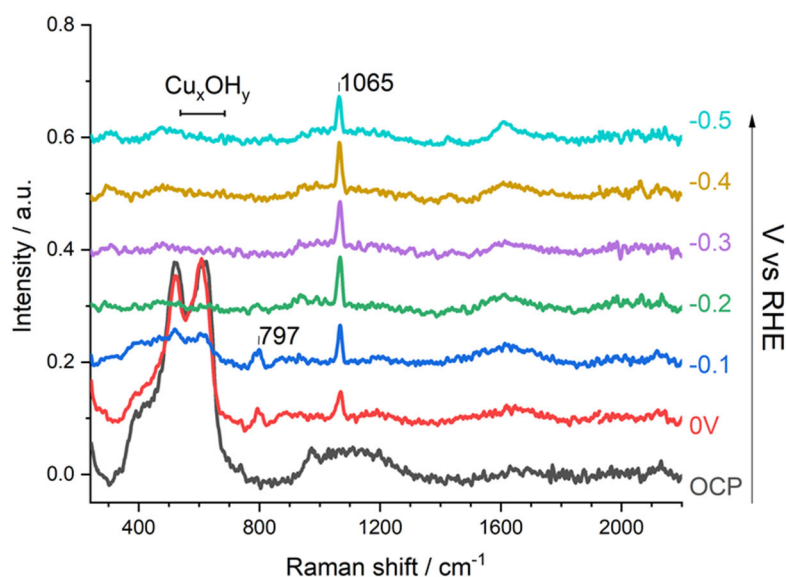


Figure 8.20: *Operando* SERS spectra of Cu foam in  $\text{N}_2$  saturated 0.05 M  $\text{K}_2\text{CO}_3$  (pH 11.4) at various potentials (from 0 to  $-0.5\text{ V}_{\text{RHE}}$ ).

## 8.13 Electro-chemical active surface area determination for Cu foam

The estimation of the active area of the Cu-foam electrodes have been carried out by impedance spectroscopy. The active area have been estimated by the ratio of the capacitances of the Cu-foam electrode vs a planar (mirror-like) copper electrode (CPE-C foam / CPE-C foil = 61.72). Electrochemical Impedance Spectroscopy (EIS) of electrode with the same geometric area,  $1\text{ cm}^2$ , have been recorded with a sp-200 Biologic potentiostat (in  $\text{NaClO}_4$  0.1 M solution at  $-0.25\text{ V}_{\text{RHE}}$  (in a potential region where no e-chem activity was measured)) and analyzed with a Z-view software. For the fitting a simple Randles circuit was used. The experimental data, the resulting fitting and the equivalent circuit is reported in **Figure 8.21**.

Assuming that a single adsorbed carbonate molecule occupies a surface of  $1.4 \text{ \AA}$  radius (C-O bond length) then the  $61.72 \text{ cm}^2$  active area would be occupied by about  $7.9 \times 10^{16}$  molecules, i.e.  $1.3 \times 10^{-7}$  mol of carbonate. This is likely an overestimation since most likely a complete monolayer of material would not form due to equilibrium with the species in solution. Assuming that every carbonate accept one electron, the total charge exchanged in the reduction of a monolayer of adsorbed carbonate in the foam electrode would produce  $1.3 \times 10^{-7} \times F$  (Faraday constant  $96485 \text{ C/mol}$ ) =  $12.5 \text{ mC}$ .

In the Cu foam samples investigated in this study an average of  $300 \text{ mC}$  are exchanged in the CV ( $1 \text{ mV/s}$ , current peaks ranging from  $-4$  to  $-15 \text{ mA}$ , spanning a potential range of  $100$ - $200 \text{ mV}$ ). This large difference cannot be justified by the possibility that fresh carbonate can substitute reduced carbonate on the Cu surface, because this implies the instauration of a diffusion controlled regime which does not match the current behaviour of CVs. This suggest that the current observed in the CV of Cu foam cannot be related to a monolayer of material, contrarily it is attributed to the consumption/formation of several monolayer adhere to the Cu surface, i.e. a relatively thick layer of inorganic material.

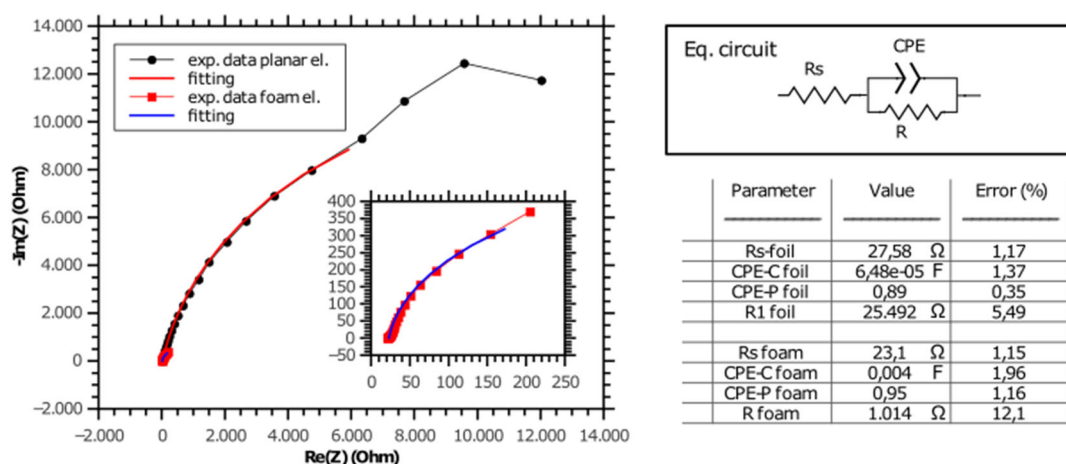


Figure 8.21: Impedance spectra of Cu foil in comparison to Cu foam (measured in  $0.1 \text{ M NaClO}_4$  solution at  $-0.25 V_{\text{RHE}}$ ) and the simulated equivalent circuit.

## 8.14 Determination of the open circuit potential of $0.1 \text{ M}$

### $\text{KHCO}_3$ solution

A three-electrode cell was assembled using  $\text{CO}_2$  saturated  $0.1 \text{ M KHCO}_3$  (pH 6.8) as electrolyte, a platinum net electrode as working electrode (the potential probe), a platinum mesh as counter electrode and a leakless  $\text{Ag/AgCl}$  sat. as reference electrode. The open circuit potential was acquired, vs. reference, after letting the system equilibrate for 5 minutes. The potential read was  $1.1 V_{\text{RHE}}$ .

## 8.15 Raman spectra of D labelled malachite sample

Compared to normal malachite sample, D<sub>2</sub>O labelled sample showed a shift for peak at 430 cm<sup>-1</sup> to 420 cm<sup>-1</sup>, which suggests that this peak is from a Cu-OH vibration.

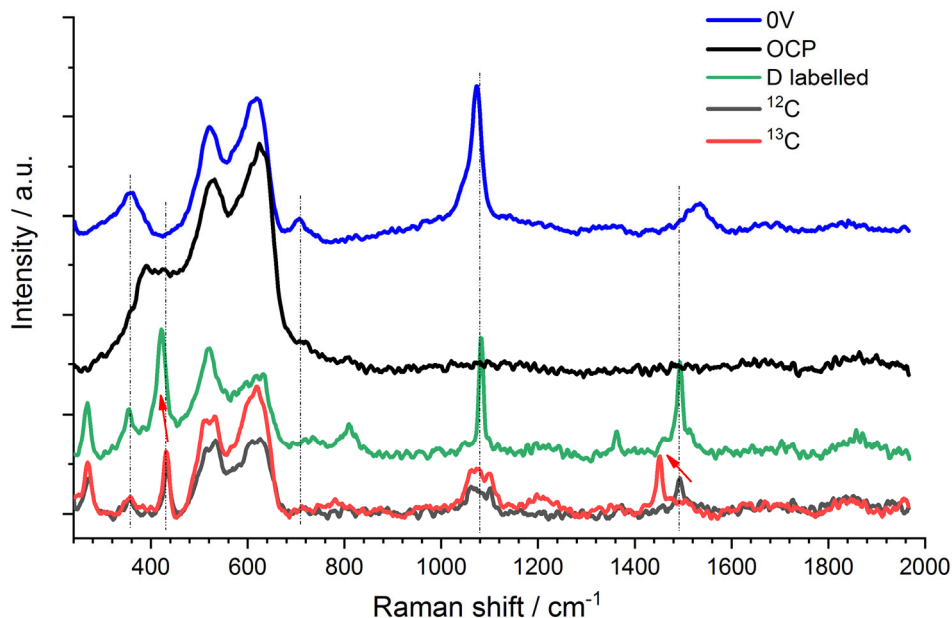


Figure 8.22: SERS spectra of prepared malachite (by putting Cu foam in <sup>12</sup>C, <sup>13</sup>C or D labelled bicarbonate solution for 6 days) under OCP in 0.1 M KHCO<sub>3</sub>, <sup>13</sup>C labelled KHCO<sub>3</sub> and KDCO<sub>3</sub> solution, in comparison to spectra of Cu foam measured in CO<sub>2</sub> saturated 0.1 M KHCO<sub>3</sub> at OCP and 0 V<sub>RHE</sub>.

## 8.16 CV series data

In order to investigate the electrochemical redox process of Cu foam electrode, a series of CV (10mV/s) was measured in N<sub>2</sub> saturated 0.5 M KHCO<sub>3</sub> with gradually enlarged scanning range as shown in **Figure 8.23**. The first panel shows the initial cycles performed starting from OCP (around 0.5 V<sub>RHE</sub>) and sweeping towards cathodic potentials to 0.05 V<sub>RHE</sub> first vertex, and the second vertex back towards anodic potentials gradually up to 1 V<sub>RHE</sub> (the OCP potential is about at the center of the scan). Three anodic peaks can be seen as a1, a2 and a3. Correspondingly, three cathodic peaks were observed labelled as c1, c2 and c3. According to literature, they could be assigned to Cu to Cu<sub>2</sub>O (a1), Cu<sub>2</sub>O to CuO/Cu(OH)<sub>2</sub> (a2, a3). It should be noted that, the first scan towards negative potential does not show any relevant cathodic peaks in the range of 0 to 0.5 V<sub>RHE</sub>. However, in the subsequent scans of 2<sup>nd</sup> to 4<sup>th</sup> cycle, anodic currents are coupled to respective cathodic peaks, this indicates that the cathodic currents observed in the first four cycles are due to the artificial anodic processes, in other words, the oxide/hydroxide naturally present on Cu was not (substantially) reduced in the first four cycles. The confirmation of this

interpretation is observed in the 5<sup>th</sup> cycle, where a large reduction peak (c') appeared in the first scan of the cycle series. In order to investigate the origin of this peak, hypothesized to be the spontaneous Cu oxide/hydroxide, samples which are dried with O<sub>2</sub> and stored in O<sub>2</sub> environment and without drying left with a water layer on the surface (for 4 days) respectively were prepared. The same CV series were performed for these two samples, the first and second scans of the 5<sup>th</sup> cycle of every kind of sample is compared in **Figure 8.24**. Interestingly the reduction peak (c') became more prominent for the sample stored with water layer on the surface, and even remained in the 2<sup>nd</sup> scan, whereas less obvious for O<sub>2</sub> stored sample, which suggest a relation of this peak to the amount of hydroxide. In the main text, this result is further discussed.



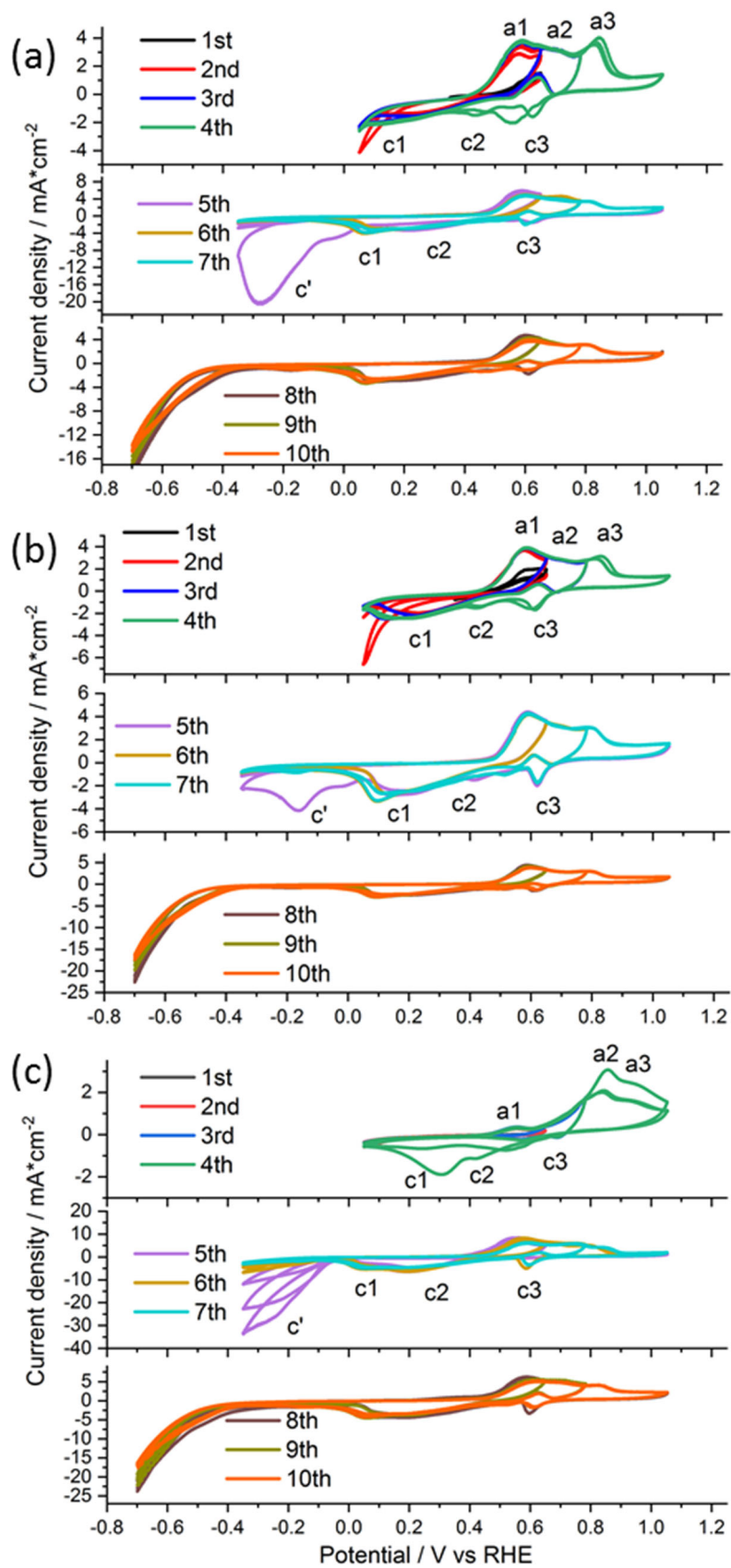


Figure 8.23: CV series (10mV/s) data of Cu foam (a); Cu foam dried with O<sub>2</sub> and stored in O<sub>2</sub> environment (b); and Cu foam without drying stored with water layer on the surface (4 days) (c), measured in N<sub>2</sub> saturated 0.5 M KHCO<sub>3</sub> (pH 8.7).

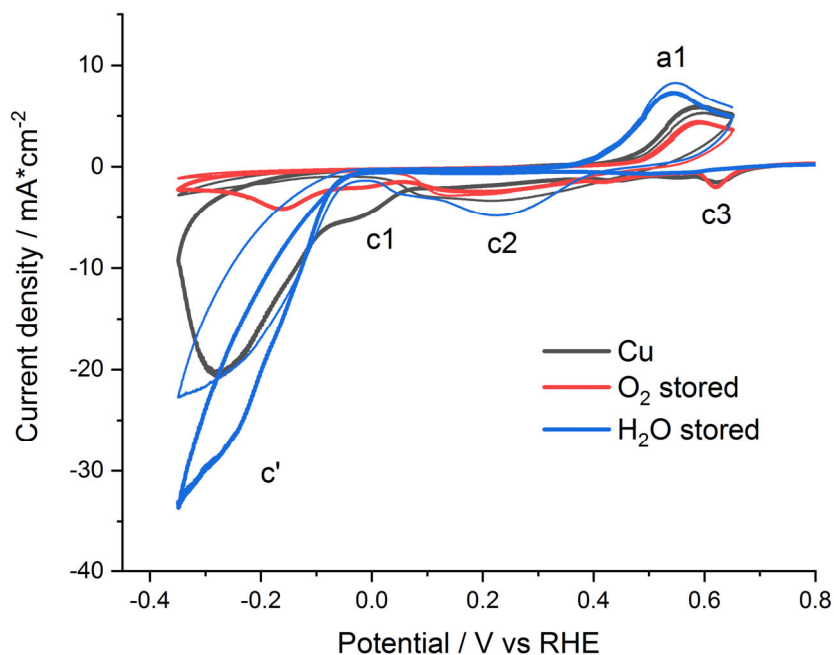


Figure 8.24: Comparison of 5<sup>th</sup> cycle of CV series measured on Cu foam, Cu foam dried with O<sub>2</sub> and stored in O<sub>2</sub> environment (O<sub>2</sub> stored) and Cu foam without drying stored with water layer on the surface (H<sub>2</sub>O stored).

## 8.17 Cyclic-voltammograms and full Raman spectra

By storing the Cu foam electrode with water layer on the surface for 4 days, the film seems to form more hydroxide as has been discussed in the **Section 8.16** in CV series data. This can also be seen in the CV data shown in **Figure 8.25(a)**, where the huge reduction band in the first but not second cycle. The Raman spectra acquired during the 1<sup>st</sup> cycle is shown in **Figure 8.25(b)**. The malachite enriched sample was also used to perform the same CV in carbonate electrolyte (**Figure 8.26(a)**). The full Raman data of the 1<sup>st</sup> cycle is shown in **Figure 8.26(b)**. The peak intensities of CO read in the Raman data of 1<sup>st</sup> CV cycle of these two samples together with Cu foam sample shown in **Figure 3.12, 3.13** were analyzed by a home-made software gloFit and plotted in **Figure 3.17** in the main text. The 1<sup>st</sup> and 2<sup>nd</sup> CV of malachite measured in bicarbonate electrolyte show similar reduction current within each other, this suggests that even in the second cycle, malachite is still not fully reduced, this will be discussed in **Section 8.19**.

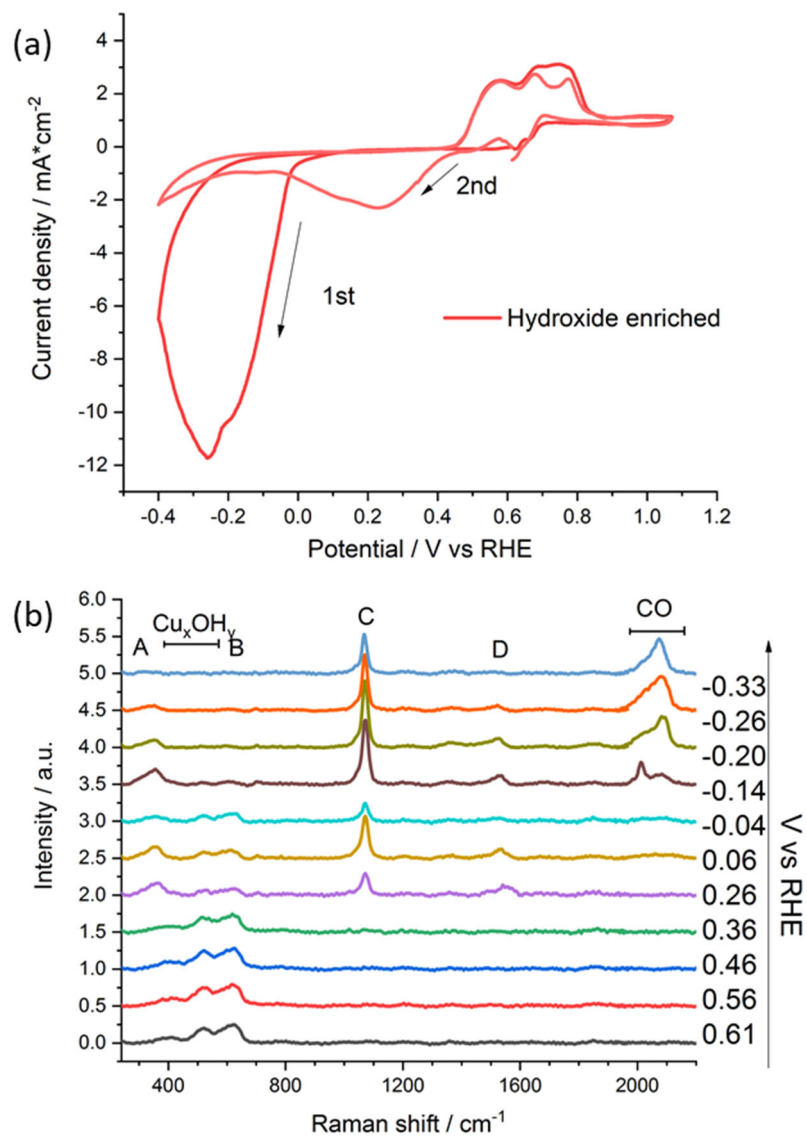


Figure 8.25: (a) CV 1mV/s of hydroxide enriched Cu foam measured in N<sub>2</sub> saturated 0.5 M KHCO<sub>3</sub> (pH 8.7); (b) Raman spectra of the first cycle from 0.61 to -0.4 V<sub>RHE</sub>.

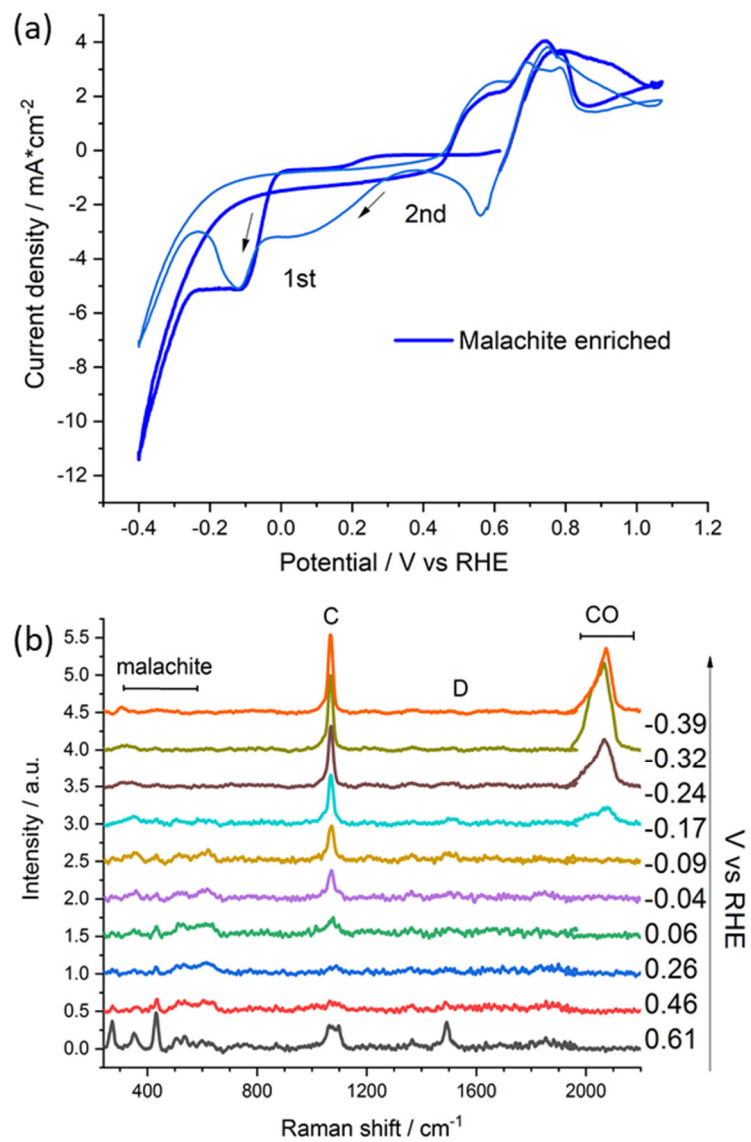


Figure 8.26: (a) CV 1mV/s of malachite enriched sample measured in N<sub>2</sub> saturated 0.5 M KHCO<sub>3</sub> (pH 8.7); (b) Raman spectra of the first cycle from 0.61 to -0.4 V<sub>RHE</sub>.

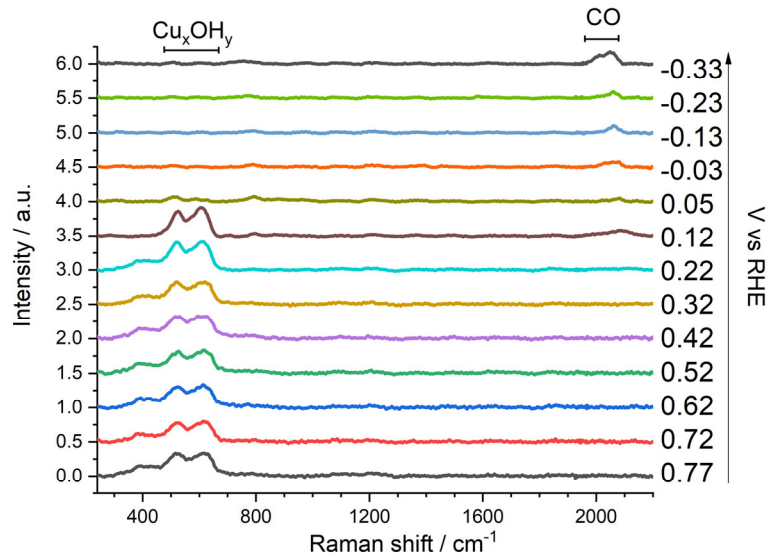


Figure 8.27: Raman spectra of Cu foam measured in  $N_2$  saturated 0.1 M KOH (pH 13) during the first cycle of CV from 0.77 to  $-0.4 V_{RHE}$ . Minor CO peak might come from the minor malachite formation on Cu foam due to the  $CO_2$  gas in the air.

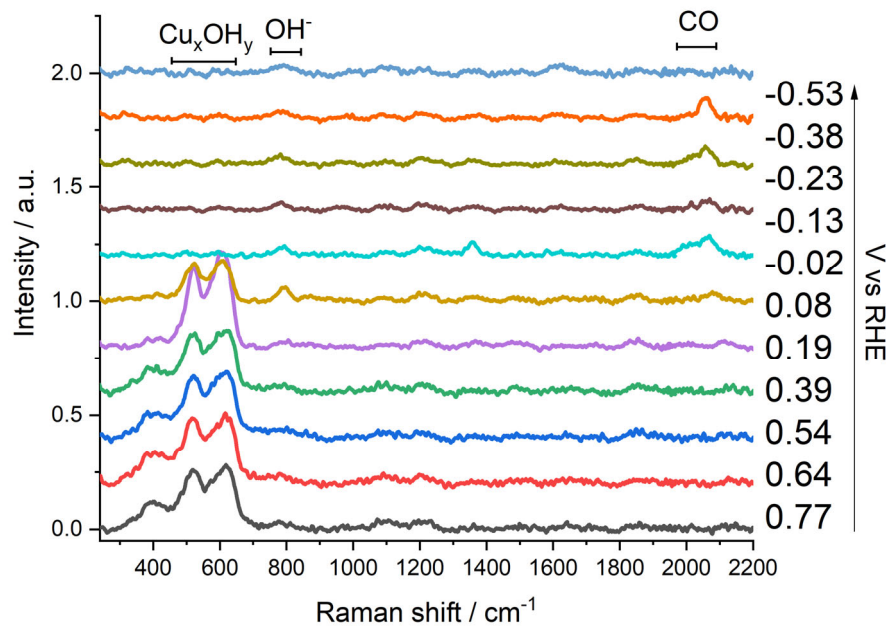


Figure 8.28: Raman spectra of hydroxide enriched sample measured in  $N_2$  saturated 0.1 M KOH (pH 13) during the first cycle of CV from 0.77 to  $-0.6 V_{RHE}$ . Minor CO peak might come from the minor malachite formation on Cu foam due to the  $CO_2$  gas impurity presence.

## 8.18 CO presence at low overpotential relates to (hydro)oxide

In order to further illustrate the role of oxide, long time operation experiments on “oxide” containing samples and *in-situ* “reduced Cu” surface were performed. The “oxide” sample is just the Cu foam catalyst with a naturally formed surface oxide layer, and the “reduced Cu” sample is prepared by cycling the “oxide” sample 4 cycles and scanning 3 times linear sweeping voltammetry both between -0.1 to -0.9  $V_{\text{RHE}}$  before measurement (**Figure 8.29a**). A similar experiment to the normal *operando* Raman experiments as shown in **Figure 8.10** was performed but instead of 2 mins the potential was applied for 10 mins. A longer operation allowed the reaction to accumulate products enabling the detection of the most abundant species. The long-time measurement on “reduced Cu” was performed starting from -0.1  $V_{\text{RHE}}$  (2 mins), -0.2  $V_{\text{RHE}}$  (4 mins), and then from -0.3 to -0.8  $V_{\text{RHE}}$  with each potential for 10 mins (**Figure 8.29b** upper panel). The steps with shorter times than 10 min were used only on the “reduced Cu” sample since at these potentials, with such sample, no product is seen in the Raman spectra. On oxide sample the long-time experiment was done by applying a constant potential starting from 0 to -0.8  $V_{\text{RHE}}$  with each potential for 10 mins (**Figure 8.29b** bottom panel). The last spectrum of each potential acquired on “oxide” surface and “reduced Cu” surface are compared in **Figure 3.18**. Complete spectra for “oxide” and “reduced Cu” are shown in **Figure 8.30, 8.31** respectively. The spectra especially at low potential show significant differences between the two samples. When starting from oxide, the CO band at around  $2060\text{ cm}^{-1}$  appeared at low overpotential (-0.2  $V_{\text{RHE}}$ ) which is unexpected given that its reduction potential is -0.10  $V_{\text{RHE}}$ . The intensity of CO peak in the oxide sample is also higher than on reduced Cu sample through all potentials. The carbonate peak intensity is more prominent on the “oxide” sample. The assignment of peak  $2060\text{ cm}^{-1}$  to CO was confirmed by experiment in  $\text{D}_2\text{O}$  electrolyte (**Figure 8.32**). Overall, this means that the CO production overpotential is lower on oxide surface, this can be explained by the presence of the hydroxyl-carbonate as discussed in the main text. The early appearance and the abundance of \*CO might be the reason for high selectivity of oxide derived Cu for  $\text{C}_2$  product. It has been proposed that \*CO coverage is decisive for  $\text{C}_2\text{H}_4$  production, when \*CO accumulate to a certain amount at appropriate potential they might form CO dimer and further to  $\text{C}_2\text{H}_4$  (Y. Huang et al., 2017; Sandberg, Montoya, Chan, & Nørskov, 2016). In line with this the lower overpotential for CO production will also help decrease  $\text{C}_2\text{H}_4$  production overpotential.

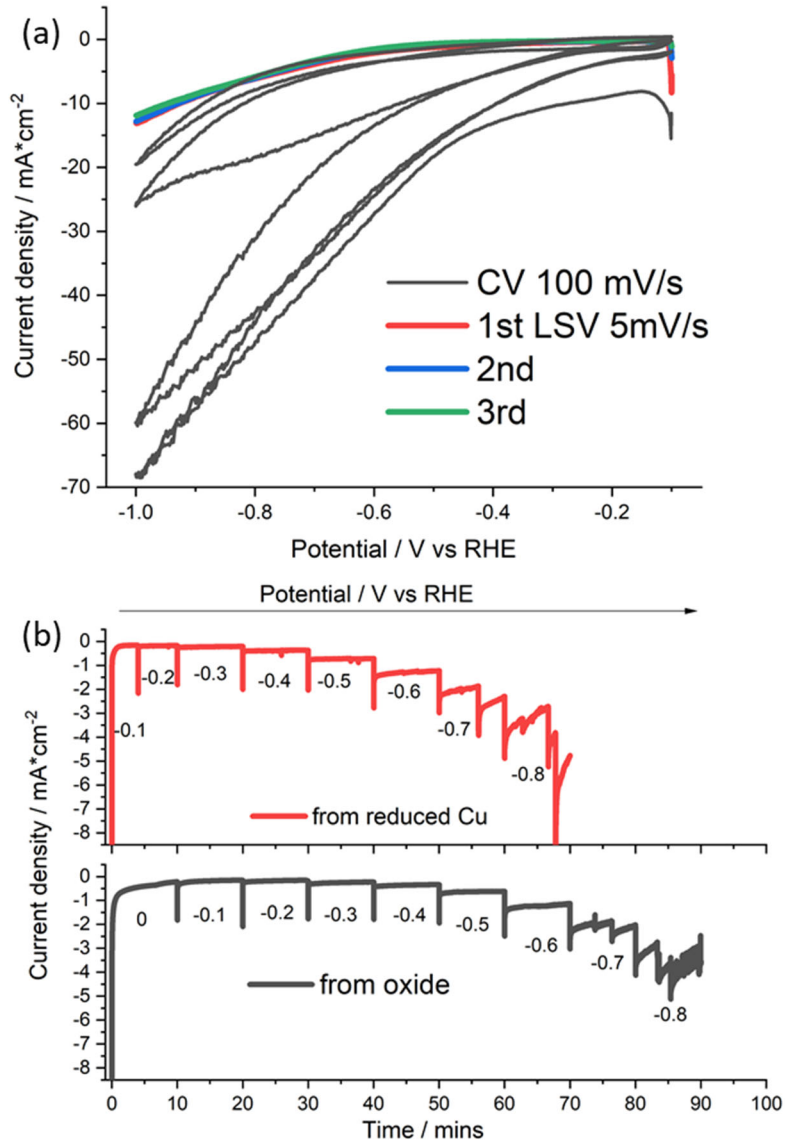


Figure 8.29: Electrochemical data of long-time measurement on reduced Cu foam, the reduction procedure is scanning CV (100 mV/s) 4 cycles, and LSV (5 mV/s) 3 times (a). After that starting from -0.1 V<sub>RHE</sub> 2 mins, -0.2 V<sub>RHE</sub> 4 mins, then -0.3 to -0.8 V<sub>RHE</sub> each potential 10 mins. The data is shown in (b) upper panel. The experiment on Cu foam with natural oxide started from 0 to -0.8 V<sub>RHE</sub> with each potential for 10 mins, and the data is shown in (b) bottom panel, the last Raman spectrum of each potential for both situation in comparison is shown in Figure 3.18.

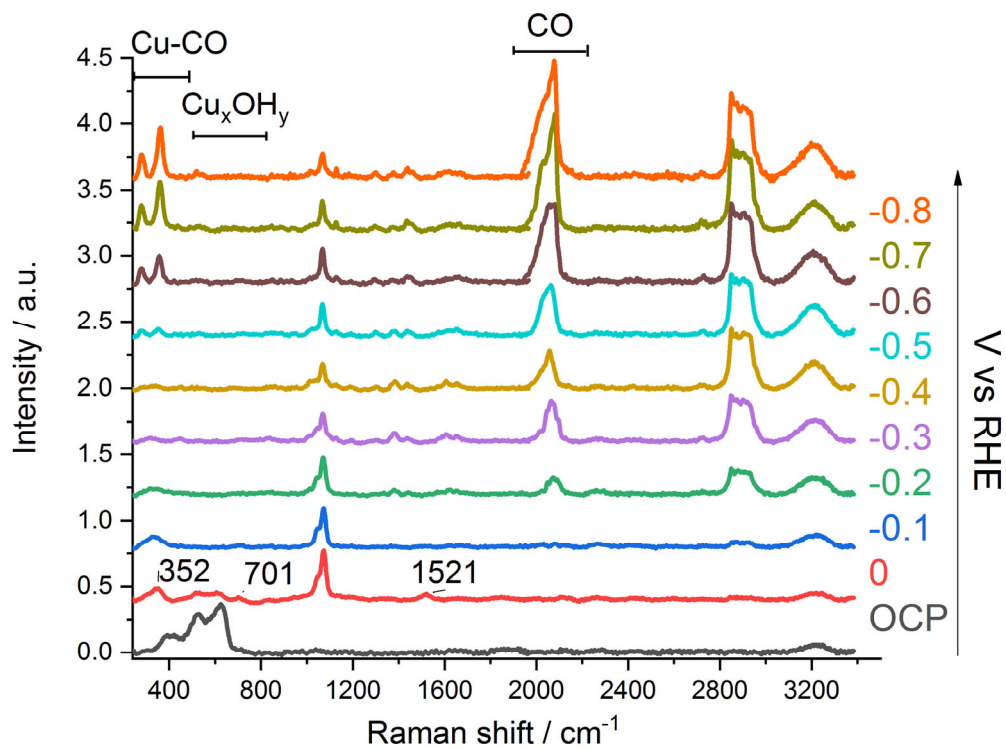


Figure 8.30: Complete spectra for long time measurement of Cu foam electrode starting from oxide. CO<sub>2</sub> gas was constantly purged to 0.1 M KHCO<sub>3</sub> electrolyte (pH 6.8), spectra was taken in the end of each potential.

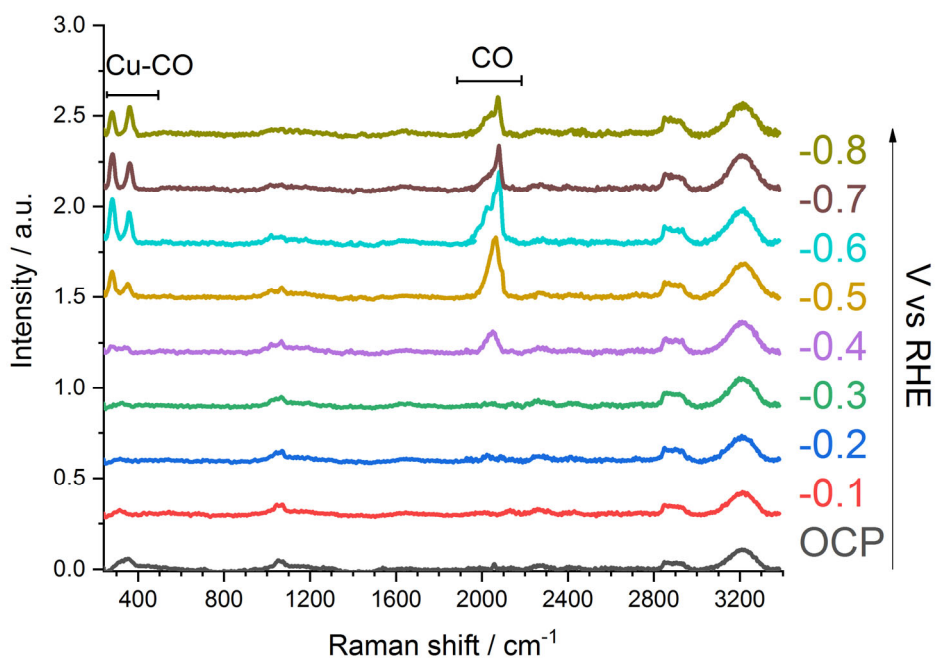


Figure 8.31: Complete spectra for long time measurement of Cu foam electrode starting from reduced state. CO<sub>2</sub> gas was constantly purged to 0.1 M KHCO<sub>3</sub> electrolyte (pH 6.8), spectra was taken in the end of each potential.



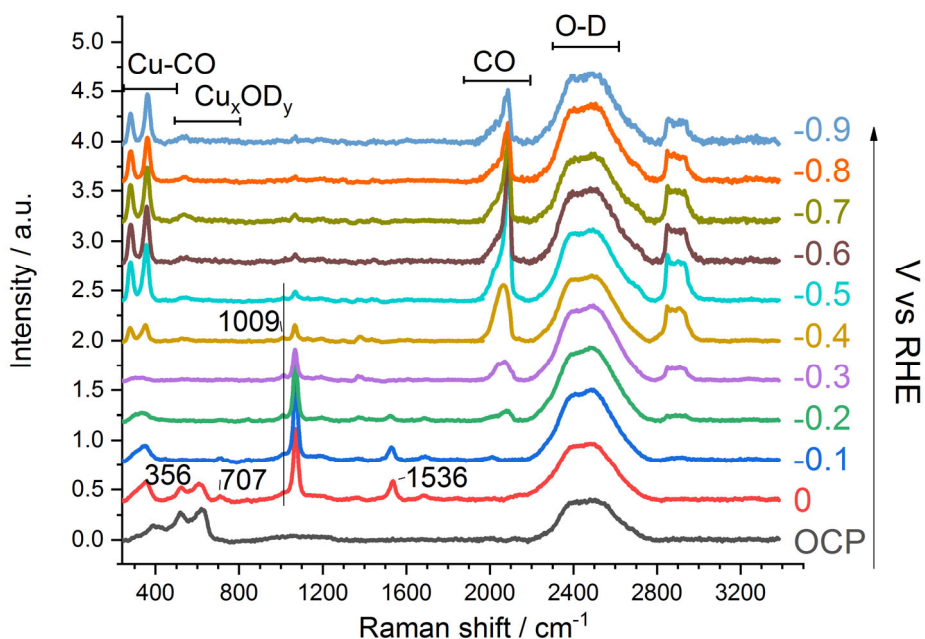


Figure 8.32: Long time measurement for Cu foam electrode starting from oxide in D<sub>2</sub>O prepared electrolyte. CO<sub>2</sub> gas was constantly purged to 0.1 M KDCO<sub>3</sub> electrolyte (pH 7.2), spectra were taken in the end of each potential.

## 8.19 Different behaviour of malachite enriched Cu electrodes in KOH and KHCO<sub>3</sub> electrolyte

The comparison of CV of a malachite enriched Cu electrode measured in N<sub>2</sub> saturated 0.1 M KOH and 0.5 M KHCO<sub>3</sub> is shown in **Figure 8.33**. The CV scan range is shorter in bicarbonate buffer than in KOH. In bicarbonate the range is limited in the cathodic side by hydrogen evolution reaction, in the anodic direction, the oxidation enters a regime of pitting corrosion after +1.0 V<sub>RHE</sub> which makes pointless a further sweep to positive potentials. A series of microscope photos were taken during these CVs, they are shown in **Figure 8.34**. In the pictures, the green colour is from malachite, the red is the remaining unchanged Cu foam.

In **Figure 8.33**, the two reduction waves in KOH solution have already been explained in this supporting material and it is attributed to the reduction of the Cu hydroxide for the first wave, and then malachite for the second (at more negative potentials). The difficulty of reduction of malachite in carbonate buffer further suggest that the carbonate in solution is spontaneously pushed to form hydroxycarbonate when local hydroxide is present/produced in the cathodic process, therefore it prevents the complete reduction of malachite. This can be confirmed by the picture shown in **Figure 8.34**. In the bicarbonate set, the green colour (malachite) is persistent after the first cycle and it seems to turn slightly blue. The shift to blue could be simply an optical effect due to a white balance correction, or it could be a real chemical transformation

of the malachite possibly into  $\text{Cu}(\text{OH})_2$ , though this was not proven by any other mean and it remain a speculation. In the KOH solution experiment, the disappearance of green colour occurs fully reaching  $-0.53 \text{ V}_{\text{RHE}}$ , only the red colour from the Cu foam remains in the microscope photos. The overall analysis of the electrochemistry, of the recorded Raman spectra and captured picture, suggest that the reduction of malachite cannot complete with one cycle in bicarbonate buffer. Whereas in KOH solution the reduction of malachite can be completed in the first cycle.

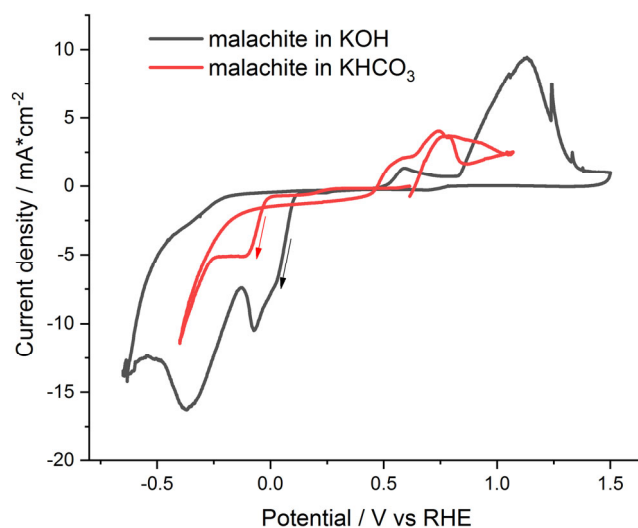


Figure 8.33: CV 1st cycle of Cu formed malachite measured in  $\text{N}_2$  saturated 0.1 M KOH (pH 13) in comparison to the data measured in  $\text{N}_2$  saturated 0.5 M  $\text{KHCO}_3$  (pH 8.7).

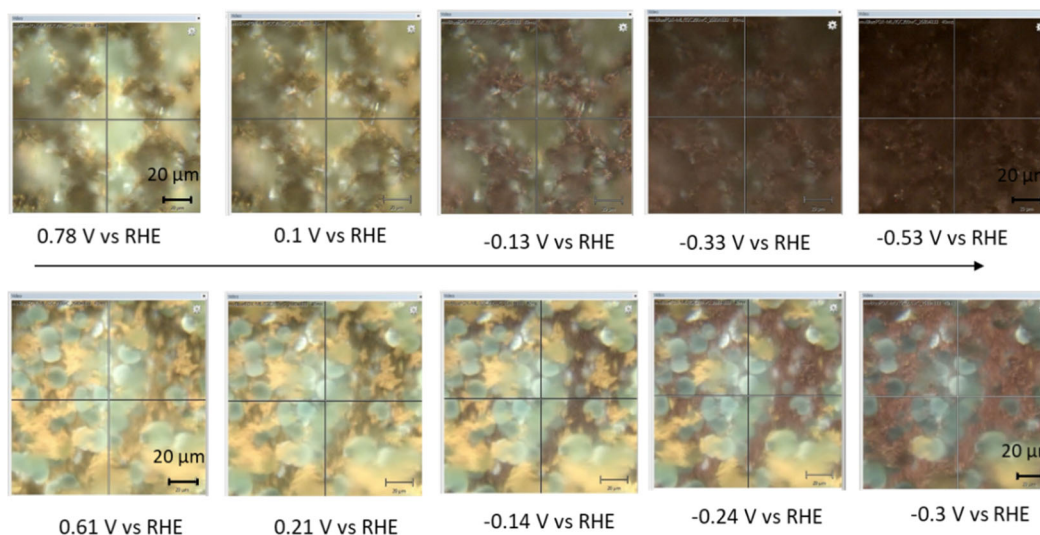


Figure 8.34: Microscope pictures of Cu formed malachite under potential in the first cycle of CV measured in  $\text{N}_2$  saturated 0.1 M KOH (pH 13) (top) and  $\text{N}_2$  saturated 0.5 M  $\text{KHCO}_3$  (pH 8.7) (bottom). After applying potential until  $-0.33 \text{ V}_{\text{RHE}}$  in KOH, mostly malachite green colour disappeared, whereas in bicarbonate electrolyte, the malachite green colour changed to blue and remained.

## 8.20 Spectra in between 0-200 $\mu\text{m}$

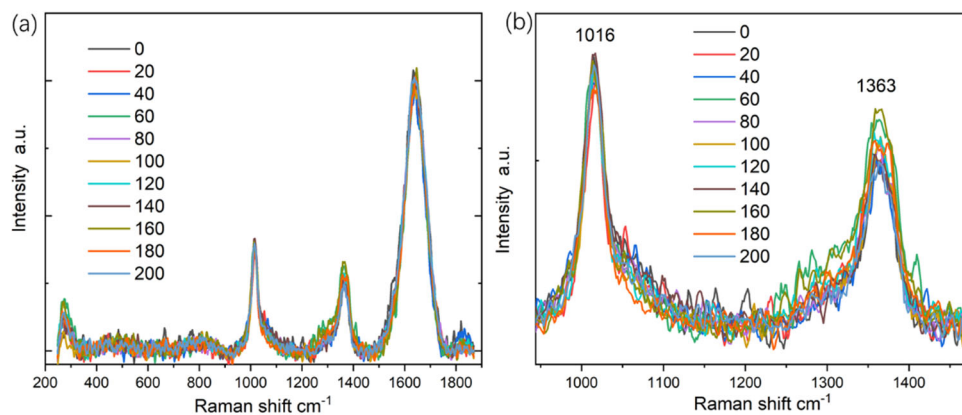


Figure 8.35: (a) Raman spectra of solution from 0 to 200  $\mu\text{m}$  under OCP. (b) amplification for (bi)carbonate bands region.

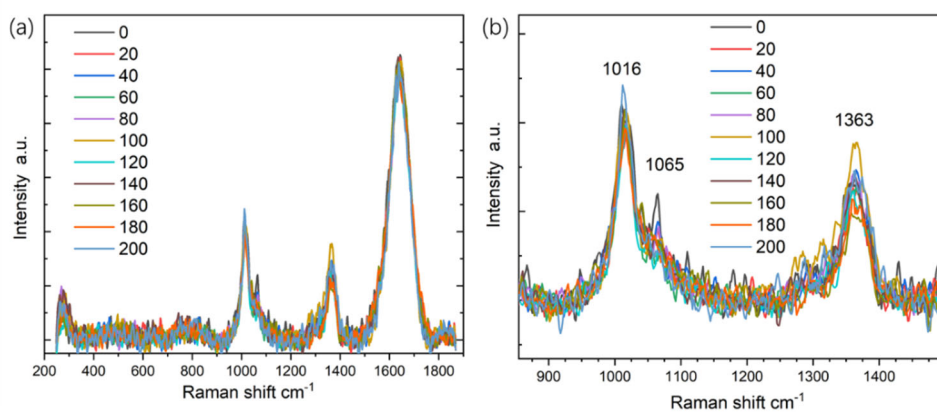


Figure 8.36: (a) Raman spectra of solution from 0 to 200  $\mu\text{m}$  under  $-0.6 V_{\text{RHE}}$ . (b) amplification for (bi)carbonate bands region.

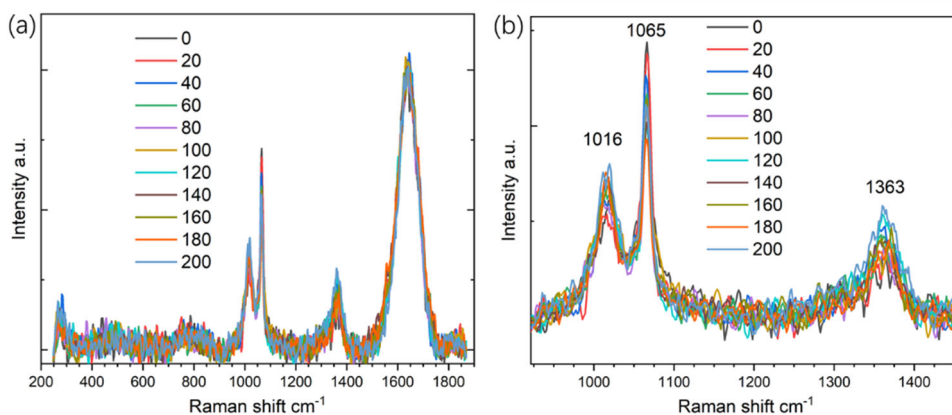


Figure 8.37: (a) Raman spectra of solution from 0 to 200  $\mu\text{m}$  under  $-0.7 V_{\text{RHE}}$ . (b) amplification for (bi)carbonate bands region.

## 8.21 Local pH determination in flow cell

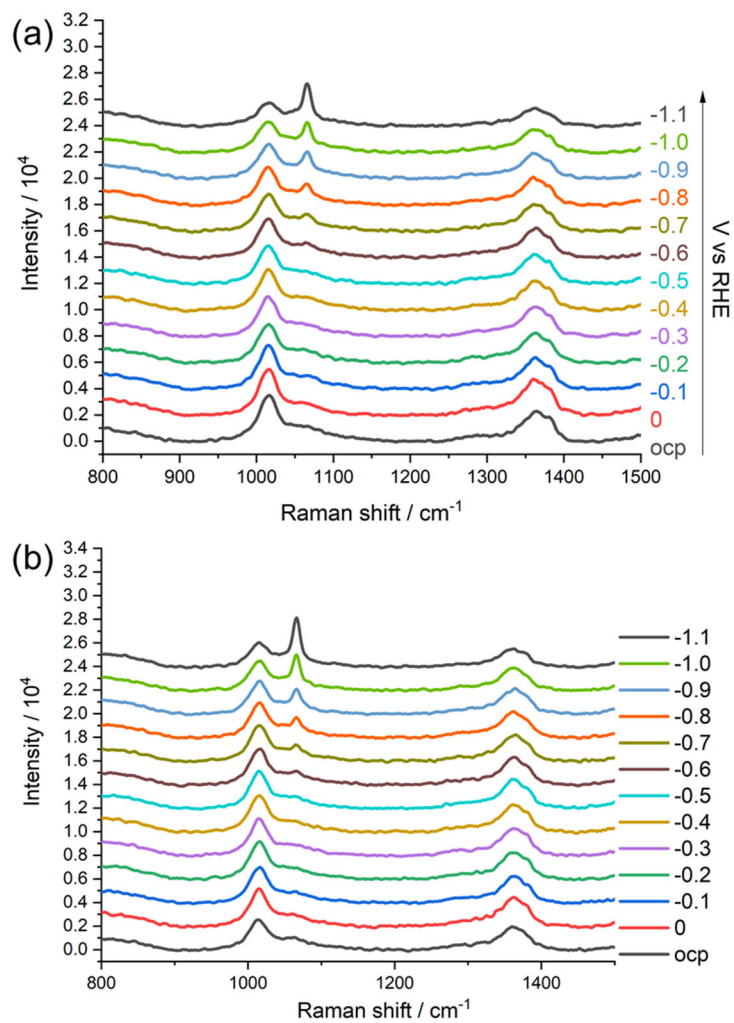


Figure 8.38: Raman spectra of solution on Cu foam in flow cell (flow rate 10 mL/min): (a) first CA on fresh catalyst; (b) second CA on reduced catalyst from 0 to -1.1  $V_{\text{RHE}}$ .

## 8.22 CA data for local pH measurement in flow cell and normal Raman cell

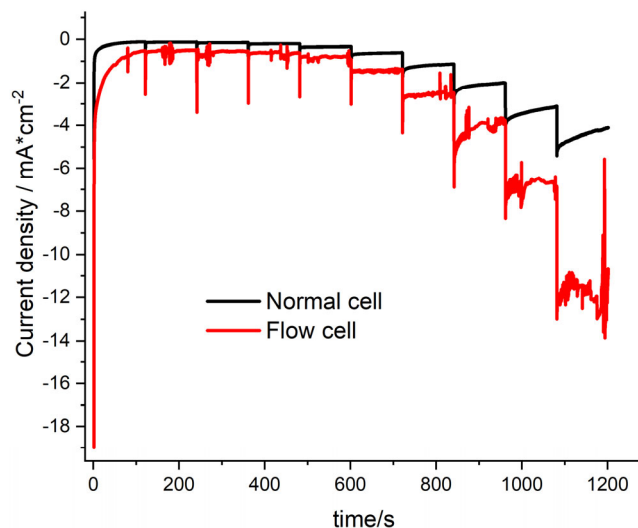


Figure 8.39: The CA data of local pH measurement experiment in flow cell (flow rate 10 mL/min) and normal cell at potentials from 0 to -0.9 V<sub>RHE</sub>.

## 8.23 Comparison of H<sub>2</sub>O and D<sub>2</sub>O prepared bicarbonate solution spectra

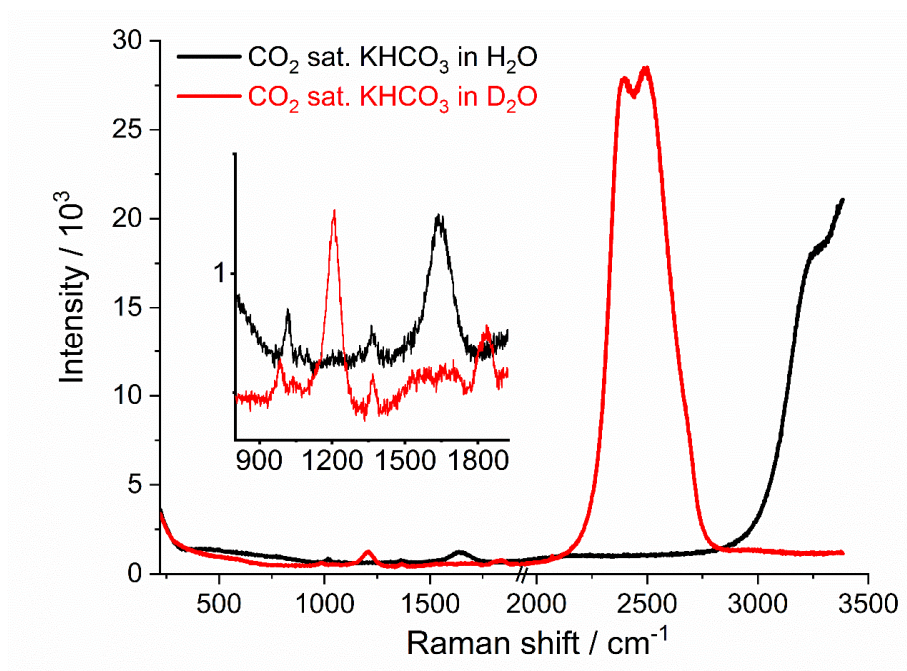


Figure 8.40: Solution spectra of H<sub>2</sub>O and D<sub>2</sub>O prepared 0.1 M KHCO<sub>3</sub>.

Table 8.5: Assignments of Raman shift of bicarbonate bands in H<sub>2</sub>O/D<sub>2</sub>O prepared bicarbonate solutions.

Raman shift / cm <sup>-1</sup>		Mode
KHCO <sub>3</sub> in H <sub>2</sub> O	KHCO <sub>3</sub> in D <sub>2</sub> O	
1015	986	S(C-OH)
1365	1366	SS(CO)
1642	1209	B(OH)
2950-3730	2200-2800	S(OH)

## 8.24 CA data for H<sub>2</sub>O and D<sub>2</sub>O local pH measurement

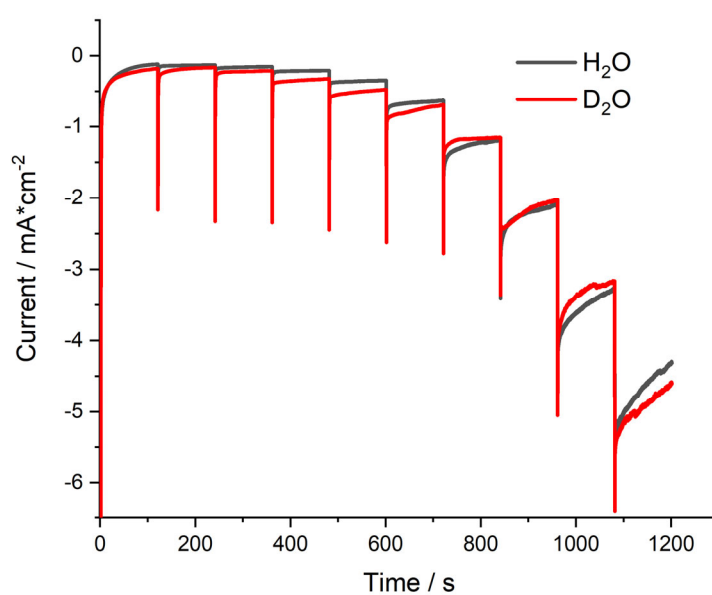


Figure 8.41: Current comparison for pH determination measurement in H<sub>2</sub>O and D<sub>2</sub>O prepared bicarbonate solutions under CA series potentials from 0 to -0.9 V<sub>RHE</sub>.

## 8.25 GC data for CO<sub>2</sub> RR in D<sub>2</sub>O prepared electrolyte

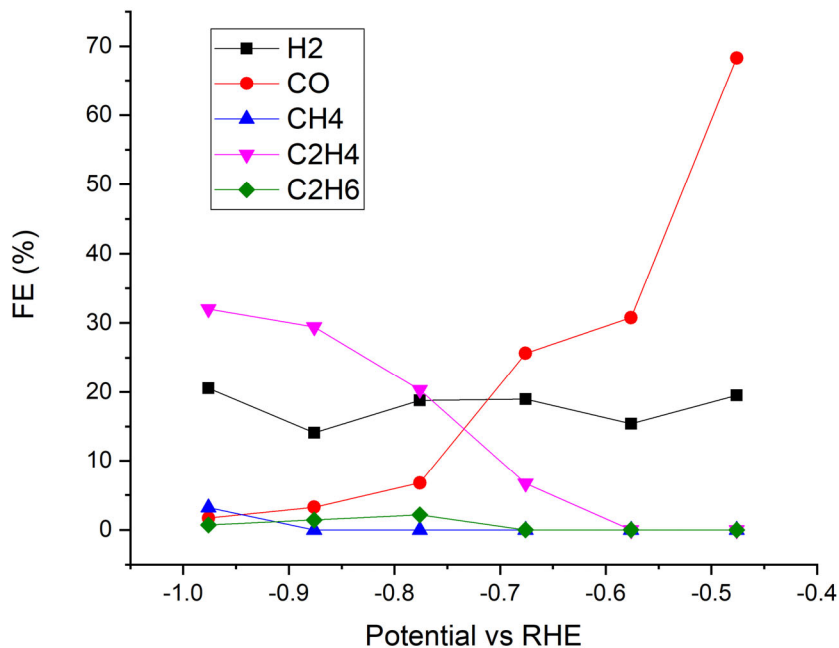


Figure 8.42: FE for products detected from D<sub>2</sub>O stored sample measured in CO<sub>2</sub> saturated D<sub>2</sub>O prepared 0.1 M KHCO<sub>3</sub> solution.

## 8.26 Cu foam after 1 hour at -0.9 V<sub>RHE</sub> spectrum

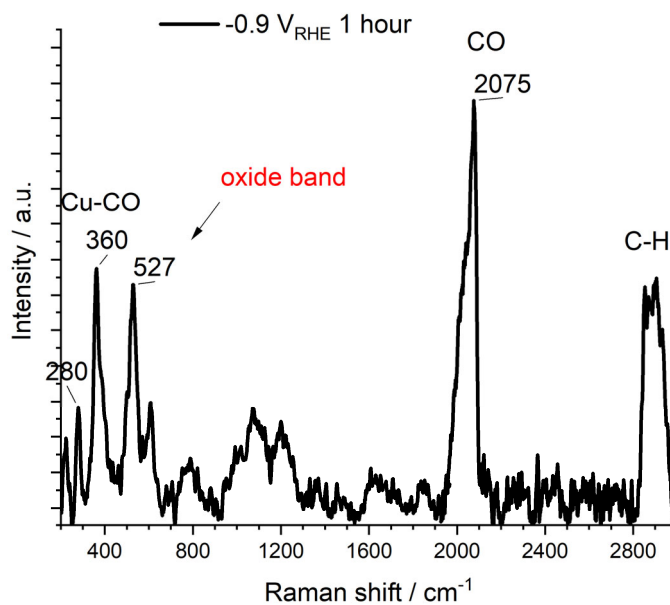


Figure 8.43: Raman spectra after -0.9 V<sub>RHE</sub> for 1 hour in CO<sub>2</sub> saturated 0.1 M KHCO<sub>3</sub>.

## Acknowledgement

Foremost, I sincerely thank my supervisor Prof. Dr. Holger Dau for inviting me to join the group, so that I can have this opportunity to learn cutting-edge techniques and to pursue a PhD degree in a free academic environment. Your attitude towards high standard scientific research and enthusiasm of pursuing science always inspires me. You always encourage us to join conferences, to communicate our science and to collaborate. It made me feel that we are seeking the answers to the questions that are of great importance to the world which I think is the meaning to do science.

I should also thank Chinese Scholarship Council for their financial support, it helps many people like me to have this valuable opportunity to study abroad.

My sincere gratitude goes to Prof. Dr. Peter Strasser for being my second supervisor. I am grateful to my defense committee.

I was lucky to have two extraordinary researchers Dr. Katharina Klingan and Dr. Luca D'Amario instructing me closely during my PhD. Thank you to Dr. Katharina Klingan for teaching me all the experimental skills patiently so that I could start quickly in the early phase. I am so grateful that you accompany me through the hard times in the beginning and help me to grow from knowing only basics to a primary researcher of CO<sub>2</sub>RR.

Thank you to Dr. Luca D'Amario for helping me with data analysis and designing a flow cell and answering my all kinds of questions and confusions explicitly. Without your encouragement, I may not have gone so far and deep in finding the message. Thank you for consistently helping me to revise manuscripts and my thesis, without it my writing skill would have not improved so much. Most importantly, I had a lot of fun in discussing with you.

There were many excellent scientists who had an influence on me. Thank you to Dr. Stefan Mebs for all kinds of help and discussions, especially for reading my thesis when it was in a raw version and patiently giving me countless useful comments. It was always fun in talking to you, thank you for being an excellent chemist who can inspire people's enthusiasm in chemistry.

Thank you to Chiara Pasquini for helping me with Raman spectroscopy and the design of Raman cell. I appreciated those insightful talks and the encouraging words. I realize a physicist can switch interest to do chemistry because it is more practical and useful to solve the urgent problems that the world is facing.

I feel lucky to have this interesting project. And I am fortunate to have received all kinds of help so that I can achieve this milestone. I would like to thank Prof. Dr. Christina Roth for the support when I was working in their lab, and my cooperation partner Dr. Tintula Kottakat for her professional help with GC and preparing CuAg foam samples. I also appreciate the technical support from Michael Labza from Prof. Dr. Christina Roth's group. I appreciated the talk with Dr. George Gordeev for his interesting suggestion. Thank you to Dr. Petko Chernev for writing so many useful softwares including glofit. The workshop helped me cut dozens of pieces of Cu substrates and design a flow cell. I appreciated that. Thank you to Mrs. Stapel for the help in ordering isotope gasses.

I am grateful to Mrs. Endrias for all the paper works regarding ordering resources and my work



here and many thanks to the supporting team of our department.

A PhD study spans more than four years. It is one of the most important periods in my life. I feel lucky that when I encountered obstacles and experienced difficulties there were always so many good friends who gave me support.

In the first three months of my study here, I had a nice time with my batch member of 2016 of Big-NSE graduate school. They helped me quickly adapt to the local life and gave me courage to face the upcoming challenges. I am very grateful that Dr. J.P. Lonjaret introduced me to Unisyscat. I would also like to thank him for organizing Unisyscat's retreat and other events for us. It is my honor to be a member of Unisyscat.

I had a lot of fun in talking with Paul Kubella, Reza Mohammadi, Sarah Mäusle, Yanqin Liang and Si Liu in our lab and office. It made my working days colorful.

Many thanks to all the group members of Prof. Dr. Holger Dau: Dr. Ivelina Zaharieva, Dr. Michael Haumann, Dr. Dennis Nürnberg, Janis Hantke, Dr. Philipp Simon, Paul Greife, Ricardo Assunção, Fan Yang, Paul Beyer, Nicholas Oliver, Neno, Younes, Jacob, Aiga and the others that have been in the group. They have made this group a lovely family.

Special thanks go to my friends: Xiuxian for being such a nice person who accompanies me through good and bad days; Yong for giving me good advice; Xuejiao for being the best roommate ever; Wei, Bodan and the others for the interesting talks.

Last but not least, I would like to thank my mother for supporting me all the way here. My grandmother inspired me to be a person who is self-disciplined and who pursues self-improvement consistently. I will always miss her. And I wish to dedicate this to her.

## List of Publications

1. **Jiang, S.**, Klingan, K., Pasquini, C. and Dau, H. (2019). New aspects of operando Raman spectroscopy applied to electrochemical CO<sub>2</sub> reduction on Cu foams. *The Journal of Chemical Physics*, *150*, 041718.
2. Klingan, K., Kottakkat, T., Jovanov, Z. P., **Jiang, S.**, Pasquini, C., Scholten, F., Kubella, P., Bergmann, A., Cuenya, B. R., Roth, C. and Dau, H. (2018). Reactivity determinants in electrodeposited Cu foams for electrochemical CO<sub>2</sub> reduction. *ChemSusChem*, *11*, 3449-3459.
3. Kottakkat, T., Klingan, K., **Jiang, S.**, Jovanov, Z. P., Davies, V. H., El-Nagar, G. A., Dau, H. and Roth, C. (2019). Electrodeposited AgCu foam catalysts for enhanced reduction of CO<sub>2</sub> to CO. *ACS Applied Materials & Interfaces*, *11*, 14734-14744.
4. **Jiang, S.**, D'Amario, L. and Dau, H. (2021). Copper carbonate hydroxide as CO precursor in CO<sub>2</sub> electroreduction. (in preparation).

## **Selbständigkeitserklärung**

Hiermit versichere ich, dass die vorliegende Dissertation eigenständig und ausschließlich unter Verwendung der angegebenen Hilfsmittel angefertigt wurde. Alle Literaturquellen sind als solche kenntlich gemacht. Die vorliegende Arbeit ist in dieser oder anderer Form zuvor nicht als Prüfungsarbeit zur Begutachtung vorgelegt worden.

.....

Shan Jiang